Towards the DRIFT-III Directional Dark Matter Experiment

Stephen W Sadler

Department of Physics and Astronomy

The University of Sheffield

A thesis submitted in partial fulfilment for the degree of

Doctor of Philosophy

February 2014

For Madre and Padre.

Abstract

There exists compelling evidence that baryonic matter constitutes only 15% of the matter budget of the Universe. Results from a diverse range of experiments suggest that the remaining 85% is in the form of weakly-interacting particle dark matter, with a particular class of particle, the WIMPs, being favoured on theoretical grounds. Recently, hints of a WIMP signal have appeared at low WIMP mass in several solid-state direct dark matter detectors. However, these appear to be at odds with the exclusion limits from the most sensitive detectors in the world, which employ liquid noble gases as their target media.

The DRIFT experiment aims to measure not only the energy, but also the directionality of WIMP-nucleon interactions, which would provide an unambiguous signal of dark matter. The current generation of the detector, the 1 m^3 negative ion time projection chamber DRIFT-IId, is currently taking data underground at the Boulby Underground Science Facility. This thesis presents work toward the next generation of the experiment, DRIFT-IIe, which is acting as a technology testbed for the planned 24 m^3 DRIFT-III detector.

The main background contributor, radon gas, is investigated, and reduced by a factor of 2 through a program of materials screening and substitution. Simplification of the electronics scheme is investigated, and found to be possible with no measurable reduction in directionality or background discrimination. A new gas mixing system for the DRIFT-IIe detector is designed and commissioned, which is more remotely-controllable and incorporates lower-cost components than its predecessor. Finally, a new technique for fiducialising events in the z dimension is presented and a new automated analysis of this data developed, which is shown to improve the efficiency for detecting WIMPs by up to a factor of 3.5.

Acknowledgements

Author's Contributions

Chapter 4. A new notch filtering routine was written by the author to allow high-frequency noise to be removed for waveforms longer than the nominal 10 ms. The introduction of a Savitzky-Golay smoothing filter to replace the previous boxcar averaging was implemented in the analysis software by the author.

Chapter 5. All radon emanation experiments and analysis were performed by the author, excepting several individual component emanation tests as highlighted in the text. The full detector emanation test was proposed and carried out by the author. This is the first time that the radon emanation rate implied by DRIFT data has been corroborated by independent measurements (using an alpha spectrometer). Substitution of low-radon alternative detector materials was the author's responsibility.

Chapter 6. The investigation of the directional capability and background discrimination of an alternative DRIFT-IId electronics configuration is a first, and was the author's work.

Chapter 7. Development, testing, installation and commissioning of the DRIFT-IIe gas mixing system was led by the author. Preliminary work with the RGA was undertaken in collaboration with Leonid Yuriev and Bernard McCluskey.

Chapter 8. The automated analysis of minority carrier DRIFT data is the first of its kind, and was performed by the author. The same is true of the technique for estimating the efficiency improvement from same-source-position neutron runs with and without an oxygen admixture.

Contents

List of Figures

Chapter 1

Introduction to Dark Matter

There is now a wealth of evidence from a wide variety of independent sources to suggest that the Universe is pervaded by unseen, weakly-interacting mass called dark matter (DM). The following chapter presents a summary of this evidence, and explores some of the constraints on the properties that DM can take. Out of an interconnected web of evidence spanning cosmology, astrophysics and particle physics will emerge the particle nature of DM, and the final section of this chapter introduces several well-motivated candidate particles along with brief overviews of the theories from which they appear.

1.1 ΛCDM Cosmology

Considering the Universe as an isotropic, homogenous, expanding medium, and invoking energy conservation, the Friedmann Equation (Equation 1.1) can be derived to describe its time evolution [1]:

$$\left(\frac{\dot{a}}{a}\right)^2 = \frac{8\pi G}{3}\rho - \frac{kc^2}{a^2},\tag{1.1}$$

where k is the geometry parameter (negative for a closed Universe, positive for an open Universe, and zero for a flat Universe), ρ is the mean mass density, and a is the 'scale factor': a time-dependent number describing the overall size of the Universe. G is the gravitational constant ($6.67 \times 10^{-11}\ \mathrm{N\,m^{-2}\,kg^{-2}}$) and c is the speed of light ($3.00 \times 10^8\ \mathrm{m\,s^{-1}}$). The left hand side of the equation is equal to H^2, where H is the

1

(time-dependent) Hubble parameter:

$$\dot{a}(t) = H(t)a(t). \tag{1.2}$$

Enshrined in this equation is the observation that wherever we look in the Universe, galaxies and clusters of galaxies are receding with velocity proportional to their distance, one of the most important discoveries of 20th Century cosmology [2]. The proportionality constant at the present epoch has been measured many times since the publication of Hubble's 1929 paper, with the most recent measurement coming from the Planck collaboration [3]:

$$H(0) = 100h = 67.3 \pm 1.2 \, \text{km} \, \text{s}^{-1} \, \text{Mpc}^{-1}, \tag{1.3}$$

where h is known as the 'reduced Hubble parameter'. This result is in slight tension with previous previous measurements, for example the 9-year WMAP data which yields a slightly higher value of $H(0) = 69.3 \pm 0.8 \, \text{km} \, \text{s}^{-1} \, \text{Mpc}^{-1}$ [4]. The critical density, ρ_c, required to produce a flat 'Euclidian' ($k = 0$) geometry can be calculated by substituting this measurement into Equation 1.1, yielding a value of:

$$\rho_c = (1.265 \pm 0.022) \times 10^{11} \, M_\odot \text{Mpc}^{-1}, \tag{1.4}$$

which sets a natural scale for the density of the Universe and leads to a definition of the 'density parameter':

$$\Omega(t) \equiv \frac{\rho(t)}{\rho_c}. \tag{1.5}$$

A density parameter of unity therefore implies a flat Universe. The fact that 1 Mpc is the typical observed separation between galaxies, and that 10^{11} $M_\odot$ is the mass of a typical galaxy suggests that the true density of the Universe cannot be far removed from ρ_c [1], and indeed this has been confirmed by observations of oscillations in the CMB temperature power spectrum by the space-based experiments COBE [5], WMAP [6], and most recently and precisely Planck [3] (see Section 1.2.2 for details). There are three principal contributors to Ω at the present epoch, as shown by Equations 1.6 and 1.7:

$$\Omega = \Omega_m + \Omega_\Lambda, \tag{1.6}$$

Parameter	Value	Description
H_0	67.3 ± 1.2	Present-day Hubble parameter
Ω_m	0.314 ± 0.020	Matter density parameter
Ω_b	0.0486 ± 0.0016	Baryonic matter density parameter
Ω_{DM}	0.263 ± 0.010	Cold dark matter density
Ω_λ	0.686 ± 0.020	Dark energy density parameter
N_{eff}	3.30 ± 0.27	Number of relativistic degrees of freedom

Table 1.1: Cosmological parameters measured by the Planck experiment [3]. Uncertainties are 1σ confidence intervals.

where

$$\Omega_m = \Omega_b + \Omega_{DM}. \tag{1.7}$$

Here, the subscripts m, Λ, b and DM represent matter, dark energy, baryonic matter and dark matter, respectively. CMB experiments have successfully measured the contributions to Ω from each of these components (under certain cosmological assumptions, including that of a flat Universe), which are presented in Table 1.1. One of the most striking results is that the energy density of matter accounts for only 31% of the total energy density of the Universe, the remainder being attributed to some form of dark energy which exerts a negative pressure, counteracting gravity and giving rise to the observation that the expansion rate of the Universe at the current epoch is actually accelerating [7]. In the ΛCDM model, this dark energy takes the form of Einstein's 'Cosmological Constant' Λ: a zero-point energy field that pervades the vacuum of space-time. Quantum Field Theories predict the existence of such a field, but a discrepancy of order 10^{120} exists between the natural scale for the energy density and the value observed by experiments such as Planck. This has come to be known as the Cosmological Constant Problem [8].

Another important result from Table 1.1 is that only around 15% of the matter density Ω_m can be accounted for with baryons. The remaining 85% of the matter density is in the form of thus-far unseen cold dark matter (CDM), which turns out to play a crucial role in the formation of the large-scale structure of the Universe as observed today.

1.2 The Case for Dark Matter

1.2.1 Motion Within Galaxies

The existence of DM was first postulated in 1933, by a Swiss astrophysicist called Fritz Zwicky working at the California Institute of Technology [9]. Zwicky observed that the velocities of 8 galaxies in the Coma cluster were too high to be consistent with the luminous mass of the cluster, which led him to conclude that there must be some unobserved gravitating DM holding the cluster together. Applying the virial theorem to a galaxy cluster of mass M, velocity dispersion $\langle v^2 \rangle$ and radius r, and the total dynamical mass of the cluster can be estimated as

$$M = \frac{2r\langle v^2 \rangle}{G}. \tag{1.8}$$

When Zwicky substituted his measured values of r and $\langle v^2 \rangle$ for the Coma cluster, he discovered that the mass required to keep the cluster gravitationally bound was ≈ 400 times that which was observed. In fact, Zwicky's assumed value of the Hubble constant, $H_0 = 558 \ \mathrm{km\,s^{-1}\,Mpc^{-1}}$, was wrong by a factor of 8, the current best estimate at the time of writing coming from Planck: $H_0 = 67.3 \pm 1.2 \ \mathrm{km\,s^{-1}\,Mpc^{-1}}$ [3]. Substituting this value of H_0 leads to an only-slightly-less-compelling required overdensity of $\times 50$. Three years later, Sinclair Smith observed a similar overdensity in the Virgo cluster [10], confirming the existence of a non-luminous component of mass at cosmological scales.

An independent source of evidence for DM was discovered in 1970 by Rubin and Ford, who made observations of the spectrum of the M31 (Andromeda) galaxy at various distances from the galactic centre. Andromeda appears almost edge-on to the Milky Way, which allows a direct measurement of the rotation velocity at a given radius to be made by measuring the Doppler shift of known spectral lines.

According to Newtonian gravity, the gravitational force between a point test mass m and a spherically-symmetric extended mass $M(r)$, separated by a distance r is given by

$$F = G\frac{mM(r)}{r^2}. \tag{1.9}$$

In a spiral galaxy, a radiating gas cloud can suffice as a test mass, whilst the extended

mass $M(r)$ represents the total mass of the galaxy interior to radius r. In the rest frame of the galaxy, this gravitational attraction provides the centripetal force necessary to maintain the circular orbit of the test mass:

$$F = \frac{mv_{rot}^2(r)}{r},$$

(1.10)

where v_{rot} is the tangential velocity of the test mass on a circular orbit about the galactic centre. Combining Equations 1.9 and 1.10 yields the expected form of $v_{rot}(r)$ according to Keplerian dynamics,

$$v_{rot} = \sqrt{\frac{M(r)G}{r}}.$$

(1.11)

Equation 1.11 predicts that in the outer regions of Andromeda, where the mass is a slowly varying function of orbital radius, the rotational velocity of gas cloud test masses should fall off as $1/\sqrt{r}$. Instead, Rubin and Ford found that the curve approached a constant value (≈ 200 km s^{-1}), and remained flat out to the limit of their optical observations at 24 kpc. Figure 1.1 shows 14 M31 rotation curves presented in their 1970 paper [11].
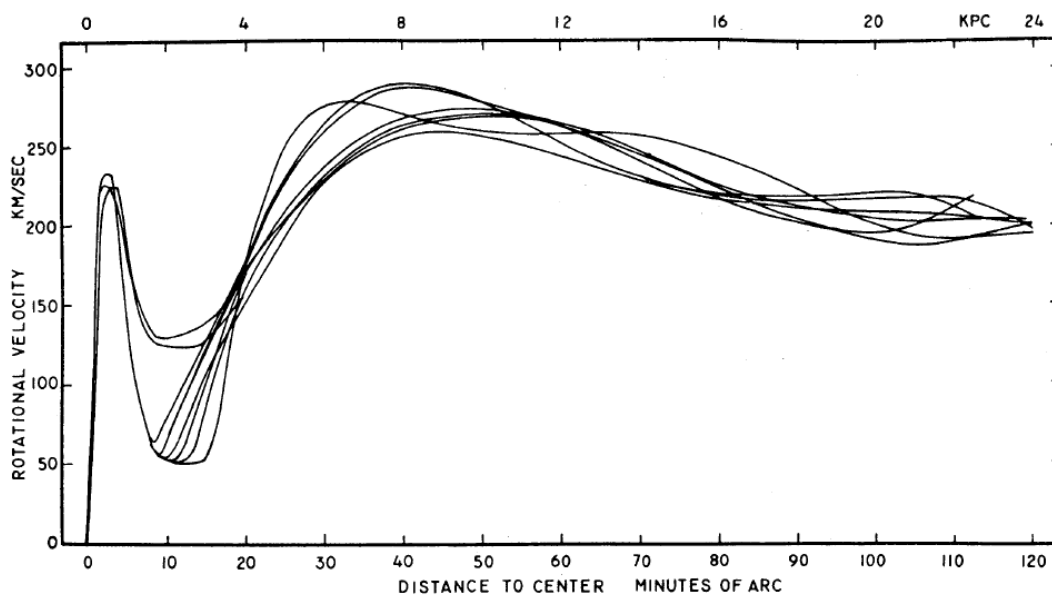
Figure 1.1: 14 rotation curves of M31(Andromeda) measured by Rubin and Ford. Reproduced from Rubin and Ford Jr. [11].

In their 1975 paper, Roberts and Whitehurst [12] presented measurements of the hydrogen 21 cm emission line of Andromeda, which extended its measured rotation curve to 35 kpc. The curve they measured was unambiguously flat across half of the disc, including the region outside the limit of the luminous mass at $\approx$ 24 kpc. There was now clear evidence that M31 contained at least 10$\times$ more unseen matter than visible matter, as well as mounting evidence from 21 cm studies of other galaxies (see, for example, Bosma [13]).

1.2.2 Cosmic Microwave Background

Since its serendipitous discovery by Penzias and Wilson in 1965 [14], the Cosmic Microwave Background (CMB) has been revealing the secrets of the very early Universe. Its light originated at the surface of last scattering 380,000 years after the Big Bang when temperatures fell below $\sim$ 3000 K, allowing photons to decouple from matter and free-stream through the Universe. What is observed today is a very uniform emission from all regions of the sky, with a temperature that has been reduced by the expansion of the Universe to 2.73 K. Small temperature fluctuations do exist however, and these reveal the seeds of structure that would go on to form galaxies and galaxy clusters. The most recent measurements of the energy density composition of our Universe by the Planck CMB experiment have been presented in Table 1.1. These measurements are a probe of the matter content of the Universe, and provide direct evidence that the majority of this mass is non-baryonic.

In order to obtain estimates for the various density parameters of Table 1.1, a baseline cosmological model, ΛCDM, is assumed, and its $\sim$ 10 free parameters are determined using a maximum likelihood fit to the acoustic peaks ($100 \lesssim l \lesssim 1000$) in the measured CMB power spectrum shown in Figure 1.2 [15]. In this plot, increasing multipole moment l corresponds to decreasing length scales. The peaks in this spectrum arise from oscillations in the plasma before the surface of last scattering, which became 'frozen in' when photons decoupled from matter. The positions and relative heights of the peaks contain information about the overall density, and the density of baryons in the plasma at the instant of photon decoupling, respectively. These are used to extract estimates for the parameters of the ΛCDM model, including the matter density of CDM, Ω_{DM} (see Table 1.1). Whilst this estimate is strongly model-dependent,

Section 1.2.3 will reveal that it is in good agreement with the results of a completely different technique based upon measurements of elemental abundances at the present epoch.
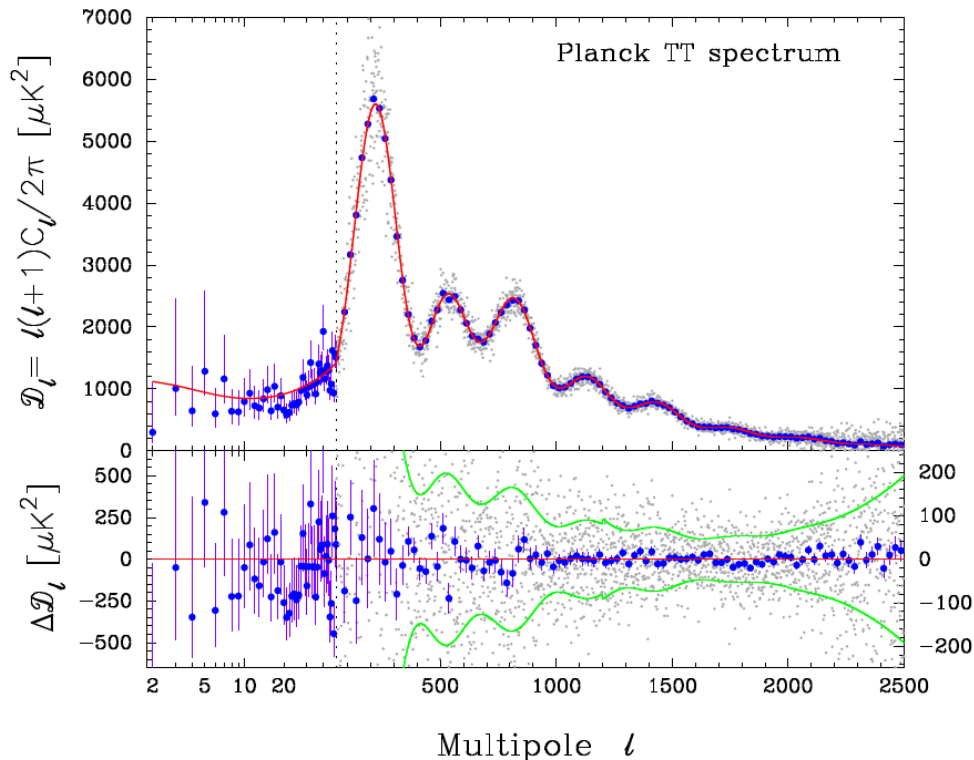
Figure 1.2: Temperature power spectrum of the CMB, as measured by the Planck experiment. Increasing multipole moment corresponds to decreasing length scales. Blue points: data averages in bins of width $\Delta l \approx 31$. Red line: temperature spectrum from the best-fit base ΛCDM cosmology. The position and height of the peaks encodes information about the density components of the early Universe. Green lines: $\pm 1\sigma$ errors on the individual power spectrum estimates. Reproduced from Ade et al. [3].

The CMB can also be used as a probe of the number of relativistic particle species in the early Universe, N_{eff}, since this number affects the radiation density. The radiation density, in turn, modifies the high-l damping tail of the temperature power spectrum (Figure 1.2) by increasing the expansion rate before the surface of last scattering, thereby providing a handle on N_{eff} [3]. This number will be important in Section 1.3.5, where sterile neutrinos are considered as a potential DM candidate.

1.2.3 Big Bang Nucleosynthesis and the Concordance Model

An independent estimate of Ω_b, and hence the fraction of matter in the Universe that is baryonic, is provided by the measured abundances of light elements at the present epoch [15]. This is determined in large part by primordial nucleosynthesis during the first three minutes after the Big Bang, when the light isotopes ^{2}H (d), ^{3}He, ^{4}He and ^{7}Li were forged in its afterglow.

Before the Universe was ~ 1 s old, temperatures were high enough to maintain thermal equilibrium in weak interactions:

$$p + e^- \longleftrightarrow n + \nu \tag{1.12}$$

$$n + e^+ \longleftrightarrow p + \bar{\nu}. \tag{1.13}$$

As the temperature dropped, the ratio of protons to neutrons (n/p) fell as

$$n/p = e^{-Q/T}, \tag{1.14}$$

where Q is the neutron-proton mass difference. The neutron-proton inter-conversion rate is proportional to T^5, whereas the Hubble expansion rate of the Universe drops as T^2, so at a critical temperature, T_{fr} (~ 1 MeV), the n/p ratio 'froze out' at a value of $\sim 1/6$. Free neutrons are unstable to β decay with a mean lifetime of 615 s (Equation 1.15), and their decay resulted in a reduction of n/p to $\sim 1/7$ before 100 s after the Big Bang. At this time the temperature fell below 0.1 MeV, allowing the neutrons to interact with protons to form deuteron (Equation 1.16).

$$n \rightarrow p + e^- + \bar{\nu} \tag{1.15}$$

$$p + n \longleftrightarrow d + \gamma. \tag{1.16}$$

The newly-formed deuterons were then able to interact with each other and the remaining protons and neutrons to form ^{3}H, ^{3}He and ^{4}He. By 180 s after the big bang, the temperature had become too low for any of these reactions to overcome the Coulomb barrier and the primordial abundances were 'frozen in'. The ultra-stable ^{4}He dominated the primordial mass fraction, Y_p, with 25% of the mass. The remaining 75% is accounted for by free protons (that would go on to form hydrogen atoms), and trace

amounts of the other light isotopes, including d, ^{3}He and ^{7}Li.

These interactions all obey well-understood standard model (SM) physics, and can be modelled to produce predictions for relative abundances of the various species at the end of the big bang nucleosynthesis (BBN) process [16]. If one chooses to adopt the N_{eff} inferred from CMB measurements, then the BBN models contain a single free input parameter: the baryon-to-photon ratio $\eta = n_b/n_\gamma$, and output the relative abundances of the light elements discussed above. Furthermore, if one chooses to fix n_γ to the value implied by the CMB temperature, this can be converted into a dependence on the baryon density, Ω_b.

The solid, coloured curves in Figure 1.3 show the abundances of light elements output by such simulations. The white and yellow boxes in this figure represent as-
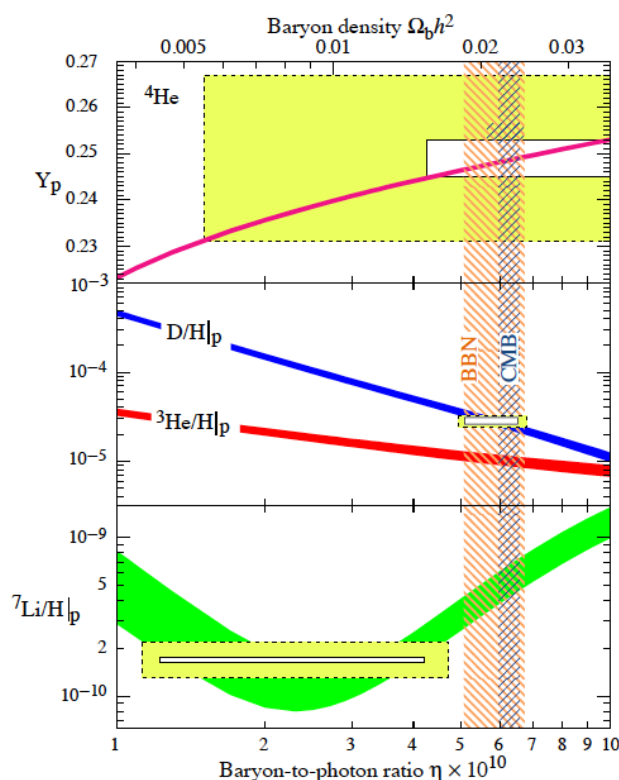
Figure 1.3: Light element abundances as predicted by the standard model of Big Bang nucleosynthesis. Yellow boxes represent 2σ confidence statistical errors + systematic errors. The blue hatched vertical band represents the CMB measurement of the baryon density, Ω_b (see Section 1.2.2). From Beringer et al. [15].

tronomical measurements of various elemental abundances. The white regions include only statistical errors, whilst the yellow ones include both statistical errors, and systematic errors arising from astrophysical processes that may have altered the abundances between the era of BBN and the present time. Of particular interest is the deuterium abundance shown in the second panel, which is measured via Lyman-α absorption in high-redshift, low-metallicity quasars [17]. Since there are no known astrophysical processes that produce deuterium, any measurement of the deuterium abundance can be taken as a lower limit on its primordial mass fraction, implying an upper limit on the baryon density parameter Ω_b. The lack of a production mechanism for deuterium also means that it does not suffer from many of the astrophysical processing systematic errors that the other light elements do, which explains the comparatively small uncertainties on this measurement.

There is impressive agreement between the model prediction (blue curve) and measured value (white/yellow boxes) for the baryon density parameter implied by deuterium abundance in Figure 1.3. Furthermore, the value of $\Omega_b h^2$ that this implies ($0.019 - 0.024$) provides very good agreement between model and prediction for the mass fraction of ^{4}He (top panel), and also agrees remarkably well with the value of Ω_b derived from the acoustic peaks of the CMB temperature power spectrum (see Section 1.2.2). There is some tension with the Lithium abundance (bottom panel), which may be a sign of new physics, or possibly the result of an uncontrolled systematic error in the properties of the Population II stars from which these abundances are derived. The Lithium Problem is an ongoing topic of research [18, 19], but setting this to one side, the BBN and CMB results provide a firm foundation to what has become known as the concordance model of modern cosmology. Contrary to our everyday experience, we live in a Universe dominated by dark energy, and the small contribution that matter does make to the energy budget of the Universe is dominated by non-baryonic and as-yet undetected new particles.

1.2.4 Gravitational Lensing

Gravitational lensing is the bending of the space-time of General Relativity by a concentration of mass. Observationally, this manifests itself as the brightening or distortion of background celestial bodies by unseen massive objects in the line of sight

between them and the observer [20]. The technique has been used to search for populations of dark objects of all scales, from microlensing surveys within the Milky Way [21] to dramatic strong lensing images of high redshift galaxies distorted by galaxy-cluster scale concentrations of DM [22], to whole-sky weak lensing surveys measuring the 'cosmic shear' on cosmological scales [23].

Gravitational lensing as a probe of DM in our own Galaxy was first proposed in 1986 [24] by Bohdan Paczynski. He suggested that, by monitoring changes in brightness of background stars for a period of $\gtrsim$ 2 yr, it should be possible to detect 'dark halo objects' such as black holes, brown dwarfs and unassociated planets within the Milky Way, if they were causing lensing. In order to put constraints on the mass of DM in the Galactic halo, several million stars would have to be monitored, and since the minimum detectable mass scales as $\frac{1}{D_s}$, where D_s is the distance to the source, by observing stars in a nearby galaxy such as the Large Magellanic Cloud (LMC) the technique had the potential to be sensitive to objects as small as a 1000 km asteroid [24]. Surveys of this kind were attempted by several groups including the MACHO (for Massive Compact Halo Objects) collaboration [25]. However, their 5.7 yr survey of 12 million LMC stars revealed only 13–17 microlensing events. With a careful calculation of their detection efficiency, this detection rate was used to rule out a 100% MACHO halo at the 95% confidence level, and to estimate the MACHO mass within 50 kpc to be $9^{+4}_{-3} \times 10^{10}$ M$_\odot$: a number similar to the total mass in stars, but only 17% of the total mass of the Milky Way [26]. Thus, the question of whether or not the missing mass in spiral galaxies could be explained by a population of baryonic DM (brown dwarfs or black holes, for example) was answered, and attention has since focused on particle DM of an as-yet unknown origin.

It is possible to learn a great deal about mass distributions on larger scales by conducting whole-sky surveys and analysing the very weak distortions of shape (shear) and magnification (convergence) of background galaxies by foreground galaxies, galaxy clusters, or the large-scale Cosmic Web [27]. In weak lensing surveys, a large sample of background galaxies is collected in an area of the sky under study, and some basic assumptions made about its properties. One important assumption for the case of a sample of elliptical galaxies is random orientation. The convergence and shear are computed for each background galaxy, and the results treated statistically in order to reduce or remove the confounding effect of intrinsic galaxy morphology, to reveal the

properties of the intervening lensing mass under study. This technique has been applied to large numbers of galaxy clusters by groups such as the Deep Lens Survey [28, 23] and the Canada-France-Hawaii Telescope Wide Synoptic Legacy Survey [29], and the results reveal that the total mass in clusters is also dominated by DM.

One particularly important weak lensing study was carried out on the Bullet cluster, which is actually two galaxy clusters that passed through one another 0.1–0.2 Gyr ago [30]. A composite false-colour image of the cluster is shown in Figure 1.4, where red represents the previously-measured x-ray emission from baryonic hot gas, and blue represents the mass profile reconstructed using weak gravitational lensing of background galaxies [30]. There is a clear separation between the visible mass and the lensing-inferred mass, indicating that whilst the baryonic hot gas was slowed by collisions during the merger, a dark component making up the majority of the mass in both of the clusters continued on its initial trajectory, experiencing weaker, if any, interactions that would otherwise have slowed it down. This result is very difficult to explain with theories that attempt to modify gravity, such as Modified Newtonian Dynamics (MOND) [31], and can be taken as direct evidence for the existence of feebly-interacting DM.
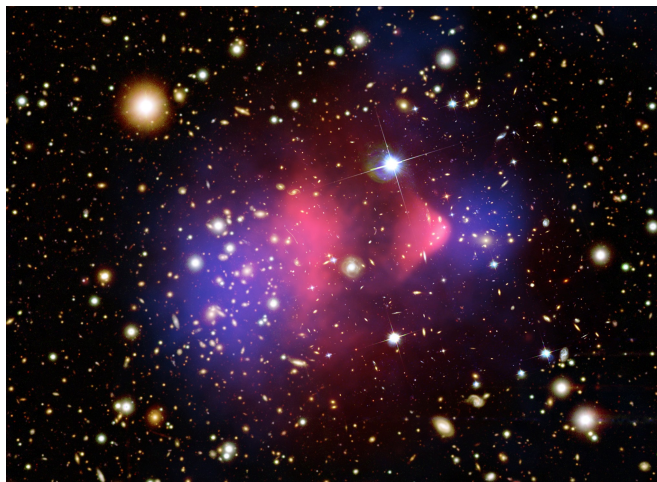
Figure 1.4: Composite image of the Bullet cluster, showing hot x-ray gas (red) and the mass distribution inferred from weak gravitational lensing (blue). During the merger, the baryonic matter traced by the x-ray emission was slowed by collisions, whereas the collisionless DM interacted only gravitationally and continued more-or-less unimpeded [30].

Weaker still are the lensing effects caused by galaxy-galaxy lensing, where both the background source and foreground object under study are individual galaxies. Results from large surveys of such systems probe the total DM mass and distribution within galaxies, and can be used to constrain models of galactic DM halos, such as the Navarro-Frenk-White (NFW) profile introduced in Chapter 2.

The weakest, and largest-scale, of the weak lensing effects is cosmic shear, which is caused by the bending of light around the large-scale structure of the Universe, as shown in Figure 1.5. Measurements of cosmic shear only became possible with the maturation of CCD readout technology in the late 90s, before which time irregularities in photographic plates obscured the subtle percent-level brightness variations that trace out the shapes of faint elliptical background galaxies. Analysis of the orientation of these shapes allows the computation of the convergence and shear [32], which can be used to probe the properties of the superclusters, walls, filaments and voids that make up the large-scale structure of our Universe [23]. In analogy to the acoustic peaks of the CMB temperature power spectrum (see Section 1.2.2), it can be used to find Ω_m and σ_8, which are the free parameters in the DM angular power spectrum of Equation 1.17 (see, for example, Fu et al. [33]):

$$P_\kappa(\theta) \sim 10^{-4} \sigma_8 \Omega_m^{1.5} z_s^{1.5} \theta^{-(n+2)}, \tag{1.17}$$

where $P_\kappa(\theta)$ is the angular power spectrum as a function of angle subtended on the sky θ, Ω_m is, as usual, the total matter density parameter, σ_8 is the standard deviation of background galaxy count fluctuations, z_s is the mean redshift of background galaxies, and n is the spectral index, which is usually fixed to unity. This measured power spectrum can be compared with the output of simulations of large-scale structure formation, which are the subject of the following section.

1.2.5 Large-Scale Structure Formation

The inexorable advance of modern computing power made possible, in 2005, the first high-resolution simulation of the Universe's large-scale structure [34]. The Millennium Simulation modelled the evolution of the Universe by tracking the motion of 10 billion particles from redshift z = 127 to the present day, in a cubic volume of space-time of side $500h^{-1}$ Mpc. A smaller simulation called MS-II was also performed, in a cubic
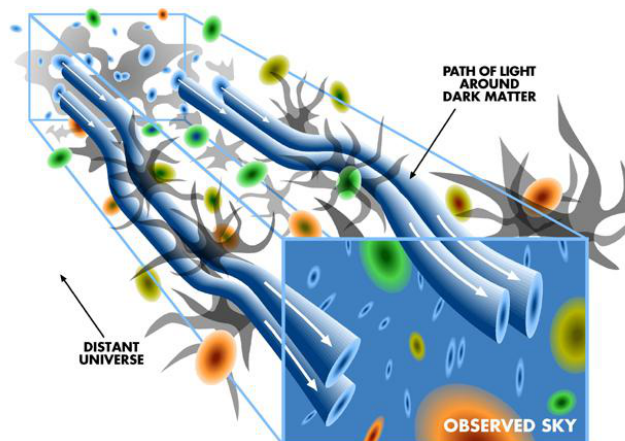
Figure 1.5: Cartoon showing the distortion of light rays by the gravitational potential of large-scale structure. Measuring these distortions gives us a handle on the cosmology that underlies them. From Wittman et al. [27].

volume with sides 5× shorter, giving 125× greater mass resolution, and enabling more detailed structure to be resolved [35]. Structure was observed to form in a 'bottom up' fashion, with galaxies, clusters, filaments and walls forming around regions of space-time with slight over-density of mass. These over-densities are the result of quantum fluctuations in the pre-inflation Universe, which were expanded to macroscopic scales to form the seeds of structure during the first 10^{-32} s after the Big Bang. It is the red-shifted relic of these early over-densities that we observe today as the CMB radiation.

The large-scale structure maps generated by the Millennium Simulation are almost indistinguishable by-eye from those obtained from galaxy redshift surveys [36] (see Figure 1.6). More quantitative analyses of clustering, and of the power spectrum introduced in Section 1.2.4, are also in excellent agreement with data [34]. The simulation was based upon the ΛCDM cosmology introduced in Section 1.1, the parameters of which have been determined experimentally using the techniques outlined in the preceding subsections. Its success in producing a Universe that looks the same as that which we observe is further confirmation of the validity of the DM- and dark-energy-dominated ΛCDM cosmology. The simulations also showed that it is only possible to
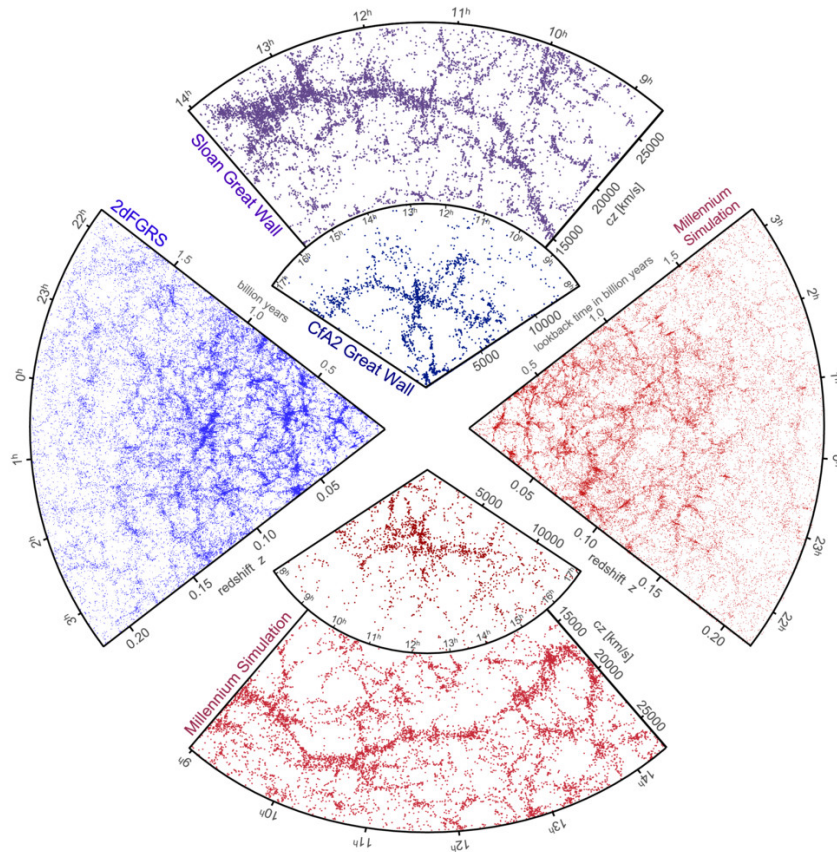
Figure 1.6: Maps of the Universe's large-scale structure from data (blue, purple), and the Millennium simulation (red). From Springel, Frenk, and White [36].

produce a Universe with the density contrast which we observe by requiring a dominant DM component that is *cold*: that is, moving with extremely non-relativistic velocity [37]. Any faster, and the DM 'smooths out' the over-densities and retards structure formation on the timescales that we observe. Simulations based upon modified gravity have been attempted, but failed to produce large-scale structure resembling that which we observe [38].

1.3 Particle Candidates

Section 1.2 presented the evidence, from multiple, independent measurements and simulations, that the Universe's mass is dominated by non-baryonic particle DM that in-

teracts very weakly, if at all, with baryonic matter. The following section explores a few examples of what this DM might be.

A 2008 paper by Taoso, Bertone and Masiero gives a 10-point checklist for a good DM candidate [39]:

1. Does it match the appropriate relic density Ω_{DM}?

2. Is it cold?

3. Is it neutral?

4. Is it consistent with Big Bang nucleosynthesis?

5. Does it leave stellar evolution unchanged?

6. Is it compatible with constraints on self-interactions?

7. Is it consistent with direct DM searches?

8. Is it compatible with gamma-ray constraints?

9. Is it compatible with other astrophysical bounds?

10. Can it be probed experimentally?

Point 1 requires a production mechanism that can provide the observed density, Ω_{DM}, which also implicitly requires that the candidate is stable (has a lifetime longer than the age of the Universe). Point 2 requires the DM to be cold, that is, moving at non-relativistic speeds at the surface of last scattering. This is required to generate the large-scale structure of the Universe. Point 3 arises from the fact that a DM particle charged under U(1) would be observable through its electromagnetic interactions, although one variety of charged DM has been proposed [40]. Point 4 requires that the proposed particle does not interfere with the formation of light elements in the early Universe discussed in Section 1.2.3. Point 5 considers the effects of light DM production as an energy loss mechanism for stars. Adding an energy loss mechanism to stellar astrophysics modifies observables such as stellar lifetimes, neutrino output, and the sound speed profile [39]. The capture or annihilation of DM may also affect stellar evolution [41]. Point 6 concerns DM self-interaction. Self-interacting dark matter

(SIDM) has been proposed as a solution to the 'cuspy core' and 'missing satellite' problems introduced later in Section 2.2.2; however, a tight upper limit is placed upon the strength of DM self-interactions by observations of the Bullet Cluster (see Section 1.2.4) [42]. Points 7–10 confront the proposed candidate particle with data from experimental searches, which will be described in more detail in Chapter 3. A detailed treatment of how the data constrains each of the theories that provide a DM candidate is beyond the scope of this thesis. Suffice it to say that for each of the models considered in this section, there is at least some area of parameter space in which the DM candidate can evade all observational constraints.

Particles that fit the above criteria can be broken down into two categories: WIMP and non-WIMP candidates. WIMPs, or Weakly Interacting Massive Particles, are those that feel the weak force and have a mass related to the 'weak scale' ($\sim$ TeV). These arise in extensions to the standard model, whether as a welcome byproduct as in theories such as supersymmetry (SUSY) [43], or by construction as in, for example, Minimal Dark Matter [44]. For any DM candidate particle, the experimentally-accessible properties are the rest mass, M_W, and the cross section for interaction with the chosen target nucleus (σ_{WN}).

WIMP models seek to explain the observed Ω_{DM} by a process of freeze-out in the early Universe. In the very early Universe, at energies $E \gg M_{W,Z}$, the DM was in thermal equilibrium and produced in equal abundance with all other electro-weak particles, being created and annihilated at an equal rate such that its number density remained constant. At some point (dependent upon M_W) the energy dropped low enough to suppress the pair production of DM, but the number density was still high and therefore WIMP-anti-WIMP pairs continue to annihilate, causing the number density of DM to fall. At still lower energies, the expansion of the Universe caused the number density to drop so low that the chance of two DM particles meeting became negligible, and the number density 'froze out'. The density at which this freeze-out occurred is dependent upon the DM annihilation cross section according to Equation 1.18 [45]:

$$\Omega_{DM}h^2 \approx \frac{10^{-37}\text{cm}^2}{\langle\sigma_{ann}v\rangle},\tag{1.18}$$

where $\langle\sigma_{ann}v\rangle$ is the thermally-averaged self-annihilation cross section times relative velocity [46]. Substituting the measured value of $\Omega_{DM}h^2$ yields an expected value of

17

$\langle \sigma_{ann} v \rangle \approx 3 \times 10^{-26}$ cm^3 s^{-1} [47]. This is typical of annihilation cross sections at the weak scale, suggesting a link between DM and the weak force that has been dubbed the 'WIMP miracle' (Figure 1.7).
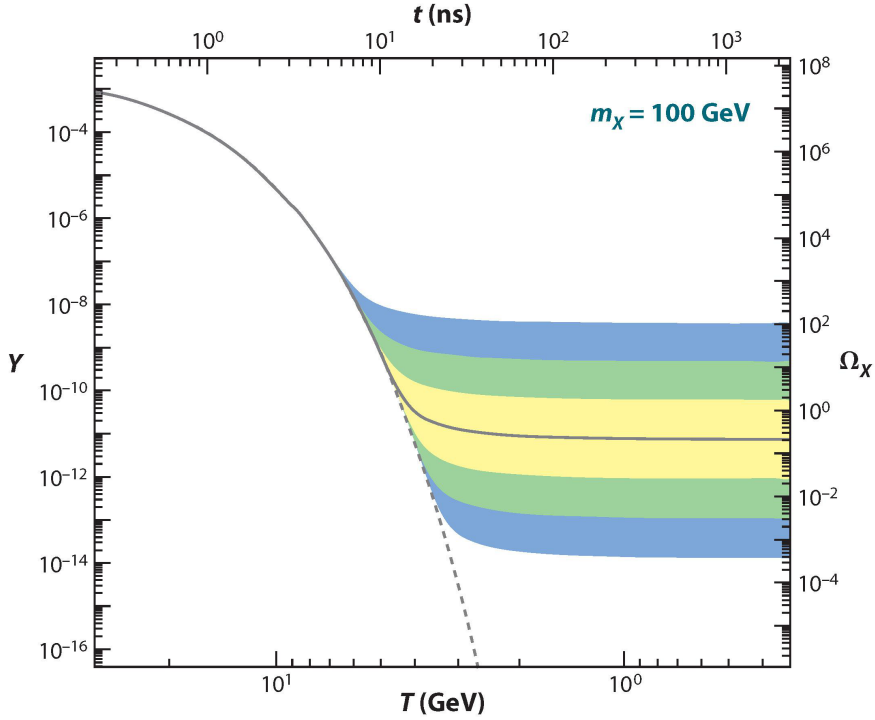
Figure 1.7: The WIMP miracle. As the energy density in the early Universe falls, the density of WIMPs 'freezes out'. Requiring the density at freeze out to be equal to its present-day value leads to an annihilation cross section at the weak scale. From Feng [48].

1.3.1 SUSY and the Gauge Hierarchy Problem

The most popular theory to explain the link between DM and the weak force was devised to solve not the DM problem, but rather another long-standing problem in particle physics: that of gauge hierarchy.

The gauge hierarchy problem refers to the question of why the Higgs boson of the SM has a mass $m_h = 126$ GeV [49] that is so much smaller than its natural scale, the Planck mass $M_{Pl} \sim 1.2 \times 10^{19}$ GeV. In the SM, the Higgs mass can be written down,

taking an effective field theory approach, as

$$m_h^2 = m_{h0}^2 + \Delta m_h^2, \text{ where} \tag{1.19}$$

$$\Delta m_h^2 \sim \frac{\lambda^2}{16\pi^2} \Lambda^2. \tag{1.20}$$

Here, m_h is the Higgs mass, m_{h0} is the tree-level contribution to this mass, Δm_h is the contribution from higher-order diagrams, λ is a dimensionless coupling of order unity, and Λ is the energy scale above which the SM is no longer a valid description of Nature [48]. In the SM, $\Lambda \sim M_{Pl}$, which would imply an extremely large higher-order correction to the Higgs mass, and require an unreasonably large degree of fine-tuning between m_{h0} and Δm_h in order to recover the measured value of the Higgs mass. This problem can be overcome if instead $\Lambda \lesssim 1$ TeV: in other words, if there is new physics at around the weak scale.

Supersymmetry (SUSY) is a group of theories that attempt to solve the gauge hierarchy problem by the addition of a new set of particles: the so-called 'super-partners'. For every SM particle, a new super-partner is added which shares many of the properties of its SM partner. The two exceptions are the spin quantum number, where the super-partners of fermionic SM particles are themselves bosons (and vice-versa), and the super-partner masses, which are not predicted by the theory, but are expected to be around the weak scale in order to automatically solve the gauge hierarchy problem. The super-partners add opposite-sign contributions to the Higgs mass correction (Equation 1.20), which becomes

$$\Delta m_h^2 \sim \frac{\lambda^2}{16\pi^2} \left(m_{\text{SUSY}}^2 - m_{\text{SM}}^2 \right) \ln \frac{\Lambda}{m_{\text{SUSY}}}, \tag{1.21}$$

where m_{SM} and m_{SUSY} are the masses of the SM particles and their super-partners. Replacing the Λ^2 dependence with the weaker $\ln \Lambda$ dependence ensures that $\Delta m_h \lesssim m_{h0}$, even for $\Lambda \sim M_{Pl}$ [48].

Many variants of the theory also add a new multiplicative quantum number: 'R-parity', which is +1 for SM particles and −1 for super-partners. Requiring R-parity conservation ensures that the lightest supersymmetric particle (LSP) is stable against decay, and therefore provides a WIMP DM candidate (the neutralino χ) for theories in which the LSP is neutral [43]. Supersymmetric particles should be produced in

interactions of SM particles provided there is enough energy available to create them. Searches with the Large Hadron Collider's ATLAS [50] and CMS [51] detectors have so far discovered no evidence for supersymmetric particles, instead ruling out large portions of parameter space and placing constraints on such theories. There remains, however, plenty of scope for SUSY theories to evade the constraints.

1.3.2 Minimal Dark Matter

Motivated by simplicity, the theory of minimal dark matter (MDM) [44] seeks to add a single electro-weak multiplet χ to the SM, in order to provide a DM candidate. Multiplets up to order 8 were considered, and checked to ensure a) neutral electric charge b) stability against decay into SM particles, and c) compatibility with direct detection bounds (Table 1.2). Two good DM candidates emerged from the exercise: a fermionic 5-plet (green) and a scalar 7-plet (yellow). The scalar multiplet was ruled out on the basis that it may have non-minimal quartic couplings to the Higgs field, leaving a single, fermionic 5-plet as the preferred DM candidate.

The theory has only a single free parameter: M_χ. If we assume that DM is made up of a single MDM component, then we can write the implied relic density as a function of M_χ and, equating this to the measured relic density (Table 1.1) may infer a mass of 9.6±0.2 TeV for the DM particle [52]. This is broadly in line with the 'weak scale' mass expected from the WIMP miracle, the slight enhancement coming from Sommerfeld corrections to the annihilation cross section [53]. The mass, in turn, implies a spin-independent WIMP-nucleon interaction cross section of $\sim 10^{-44}$ cm^2 [52], which is a region of parameter space just starting to be probed by direct DM search experiments.

1.3.3 Kaluza-Klein Particles and Universal Extra Dimensions

Another weak-scale DM candidate is provided by the theory of Universal Extra Dimensions (UED), which is based upon ideas of Kaluza and Klein dating back to the 1920s [54]. The simplest incarnation of UED invokes a single, compactified extra dimension of size $R \lesssim 10^{-18}$ m, within which the particles of the SM, as well as their 'KK partner' particles may propagate. There are an infinite number of these partner particles for each of the SM particles, with masses $m_{KK}(n) \sim nR^{-1}$, where n is an integer representing the Kaluza-Klein level, which is a result of momentum quantisation

Quantum Numbers					
$SU(2)_L$	$U(1)_Y$	Spin	DM can decay into	DD Bound?	Stable?
2	1/2	S	E L	×	×
2	1/2	F	E H	×	×
3	0	S	H H*	✓	×
3	0	F	L H	✓	×
3	1	S	H H, L L	×	×
3	1	F	L H	×	×
4	1/2	S	H H H*	×	×
4	1/2	F	(L H H*)	×	×
4	3/2	S	H H H	×	×
4	3/2	F	(L H H)	×	×
5	0	S	(H H H* H*)	✓	×
5	0	F	-	✓	✓
5	1	S	(H H* H* H*)	×	×
5	1	F	-	×	✓
5	2	S	(H* H* H* H*)	×	×
5	2	F	-	×	✓
6	1/2, 3/2, 5/2	S	-	×	✓
7	0	S	-	✓	✓
8	1/2, 3/2, …	S	-	×	✓

Table 1.2: Potential dark matter candidates generated by adding a single electro-weak multiplet to the SM. From Cirelli and Strumia [52].

due to the smallness of R. In contrast to SUSY, the partners have the same spin as their corresponding SM particle, which prevents them from cancelling out the quantum corrections to the Higgs mass and therefore means that UED fails to provide a solution to the Hierarchy problem [48].

The theory does, however, provide a DM candidate in the form of the lightest Kaluza-Klein particle (LKP), which is made stable against decay into SM particles by requiring conservation of KK-parity, analogous to the R-parity discussed in Section 1.3.1. The theory is once again constrained by the measured relic density, and combining this with the measured Higgs mass (126 GeV) implies an LKP mass of 600–1500 GeV, which is of the order required for the WIMP miracle [48, 55].

1.3.4 Other WIMP Candidates

Many other theories also seek to provide a WIMP DM candidate by extending the SM. These include Little Higgs models with T-parity, which invoke a new global symmetry 'collectively' broken at the weak scale, giving rise to a host of new non-SM particles [56]. These theories protect their lightest new weak-scale particle from decay into SM particles by invoking a new quantum number: 'T-parity': a familiar technique along the lines of SUSY and UED [57]. Little Higgs models typically predict a DM candidate with $80 < M_\chi < 500$ GeV [32].

Theories even more minimal than MDM have been proposed, where a singlet scalar of mass $M_\chi \gtrsim 50$ GeV is added to the SM that couples only to the Higgs boson. The addition of vector-like fermions to such models can alleviate the hierarchy problem [58]. The common features of all WIMP models are that they postulate the existence of stable particles with weak coupling to SM particles, that are the relic of a thermal population which froze out in the early Universe, and they predict the existence of new physics at the weak ($\sim$ TeV) scale.

1.3.5 Non-WIMP Candidates

Sterile Neutrinos

The sterile neutrino is a consequence of the fact that neutrinos possess mass [59]. Neutrino masses can be generated by adding a set of (unobserved) right-handed chiral neutrinos to the standard model, which combine with the left-handed ones to produce a mass term in the SM Lagrangian. Mass eigenstates are linear combinations of chiral eigenstates, with those dominated by left-handed states labelled 'active', and those dominated by right-handed states labelled 'sterile'. Through a process called the 'seesaw mechanism' [60], the mass of the active states can be made small (as observed) without fine-tuning, with the desirable side effect that the mass of the sterile state becomes large ($\sim$ keV), as required for a successful DM candidate.

Sterile neutrino models are constrained by space-based x-ray telescope and CMB data [61]. Recently though, Canetti, Drewes and Shaposhnikov have shown [62, 63] that in a minimal three-sterile-neutrino model, which they call the νMSM, the lightest sterile neutrino can be given a mass in the range required for DM ($1 < M_1 < 50$ keV)

whilst evading constraints from the non-observation of x-ray lines from sterile neutrino decay in experiments such as Chandra [64] and XMM-Newton [65], and the measured value of Ω_m from Planck (Table 1.1).

Axions

'Axion' is the name given to the quantum of the scalar field which arises in the theory of Peccei-Quinn symmetry breaking [66], invoked to solve another long-standing problem in particle physics: the strong CP problem. This is another fine-tuning problem similar to the gauge hierarchy problem of Section 1.3.1. There is no *a priori* reason to expect that CP is conserved in strong interactions (after all, it is not conserved in weak interactions), however constraints from, for example, measurements of the neutron electric dipole moment suggest that CP is at least almost exactly conserved. The degree of strong CP violation is given by the parameter $\bar{\theta}$, which is experimentally constrained to be $< 0.7 \times 10^{-11}$ [67, 68]. Invoking the axion provides a natural way for $\bar{\theta} \rightarrow 0$. Astrophysical constraints set an upper limit on the axion mass of $m_a < 15.4$ meV [69], with masses in the μeV - meV range being required for a DM candidate. The ADMX collaboration is searching for the signature of axion-to-photon conversion in a resonant cavity via the inverse Primakoff effect [70], and their most recent results constrain the axion-to-photon coupling $g_{a\gamma\gamma} \lesssim 10^{-15}$ GeV^{-1} in the mass range 1.9–3.53 μeV [71].

Asymmetric Dark Matter

A model called asymmetric dark matter (ADM) [72, 73] has received considerable attention recently. ADM focuses on the result encountered in Section 1.1:

$$\Omega_{DM} \sim 5 \times \Omega_b, \tag{1.22}$$

and asks the question: why should it be that the baryonic and DM densities are so similar? The authors suggest that the similarity implies a common production mechanism for the asymmetries between $b - \bar{b}$ and $\chi - \bar{\chi}$. The theory predicts a low WIMP mass of $5 - 15$ GeV, which is compatible with several of the low-mass signal hints that will be met in Chapter 3.

1.4 Conclusions

This chapter has highlighted the need for particle DM to explain observed phenomena across a broad range of distance scales in the Universe. One property of DM is well known: the density parameter Ω_{DM}. For others such as the 'temperature' of DM, and the structure of DM halos, we have been able to infer some information, but much more work is still to be done. These properties have been used to constrain theories that provide a DM candidate, which are themselves motivated in a variety of ways, often not directly seeking to solve the dark matter problem. Quantum theories and cosmological observations together paint a picture of an elusive suspect, and attempts to discover it will be discussed in Chapter 3. The most promising class of candidate, and the one that has received the most theoretical and experimental attention, is the WIMP, and the following chapter will be concerned with producing an estimate of the rate of WIMP interactions that we can expect in an Earth-based particle detector, along with a discussion of the main astrophysical uncertainties that affect this estimate.

Chapter 2

Theory of WIMP Detection

The purpose of this chapter is to construct, from first principles, the equation for the differential event rate of WIMP-induced nuclear recoils (elastic scatters) as a function of energy in a dark matter detector. In the event of a discovery, analyses can be performed to extract the most likely WIMP mass, M_W, and cross section, σ_{WN}, where the latter can be spin-independent (SI) or spin-dependent (SD) depending on the spin of the target nucleus employed. On the other hand, if a detector is run for a period of time and no events are observed, then this expected rate can be combined with knowledge of the detector sensitivity to set an upper limit (under the stated astrophysical assumptions) on σ_{WN} as a function of M_W. The details of an analysis to extract a limit on the spin-dependent WIMP-proton cross section as a function of WIMP mass $\sigma_{WN}^{SD}(M_W)$ using DRIFT data is presented at the end of Chapter 4, and improved upon in Chapter 8 by the introduction of a new mode of detector operation. This chapter's derivation of the differential event rate is followed by a discussion of the uncertainties on the astrophysical inputs that go into it.

2.1 Nuclear Recoil Differential Event Rate

2.1.1 Classical Scattering Rate

Consider a dark matter particle of mass M_W scattering elastically off a target comprised of individual, independent nucleons of mass m_T. Treating the dark matter and target particles as hard spheres, Figure 2.1 shows that the interaction will only occur if the

25

centres of the spheres pass within a distance $R = R_T + R_W$ of each other. Alternatively, the interaction will only occur if the trajectory of the dark matter particle passes through a disc of area $\sigma = \pi R^2$ centred on the centre of the target nucleon and with its normal parallel to the trajectory vector. This is known as the classical scattering cross section of the interaction.
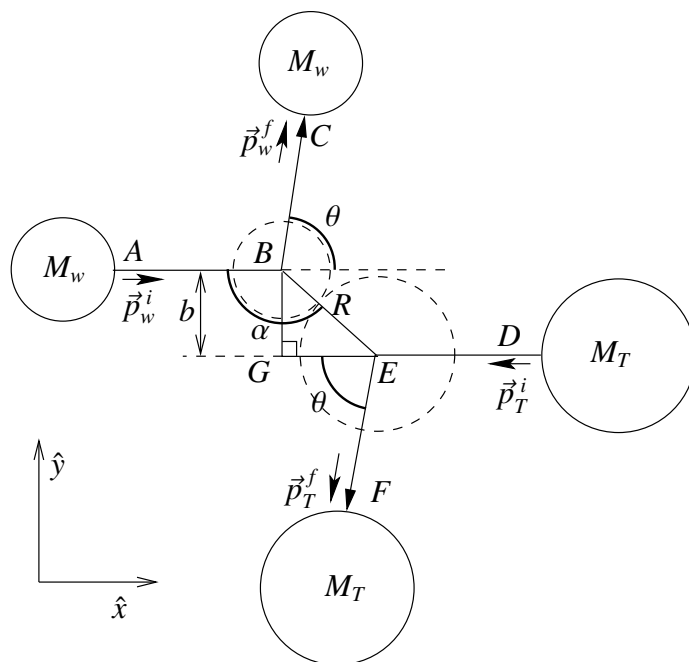
Figure 2.1: Diagram of dark matter - target nucleon scattering in the hard sphere approximation. From Daw [74].

The total classical scattering cross section for a dark matter-nucleon interaction in a detector containing N independent nuclei not obscured by one another, is $N\sigma$. Therefore, for a single dark matter particle traversing the length of a cubical detector of side L, the number of elastic collisions with the N target nucleons is given by $N_{col} = N\sigma/L^2$. If the dark matter particle travels at a speed v, the traversal of the detector takes a time L/v, or alternatively, there are v/L dark matter particle detector traversals in one second. Assuming that there is a single dark matter particle in the detector at any given time, the classical rate equation for elastic scatters in this idealised cubical detector is then

$$R = \frac{v}{L} \times \frac{N\sigma}{L^2} = \frac{Nv\sigma}{L^3} \text{ [74]}. \tag{2.1}$$

The true number of dark matter particles in the detector is a function of the local dark matter density ($\rho_W = 0.3$ GeV/cc [75]) and the mass of the dark matter particle (M_W), which is unknown. With ρ_W in units of GeV/cc and M_W in GeV/c^2, the number of dark matter particles in the detector is then given by $N_W = 10^6 L^3 \rho_W / M_W$. This factor will multiply Equation 2.1 to yield the total rate. Finally, it is helpful to replace N in Equation 2.1 by a physically measurable quantity, namely the total detector mass (M_D). This is done via Avogadro's number ($N_A = N/M_D[kg] \times 1000$), yielding the final equation for the classical rate of elastic scatters in the detector, in terms of measurable quantities

$$R = N_A \times 1000 M_D \times \frac{10^6 L^3 \rho_W}{M_W} \times \frac{v\sigma}{L^3}. \tag{2.2}$$

Note that the v appearing in this equation means that it has been implicitly assumed that all the dark matter particles have the same velocity, which is a highly unlikely scenario for a real dark halo. This will be addressed in Section 2.1.3 with the introduction of a more realistic velocity distribution.

In order to connect experiment with theory, the rate can be re-written as a differential rate integrated over the energies to which the detector is sensitive:

$$R = \int_{E_R=E_{min}}^{E_{max}} \frac{dR}{dE_R} \, dE_R, \tag{2.3}$$

where

$$\frac{dR}{dE_R} = R \, p(E_R) \text{ [75]}. \tag{2.4}$$

R is the total rate given in Equation 2.2, and $p(E_R)$ is the probability density for an interaction to produce a recoil of energy E_R. Equation 2.2 is an expression, albeit an oversimplified one, for the total rate R; therefore it will be the subject of the following section to obtain an expression for $p(E_R)$.

2.1.2 Scattering Kinematics

Continuing to consider the dark matter and target particles as hard spheres, the purpose of this section is to derive an expression for $p(E_R)$ in terms of measurable parameters, by requiring conservation of energy and momentum. This is most easily achieved by working in the centre of mass (CM) frame: the frame of reference in which the

total momentum is zero. Figure 2.1 shows a diagram of the interaction. Important kinematic parameters are highlighted: initial and final momenta of the dark matter and target ($\vec{p}_{W,T}^{\,i,f}$), impact parameter (b), scattering angles of the dark matter (α) and target (θ) particles.

Defining x_{CM} as the distance of the target from the system CM, and x_W as the distance of the target from the dark matter particle, the following can be written

$$M_T x_{CM} = M_W(x_W - x_{CM}), \tag{2.5}$$

which simplifies to

$$x_{CM} = \frac{M_W}{M_W + M_T}\, x_W. \tag{2.6}$$

Therefore, the velocity of the CM frame relative to the target nucleon is given by

$$v_c = \frac{\mathrm{d}x_{CM}}{\mathrm{d}t} = \frac{M_W}{M_T + M_W}\frac{\mathrm{d}x_W}{\mathrm{d}t} = \frac{M_W}{M_T + M_W}\, v. \tag{2.7}$$

Here, v is the relative velocity of the dark matter and target particles. It will also be useful to define the reduced mass of the dark matter and target system as

$$\mu = \frac{M_T M_W}{(M_T + M_W)}. \tag{2.8}$$

Comparing Equations 2.7 and 2.8, it then becomes clear that the initial state momentum of the target (or dark matter particle, since their momenta are equal in magnitude) in the CM frame can be written as

$$p_i = M_T v_c = \mu v. \tag{2.9}$$

Since the dark matter particles are constrained by observations of galaxy rotation curves to have highly non-relativistic velocities [76], the equations of energy conservation in the CM frame can be written in their non-relativistic form as

$$\frac{p_i^2}{2M_W} + \frac{p_i^2}{2M_T} = \frac{p_f^2}{2M_W} + \frac{p_f^2}{2M_T}, \tag{2.10}$$

where p_i and p_f are the initial and final momenta of the particles before and after the

collision, which are, by the definition of the CM frame, the same for the dark matter and target particles. Furthermore, by inspection of Equation 2.10 it can be seen that $p_i = p_f = p_c$, which in turn implies that the two different particles maintain their respective velocity magnitudes throughout the collision which, in the CM frame, is v_c for both target and dark matter particles.

Defining the $\vec{x}$-direction as the one parallel to the incident dark matter particle's trajectory, and the $\vec{y}$-direction as the direction orthogonal to this and in the plane of the particles' final state velocities, the velocity of the recoiling target nucleon in the CM frame can be decomposed as

$$\vec{v}_T^{f,C} = \begin{pmatrix} -v_c \, \cos\theta \\ -v_c \, \sin\theta \end{pmatrix}, \tag{2.11}$$

where θ is the CM scattering angle. It is then possible to transform into the rest frame of the target nucleon (the Lab frame) by adding the relative velocities of the two frames, giving

$$\vec{v}_T^{f,L} = v_c \begin{pmatrix} 1 - \cos\theta \\ -\sin\theta \end{pmatrix}. \tag{2.12}$$

Therefore, the energy imparted to the target in the lab frame is

$$\begin{aligned} E_R &= \frac{1}{2} M_T |\vec{v}_T^{f,L}|^2 \\ &= \frac{1}{2} M_T v_c^2 \left((1 - \cos\theta)^2 + \sin^2\theta \right) \\ &= M_T v_c^2 \left(1 - \cos\theta \right) \\ &= \frac{\mu^2 v^2}{M_T} \left(1 - \cos\theta \right). \end{aligned}$$

Here Equation 2.9 has been used to re-write the equation in terms of μ and v. The maximum value that E_R can take occurs in the case of a head-on collision where $\theta = \pi$:

$$E_R^{max} = \frac{2\mu^2 v^2}{M_T}. \tag{2.13}$$

E_R^{max} is maximised when $M_T = M_W$, which motivates the choice of targets of mass similar to the expected WIMP mass. E_R is free to take any value between 0 and E_R^{max}, with probabilities determined by the probability distribution $p(\theta)$. However, it will

turn out that it is simpler to work in terms of the impact parameter b. Therefore, a relationship between θ and b is required, which comes directly from consideration of the geometry of Figure 2.1. Considering triangle BEG, and the symmetry about line BE:

$$
\begin{aligned}
2\alpha &= \theta + \pi \\
\cos\left(\alpha - \frac{\pi}{2}\right) &= \frac{b}{R} \\
\cos\left(\frac{\theta}{2}\right) &= \frac{b}{R}.
\end{aligned}
\tag{2.14}
$$

Substituting into Equation 2.13 and making use of the double-angle formula, the recoil energy distribution as a function of b can be written as

$$
E_R(b) = \frac{2\mu^2 v^2}{M_T}\left(1 - \frac{b^2}{R^2}\right).
\tag{2.15}
$$

The aim of this section was to obtain an expression for $p(E_R)$. An expression for $p(E_R)$ can be constructed by noting that the range of all possible impact parameters covers the total range of possible recoil energies available to the recoiling particles:

$$
p(b)\,|\mathrm{d}b| = p(E_R)\,|\mathrm{d}E_R|.
\tag{2.16}
$$

Rearranging,

$$
p(E_R) = \frac{p(b)}{\left|\frac{\mathrm{d}(E_R)}{\mathrm{d}(b)}\right|}.
\tag{2.17}
$$

The denominator is just the differential with respect to b of Equation 2.15:

$$
\left|\frac{\mathrm{d}(E_R)}{\mathrm{d}(b)}\right| = \frac{4\mu^2 v^2 b}{M_T R^2}.
\tag{2.18}
$$

To calculate the numerator of Equation 2.17, consider a thin ring of radius b and width $\mathrm{d}b$, centred on the centre of the target nucleon (point E in Figure 2.1). The probability of any given interaction having an impact parameter in this infinitesimal range is given by

$$
p(b)\,\mathrm{d}b = \frac{2\pi b\,\mathrm{d}b}{\pi R^2} = \frac{2b\,\mathrm{d}b}{R^2}.
\tag{2.19}
$$

Finally, substituting Equations 2.18 and 2.19 into Equation 2.17, produces the recoil energy probability distribution as a function of impact parameter b:

$$p(E_R) = \frac{\frac{2b}{R^2}}{\frac{4\mu^2 v^2 b}{M_T R^2}} = \frac{M_T}{2\mu^2 v^2}. \tag{2.20}$$

The striking result of Equation 2.20 is that not only is $p(E_R)$ independent of the impact parameter b, but it is also independent of the recoil energy E_R. That is, the probability of an interaction falling in the range ΔE_R is uniform across all recoil energies to which the detector is sensitive [74].

The differential rate equation can now be constructed by substituting Equations 2.2 and 2.20 into Equation 2.4:

$$\frac{\mathrm{d}R}{\mathrm{d}E_R} = \frac{10^9 \rho_W N_A M_D M_T \sigma}{2 M_W \mu^2 v}. \tag{2.21}$$

2.1.3 Realistic Velocity Distribution

Up to now the relative velocity of the dark matter and target particles has appeared in the equations as a single number, implying a flat distribution of velocities from 0 to v_{esc}, the escape velocity of the Galaxy. It is the purpose of this section to replace this unrealistic velocity distribution with a theoretically motivated one. The form of the velocity and density distributions of the dark matter halo are topics of active research amongst the dark matter community (see Section 2.2.2). One particularly simple velocity distribution is that of an isothermal sphere: old enough for the dark matter to have reached thermal equilibrium, but young enough not to have had sufficient time to collapse and form a disc. This model has been adopted as the standard by the experimental community, to facilitate comparison between different experimental results [75].

The velocity distribution that arises from the assumption of an isothermal sphere of collisionless particles is the Maxwell-Boltzmann distribution

$$f(v) = \frac{4\pi v^2}{(\pi v_0^2)^{\frac{3}{2}}} \exp\left(\frac{-v^2}{v_0^2}\right), \tag{2.22}$$

where v_0 is related to the mean square velocity of the dark matter particles by

$$v_0 = \sqrt{\frac{2}{3}} \sqrt{\overline{v^2}}.$$ (2.23)

The distribution can be incorporated into Equation 2.21 by making the substitution

$$\frac{1}{v} \rightarrow \int_{v_{min}}^{v_{esc}} \frac{f(v)}{v} \, dv,$$ (2.24)

where v_{min} is the minimum velocity that can result in a recoil of energy E_R and v_{esc} is the galactic escape velocity (492–594 km s^{-1} [76]), which sets the upper bound on the speed of dark matter particles gravitationally bound to the galaxy. Making the assumption that the detector is sensitive to most of the range of v, the truncation of the integral at v_{esc} makes little difference, and the integration can be simplified by making the substitution $v_{esc} \rightarrow \infty$ [75]. The integral on the right hand side can then be calculated as

$$\frac{4v_0^2}{v_0^3 \sqrt{\pi}} \int_{v_{min}}^{\infty} v \exp\left(\frac{-v^2}{v_0^2}\right) dv = \frac{2}{v_0 \sqrt{\pi}} \exp\left(-\frac{v_{min}}{v_0}^2\right).$$ (2.25)

Substituting this into Equation 2.21, the expression for the differential rate of interactions from particles in an isothermal halo is obtained:

$$\frac{dR}{dE_R} = \frac{10^9 \rho_W N_A M_D M_T \sigma}{2 M_W \mu^2} \frac{2}{v_0 \sqrt{\pi}} \exp\left(-\frac{v_{min}}{v_0}\right)^2.$$ (2.26)

2.1.4 Enhancement due to Binding

The assumption that the target mass in the detector fiducial volume is made up of isolated nucleons of mass M_T and cross section σ does not correspond to the physical reality. In fact, the target nucleons are bound together into nuclei by the strong nuclear force, which leads to an enhancement of the scattering cross section by a factor of A^2 in the case of spin-independent interactions. In the case of spin-dependent interactions, the WIMP effectively interacts only with the single, unpaired nucleon, therefore the following does not apply in this case.

In order to understand the enhancement, consider Fermi's Golden Rule [77]:

$$R = nv\sigma = \frac{2\pi}{\hbar} \left| M_{fi} \right|^2 \frac{\mathrm{d}N}{\mathrm{d}E_R}, \tag{2.27}$$

where $\left| M_{fi} \right|$ is the matrix element for the interaction, $\frac{\mathrm{d}N}{\mathrm{d}E_R}$ is the density of final states, and R is the rate that appears in Equation 2.1. Substituting Equation 2.1 into Equation 2.27 and taking the ratio of the bound and independent nucleon cases:

$$\frac{\sigma^{bound}}{\sigma^{indep}} = \frac{\left| M_{fi}^{bound} \right|^2 \frac{\mathrm{d}N}{\mathrm{d}E_R}^{bound}}{\left| M_{fi}^{indep} \right|^2 \frac{\mathrm{d}N}{\mathrm{d}E_R}^{indep}}, \tag{2.28}$$

where the ratios of numerical factors, as well as dark matter number density n and speed v, all cancel to unity.

The first factor of A enhancement to the cross section arises from the fact that the dark matter interacts *coherently* with the whole nucleus, so that rather than the total squared matrix element being the sum of A individual squared terms from each of a group of A nucleons

$$\left| M_{fi}^{indep} \right|^2 = \left| M_{fi,1}^{indep} \right|^2 + \left| M_{fi,2}^{indep} \right|^2 + \left| M_{fi,3}^{indep} \right|^2 \ldots \left| M_{fi,A}^{indep} \right|^2 , \tag{2.29}$$

it is instead the square of the sum of the matrix elements for each individual nucleon

$$\left| M_{fi}^{bound} \right|^2 = \left| M_{fi,1}^{bound} + M_{fi,2}^{bound} + M_{fi,3}^{bound} + \ldots M_{fi,A}^{bound} \right|^2 , \tag{2.30}$$

which contains a factor of A more contributions to the total squared matrix element than Equation 2.29 by virtue of the extra A cross-terms:

$$\left| M_{fi}^{bound} \right|^2 = A \left| M_{fi}^{indep} \right|^2 \; [74]. \tag{2.31}$$

The second factor A enhancement from binding comes from the density of final states in Equation 2.28. Re-writing the density of final states in terms of the lab-frame momentum of the recoiling particle, p:

$$\frac{\mathrm{d}N}{\mathrm{d}E_R} = \frac{\mathrm{d}N}{\mathrm{d}p} \times \frac{\mathrm{d}p}{\mathrm{d}E_R}. \tag{2.32}$$

The first factor in Equation 2.32 can be calculated as follows. At fixed E_R and M_T, the momentum states available to the recoiling particle form a thin ring in 2D momentum space of radius p and width dp, where each of the two momentum dimensions is quantised in units of $\hbar$, so that a single state takes up an 'area' of $\hbar^2$ in momentum space. Then, the number of states in the infinitesimal ring is given by the total area of the ring divided by the area of a single state:

$$dN = \frac{2\pi p \, dp}{\hbar^2}.$$

(2.33)

Taking the dp to the LHS gives an expression for $\frac{dN}{dp}$. The second factor in Equation 2.32 is simply the inverse of the differential with respect to dE_R of the energy of the recoiling nucleus:

$$\frac{dp}{dE_R} = \frac{1}{\frac{dE_R}{dp}} = 1 / \left(\frac{d}{dp} \frac{p^2}{2M} \right) = \frac{M}{p},$$

(2.34)

where M is the mass of the recoiling object. Finally, substituting Equations 2.33 and 2.34 into Equation 2.32 yields the density of states in terms of M, the mass of the recoiling object:

$$\frac{dN}{dE_R} = \frac{2\pi p}{\hbar^2} \times \frac{M}{p} = \frac{2\pi}{\hbar^2} M \ [74].$$

(2.35)

The density of final states for the interaction is directly proportional to M. Therefore if the recoiling object is a nucleus of mass $A M_T$ rather than a nucleon of mass M_T, the density of states gains a factor of A which, taken together with the factor A enhancement from coherence, means that the differential rate acquires an overall enhancement factor of A^2 when the binding of nucleons into nuclei is taken into account. Therefore, multiplying Equation 2.26 by A^2 yields an expression for the differential event rate of spin-independent interactions between dark matter particles and nuclei comprised of A nucleons bound into nuclei of mass M_T:

$$\frac{dR}{dE_R}^{SI} = \frac{10^9 \rho_W N_A M_D A^2 M_T \sigma}{2 M_W \mu^2} \frac{2}{v_0 \sqrt{\pi}} \exp\left(-\frac{v_{min}}{v_0} \right)^2.$$

(2.36)

2.1.5 Nuclear Form Factor Corrections

Up to this point the interaction has been assumed to be between two hard spheres: a classical approximation that is valid in the limit that the recoiling particle's de Broglie wavelength

$$\lambda = \frac{2\pi\hbar}{q} \qquad (2.37)$$

is much greater than its size (here, q represents the lab-frame momentum of the recoiling target particle). In order to test the validity of this assumption, the recoil energy of a DRIFT SD target fluorine nucleus after a head-on interaction with a dark matter particle travelling at speed v_0 is calculated. DRIFT's potential fill gases are discussed in more detail in Chapter 4. Substituting $M_T = 17.7$ GeV/c^2 (F nucleus), $M_W = 100$ GeV/c^2 and $v_0 = 230$ km s^{-1} into Equation 2.13 and making use of Equation 2.8 gives a recoil energy of $E_R^{max} = 15$ keV. This recoil is highly non-relativistic, so the lab-frame momentum can be calculated using

$$q = \sqrt{2M_T E_R} = 23 \text{ MeV/c}. \qquad (2.38)$$

Finally, substituting this momentum into Equation 2.37 yields a de Broglie wavelength of 53.8 fm for a fluorine nucleus that has been scattered by a 100 GeV/c^2 dark matter particle travelling at a speed of $v_0 = 230$ km s^{-1}.

This should be compared with the approximate size of one of DRIFT's F target nuclei ($A = 19$),

$$r_n = r_0 A^{\frac{1}{3}} \simeq 3.2 \text{ fm}, \qquad (2.39)$$

where $r_0 = 1.2$ fm. The fact that the scattered particle's De Broglie wavelength is only $\sim$ one order of magnitude larger than the nuclear effective radius indicates that the hard sphere approximation may not be valid. Instead, a model for the interacting particles is required which takes into account the finite momentum transfer and 'soft', quantum mechanical nature of interaction, including the spin of the nucleus. The effects of changing to this more realistic interaction model appear in the rate equation as a factor multiplying the effective cross section σ:

$$\sigma \rightarrow F(qr_n)^2\, \sigma_0, \qquad (2.40)$$

35

where σ_0 is the zero-momentum-transfer limit of σ, and r_n is the nuclear effective radius appearing in Equation 2.39 [75]. $F(qr_n)$ is the nuclear form factor, whose purpose is to introduce the q-dependent suppression of the cross section, the calculation of which will be the object of the rest of this section.

DRIFT, along with several of the direct detection experiments introduced in Chapter 3, aims to probe spin-dependent dark matter interactions via the spin of the fluorine nucleus ($J = \frac{1}{2}$). Therefore, the form factor must include all the q-dependent details of the interaction, including the part that interacts with the spin. Approximating the incoming and outgoing particles as plane waves (the first Born approximation), the form factor is the Fourier transform of the density distribution of the nucleus. Approximating this distribution as a thin shell at the effective nuclear radius containing the single unpaired nucleon (a single proton in the case of fluorine), the form factor can be calculated as follows [75]:

$$F(qr_n) = \int V(r) \exp{(i\vec{q} \cdot \vec{r})} \, \mathrm{d}^3\vec{r}, \tag{2.41}$$

where the scattering potential $V(r)$ is given by

$$V(r) = \frac{Q \, \delta(r - r_0)}{4\pi r_0^2}. \tag{2.42}$$

Substituting Equation 2.42 into Equation 2.41 and solving:

$$F(qr_n) = j_0(qr_n), \tag{2.43}$$

where j_0 is the first Bessel function given by

$$j_0(x) = \frac{\sin(x)}{x}. \tag{2.44}$$

It has been shown by Engel [78] that a more realistic form factor arises when the distribution of all nucleons of the same type as the unpaired one are taken into account, rather than just the single unpaired nucleon: the so-called 'odd-group' model. A very good approximation to this solution is obtained by simply replacing the first dip in the unpaired nucleon form factor of Equation 2.43 with its value at the following maxi-

mum, in which case the form factor of Equation 2.45 is obtained:

$$F(qr_n) = \begin{cases} j_0(qr_n) & (qr_n < 2.55, \ qr_n > 4.5) \\ \sqrt{0.0047} & (2.55 \leq qr_n \leq 4.5) \end{cases}.$$ (2.45)

The correspondence between q and E_R in Equation 2.38 allows to plot $F(E_R)$ against E_R, which is shown in Figure 2.2 for several different elements used in direct and directional dark matter search experiments. In each case, the effect of the form factor is a reduction in the effective cross section with increasing momentum transfer, whereas in the limit of zero momentum transfer the classical 'hard sphere' approximation is recovered. At the recoil energies of interest ($E_R \lesssim 300$ keV) the reduction factor is fairly modest for low-A nuclei such as fluorine, but becomes important in this energy regime for higher-mass nuclei such as germanium or iodine.
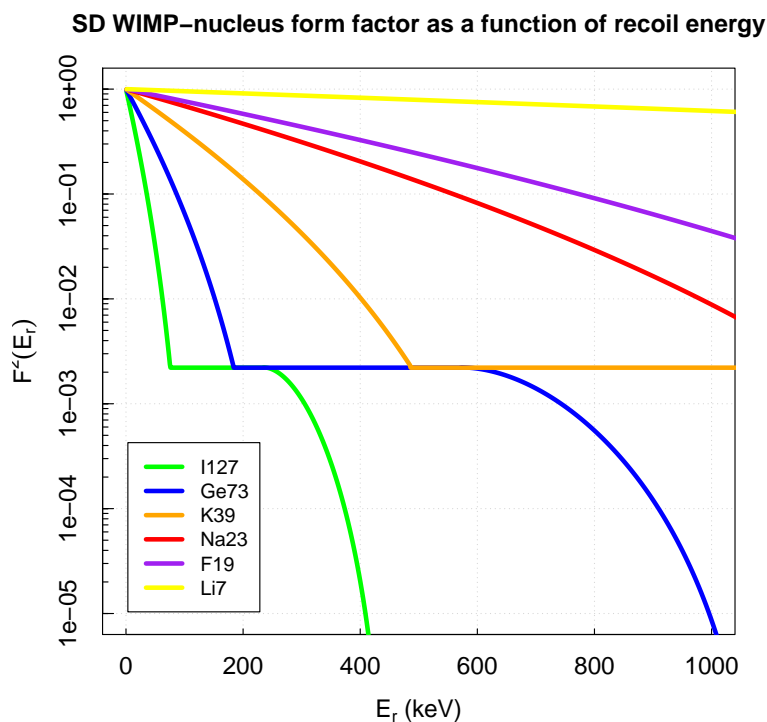
Figure 2.2: Odd-group form factors for various spin-dependent target nuclei.

2.1.6 WIMP-Nucleon Cross Sections

In order to compare cross section measurements made by detectors using target molecules of different masses, and to compare the results of experiments with predictions from theoretical models, it is useful to re-write the WIMP - nucleon cross section in terms of the cross section with a free proton or neutron. This can be done in a model-independent way, provided that the spin of the nucleus is dominated by *either* neutron *or* proton contributions [79]. This is the case for the spin-dependent (SD) cross section of DRIFT's fluorine target, which satisfies $\sigma_{WN} \sim \sigma_{WN}^p$.

The total WIMP-nucleus cross section can be decomposed into its proton and neutron components as follows [75]:

$$\sigma_{WN} = \left(\sqrt{\sigma_{WN}^p} + \sqrt{\sigma_{WN}^n} \right)^2, \text{ where} \tag{2.46}$$

$$\sigma_{WN}^p = 4 G_F \mu^2 C_{WN}^p, \tag{2.47}$$

$$\sigma_{WN}^n = 4 G_F \mu^2 C_{WN}^n. \tag{2.48}$$

Here, G_F is the Fermi coupling constant ($= 1.16637 \times 10^{-5}$ GeV^{-2} [80]), and $C_{WN}^{[p,n]}$ are the [proton, neutron] contributions to the total enhancement factor C_{WN}. which are defined as:

$$C_{WN} = \frac{8}{\pi} \left(|a_p \langle S_p \rangle| \pm |a_n \langle S_n \rangle| \right)^2 \frac{J+1}{J}, \tag{2.49}$$

$$C_{WN}^p = \frac{8}{\pi} \left(a_p \langle S_p \rangle \right)^2 \frac{J+1}{J}, \tag{2.50}$$

$$C_{WN}^n = \frac{8}{\pi} \left(a_n \langle S_n \rangle \right)^2 \frac{J+1}{J}. \tag{2.51}$$

Here, $\langle S_{[p,n]} \rangle$ is the expectation value for the spin of the [proton, neutron] inside the nucleus, J is the nuclear spin, and $a_{[p,n]}$ is the effective WIMP-[proton,neutron] coupling arising from the chosen theoretical model of the WIMP. Making the aforementioned simplifying assumption that $\sigma_{WN} \sim \sigma_{WN}^p$, and making use of the above equations, the effective WIMP-proton cross section σ_{Wp} can be defined in terms of the measurable σ_{WN} as follows:

$$\sigma_{Wp} = \sigma_{WN} \frac{\mu_p^2}{\mu^2} \frac{C_{Wp}}{C_{WN}^p}, \tag{2.52}$$

where μ_p is the reduced mass of the WIMP-proton system, and C_{Wp} is the enhancement factor for a WIMP interaction with a free proton, which is obtained by substituting $J = \langle S_p \rangle = \frac{1}{2}$ into Equation 2.49. In this way, the model-dependent a parameters cancel in the ratio, and the final factor of Equation 2.52 becomes

$$\frac{C_{WN}^p}{C_{Wp}} = \frac{4}{3}\langle S_p \rangle^2 \frac{J+1}{J}. \tag{2.53}$$

Equation 2.52 can be used, along with a lookup table of proton nuclear spin factors and nucleus spin data (for example, Tovey et al. [79], and references therein) to convert a measured WIMP-nucleus cross section into an effective WIMP-proton cross section, for comparison between experiments or with predictions from theory. Finally, putting this together with Equation 2.26, and incorporating the form factor correction, an expression for $\frac{\mathrm{d}R}{\mathrm{d}E_R}^{SD}$ in terms of measurable quantities is obtained:

$$\frac{\mathrm{d}R}{\mathrm{d}E_R}^{SD} = 10^9 N_A M_D M_T \cdot \frac{4}{3}\langle S_p \rangle^2 \frac{J+1}{J} \cdot \frac{F^2(E_R)\sigma_{Wp}}{M_W \mu_p^2} \cdot \frac{\rho_W}{v_0 \sqrt{\pi}} \exp\left(-\frac{v_{min}}{v_0}\right)^2. \tag{2.54}$$

This is plotted for DRIFT's fluorine target in Figure 2.3, and is a crucial input into the limit-setting analysis presented in Chapters 4 and 8. The first two terms of this expression contain macroscopic and microscopic information about the target material, whist the third contains information on the WIMP interaction, which includes σ_{Wp} and M_W: the physical dark matter parameters of interest. The final term contains information on the dark matter halo, and it is here that a large amount of the uncertainty associated with interpretation of dark matter search data enters the equations. These will be discussed in the following section.

SD differential event rate. WIMP mass = 100 GeV
SD WIMP–proton cross–section = 0.484 pb
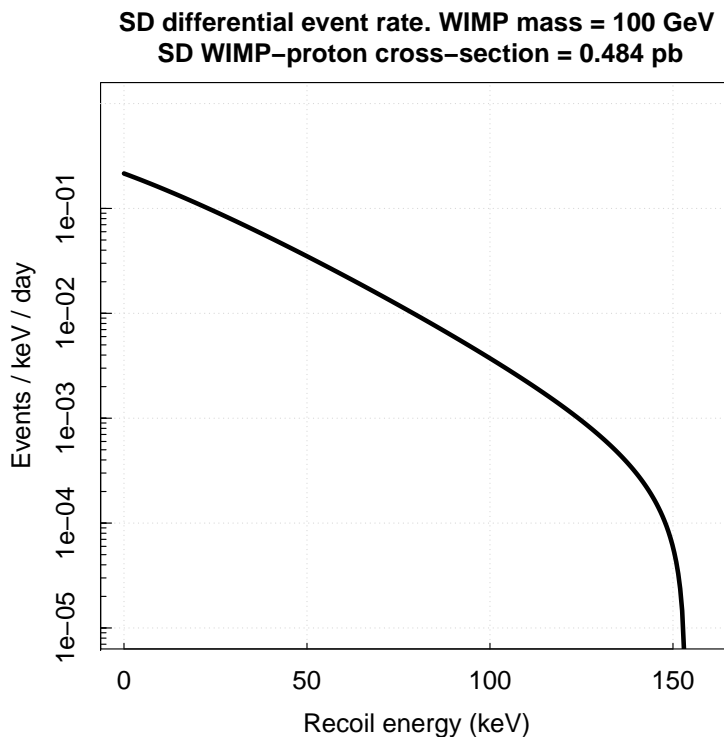
Figure 2.3: Expected rate of spin-dependent WIMP-nucleus interactions as a function of energy for a 100 GeV WIMP scattering elastically on fluorine with an arbitrary WIMP-nucleus cross section of 1×10^{-34} cm^2 (4.84×10^{-37} cm^2 WIMP-proton) in a detector with 100 g fiducial mass.

2.2 Astrophysical Uncertainties

2.2.1 The Standard Halo Model

Several assumptions were made in Section 2.1 about the Milky Way's DM halo (see Figure 2.4), which are collectively known as the Standard Halo Model (SHM). As well as fixing the value of several critical inputs into the differential event rate equation (see Table 2.1) and requiring the halo density profile $\rho(r)$ to be smooth, the SHM also specifies a global velocity distribution for the halo which, as seen in Section 2.1.3, is the Maxwell-Boltzmann distribution arising from the assumption of an isothermal, spherical distribution of DM. This model has been adopted by the experimental DM
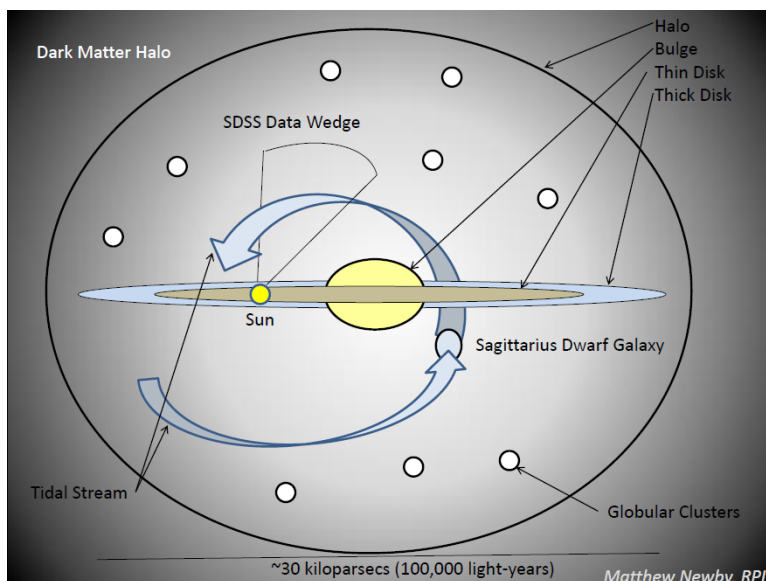
Figure 2.4: Illustration of the dark matter halo and our place within it [81].

community in order to facilitate comparisons between limits (and more recently, hints of signal - see Chapter 3) in direct search experiments, however it is generally accepted that the properties of DM halos are poorly understood, and may differ significantly from those assumed by the SHM.

Directional detectors such as DRIFT are uniquely placed to shed light on the detailed properties of DM halos. For example, work by Green, Morgan and Spooner has shown that as few as ∼ 300 events could be needed to discover a tidal stream component of the DM halo (see Figure 2.4) with 25% of the mean density in the solar neighbourhood [82]. Chapter 6 includes a study of DRIFT's directional sensitivity using calibration runs with a directed neutron source.

Parameter	Value	Description
ρ_W	0.3 ± 0.1 GeV/cc [83]	Local dark matter density
v_0	243 ± 7 km s^{-1} [84]	Circular speed at the solar radius
v_{esc}	544^{+64}_{-46} km s^{-1} [76]	Galactic escape velocity

Table 2.1: Measured parameters of the Standard Halo Model assumed by direct dark matter detection experiments.

2.2.2 Halo Simulations

The precise form of the velocity distribution has become a topic of intense interest in recent years, and many attempts have been made to deduce it by fitting the output of galaxy-scale N-body simulations similar to those described in Section 1.2.5. The Via Lactea II simulation [85] is one such attempt. These simulations also cast light on the density profile $\rho(r)$ of dark matter within collapsed galactic halos, and produce outputs such as the mass power spectrum, which can be directly compared with observation.

Simulations of halo formation begin by defining a cosmological-scale region of space, applying a set of initial conditions based upon measurements of cosmological parameters, and generating a large number (1 billion in the case of the GHALO simulation [86]) of test particles. These particles are then allowed to collapse together under gravity, forming structures of increasing size in a process of hierarchical growth that leads to the formation of fractal structures. Improvements in computing power are continually increasing the number of particles that can be simulated, and consequently reducing the size of the smallest structures that can be resolved in their outputs. The Via Lactea II simulation, for example, simulates 10^9 particles of mass 1000 $M_\odot$, and is able to resolve structures down to 1% of the virial radius of the halo [85].

The radial density profile of a collapsed halo, $\rho(r)$, is proportional to $1/r^2$ in the isothermal sphere case (Equation 2.55):

$$\rho(r) = \frac{\sigma_v^2}{2\pi G r^2}. \tag{2.55}$$

However, the $\rho(r)$ obtained from N-body simulations are found to be shallower at small r and steeper at large r, which motivated several groups to come up with analytical forms such as those in Equations 2.56 [87] and 2.57 [88]. These are the 'Einasto' and 'NFW' profiles, respectively:

$$\rho(r) = \rho_s exp\left(-\frac{2}{\alpha}[(r/R_s)^\alpha - 1]\right), \tag{2.56}$$

$$\rho(r) = \frac{\rho_s}{\frac{r}{R_s}\left(1 + \frac{r}{R_s}\right)^2}. \tag{2.57}$$

Here, ρ_s and R_s are the density scale and scale radius, respectively, which are the free

parameters of the fit (different for different galaxies). The other symbols have their usual meanings. R_s is the radius at which the circular velocity profile peaks (see, for example, Figure 1.1). Whilst it is only the density in the solar neighbourhood, ρ_W, that enters the differential event rate calculation explicitly, the form of the $\rho(r)$ profile determines the velocity distribution at a given radius, and this can have a significant impact on the expected event rate.

There are two long-standing discrepancies between the predictions of halo simulations and observation. The first involves small-scale structure in the form of satellite dwarf galaxies, which are far less numerous in observations than in simulations such as MS-II [89]. This has been dubbed the 'missing satellite problem'. The second concerns the central regions of galaxies, which end up, on average, significantly more 'cuspy' in simulations than observations of low surface brightness galaxies would suggest [90]. Whilst some have sought astrophysical explanations these discrepancies [91], others have attempted to replace *cold* with *warm* [92] or self-interacting [93] dark matter to bring the results into agreement.

2.2.3 Velocity Distribution

The velocity distribution *at the solar radius, r_0*, enters the differential event rate via Equation 2.24, where it can be seen that any departure from the Maxwell-Boltzmann velocity distribution of the isothermal sphere (Equation 2.22) will modify the integral, and hence the predicted rate. The results of N-body simulations suggest that in fact the velocity distribution is only of this form at moderate radii close to the scale radius, R_s. At $r < R_s$, the velocity distribution tends to be more peaked, whereas at $r >> R_s$, it becomes flatter and broader [94]. This departure from the SHM Maxwell-Boltzmann velocity distribution is confirmed by recent work by Bhattacharjee *et al.*, who inferred the local velocity distribution function from the measured $v(r)$ galactic rotation curve [95].

Fairbairn, Douce and Swift argue that in fact we should not expect a Maxwell-Boltzmann velocity distribution at all. The conditions that give rise to this distribution are: 1) particle size is negligible compared with mean separation, and 2) there are no long-range interactions between particles [96]. Condition 1) is certainly fulfilled for a WIMP halo, but condition 2) is not, since the halo is held together by gravity, a

long-range force. Furthermore, the observations of the Bullet cluster constrain DM self-interactions to be so feeble that they cannot be responsible for thermalising the halo, and therefore this must have been accomplished by gravity alone [97].

A subtle yet important uncertainty in the velocity distribution arises in the case of low-mass WIMPs. For particles with $M_W \lesssim 15$ GeV, the minimum speed v_{min} that a WIMP must possess in order to generate a recoil above threshold in a state-of-the-art dark matter detector is in the high-speed tail of the distribution, where the uncertainties in the distributions obtained from simulations are the largest [97]. Therefore, even with confidence of the general form of the velocity distribution, a large uncertainty in the expected rate from low-mass WIMPs is generated by the high-v tail.

2.2.4   Halo Substructure

The SHM assumes that the DM halo is smooth, however during their evolution, simulated halos exhibit structure all the way down to solar-system length scales [98]. Indeed, structure forms in a bottom-up manner such that structure might be expected on scales even smaller than the resolution limit of state-of-the-art simulations. Substructure on such small scales poses a problem for direct detection experiments, because it begs the question: what if we find ourselves in a region of space devoid of DM?

Fortunately, simulations such as that of Schneider, Krauss, and Moore [99] show that, although structures such as caustics and streams are able to survive in the outer regions of the halo, in the inner regions where the solar system resides ($r_0 = 8.38 \pm 0.18$ kpc [84]), there are so many overlapping streams, and so much tidal disruption, that the density is smooth to one part in 10^3 [100]. These results vindicate the adoption of the local DM density from stellar kinematics (0.3 GeV/cc) [83] as the density in the vicinity of an Earth-based detector.

2.2.5   The Effect of Baryons

Unlike DM, baryons experience collisions, and they are therefore able to shed angular momentum and fall in towards the centre of the Galaxy. It is this process of adiabatic contraction that gives rise to the bright 'bulge' of the Galaxy, which is dominated in mass by baryonic matter. It is thought that the infall of baryons causes a corresponding infall of DM, but this exacerbates the aforementioned 'cuspy core' problem with halo

N-body simulations, increasing the discrepancy between the steepness of observed and simulated core density profiles. The role of baryonic contraction in the evolution of DM halos is an active topic of research, and it has recently been shown that the 'cuspy-core' problem may be alleviated by non-adiabatic ejection of DM from the central $r \lesssim$ 2 kpc of the Galaxy [101]. Whilst this has a large impact on the observable signatures of DM annihilations in the Galactic centre sought by indirect DM search experiments (see Section 3.2), the effect on ρ_W at the radius of the Sun's orbit is minimal. Modification of the shape of $\rho(r)$ by baryons may have an indirect effect on the expected rate, via the velocity distribution, however [97].

2.2.6 Combined Effect of Astrophysical Uncertainties

A recent analysis by Fairbairn, Douce and Swift [97] investigated the combined effect of several of the above uncertainties upon the limits in $\sigma_{WN}^{SI} - M_W$ space set recently by the XENON-100 collaboration [102]. They adopted the Einasto density profile of Equation 2.56, allowing all three parameters to vary, and also a velocity anisotropy parameter of the form of Equation 2.58:

$$\beta(r) = \frac{\beta_0 + \beta_\infty (r/r_\beta)^\eta}{1 + (r/r_\beta)^\eta}, \tag{2.58}$$

in which the parameters $\beta_0, \beta_\infty, r_\beta$ and η were allowed to float within some reasonable limits, reflecting the uncertainty on the DM velocity distribution in the solar neighbourhood. The SHM astrophysical inputs from Table 2.1 were assumed, and the possibility of a dark disk was also included. Baryonic contraction was not modelled, the authors noting that its effect on the density at the radius of the Sun's orbit is expected to be minimal, as discussed in the previous section.

The results of this study appear in Figure 2.5, where it can be seen that despite the uncertainty over the properties of the dark matter halo, the limits on $\sigma_{WN}(M_W)$ are robust to within an order of magnitude across most of the mass range of interest. This result goes some way towards vindicating the use of the SHM, despite knowing that many of its assumptions are over-simplifications.
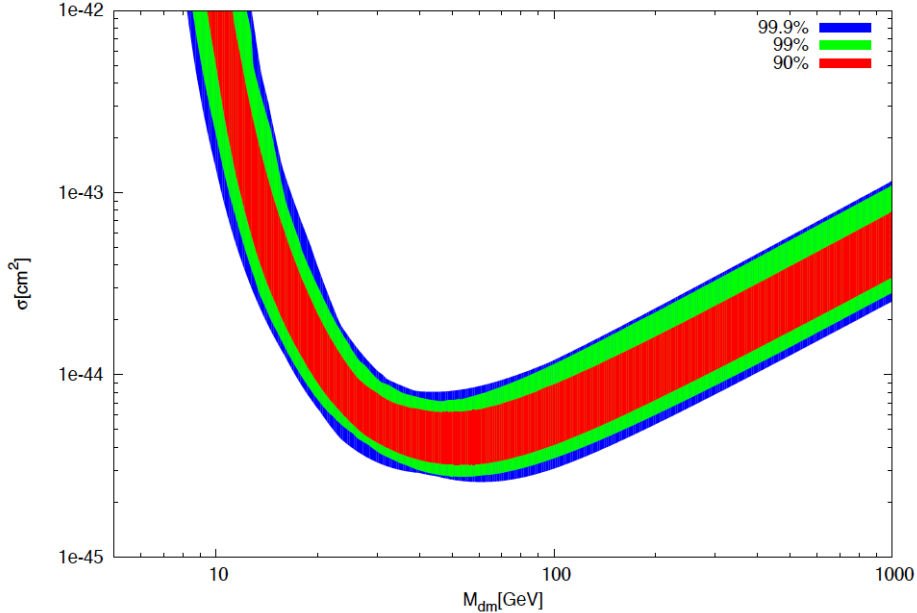
Figure 2.5: Limits on $\sigma_{WN}^{SI}(M_W)$, including the astrophysical uncertainties discussed in the text. Despite allowing $\rho(r)$ & $v(r)$ to vary within physically-motivated bounds, the limit remains robust to within an order of magnitude. From Fairbairn, Douce, and Swift [97].

2.3 Conclusions

The expected rate of spin-dependent WIMP-nucleus interactions in a perfectly efficient dark matter detector was derived in Section 2.1, and converted to an equivalent WIMP-proton interaction rate for comparison with theory and other experiments. This was done using a set of standard halo parameters, a Maxwell-Boltzmann velocity distribution, and a $1/r^2$ density profile, which arise from the assumption that the Galactic DM comprises an isothermal sphere. The various sources of uncertainty in this calculation were introduced in Section 2.2, but were seen to have at most an order-of-magnitude effect upon the limits set by a direct dark matter search experiment. The next chapter will explore the varied landscape of dark matter searches, on the earth at colliders and telescopes, in underground laboratories, and in space.

Chapter 3

Experimental Searches for Dark Matter

Figure 3.1 shows the three main ways to search for dark matter. The first, direct detection, appears in red, and involves the detection of scattered target molecules following a DM-nucleus interaction in a particle detector. These detectors are necessarily sited in deep underground laboratories in order to escape the flux of cosmic ray muons at the Earth's surface. The method of indirect dark matter detection appears in orange and is concerned with the detection of the standard model (SM) products of DM self-annihilation. Since the rate of this signal is proportional to the number density of DM particles, the ground- and space-based telescopes involved in indirect dark matter searches point toward regions of space expected to be DM rich, such as the Galactic centre and dwarf galaxies.

The final method, shown in blue, is the production of DM at particle colliders such as the Large Hadron Collider (LHC) at CERN, where the annihilation of gluon pairs may provide the mass-energy necessary to generate pairs of DM particles. Collider searches are limited to probing DM with $M_W \lesssim \frac{1}{2}M_{COM}$ and are only able to infer the existence of DM from a missing energy signature, but in the low-mass regime and within the framework of the chosen model, such searches can be competitive with, or even outperform direct search experiments. This chapter gives an overview of these three types of searches and their latest results, and ends with a discussion of a fourth dark matter signature, directionality, that would truly be a 'smoking gun' if discovered.
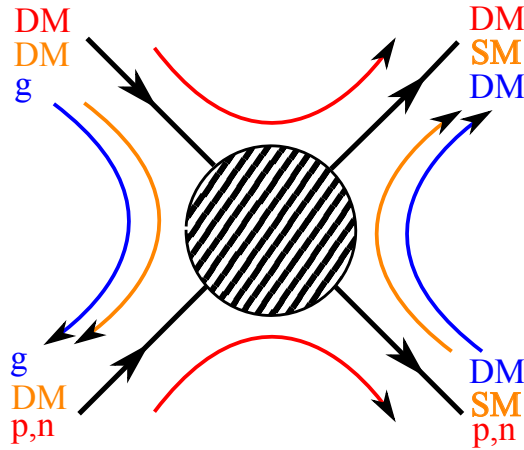
Figure 3.1: Cartoon interaction diagram showing the three methods of probing dark matter. Red: direct detection. Orange: indirect detection. Blue: production at colliders. The shaded circle represents our ignorance of the interaction details.

3.1 Direct Searches

Direct dark matter searches aim to measure the differential event rate of Equation 2.54 in order to discover, or set limits on, the properties of WIMP DM. In order to do this, they must accurately measure the energy of WIMP-nucleus interactions in their fiducial volume (FV) on an event-by-event basis, and be able to distinguish such 'signal' interactions from 'background' events that may be mistaken for a WIMP signal. The sensitivity of a detector must be checked using an artificial sample of nuclear recoil events from a neutron source such as ^{252}Cf or Am:Be. Direct detection experiments strive to lower the energy threshold of their sensitivity to DM events, since the rate of WIMP-nucleus elastic scatter events is expected to rise steeply at low energy (see Figure 2.3). Matching the mass of the target to the (unknown) WIMP mass also helps to maximise the rate (Equation 2.13), although the nuclear form factor of Equation 2.43, including the possible spin factor, must also be considered. In the case of spin-independent (SI) interactions, the A^2 enhancement of the cross section due to coherent scattering off the whole nucleus (Section 2.1.4) motivates the use of high-mass targets such as iodine, germanium and xenon.

3.1.1 Backgrounds

Sources of background events vary between detector types, but they can be broadly classified as either electromagnetic or nuclear. Most modern direct detector technologies have good electron/nuclear recoil discrimination, but in some cases it may be possible for electron recoils from electromagnetic interactions to mimic nuclear recoils from nuclear interactions, especially at low energy. Electron recoils are caused by γ emitters in detector materials.

Nuclear recoil backgrounds are usually much more difficult to distinguish from signal events, and therefore the focus of the direct detection community for the past 20 years has been the reduction or removal of potential sources of nuclear backgrounds. One of the first sources of such events to be identified was spallation neutrons caused by cosmic ray muons interacting with detector materials. This source of background can be removed by siting detectors in deep underground laboratories, where the cosmic ray muon flux is reduced to tolerable levels: $(4.09 \pm 0.15) \times 10^{-8}$ cm^{-2} s^{-1} in the case of the UK's Boulby mine [103]. Radioisotopes in the U and Th decay chains may be present in detector materials, and these can contribute a nuclear recoil background directly when they decay (either an emitted α particle, the recoiling nucleus, or both), or indirectly through α-decay and subsequent (α,n) reactions. These decay chains also produce radon gas, which contributes in the same way, and is chemically inert, making it extremely difficult to remove. Chapter 5 presents extensive work to measure and reduce radon backgrounds in DRIFT.

3.1.2 Solid-State Detectors

Early solid-state dark matter detectors used high-purity germanium (HPGe) crystals as their target for measuring the ionisation caused by spin-independent WIMP-nucleus interactions, but their sensitivity was limited by their lack of discrimination between electron and nuclear recoils [104]. Experiments such as CoGeNT have refined this technique to produce point-contact HPGe detectors with pulse-shape discrimination, and in 2011 they published a possible WIMP signal at low mass $7 < M_W < 11$ GeV/c^2 [105] . An alternative solution to the discrimination problem was found by the CDMS collaboration who, by cooling their detectors to < 100 mK temperatures, were able to measure not only the ionisation but also the heat deposited in phonons. The ratio of ionisation

yield to phonon energy is larger for electron recoils than for nuclear recoils, providing a means by which to discriminate signal from background [104]. The ionisation-phonon technique has recently been used by the CDMS-II collaboration on both silicon [106] and germanium [107] targets. A recent silicon run found three events in the pre-defined background-free signal region which, if interpreted as a signal, imply a WIMP mass of 8.6 GeV/cc and an SI WIMP-nucleon cross section of 1.9×10^{-41} cm^2 [106]. The same technique was employed by the EDELWEISS experiment at the Modane underground laboratory [108], although they found no evidence for DM.
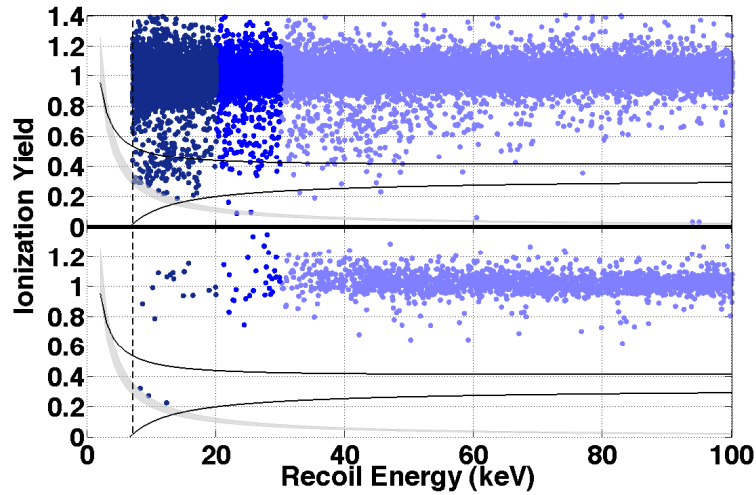
Figure 3.2: Discrimination between electron and nuclear recoils in the CDMS-II experiment before (top) and after (bottom) applying a final cut on phonon timing. If interpreted as dark matter, the three events in the bottom-left corner suggest a WIMP mass of 8.6 GeV/cc and an SI WIMP-nucleon cross section of 1.9×10^{-41} cm^2. From Agnese et al. [106].

The CRESST collaboration are exploiting a slightly different design of detector using a CaWO$_4$ crystal as the target material and scintillation light, rather than ionisation yield, as the discriminating variable [109]. This experiment has also detected a small population of events in the signal region which, if interpreted as DM, imply a WIMP mass of either 25.3 GeV /cm^2 or 11.6 GeV /cm^2 and corresponding SI WIMP-nucleon cross section of 1.6×10^{-42} cm^2 or 3.7×10^{-41} cm^2 in a maximum likelihood analysis that found two maxima.

These three results (CoGeNT, CRESST and CDMS-Si) are broadly in agreement,

although the results could be explained by an unidentified common source of background peculiar to solid-state semiconductor detectors. Indeed, Section 3.1.6 will show that the area of DM parameter space on which these three results converge is now ruled out by two independent experiments, which strongly disfavours the DM interpretation.

3.1.3 Liquid Noble Gas Detectors

Liquid noble gas detectors combine high-*A* targets with excellent discrimination to provide a powerful probe of the SI WIMP-nucleon cross section. There are several experiments running or under commissioning at the time of writing, which can be classified according to their target material (xenon/argon), or technology (single/dual phase). So far these detectors have seen no evidence for DM. Instead, the current world-leading limit on $\sigma_{WN}^{SI}(M_W)$ has recently been set by the LUX experiment, a two-phase liquid xenon detector operating out of the Sanford Underground Research Facility [110] (see Section 3.1.6). A schematic of a such a detector can be found in Figure 3.3. LUX is a time projection chamber (TPC), which uses an array of PMTs to
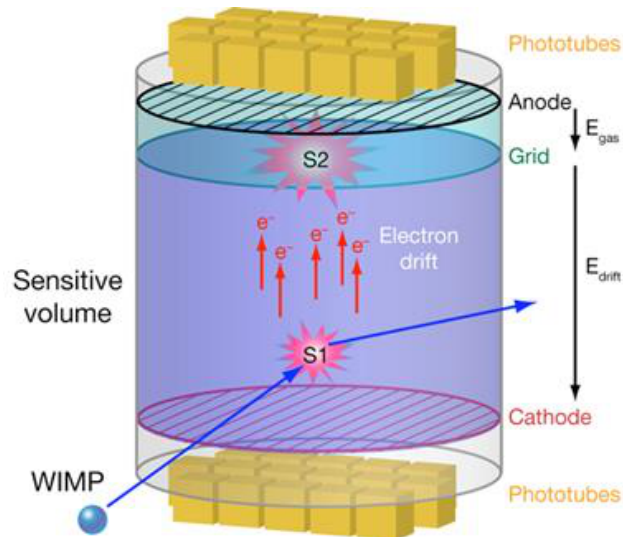
Figure 3.3: Schematic of a dual-phase liquid xenon time projection chamber. See text for explanation. From Cushman et al. [104].

measure the prompt scintillation light (S1) output from recombining xenon atoms in

the fiducial volume following an elastic scatter with a WIMP, as well as the delayed (S2) light from the remaining ionisation electrons that have been drifted by a carefully-tuned electric field, to the gas phase at the top of the detector. The ratio S2/S1 is larger for electron recoils than for nuclear recoils and this, combined with the self-shielding nature of liquid xenon, allows a background-free signal region to be defined all the way down to ∼ 5 keV, making the detector sensitive to the expected abundance of low-energy WIMP-nucleus interactions. Two-phase xenon technology was pioneered by the ZEPLIN collaboration [111] at the Boulby Underground Laboratory, and later by the XENON collaboration [102] at Gran Sasso.

Argon detectors operate in a very similar way to their xenon sisters, except that wavelength-shifters are used to bring the shorter-wavelength argon scintillation light into the UV region where the PMTs are sensitive. The use of argon also opens up an alternative channel of discrimination through pulse shape analysis, where the relative populations of short-lived singlet and long-lived triplet states are different for electronic and nuclear recoils. This removes the need for the gas phase, and makes possible single-phase argon scintillation detectors such as DEAP-3600 [112] and mini-CLEAN [113] at SNOLAB, and DarkSide50 [114] at Gran Sasso.

3.1.4 Superheated Liquid Detectors

Superheated liquid detectors are a variation on decades-old bubble chamber technology, and come in two distinct varieties. The first employs superheated droplets of liquid embedded in a gel target matrix: so-called 'droplet detectors'. When a WIMP scatters off a target molecule inside a droplet, the energy deposited causes an explosive phase change to occur, and bubbles to form around the droplet. No direct measurement of the deposited energy is made. Instead, the detectors operate in 'threshold' mode, whereby only an event depositing an energy ≥ the thermodynamically-defined minimum energy can cause bubble nucleation. Such detectors are insensitive to electron backgrounds, since their energy loss per unit distance ($\frac{dE}{dx}$) is too small to induce nucleation, but they do suffer from backgrounds from α particles. The removal of α backgrounds using their acoustic signals has been developed by the PICASSO experiment [115], and has also been adopted by the similar SIMPLE experiment [116]. Both use fluorine-rich targets (C_4F_10 and C_2ClF_5, respectively) to probe the spin-dependent WIMP-proton

cross section.

The second superheated liquid detector technology is similar to the droplet detectors, except that a single, monolithic volume of spin-dependent target liquid is used instead of a matrix of droplets. The COUPP collaboration [117] have presented results from a 437 kg d run of a bubble chamber detector of this design, ruling out σ_{Wp}^{SD} down to a minimum at $\approx 7 \times 10^{-39}$ cm for $M_W \approx 70$ GeV/cc.

3.1.5 Scintillating Crystal Detectors

The DAMA [118] collaboration have taken a different approach to the dark matter problem. Instead of seeking to carve out a background-free signal region of parameter space within which to search for rare DM recoil events, they opted instead to search for the annual modulation of the total event rate due to the Earth's motion around the Sun, as we move first with, then against the 'WIMP wind'. Whilst DAMA have worked extremely hard to improve their background rejection through pulse shape analysis and coincidence vetoing between their NaI detector crystals (reaching $90 - 99\%$ electron/nuclear recoil discrimination in the most recent run), there still exists an underlying background from other sources. Nevertheless, they have, since 1998 [118], claimed a discovery at the 5σ confidence level, which has risen to 9σ in the intervening years with the help of an upgrade to the radiopurity of detector materials, new thallium-doped NaI(Tl) crystals, and improved 3-level sealing system to mitigate the effects of radon [119]. The low-energy event rate modulation can be clearly seen in Figure 3.4. However, there is no consensus in the community that all possible terrestrial sources of such a modulation have been ruled out. Their maximum likelihood fit is comfortably ruled out by several experiments using different detector technologies (see Figure 3.5).

A very similar experiment called DM-Ice is currently taking data at the bottom of the IceCube array in the South Pole icecap, in an attempt to reproduce the signal from DAMA [120] and to test for the phase reversal expected from a detector in the opposite hemisphere. Other groups such as ANAis [121], KIMS [122] and PICO-LON [123] are attempting similar searches to DAMA, using scintillating crystals such as CsI, CsI(Tl), NaI(Tl), and CsI(Na).
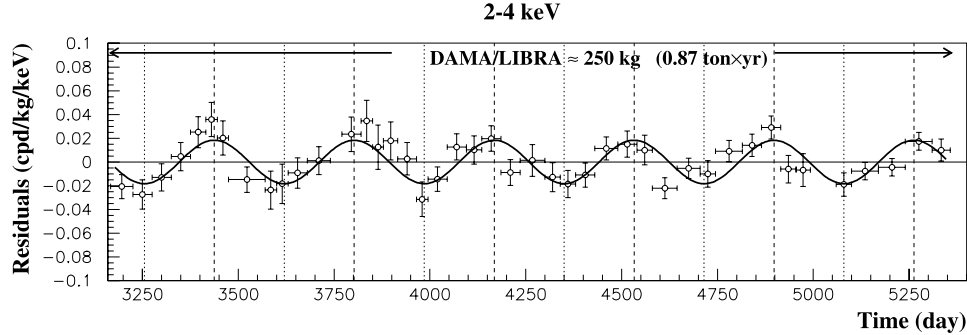
Figure 3.4: Modulation of the event rate in the NaI(Tl) crystals of the DAMA/NaI and DAMA/LIBRA experiments, spanning 13 yr. From Bernabei et al. [119].

3.1.6 Current Status and Outlook

Spin-Independent

Thanks to the A^2 cross section enhancement factor due to binding, it is the SI interaction that has received the most experimental attention to date. However, the picture being painted by SI search experiments at the time of writing is one of some confusion. The low-mass signals from CRESST, CoGeNT and CDMS appear to hint at a WIMP with $M_W \sim 10$ GeV$/$c^2 and $\sigma \sim 10^{-40}$ cm^2 where their 95% confidence regions overlap in Figure 3.5. The low-mass DAMA region (shown in yellow on the plot) is also broadly consistent with these three results. Frandsen *et al.* have shown that it is possible to fully reconcile the signals by assuming a highly anisotropic velocity distribution [124], however it is not possible to adjust the astrophysics enough to move the results out of the region of parameter space that is now excluded by the XENON-100 (black line) [102] and LUX (blue line) [110] experiments.

The favoured regions of parameter space for some of the theoretical models discussed in Section 1.3 appear as shaded regions on Figure 3.5. The solar and atmospheric neutrino coherent scattering can also be seen at the bottom of the figure, which will be an irreducible and prohibitive background to direct dark matter searches, putting an end to such 'energy only' searches if WIMPs are not discovered before the exclusion curves reach it. At this point, we will require alternative signatures such as annual modulation, or directional detection (see Section 3.4) in order to continue looking for DM.
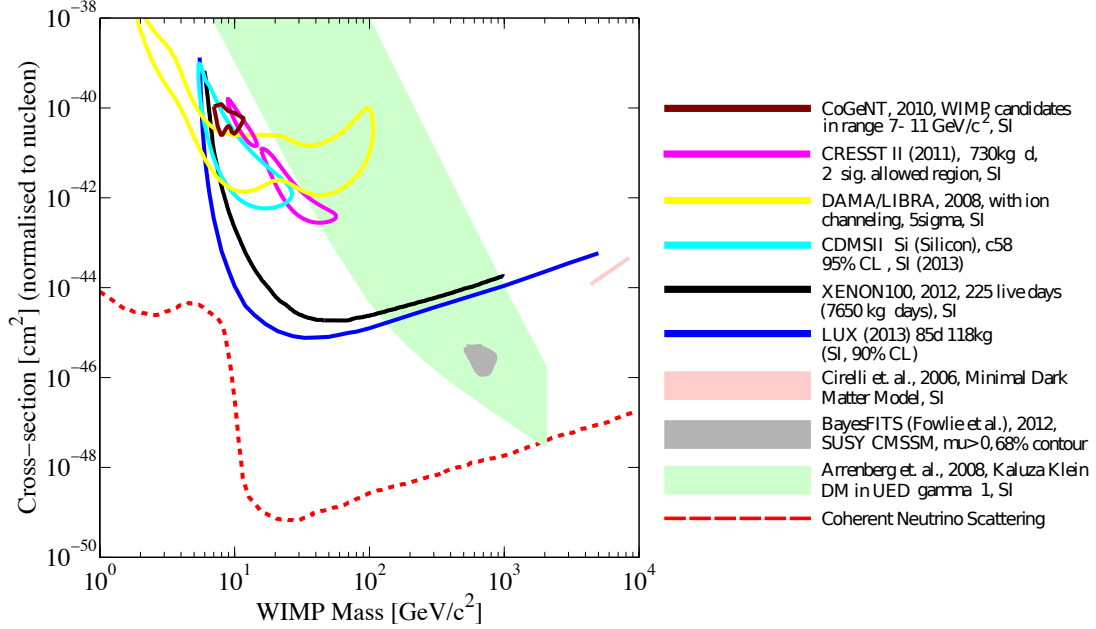
Figure 3.5: Recent hints and limits on the spin-independent WIMP-nucleon cross section as a function of M_{DM}, along with preferred regions of parameter space for the candidate particles of several theoretical frameworks. Plot created using DM Tools [125].

Spin-Dependent

The spin-dependent parameter space is less well-investigated, thanks to the lack of the aforementioned A^2 enhancement factor. However, several experiments have set limits on $\sigma_{W[n,p]}^{SD}(M_W)$, and these are presented in Figure 3.6. Experiments incorporating spin-$\frac{1}{2}$ nuclei in which the unpaired nucleon is a neutron appear in the left-hand plot, whereas those with an unpaired proton (usually fluorine) appear on the right. A similar plot showing the latest published limit from the DRIFT collaboration is presented at the end of Chapter 4, whilst Chapter 8 is concerned with the calculation of an improved limit using a novel background rejection technique. As discussed in Chapter 2, all experiments assume the parameters of the Standard Halo Model to facilitate comparison on plots such as Figures 3.5 and 3.6.
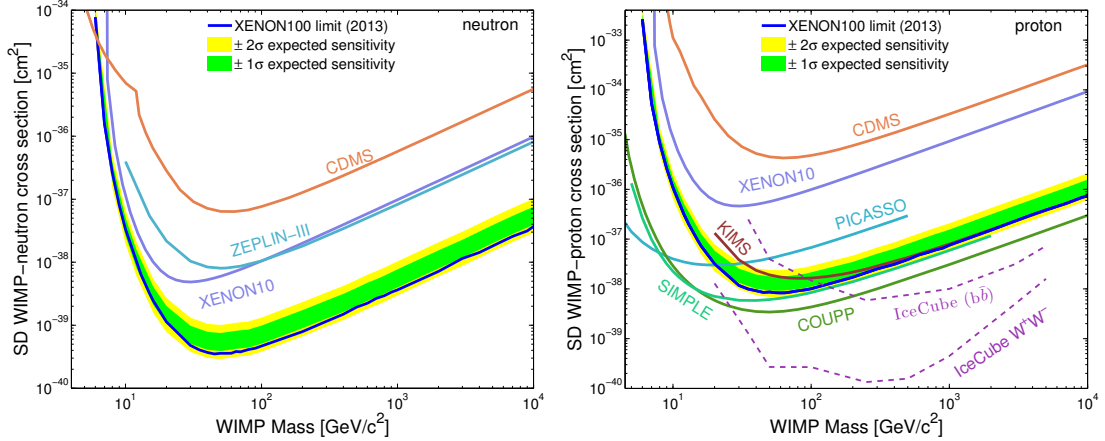
Figure 3.6: Limits on spin-dependent WIMP-neutron (left) and WIMP-proton (right) cross sections as a function of M_W. From Cushman et al. [104].

3.2 Indirect Searches

As shown in Section 1.3, the annihilation cross section that gives the observed present-day relic abundance of WIMP DM is $\langle\sigma_{ann}v\rangle \approx 3 \times 10^{-26}$ cm^3 s^{-1}. Although the present-day rate of WIMP self-annihilation is effectively zero, this process can still take place in regions of space where the local density is high enough (provided that DM undergoes annihilation at the present epoch, which is not the case in models such as asymmetric DM). Furthermore, the annihilation of WIMP pairs into SM particles produces a signal that should be detectable, as shown in Figure 3.7. Searches are underway for these annihilation products, and these are just beginning to reach the sensitivities that can exclude thermal relic WIMP models.

3.2.1 Gamma-ray searches

DM particles annihilating according to the diagram on the right-hand side of Figure 3.7 would leave a signature of DM in the form of a narrow peak in the gamma ray spectrum at $E_\gamma = M_{DM}$ (a line signal). Interactions on the left-hand side of the same figure may also contribute to the diffuse gamma-ray background, which opens up the possibility of using the more diffuse Galactic emission to place constraints on $\langle\sigma_{ann}v\rangle$ as a function of M_W [127, 128]. The best places to look for a line signal are those in which
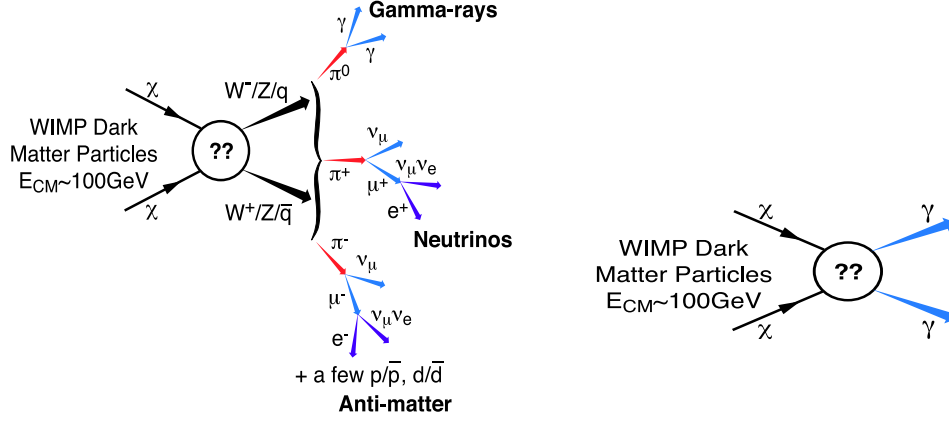
Figure 3.7: Possible detectable standard model decay channels for WIMPs. Adapted from Baltz et al. [126].

the DM density is large, and the astrophysical backgrounds are small. The Galactic centre fulfils the first of these criteria, especially when the concentrating effects of the supermassive black hole are taken into account [32]. However, the astrophysical backgrounds are large and have hampered efforts to constrain dark matter properties using gamma rays in this region. Nevertheless, stringent upper limits on $\langle\sigma_{ann}v\rangle$ have been set using data from the Fermi satellite (specifically the large area telescope – LAT – instrument) [129]. Another promising place to look is in dwarf spheroidal galaxies [130] as, although their emission is expected to be at least $10,000\times$ fainter than that from the Galactic centre [129], their astrophysical backgrounds are fewer and less severe.

Christoph Weniger has found evidence at the 3.2σ confidence level for a gamma ray line signal at $E_\gamma \approx 130$ GeV in 43 months of Fermi-LAT data [131], implying a *partial* annihilation cross section of $\langle\sigma_{ann}v\rangle_{\chi\chi\to\gamma\gamma} = 1.27 \pm 0.32 \times 10^{-27}$ cm^3 s^{-1}. Huang, Urbano and Xue have studied the energy spectrum as a function of galactic latitude of the recently-discovered Fermi bubbles [132]. These bubbles of gamma ray emission extend to $25,000$ LY above and below the galactic poles (see Figure 3.8), and the spectrum of the outer regions indicate that they are dominated by photons of the interstellar radiation field that have been up-scattered by high-energy cosmic ray electrons of as-yet unknown origin. In contrast, the spectrum of the inner region was found to exhibit an anomalous bump at $E_\gamma \sim 1 - 4$ GeV, which may be indicative of

a component from DM-DM annihilation. Interpreting the signal as such, the best-fit candidate is one that annihilates to $b\bar{b}$, with mass $M_{DM} = 61.8^{+6.9}_{-4.9}$ GeV and cross-section $\langle\sigma_{ann}v\rangle = 3.30^{+0.69}_{-0.49}\times 10^{-26}$ cm^3 s^{-1} [132]. The same study also set limits on the annihilation cross section. However, particle physics model dependence of branching ratios for the processes in Figure 3.7, and the absence of a universally-adopted set of halo parameters in the indirect detection community make comparing limits between different studies difficult.
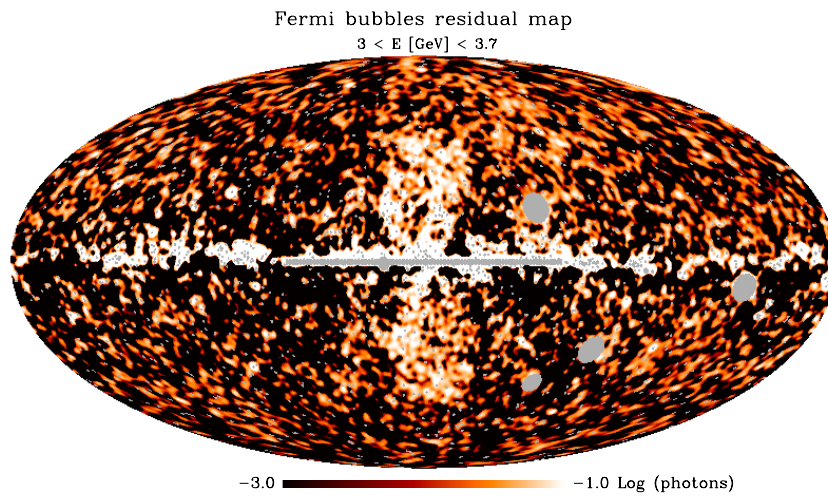
Figure 3.8: Fermi-LAT's edge-on view of the Milky Way disk showing the Fermi bubbles: a good place to search for gamma rays from dark matter annihilation. From Huang, Urbano, and Xue [132].

3.2.2 Neutrino searches

Dark matter particles entering the gravitational potential well of the Sun are scattered by protons and slowed below the escape speed (captured), at a rate C_c which is dependent upon the *scattering* cross-section σ^{SD}_{Wp}. Eventually, the DM inside the Sun reaches equilibrium:

$$\Gamma_A = \frac{C_c}{2}, \tag{3.1}$$

where Γ_A is the annihilation rate inside the Sun. By assuming a particle physics model, one can compute the branching fraction of $DM + DM \rightarrow \nu\bar{\nu}$, and thus by searching for

an excess in solar neutrinos it is possible to infer the DM capture rate and hence the WIMP-proton scattering cross-section, which allows such searches to compete with the direct search experiments of Section 3.1 [133]. Neutrinos are able to pass virtually unimpeded from their point of creation to a detector on the Earth's surface, which would make them ideal messengers but for their tiny interaction cross section. This means that a detector with large fiducial mass is necessary to build statistics on reasonable timescales.

IceCube is such a detector, and consists of an array of photomultiplier tubes (PMTs) instrumenting roughly 2 cubic km volume of antarctic ice. Neutrino charged current interactions in the ice produce leptons that travel faster than the speed of light in ice, emitting Cerenkov light, which is recorded by the PMTs. Dark matter annihilations would manifest themselves in IceCube data as a broadband excess in the neutrino spectrum at moderate energies ($10 - 100$ GeV), as opposed to a line signal, coming from the direction of the Sun. A recent search for an excess of such events has placed strict, albeit model-dependent, limits on $\sigma_{Wp}^{SD}(M_W)$ (see Figure 3.6) [134]. Neutrinos from the Galactic centre have also been used to constrain $\langle\sigma_{ann}v\rangle$ for $M_W > 100$ GeV [135].

3.2.3 Searches for Antimatter

Cosmic ray positrons may be produced by annihilating dark matter according to Figure 3.7, and have been searched for by satellite-borne particle detectors such as PAMELA [136, 137], AMS-02 [138] and indirectly by Fermi-LAT [139]. Under the assumption that the only contribution to the spectrum is from well-understood 'secondary sources' such as interactions of cosmic rays with the interstellar medium, the spectrum is expected to be smoothly-falling and featureless. Instead, the spectrum of Figure 3.9 is observed, which begins to rise at $E_{e^{\pm}} \approx 10$ GeV. This turnover has been interpreted as evidence for dark matter annihilation to positrons, but contributions from other primary sources such as pulsars, which act as cosmic particle accelerators, are also possible. Interpreting the excess as an astrophysical background facilitates the calculation of limits on $\langle\sigma_{ann}v\rangle$, and rules out WIMP models that invoke interactions of the form $DM + DM \rightarrow W^+W^-$ or Z^0Z^0 to explain the excess [15]. In order to simultaneously obtain the observed event rate and attribute the rising spectrum to $DM + DM \rightarrow e^+ + e^-$, an annihilation cross section several orders of magnitude larger
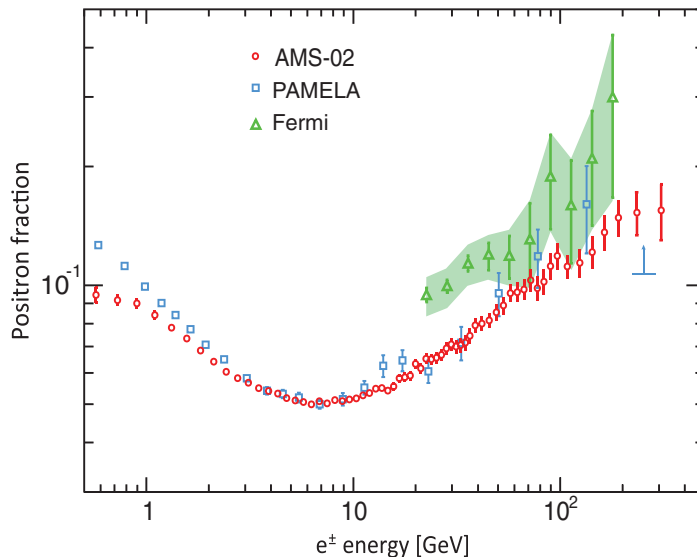
Figure 3.9: Energy spectrum of cosmic ray positrons measured by the AMS-02, Pamela, and Fermi satellite experiments. From Aguilar et al. [138].

than that implied by the relic density is necessary. A possible mechanism for achieving such a late-time enhancement of the annihilation cross section is the Sommerfeld process, which is suppressed for fast DM particles in the early universe (which saves the WIMP miracle), but active at late times when particle speeds are lower [48]. Application of Occam's razor, however, would seem to favour the alternative astrophysical source explanation [15].

The AMS-02 instrument is also able to detect antiprotons, but no excess is seen in this spectrum. In the future, comparison of the positron and antiproton excesses should yield strong constraints on the particle physics model behind DM. For example, any excess observed in the antiproton fraction is suggestive of a non-zero branching to quarks or gauge bosons, so the fact that this excess has not been observed favours purely-leptonic DM models [32].

3.3 Collider Searches

Dark matter should be produced at the LHC according the process labelled in blue in Figure 3.1, provided the centre-of-mass energy is large enough. Whether or not the

energy is sufficient is determined by both the size of M_{DM} and the specifics of the interaction that leads to its production, which is represented by a shaded circle in the figure to highlight our lack of knowledge of the underlying particle physics. If a pair of DM particles were to be produced alone in a collision, they would leave no trace except for missing energy, and no signature on which to trigger the data acquisition system (DAQ). Therefore, DM searches at the LHC's ATLAS [140] and CMS [51] detectors have focused on searching for missing energy (MET) in events triggered on initial state radiation in the form of either a single photon (monophoton), or single gluon (monojet) [141]. Since backgrounds to such searches are much less of a problem at higher energies, DM searches at colliders are mainly sensitive to low-mass DM particles, which are more easily produced with higher momentum [32].

LHC data has been used to set limits on DM properties following an effective field theory (EFT) approach similar to that used for SUSY in Section 1.3.1. Effective field theory is a useful tool that enables the investigation of low-energy phenomena by averaging over the behaviour of an interaction at high-energy, which remains 'unresolved'. EFTs are characterised by the contact interaction scale Λ, above which the EFT approach breaks down and the detailed structure of the interaction must once again be considered. Their employment facilitates the setting of limits on DM properties in $\sigma_{W[p,n]}(M_W)$ space using data from the LHC, however care must be taken to ensure that the EFT is valid. Buchmueller, Dolan and McCabe have recently highlighted the fact that the EFT approach is only valid in the limit that the mediator mass $m_{med} \gg$ the typical energy transfer [142]. For mediator masses comparable or smaller than the typical energy transfer, effects such as resonant enhancement must be resolved.

Figure 3.10 shows the limits on $\sigma_{W[p,n]}(M_W)$ under the assumption that Nature has chosen $m_{med} \gg M_{DM}$ (which may or may not be valid), alongside a plot illustrating the areas of $m_{med} - M_{DM}$ space in which direct detection experiments are outperformed by CMS searches. This plot also highlights the complementarity of collider and direct searches, with direct experiments outperforming colliders at high M_{DM} and *vice versa*.

Finally, it is important to note that collider searches for DM place only very weak limits on the lifetime of the particle, which is required to be greater than the age of the Universe in order to satisfy point 1 of the DM candidate checklist in Section 1.3. Therefore, a positive discovery at the LHC would need to be confirmed by at least one
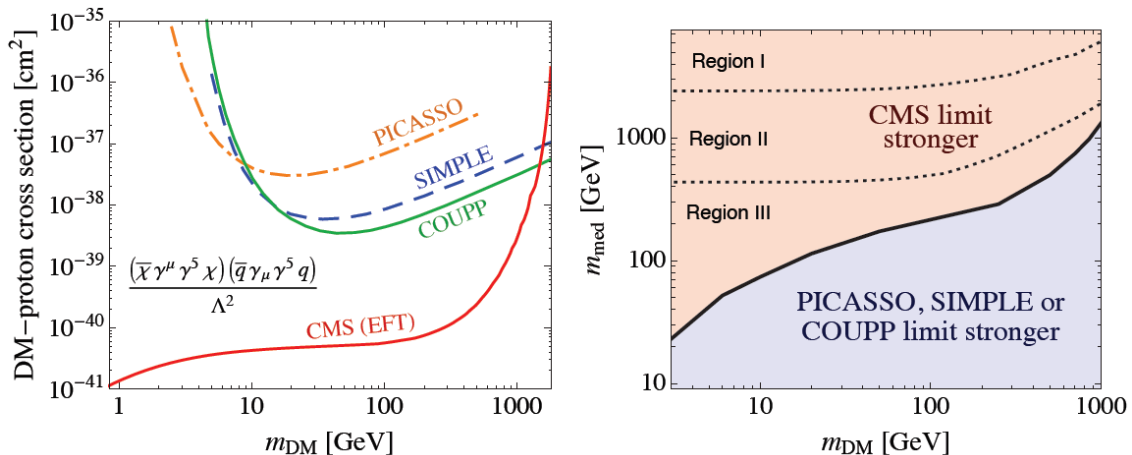
Figure 3.10: Left: limits on the spin-dependent WIMP-proton cross section from DM searches as the LHC's CMS experiment, assuming that the effective field theory approach is valid. Right: plot showing the regions of $m_{med} - M_{DM}$ space in which collider and direct detection experiments are more sensitive. The EFT approach is only valid in Region 1. From Buchmueller, Dolan, and McCabe [142].

direct or indirect detection in order to be generally accepted [141]. On the other hand, DM signatures in direct and indirect searches are fairly similar for a broad range of particle physics DM models, therefore colliders will be invaluable post-discovery for pinning down the exact nature of the interactions.

3.4 Directional Searches

It is clear that, although some hints have appeared, a consistent picture of DM has yet to materialise from the three-pronged search strategy outlined in the previous section, the limiting factor in all cases being a clear signal identification. There is a fourth technique that could provide an unambiguous signal of dark matter: directional detection. In contrast to direct, indirect and collider searches, a positive signal in a single directional detector would constitute a concrete discovery [143]. All operational directional detectors are currently in the R&D phase, however the DRIFT collaboration has successfully operated $\mathcal{O}(1)$ m^3 detectors with limit-setting power approaching that of more massive direct detection experiments for over 10 years.

Directional DM detectors seek to reconstruct not only the energy, but also the direction of incident DM particles. The motion of the solar system through the dark matter halo causes a 'WIMP wind' to blow from the direction of the constellation Cygnus, which gives rise to a preferred direction of nuclear recoils in the opposite direction [144] (see Figure 3.11). It is very difficult to think of a background process that could mimic such a signal. Morgan and Green have worked extensively on calculating the number of events in a directional dark matter detector that are required to reject the null hypothesis of an isotropic distribution of recoil directions, and this turns out to be ~ 11 [143] for a realistic detector configuration with 3D readout. This number increases to ~ 130 if only the axial direction of the recoil can be reconstructed, therefore track head-tail discrimination is extremely important [145]. The DRIFT collaboration have pioneered the use of directional detectors to search for DM at the Boulby Underground Science Facility in Cleveland, UK [146]. Moving to an optimally-aligned 2D configuration with head-tail discrimination only modestly increases the number of events required to reject isotropy, to ~ 26 [143].

Typical track lengths in solid- or liquid-state direct detection experiments are $\sim \mu$m, which would require a readout granularity far beyond the reach of current real-time-readout technology to resolve. Instead, directional detectors employ gaseous targets and state-of-the-art μm resolution readout schemes such as MICROMEGAS, μPIX and CCD imaging, combined with a uniform electric field to form a low-pressure (≈ 100 mbar) time projection chamber (TPC). The price to pay for moving to the gas phase is a $\approx$ 3-orders-of-magnitude reduction in target density, with directional detectors presenting only of order 100 g target mass to the incoming WIMPs (cf. ≈ 100 kg for direct detectors). However, the extra information provided by the several-mm particle tracks enables extremely efficient background rejection [148], as long as diffusion of the ionisation along its drift path can be suppressed effectively [149]. It is a generic feature of directional detectors that the target gas can be easily changed in order to optimise the search for different types of DM. Currently all directional DM detectors employ targets with non-zero spin (usually fluorine), in order to probe the SD WIMP-nucleon cross sections, however there is no reason why SI targets could not be used as well. Indeed, in the event that the march of the liquid noble gas detector limits continues all the way down to the neutrino coherent scattering background (see Figure 3.5), directionality and annual/diurnal modulation will remain as the only direct signatures
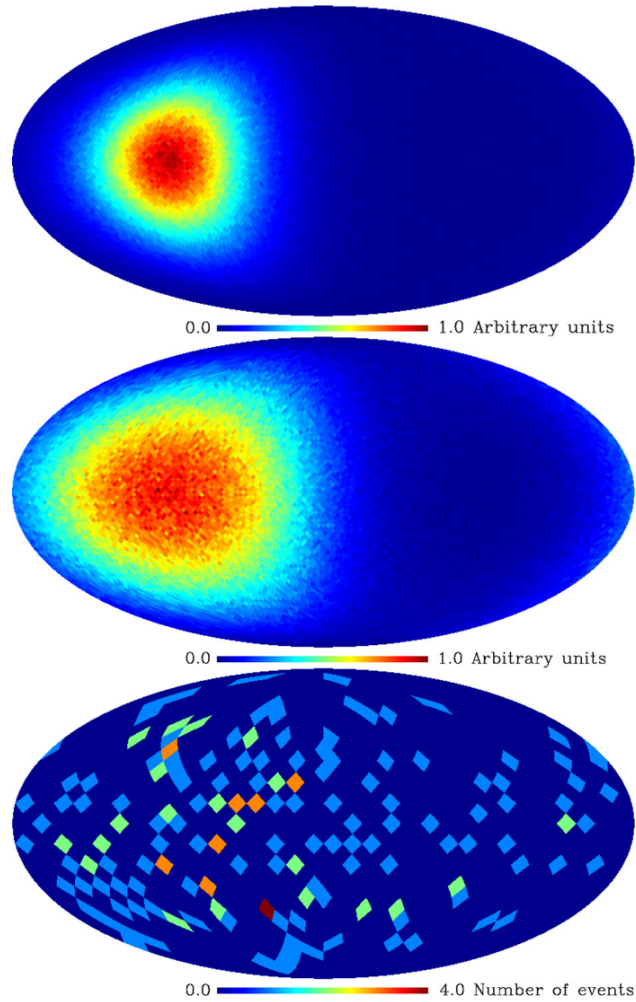
Figure 3.11: Top: WIMP distribution assuming an isothermal DM halo. Middle: Distribution of recoils arising from elastic scattering of these WIMPs off target nuclei. Bottom: Simulation of 100 signal and 100 isotropic background events in the energy range $5 < E_R < 50$ keV. All panels are in Galactic co-ordinates. From Billard et al. [147].

of DM left open to observation.

3.4.1 DRIFT

The Direction Recoil Information From Tracks (DRIFT-II) experiment [150] is a 1 m^3 negative-ion time projection chamber (NITPC) operating with a mixture of CF$_4$ and CS$_2$ gases, and is the main subject of this thesis. Following a nuclear recoil, the resulting ionisation electrons are captured on the moderately-electronegative CS$_2$ molecules, which act as a transport gas and suppress diffusion to thermal levels, thus preserving the spatial information contained in the track [149]. The CF$_4$ molecule's fluorine nuclei act as a SD target. The drift chamber is read out by two back-to-back multi-wire proportional counters (MWPCs) on either side of a central cathode. Chapter 4 describes the experiment and data reduction procedure in detail.

3.4.2 MIMAC

The MIMAC (MIcro-tpc MAtrix of Chambers) experiment [151] has the same shared central cathode and back-to-back TPC geometry as DRIFT, but a volume 1000× smaller [151]. The collaboration has installed a detector underground at the Laboratoire Souterrain de Modane, but no results have yet been published. They have had remarkable success with a prototype detector operating on the surface, which is read out every 25 ns using bulk micromegas segmented into 350 μm-spaced pixels and has operated with gas mixtures including CF$_4$, ^{3}He and C$_4$H$_{10}$. The detector has achieved a low energy threshold of ~ 5 keV: ~ 10× lower than DRIFT, but it is not clear how diffusion will be suppressed in a future scale-up, which will be necessary in order to provide a target mass capable of detecting WIMPs with the small SD cross section implied by direct detection experiments (Figure 3.6). An example of a reconstructed track in MIMAC is shown in Figure 3.12, where z is the drift dimension measured with timing, and x and y are the orthogonal orientations of the micromegas pixel strips [152].

3.4.3 DMTPC

The Dark Matter Time Projection Chamber (DMTPC) collaboration have chosen to read out their CF$_4$-filled TPC using a camera. Light is generated in EM avalanches in a high-field region defined by a wire mesh at the top and bottom of their fiducial volume. This optical technique has the potential to provide excellent tracking informa-
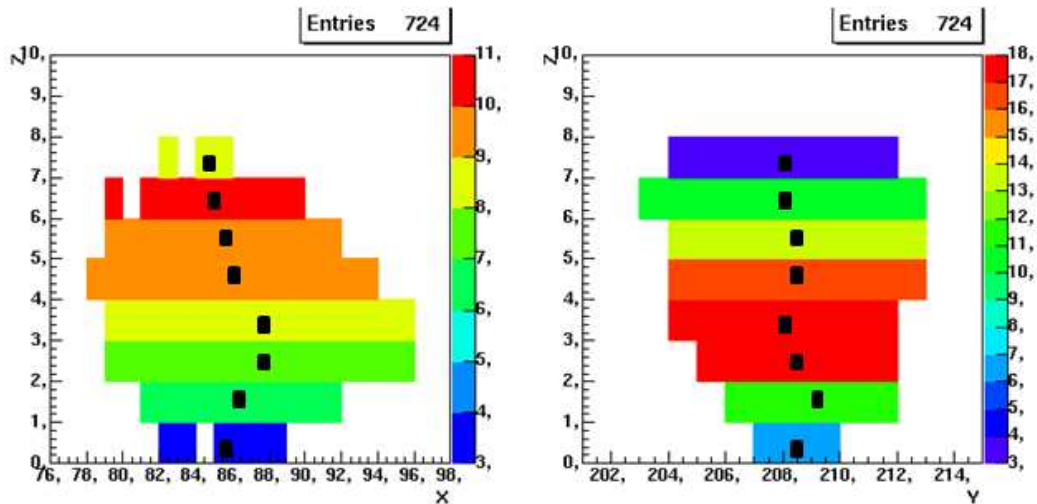
Figure 3.12: A 50 keV$_{ee}$ fluorine recoil track in 50 mbar 7:3 CF_4:CHF_3 in the MIMAC prototype detector. Left: XZ projection. Right: YZ projection. Colour represents the number of strips above threshold in a given timeslice. From Billard, Mayet, and Santos [152].

tion although reconstruction is currently only 2-dimensional due to the slow readout time of the CCD technology used to detect the avalanche photons. Another advantage is the removal of the need for many electronic read-out channels, which is likely to be the main cost associated with scaling up other directional experiments. The current prototype detector has a fiducial volume of $160 \times 160 \times 500$ mm at a pressure of 75 torr giving a total target mass of 3.3 g, but as with MIMAC, diffusion of tracks prior to avalanche is a barrier to scale-up [153, 154]. The DMTPC collaboration have demonstrated head-tail sensitivity down to 100 keV, examples of which can be found in Figure 3.13. A reduction in energy loss towards the end of the track can be clearly seen, indicating that the track moved from right to left [155].

3.4.4 NEWAGE

The NEw generation WIMP search with an Advanced Gaseous tracking device Experiment (NEWAGE) experiment [156] at the Kamioka underground laboratory uses a novel high-resolution (400 µm) electronic readout scheme called µ-PIC [157] to read
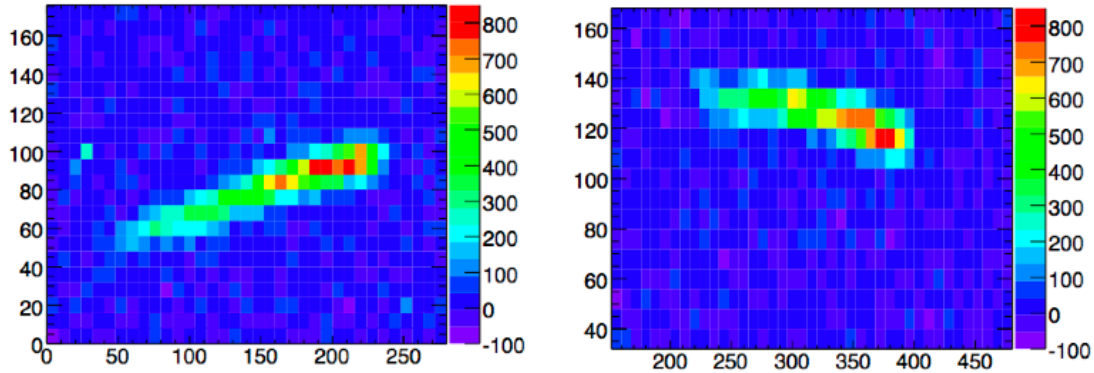
Figure 3.13: Two 100 keV$_{ee}$ neutron-induced recoil tracks in 75 torr CF$_4$ in the DMTPC detector. Neutrons were incident from the right. From Battat et al. [155].

out a 50 cm drift region filled with 152 torr CF$_4$. A gas electron multiplier (GEM) stage is placed directly above the μ-PIC to provide sufficient gain to observe nuclear recoils down to energies of 100 keV [158]. The collaboration plans to scale-up their detector by a factor of 10, demonstrate head-tail sensitivity, and are about to embark on a radon audit of their detector in order to reduce the rate of background events by a factor of 50.

3.4.5   Other R&D

Resistive μ-PIC

Ochi *et al.* have recently made improvements to the μ-PIC technology. By employing resistive electrodes, they were able to reduce the spark rate in the detector by a factor of 10^4, at the same time enabling the anode to be operated at ground potential, drastically simplifying the readout electronics [159]. Resistive cathode μ-PIC (Figure 3.14) represent the state-of-the-art in TPC readout technology.

Thick GEMs with Optical Readout

Loomba *et al.* have recently shown the discrimination power of combining a thick gas electron multiplier (TGEM) with optical readout (see Figure 3.15). Using this technique they have achieved a threshold for electron/nuclear recoil discrimination of
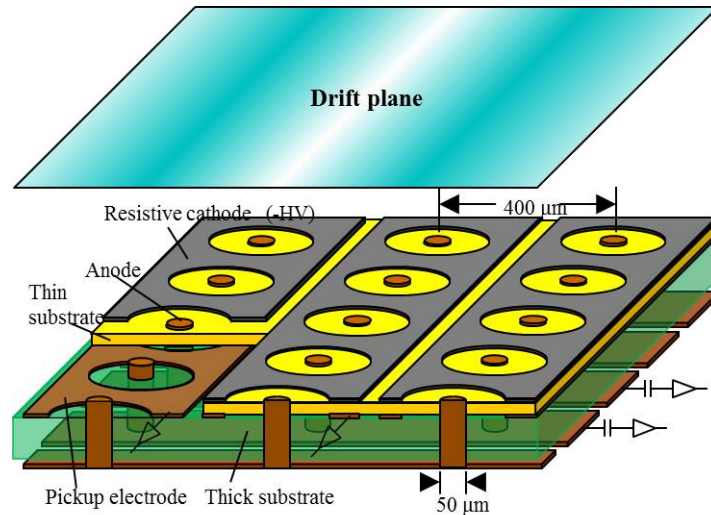
Figure 3.14: Diagram of resistive cathode μ-PIC. From Ochi et al. [159].

25 keV$_r$, and head-tail sensitivity down to 55 keV$_r$ [160].

Emulsions

A group led by Tatsuhiro Naka at Nagoya University operates a novel directionally-sensitive detector based on silver halide nuclear emulsions, a technology originally developed by the photographic industry. By measuring the shape of tracks in a solid-state 3D detector consisting of AgBr grains suspended in gelatine, it is possible to infer the direction of the recoiling particle. Since the tracks of interest are only several hundred nm long, it has been necessary to develop custom high-resolution emulsions with grain size 35 nm instead of the standard 200 nm, which are imaged using an optical or x-ray microscope [161]. In order to improve the efficiency of the imaging process, the emulsions are first physically expanded by a factor of two. Track lengths as short as 70 nm can be imaged, which corresponds to an energy threshold of ∼ 40 keV [162]. However, to date no emulsions incorporating spin-dependent nuclei have been developed, so these experiments probe the SI WIMP-nucleon cross-section. Emulsion experiments are currently at the gram scale, but the technology lends itself well to scale-up.

(a) 10 keV$_{ee}$ electron recoil.

(b) 70 keV$_{ee}$ (100 keV$_r$) nuclear recoil.
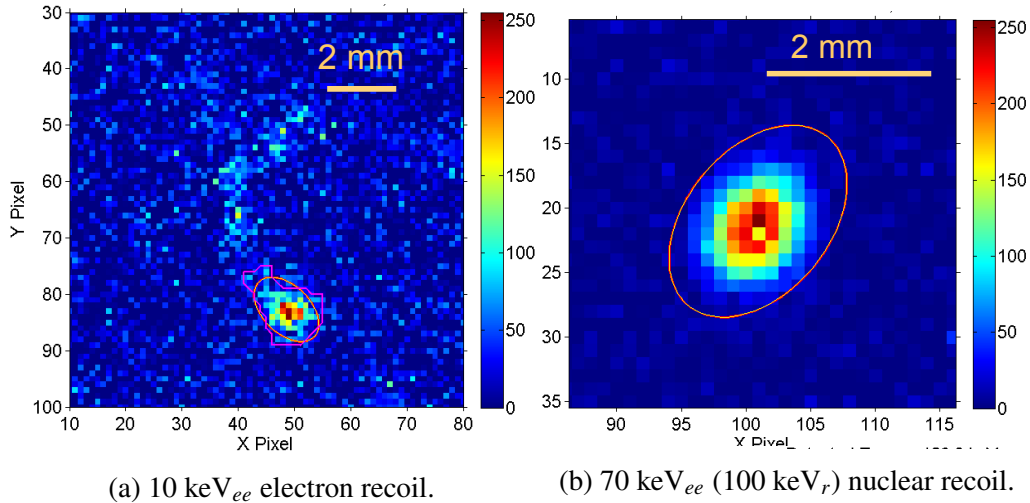
Figure 3.15: Electron (left) and nuclear (right) recoils in 100 torr CF$_4$, amplified using a TGEM and read out optically. From Loomba [160].

Columnar Recombination

Dave Nygren at LBNL has recently introduced a new concept for directional detection that has the potential to solve both the diffusion and low-detector-mass problems [163]. The concept is called 'columnar recombination', and exploits the fact that the electrons produced in a column of ionisation immediately following a WIMP-induced nuclear recoil recombine with the positive ions of the track in a way that depends upon the track's orientation relative to the drift field. Tracks perpendicular to the drift field experience minimal recombination, as the field pulls electrons away from the ions. Conversely, electrons created in tracks parallel to the drift field move alongside the ions, and therefore experience maximal recombination. Therefore, the amount of recombination relative to the total event energy contains directional information. Furthermore, measuring the amount of recombination using light provides access to a directional signal *before* diffusion, leaving the residual charge to be drifted to an amplification stage, and measured either optically or electronically to give a measurement of the total event energy, for which track shape is unimportant.

Nygren has suggested that this technique could be applied in a 10 bar mixture of xenon + trimethylamine, to create a detector that is both high-mass and directionally sensitive, although to the author's knowledge no prototype has yet been built. One drawback of the technique is the lack of any head-tail information about the track,

which has been shown to increase the number of events required to discover a directional signature by a factor of ~ 10 [143].

3.5 Conclusions

Four methods of searching for DM have been introduced: direct, indirect, collider and directional searches. It is generally accepted that a positive signal of DM from any of the first three methods would require confirmation from at least one of the others in order to be considered a concrete discovery. Directional detection stands alone as the only method which can provide an unambiguous signal with a single experiment, but such detectors are necessarily several orders of magnitude lower in target density than their direct counterparts, highlighting the need for scale-up. Several hints of a low-mass DM signal have appeared in direct DM searches with solid-state detectors in the past three years, and these are broadly in agreement with a long-standing but contentious result from the DAMA collaboration. However, two recent searches with liquid noble gas detectors (XENON-100 and LUX) have now excluded the area of parameter space favoured by the solid-state experiments, so the picture from direct searches is somewhat conflicted.

The products of DM-DM annihilations in the Galaxy are being searched for by space-based detectors and ground-based telescopes. Several recently-detected anomalies have been interpreted in terms of dark matter, but there is no consensus at the time of writing that these hints cannot be explained in terms of more mundane astrophysical sources. Interpreting them as such, indirect searches have been used to constrain DM properties; however, this is a very model-dependent process. Finally, searches for DM production at colliders have also been used to constrain DM properties, and these have been shown to be competitive with direct search experiments at low M_{DM}. At higher masses, however, the effective field theory framework within which the results are interpreted breaks down, and direct searches become more sensitive.

Chapter 4

The DRIFT-IId Detector

The DRIFT detector introduced in Section 3.4.1 is a negative ion time-projection chamber (NITPC) dark matter 'telescope', searching for not only the energy, but also the directional signature of dark matter caused by the motion of the Earth through the Milky Way's DM halo. The DRIFT collaboration have pioneered the development of TPC technology for directional dark matter searches, an R&D program that has spawned a field of research spanning the globe, and the current iteration of the experiment, the ~ 1 m^3 DRIFT-IId, remains the leader in the field, setting limits on the spin-dependent WIMP-proton cross-section approaching those of much more massive experiments. The collaboration is currently working towards scaling up to a 24 m^3 detector: DRIFT-III, and a prototype detector DRIFT-IIe on the same scale as DRIFT-IId is being installed alongside its predecessor at Boulby Underground Laboratory to act as a testbed for new directional dark matter search technology.

Boulby Mine is a working potash and salt mine near Whitby in the North East of England. The Palmer lab, which hosts DRIFT, has a rock overburden of 1.1 km that provides 2805 ± 45 m of water equivalent shielding against cosmic ray muons [103]. The lab also has very low levels of ambient radon, which can be a major source of background for dark matter experiments. Radon measurement and mitigation for DRIFT is investigated in Chapter 5. This chapter provides a detailed description of the DRIFT-IId detector, as well as the data reduction strategy, which is the foundation on which the studies presented in Chapters 5, 6 and 8 are based.

4.1 Detector Technology

DRIFT is comprised of two back-to-back NITPCs, each with a drift length of 50 cm, housed inside a stainless steel vacuum vessel and encased in a neutron shield of polypropylene pellets > 67 cm thick on all sides [164]. The 1100 m rock overburden (2800 m.w.e) of the Boulby lab ensures that the flux of cosmogenic neutrons is minimised [103]. The two detectors share a -28.4 kV central cathode which, coupled with the grounded anode of the readout plane, defines a drift field of 624 V cm^{-1} in the fiducial volume as shown in Figure 4.1.
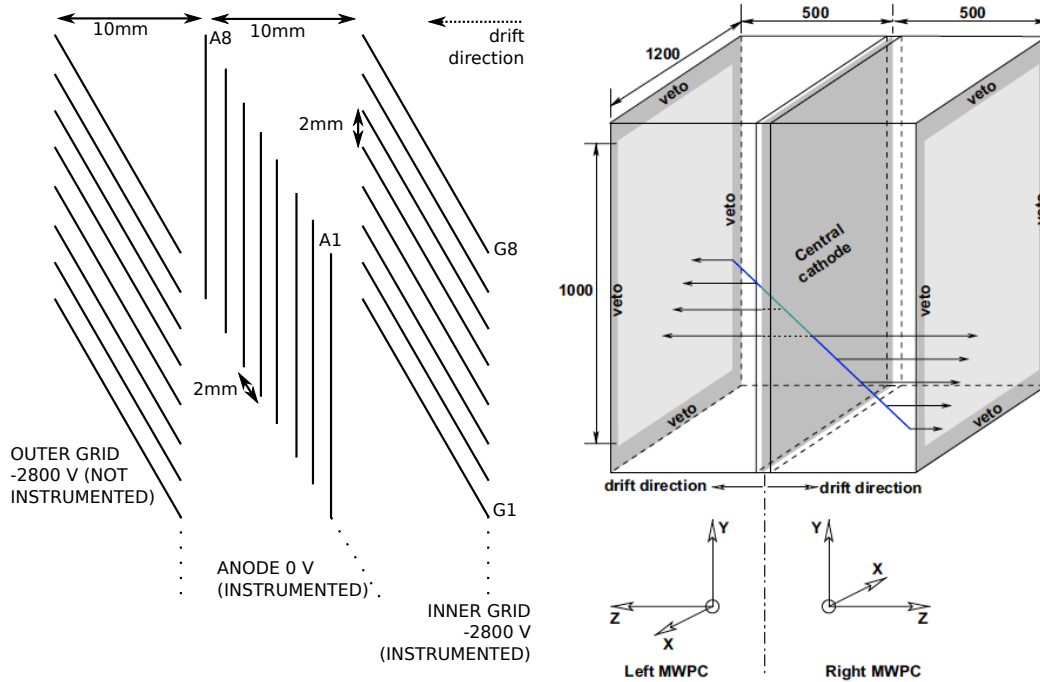
Figure 4.1: Left: zoom of one 'period' of the DRIFT-IId left MWPC detector. Right: diagram of DRIFT-IId from Burgos *et al.* [165]. Dimensions are in mm.

A field cage of stainless steel rings ensures a uniform electric field between the anode and cathode, which is necessary in order to preserve the spatial information of the ionization tracks created by particle interactions in the fiducial volume. Tracks are drifted toward two identical multi-wire proportional chamber (MWPC) detectors either side of the central cathode, themselves comprised of a grounded anode plane

sandwiched between two 2800 V grid planes (see Figure 4.1). The vacuum vessel is nominally filled with a 30:10 partial pressure mixture of CS_2:CF_4 at a total pressure of 40 torr, although one of the strengths of DRIFT technology is the ability to switch easily between different gas mixtures. CF_4 provides a half-integer spin target for spin-dependent interactions, whilst the moderately electronegative CS_2 acts as an electron transport gas. In the nominal configuration, the total fluorine target mass available for SD WIMP-proton interactions is 31.8 g.

4.1.1 Multi-Wire Proportional Counters

Each of DRIFT's two MWPCs consists of a grounded anode readout plane sandwiched between two grid planes at a distance of 1 cm, defining an amplification region with an electric field of 2.84 $kV\,cm^{-1}$. The anode is comprised of $512 \times 20\,\mu m$ thick stainless steel wires with 2 mm pitch, and y (vertical) orientation. The grids are also comprised of 512×2 mm pitch wires, but with thickness 100 μm and x (horizontal) orientation.

Dielectric epoxy is used to attach the wires to an acrylic 'strongback' structure, which maintains the carefully-controlled tension of the wires and prevents mechanical warping when detector components are swapped. Mounted on the reverse side of the strongback are a shuttered ^{55}Fe calibration source and the front-end preamplifier electronics, which instrument the anode and the inner grid.

4.1.2 Signal Formation

A rigorous treatment of charge induction on a conductor using the 'weighting field' concept is given in the Appendix. The following takes a more descriptive approach.

Events in the DRIFT detector begin with the interaction (either by the weak force or some as-yet-unknown new force) of a dark matter particle with the nucleus of C, F or S (see Section 4.1.7 for more information on fill gases). The dark matter particle is scattered, and imparts some fraction of its energy to the struck nucleus as described in Chapter 2. The nucleus recoils through the gas, scattering electromagnetically up to a few thousand times off other gas atoms, ionising them as it does so. The exact number of ion pairs (NIPs) produced is determined by the initial energy of the dark matter particle, the scattering angle, and the 'W value' of the gas, which is the energy required to produce an electron-ion pair. The average energy loss per unit length of the

recoiling nucleus is described by the Bethe-Bloch equation [166]:

$$\frac{\mathrm{d}E}{\mathrm{d}X} = -K\frac{Z}{A}\frac{\rho}{\beta^2}\left(\ln\frac{2mc^2\beta^2 E_M}{I^2(1-\beta^2)} - 2\beta^2\right), \text{ where} \tag{4.1}$$

$$K = \frac{2\pi N_A q^2 e^4}{mc^2}. \tag{4.2}$$

Here, Z and A are the proton and nucleon numbers of the medium, ρ is its density, and I is its effective ionisation potential. q and β are the charge and velocity (in units of c, the speed of light) of the recoiling nucleus, and e and m are the charge and mass of the electron. N_A is Avogadro's number, and E_M is the maximum energy that can be transferred in any single collision, given by

$$E_M = \frac{2mc^2\beta^2}{1-\beta^2}. \tag{4.3}$$

The gas of the detector now contains a track, a few mm in length, of positive ions and electrons. The positive ions immediately begin to drift toward the central cathode, which is not read out, whilst the electrons attach to the moderately electronegative CS_2 gas molecules with a capture distance of several tenths of a mm [167], and drift toward the anode. As the negative ions enter the MWPC region, they are accelerated by the electric field between the grid wires at 2.84 kV and the grounded anode wires, which is high enough to give rise to field dissociation of the negative CS_2 ions [167]. The negative ion drift lines inside a 2D approximation of the MWPC is shown in Figure 4.2, which was calculated using the electrostatic simulation package Garfield [168].

The liberated electrons are rapidly accelerated toward the nearest anode wire, ionising neighbouring gas atoms as they do so. These electrons go on to ionise other gas molecules, and so on, resulting in the formation above an anode wire of a teardrop-shaped cloud of electrons and positive ions such as that shown in Figure 4.3 [169].

The clouds of avalanche electrons and positive ions initially reside together in close proximity to an anode wire, and the image charges induced on the anode cancel exactly, therefore no net charge is seen by the preamplifier electronics (a circuit diagram of which is shown in Figure 4.4, which is identical for all grid and anode readout channels). This remains the case after the electrons have drifted to and hit the anode wire,

74
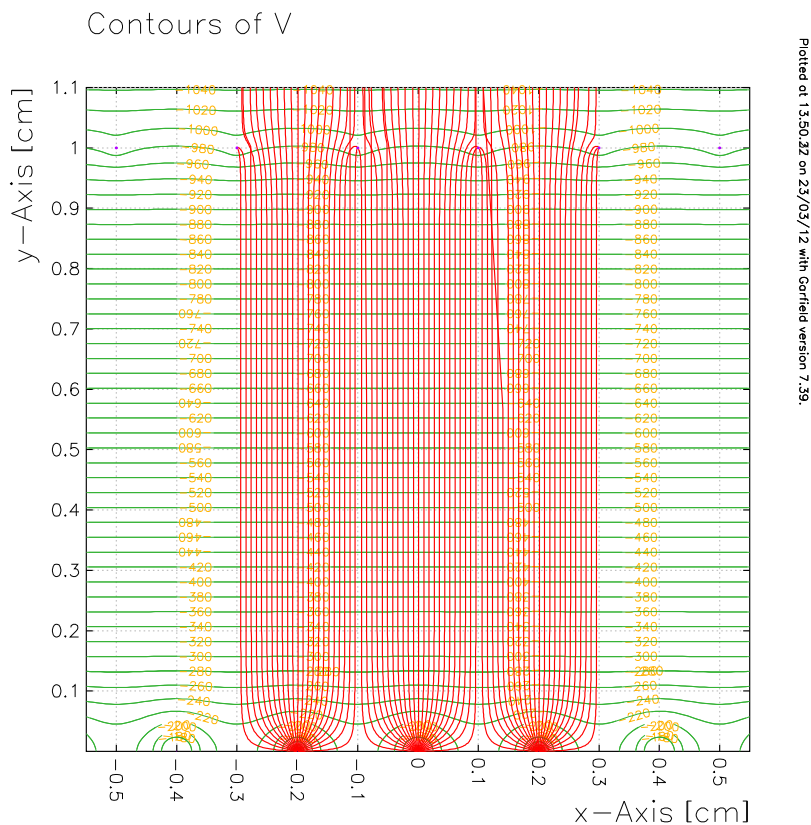
Figure 4.2: Ion drift paths (red) and equipotential lines (green) in the MWPC, calculated using the electrostatic simulation package GARFIELD. The deviation of the drift line at ~ (0.15, 0.6) is an artefact of the code, and not physical.

since the electrons make their way to the 0.01 μF decoupling capacitor where they cancel the positive charge put there by the image of the positive ions. This process happens on nanosecond timescales, before the heavy positive ions have had a chance to move any appreciable distance [170]. As the positive ions begin to drift to the grid plane, their induced positive charge on the capacitor plate gradually dissipates, leaving the residual negative avalanche image charge [171].

As the positive ions drift away from the anode and towards the grid, image charges begin to build up on the grid wires. Initially, the positive ions are ≈ 1 cm away from the grids, and therefore the image charge builds up approximately equally on each. Just as for the anodes, these image charges produce a deficit of opposite-sign charges in the rest of the circuit, particularly on the decoupling capacitor, giving rise to a signal
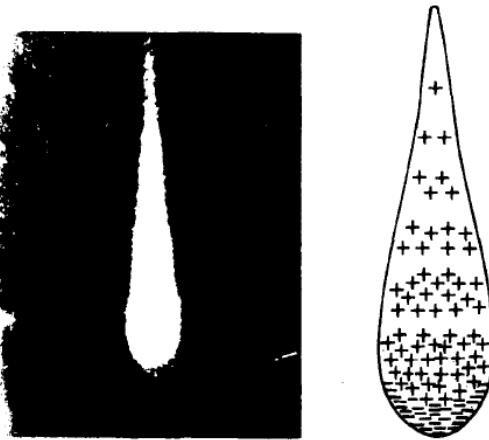
Figure 4.3: The characteristic teardrop shape of an electron avalanche. The electric field is in the upward direction, such that electrons feel a downward force. Reproduced from Sauli [169].

voltage that is detected by the preamp. After $\sim$ 38 μs, the positive ions move close enough to the grid that a significant asymmetry appears between the signals on the wires closest and furthest from the projection of the charge onto the x-y plane [172]. Finally, the charge is deposited on one, two or several of the grid wires, and the charge from the capacitor equilibrates around the grid system.

4.1.3 Fast Electronics

The signals induced on the anode and inner grid wires are read out in groups, where every 8th wire is connected together and connected to the input of a single charge preamplifier (labelled 'det.' in Figure 4.4). In this way, the anode and grid planes are periodic in x and y, with a period of $2 \times 8 = 16$ mm in both cases. A single period of the anode and grid readout scheme is shown in Figure 4.1. The capacitance of each group is measured to be 1.2 nF [173]. The front end of the DRIFT electronics chain consists of a Cremat CR-111 charge-sensitive preamplifier, which converts the instantaneous current induced by moving charges in the vicinity of the wires into a proportional voltage pulse with a risetime of 7 ns, which is much shorter than the sampling time of the ADC [174].

The output of the CR-111 is fed into a CR-200 Gaussian shaping amplifier outside the vacuum vessel, which converts the decaying exponential output of the CR-111 into

(b) CR-111 charge-sensitive preamplifier.

(a) CR-150 evaluation board.
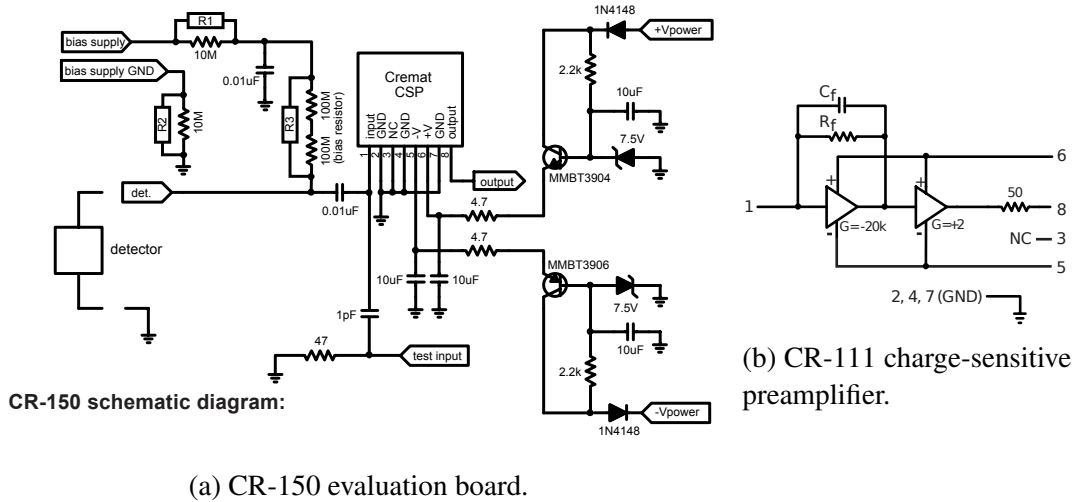
Figure 4.4: Circuit diagrams for the Cremat preamplifier front-end electronics.

a Gaussian of width 4 μs and amplitude/area proportional to the amplitude of the input pulse [175]. The primary purpose of this amplification stage is to speed up the restoration of the baseline following an event in order to prevent pileup, but it also provides a factor 10 broadband gain. The CR-160 board onto which the CR-200 chip is mounted also includes a set of three stages of factor 10 broadband amplification. DRIFT operates with one of these stages disabled, giving a total broadband amplification of ×1000 at the shaping amplifier stage.

The Gaussian voltage pulses from the CR-200 amplifiers are subject to a final stage of electronics consisting of a 2.2 μF capacitor and a 50 Ω resistor to ground, which results in a high-pass filter with a time constant of 110 μs ($\approx$ 10 kHz). Any lower-frequency signals are filtered out, which has the effect of removing any DC offset, and restoring a flat baseline to enable triggering with a fixed threshold. It has long been a concern of the collaboration that information is being lost from ionisation tracks by the aggressive shaping and filtering, at Chapter 6 presents the results of a study of a simplified electronics scheme.

DRIFT's back-end electronics consist of a National Instruments PXI-6133 data acquisition card sampling at 1 MS/s in the range $-1.25 < V < 1.25$ V with 14 bit precision. The DAQ writes data to disc in the format *drift2d-[run]-[cycle]-[type].ndd*, where *[run]* is a number in the format *YYYYMMDD-i* and *i* is an integer that is incremented each time a new run is started on a given day. *[cycle]* is also incremented, but

this is done automatically by the DAQ when either the specified maximum file size or number of events per cycle (nominally 10,000) is reached. *[type]* is a four-letter designation of the run type supplied by the user that is typically 'wimp' for normal wimp search running, 'neut' for neutron calibration, and 'lcal' or 'rcal' for left and right ^{55}Fe calibration runs, respectively. A typical drift data filename therefore looks something like: drift2d-20130501-02-0022-wimp.ndd, which would be the 22nd cycle of the second run started on 1st May 2013.

Figure 4.5 shows an event display from a particular class of background events called 'tagged RPRs', which are introduced in Section 4.1.4 and described in more detail in Chapter 5. An example event appears here because such events usefully illustrate some key features of DRIFT's event files. The left and right panels of Figure 4.5 represent the left and right MWPCs, with the grid channels appearing at the top of the figure (G1 – G8), and the anodes appearing at the bottom (A1 – A8). Grid and anode veto channels are labelled VG and VA, respectively, whilst waveforms appearing in black labelled 'S' represent the sum of either the grid, anode or veto channels. A typical neutron recoil event is shown on channel LA1 of the left MWPC, where the fact that charge was deposited on a single anode channel signifies that the x-range of the event was less than 2 mm. As described in Section 4.1.2, induced charge appears once on all eight grid channels. In contrast, the right MWPC shows a candidate α particle track. Such tracks can be long enough to cross several periods in x and y, and this 'wrapping around' can be seen clearly in Figure 4.5 on both the anode and grid. The number of charge depositions on the anode and grid are used in Chapter 5 to measure the range components of α particle tracks in the x and y dimensions, respectively.
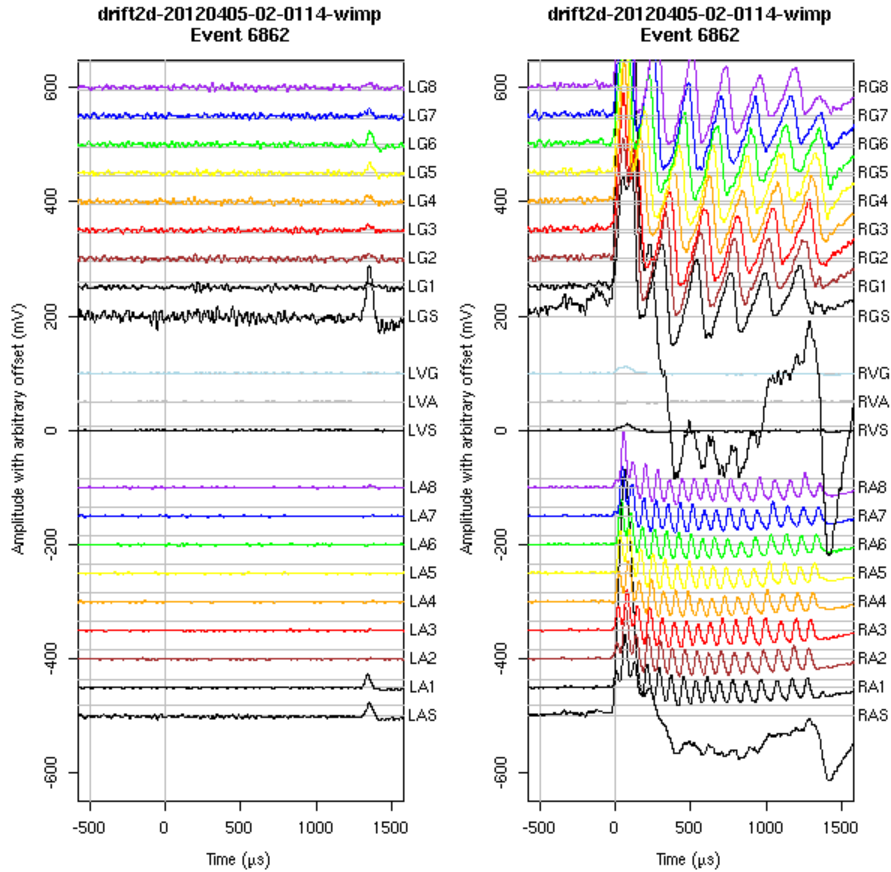
Figure 4.5: DRIFT-IId event display showing a candidate radon progeny recoil event. The α particle appears on the right hand side with its characteristic multi-hit pattern, whilst the recoiling nucleus appears on the opposite side in late-time coincidence.

4.1.4 Central Cathode

DRIFT's central cathode has evolved from a wire plane to a thin-film, and finally to a texturised thin film over the past three years, driven by R&D being carried out by collaborators at the University of New Mexico (UNM). The aim of this development program has been to reduce the rate of background events from the cathode, dubbed 'untagged radon progeny recoils' (RPRs). Such events occur when a radioactive species on the cathode decays via α emission, and the α particle is absorbed in the cathode, leaving a recoiling atom that may be impossible to distinguish from a WIMP-induced

nuclear recoil. Chapter 5 is concerned with reducing and monitoring the concentration of radon in the vacuum vessel, whilst background reduction efforts at UNM have focussed on increasing the probability of the α particles escaping the cathode, at which point they are easily detected and can be rejected in data analysis. Exchanging the wire cathode for one made from 0.9 μm-thick alumnized Mylar means that all α particles bar those that are emitted at extremely acute angles to the cathode are able to escape [160]. This was further improved by bead-blast texturising the aluminised Mylar film to ensure that no straight path inside the cathode is longer than the mean free path of ∼ 5 MeV α particles in the material (∼ 20 μm) [160].

4.1.5 Field Cage

In order to maintain uniformity of the electric field throughout the fiducial volume, the voltage is stepped down smoothly between the central cathode at −28.4 kV and the inner grid plane at −2.84 kV, using a chain of 31 × 33 MΩ resistors on either side, giving a total detector resistance of 570 MΩ. Figure 4.6 shows the effect on the field uniformity of adding a field cage to the detector. Negative ions drift along field lines from the central to cathode to the detector planes at the left and right of both figures. It can be seen that the introduction of the field cage parallelises the equipotential lines throughout the fiducial volume, except in a small region in the immediate vicinity of the field cage, ensuring that no distortion of charged particle tracks occurs due to the electric field [150].

4.1.6 Neutron Shielding

Neutrons are produced in (α, n) and spontaneous fission reactions of ^{238}U and ^{232}Th in the walls of the cavern, and also from spallation by cosmic ray muons. The vacuum vessel housing the DRIFT-IId detector is therefore surrounded on all sides by > 67 cm of hydrogen-rich polypropylene shielding, whose purpose is to thermalise fast neutrons from the lab. This shielding configuration has been designed to reduce the expected rate of neutron-induced background events to < 1 yr^{-1} [177].

(a) No field cage. (b) 2.5 cm-spaced field cage.
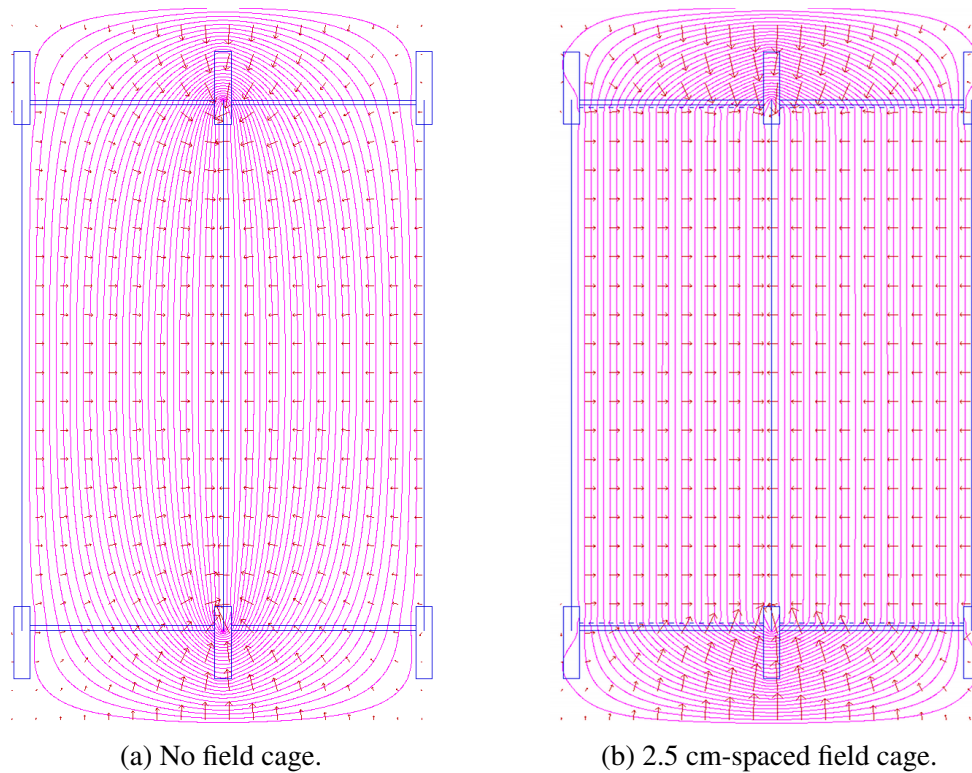
Figure 4.6: Comparison of the drift electric field without (left) and with (right) a field cage. The field cage has the effect of straightening the field lines, reducing distortion of tracks during negative ion drift. The improvement is most pronounced at the edges of the detector. From Lee [176].

4.1.7 Gas Mixing and Supply System

DRIFT-IId uses a custom-made gas mixing system to prepare the gas mixture and supply it to the vacuum vessel in Figure 4.7's open-loop configuration , which is controlled by software called GasMix [178] running on the slow control DAQ. The purpose of the flow is to flush out impurities such as water vapour, as well as chemicals containing C, S and F that may be created in chemical reactions in high-field regions of the detector, both of which are potentially detrimental to detector performance. Preliminary work to identify such contaminants is presented in Chapter 7. The gas flow also reduces the concentration of background-inducing radon gas, which is the subject of Chapter 5. R&D is underway into a closed-loop gas flow system, where the used gas is distilled and re-injected into the vacuum vessel. This will be an important simplification for

a future scaled-up DRIFT detector, both in terms of cost and manpower requirements underground.

Figure 4.7: Schematic drawing of the complete DRIFT-IId gas flow system. MFC stands for 'mass flow controller', PG for 'pressure gauge', and NV for 'needle valve'. Adapted from Pipe [178].

The system can be thought of in three parts, which are labelled 1, 2 and 3 in this Figure. The first, mixing, portion of the system prepares a mixture of the target (CF_4) and transport (CS_2) gases in a user-specified ratio inside the mixing cylinder. Mass flow controller (MFC) 1 is opened and gas 1 (nominally CS_2, although any fill gas can be substituted with ease) is allowed to flow into the 50 L mixing cylinder. CS_2 is supplied from a cylinder, from which it boils with a room-temperature vapour pressure of ≈ 350 torr. The moment that pressure gauge (PG) 1 detects that 3/4 of the user-

specifiable target pressure of 300 torr has been reached, MFC1 is closed, and MFC2 is opened to allow CF_4 to flow into the mixing cylinder. Upon reaching the target pressure of 300 torr MFC2 is closed, and MFC3 is opened, allowing the prepared mixture to flow into the 50 L supply cylinder.

The second, supply part of the system ensures that there is always an adequate pressure of mixed gas at the input of MFC4 to maintain a constant pressure in the vacuum vessel, which is constantly pumped out at a slow rate by an Edwards XDS10 scroll pump through a needle valve (NV2). The gas mixture is supplied to the vacuum vessel through MFC1 from the combined 100 L volume of the mixing and supply cylinders, until the PG1/PG2 pressure falls below a user-specifiable minimum pressure (nominally 140 torr), at which point MFC3 closes. This seals the mixing cylinder from the supply cylinder, and the cycle begins again, with the software calculating the pressure of the two fill gases required to hit the mixing cylinder target pressure with the correct mixture. At all times, the flow rate through MFC4 is controlled by a feedback loop in the GasMix software [178], which compares the vessel pressure to the target vessel pressure (40 torr), and increases or decreases the flow rate accordingly to maintain this pressure.

The third, output portion of the system passes the used gas to a scroll pump, which drives the flow. The used gas is then bubbled through a water trap, which removes ~ 85% of the CS_2, and a large activated carbon filter, before being vented past a Crowcon CS_2 monitor to ensure that an acceptably low concentration of the gas is released into the mine.

4.1.8 ^{55}Fe Calibration Sources

Each MWPC detector has a shuttered ~ 1.85 MBq ^{55}Fe source mounted on its acrylic strongback support, which decays by electron capture to ^{55}Mn, producing 5.9 keV x-rays as it does so. Such events deposit ionisation in the fiducial volume, which is detected as a voltage pulse with area proportional to the number of ion pairs (NIPs) liberated in the x-ray interaction. Pushkin and Snowden-Ifft [179] have shown that the number of ion pairs corresponding to a 5.9 keV x-ray from ^{55}Fe is 234 ± 6, which also allows a calculation of the 'W value' of the gas mixture, that is, the average energy lost by an incident particle interacting with the gas per ion pair created. For a 30:10 torr

mixture of CS_2:CF_4 this was found to be 25.2 ± 0.6 eV [179]. The ratio of the ^{55}Fe NIPs to the measured pulse area can then be used as a calibration constant to calculate the NIPs for an event of any energy, and these calibration constants (*NipsConversions*) are calculated once every six hours for the left and right MWPCs. Their stability over time is shown in Figure 4.8.
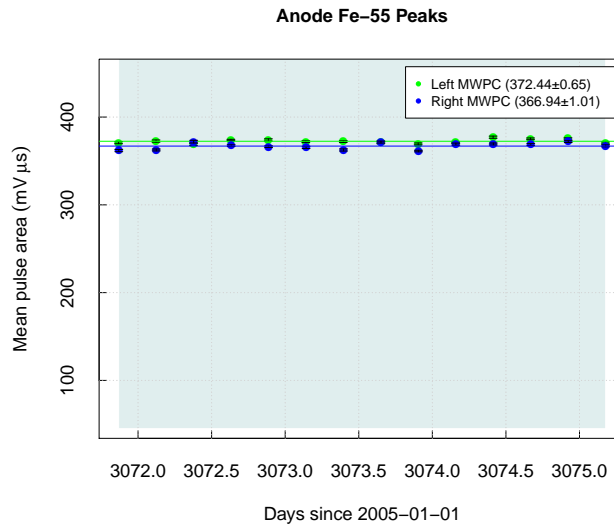
Figure 4.8: Change in the anode *NipsConversion* calibration constants as a function of time during a run from May 2013.

Finally, the detected event energy can be converted into the total energy transferred in an interaction by multiplying by the nuclear quenching factor q_{nc} for the recoiling species in question (fluorine in the case of a search for SD WIMP-nucleus scattering), in the gas mixture in question, which is defined in Equation 4.4 [180]:

$$q_{nc} = \frac{\eta}{E}.$$
(4.4)

Here, η is the detected event energy, and E is the 'true' event energy, under the assumption of a specific recoiling species. The nuclear quenching factor for 100 keV fluorine recoils in the nominal drift gas mixture is calculated to be $q_{nc} \sim 0.6$ [180]. The automated energy calibration procedure is described in Section 4.2.2.

4.1.9   Slow Control Monitoring

A collection of slow control variables are monitored remotely at all times during data taking, using a web interface called DRIFT Watch [181]. The interface is programmed to email and text a warning message to the current 'DRIFT Watcher' when either the gas pressure or currents crosses a pre-determined threshold.

HV and HHV The high voltage on both the MWPC grids (HV) and the central cathode (HHV) are nominally set to 2.84 and 28.4 kV, respectively.

Currents The current through the HV and HHV circuits (total resistance 300 and 570 MΩ, respectively). Any deviation from the baseline leakage current is indicative of a short circuit from, for example, a broken MWPC wire, or an electrical breakdown in the dielectric epoxy covering the wires. Alarms are triggered if the magnitude of the current exceeds 56.3 µA on the HHV circuit, or 10.2 µA on either the left or right HV circuits.

Gas pressure The pressure in the mixing and supply cylinders is monitored, along with the pressure in the vacuum vessel housing the detector. An alarm level of 70 torr is set for the pressure in the mixing cylinder, PG2, which under normal operating conditions should not fall below $\approx$ 100 torr. A drop in the minimum pressure indicates that the gas system is unable to prepare the mixture quickly enough to maintain a constant flow into the vessel, which occasionally occurs if the levels of the fill gases are allowed to drop too low. A strict alarm condition of < 39.9 torr is set for the vacuum vessel, as damage to the MWPC wires can occur at low pressure.

DRIFT has a set of built-in safety features such as a door interlock on the HV and HHV circuits to prevent electrocution, a beacon to indicate that the HV is live, and poison gas alarms in the vicinity of the experiment and next to the output vacuum pump to indicate a leak of CS_2. There is also a HV and HHV cutoff on the web interface, and a backup on the telephone line should this fail.

4.2   DRIFT-IId Data Reduction

The data written to disc by the NI PXI-6133 DAQ consists of 36 'physical' and 6 'virtual' readout channels, which are broken down as follows:

- 2×8 anode channels on each MWPC, plus their sum on each side, for a total of 18 anode channels.

- 2×8 grid channels on each MWPC, plus their sum on each side, giving a total of 18 grid channels.

- One grid and one anode veto channel on each side, formed by ganging together the outermost 12 wires on the inner grid and anode, respectively. Adding the anode and grid vetoes together for each side gives a further 2 channels, for a total of 6 veto channels. The veto sum channels are used to reject events originating outside the fiducial volume.

Together, these form the input to the data reduction analysis routine, which is broken down into three stages:

Stage 1. The first stage of analysis involves pre-processing noise reduction and analysis of all events on a *channel-by-channel* basis.

Stage 2. The second stage of analysis is performed on an a subset of events passing stage 1 cuts, and involves the calculation of the variables detailed in Section 4.2.5 on an *event-by-event* basis.

Stage 3. The final stage of analysis is performed on a subset of events passing stage 1 and stage 2 cuts, where the latter are a set of high-purity, low-efficiency cuts designed to remove virtually all background events whilst preserving sensitivity to DM-induced recoil events.

The DRIFT data analysis software is written in a high-level statistical data analysis language called R [182]. The CPU-intensive stage 1 analysis is performed by C routines encapsulated within a set of R scripts. The user's point of contact is an R control script called *d2.ana.r*, from which many analysis parameters (thresholds, region of interest, etc.) can be specified. Stages 1 and 2 may also be run on the Sheffield HEP

group's computing cluster, where data are farmed out to CPUs cycle-by-cycle [183]. This parallelises the analysis, dramatically reducing time requirements. Following the calculation of event variables at stage 2, the remaining analysis can be performed on a local machine using an interactive R session and user-specific R scripts.

4.2.1 Waveform Preprocessing

Before data analysis of any kind takes place the raw waveforms are subjected to three noise-reduction algorithms. The first, shown in Figure 4.9, is a high-frequency Fourier transform notch filter, which is designed to remove 55 kHz noise caused by the HHV power supply to the central cathode.
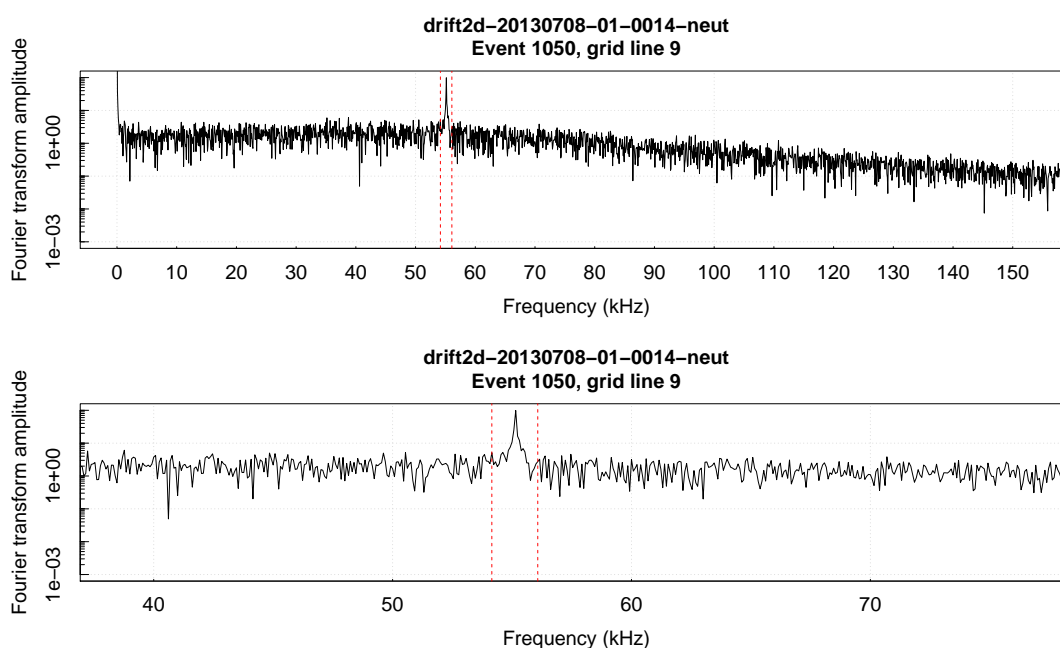
Figure 4.9: Power spectrum of a typical DRIFT waveform, showing the spike at 55 kHz caused by the cathode high-voltage power supply. The notch filter removes all frequencies between 54.2 and 56.1 kHz (limits shown in red). Bottom panel: zoom.

Following the removal of the noise peak, the data are inverse Fourier transformed to recover the noise-reduced waveforms. Secondly, a nonlinear least-squares fitting routing is used to fit a sine wave to the data, which is subtracted in order to remove the low-frequency ($\sim$ 50 Hz) ripple caused by the mains power supply.

Finally, a Savitzky-Golay smoothing filter is applied to the waveforms. This filter works by fitting adjacent input data points within a user-specified range (typically, 10 μs) to a fourth-order polynomial using the least-squares method, setting the output datapoint at the centre of the smoothing window to the value of the fit polynomial, and repeating for all data points in the input waveform [184]. The advantage of this technique over the more simple 'boxcar' averaging that has traditionally been applied to DRIFT data is that it better preserves the higher-order moments of the input data. In particular, the height of peaks is maintained, which is critical since stage 1 analysis relies upon a fixed threshold for triggering analysis of a given waveform. Smoothing in this way increases the signal-to-noise (S/N) ratio of the data, and enables a lower threshold to be set than if raw data were analysed. Figure 4.10 shows the effect of each stage of noise reduction on a typical DRIFT waveform.

4.2.2 ^{55}Fe Energy Calibration

Once every six hours during normal running, the cycle is stopped and the shuttered ^{55}Fe sources are opened first on the left, and then on the right in order to reset the energy scale of the detector. This ^{55}Fe data is acquired in 'trigger-free' mode, whereby 1000×13 ms samples of the waveforms are recorded to disc one after the other, without requiring any channels to cross a threshold. These data are then analysed offline by a C program, which picks out charge depositions caused by ^{55}Fe x-rays and measures their energy. Histograms are then generated of a) events on the side on which the source was open, and b) the opposite side. Subtracting b) from a) then yields a background-subtracted histogram of the time-integrated voltages of these ^{55}Fe x-ray events. An example ^{55}Fe 'event' is shown in Figure 4.11, alongside an example of such a histogram, fitted with a Gaussian profile. The energy scale and resolution are set by the mean and error on the mean of this distribution, respectively, according to the scheme described in Section 4.1.8, and are used to calibrate all events in dark matter runs during the following six hours.
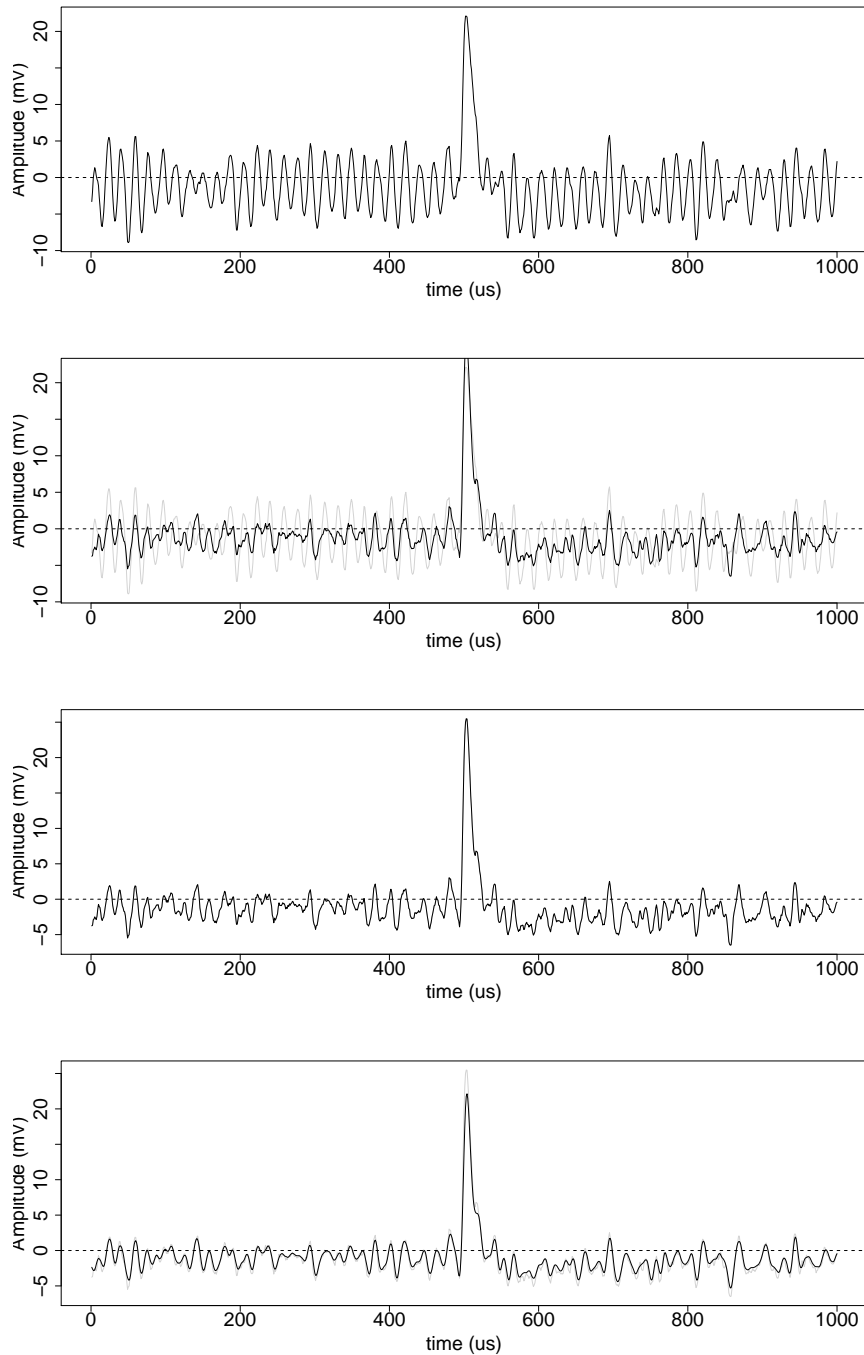
Figure 4.10: The effects of waveform preprocessing on a typical low-energy nuclear recoil candidate waveform. From top to bottom: raw waveform; after notch filter; after multi-sine fit; after Savitzky-Golay smoothing. See text for explanation.
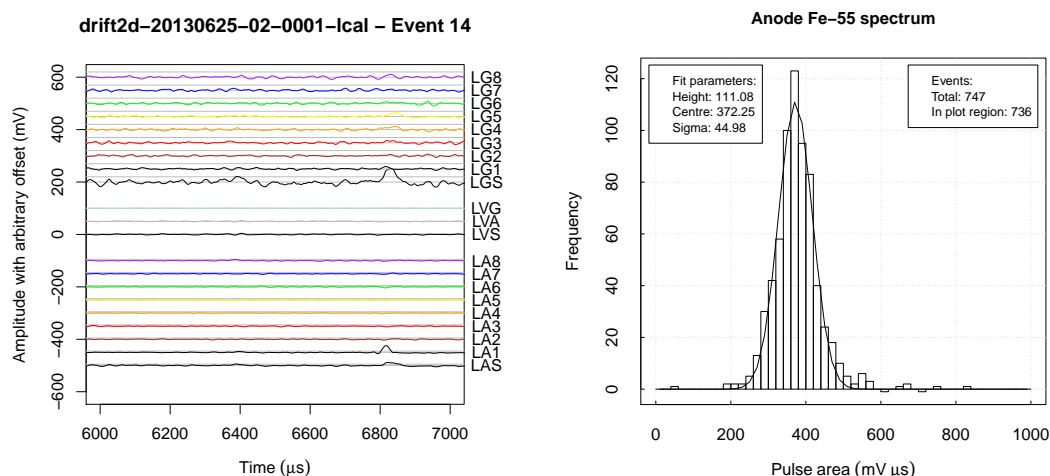
(a) Example ^{55}Fe event on channel LA1 of the left MWPC.

(b) Histogram of time-integrated voltage for a sample of ^{55}Fe events in a single 1.3 s calibration run.

Figure 4.11: ^{55}Fe calibration.

4.2.3 Stage 1: Channel-by-Channel Data Reduction

Offline analysis begins by defining a region of interest (ROI) between -0.5 and 5 ms, samples outside of which are excluded from further analysis. An analysis threshold of 10 mV is set, and the events are processed by a C script run from within R which, for each channel, calculates the following 'stage 1' analysis parameters. An example waveform labelled with these parameters is shown in Figure 4.12. These parameters are calculated for the following waveforms (thresholds in mV): anode (10), anode sum (20), grid (50), grid sum (80), and later for the anode track (20), which is the sum of all channels that crossed the analysis threshold.

Pulse Heights

V_{min} and V_{max} are the minimum (most negative) and maximum (most positive) voltage within the ROI on a channel, respectively. The times at which these occur are labelled $t_{V_{min}}$ and $t_{V_{max}}$, respectively.

90

Pulse Duration

t_{min} and t_{max} define the time extent of the hit. t_{min} is calculated by starting from the first threshold crossing inside the ROI, and stepping back sample-by-sample until the baseline (zero) is crossed. Likewise, t_{max} is obtained by stepping forward in time from the last threshold crossing.

Pulse Area

The area of a hit pulse in mV μs is given by A_p, which is calculated as the sum of all samples between t_{min} and t_{max} for each channel, including the sum channel.

Voltage-weighted mean time

The voltage-weighted mean time of the samples between t_{min} and t_{max} is calculated according to Equation 4.5:

$$\bar{t} = \frac{\sum_{t=t_{min}}^{t_{max}} tV_t}{\sum_{t=t_{min}}^{t_{max}} V_t},$$

(4.5)

where V_t is the magnitude of the voltage at time t.

Risetime

The risetime of a voltage pulse seen by the DAQ is defined as the time taken for the rising edge to increase from $0.25 \rightarrow 0.75 \times V_{max}$.

First Full-Width Half-Maximum

FFWHM is calculated by starting at $t_{V_{max}}$, and stepping forward and backward in time until a threshold of $0.5V_{max}$ is reached. FFWHM is then the time difference between the first crossing reached before, and after $t_{V_{max}}$.

Root Mean Square Time

The root mean square time (RMST) of a waveform is defined according to Equation 4.6:

$$\sqrt{\frac{\sum_{t=t_{min}}^{t_{max}} V_t(t - \bar{t})^2}{\sum_{t=t_{min}}^{t_{max}} V_t}}.$$

(4.6)

This is the RMS of the deviations of sample times from the voltage-weighted mean time, and therefore gives an alternative measurement of pulse width to FWHM. The advantage of RMST is that *all* samples between t_{min} and t_{max} are included in the calculation, which preserves more pulse-shape information than FFWHM.

SD Crossings

Simulations using the Monte Carlo simulation package Stopping Range of Ions in Matter (SRIM 2011) [185] reveal that WIMP-induced nuclear recoils are expected to have a length of several mm in the DRIFT fill gas. Since every 8th wire is connected together in the DRIFT-IId MWPCs, any event with a range $> 8 \times 2 = 16$ mm 'wraps around', creating two or more hits on a single channel. α particle tracks provide a particularly clear illustration of this effect, as can be seen on the right hand side of Figure 4.5. Any event that exhibits multiple hits on individual channels is cut. In order to count the number of hits, channels were first smoothed with a Savitzky-Golay smoothing filter [186] of half-width 10 μs and then differentiated. Smoothing in this way prevented noise peaks from being counted as hits and causing events to be erroneously removed.

4.2.4 Cross-talk

So-called 'rebound hits' (cross-talk) can be induced on channels by the movement of charges on the surface of neighbouring MWPC wires. Such signals appear as opposite-polarity hits in DRIFT, but due to the aggressive nature of the shaping electronics, the subsequent overshoot may be positive enough to cross the analysis threshold and register as an erroneous hit. Including such hits in further analysis leads to the miscalculation of many event variables. They are therefore identified using the following criteria:

$$t_{min} < t_{max} \tag{4.7}$$

$$|V_{min}/V_{max}| > 2, \tag{4.8}$$
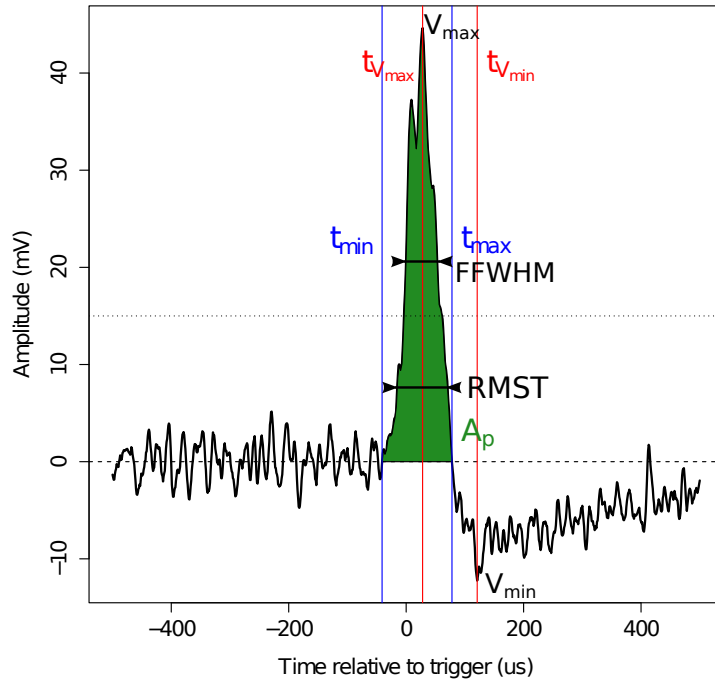
Figure 4.12: Example waveform showing the stage 1 analysis parameters.

and cut by setting the individual channel waveform to zero. This allows otherwise-legitimate events to be retained, even in the presence of large overshoots affecting channels that do not take part in the event. These cuts were applied to anode channels only.

Following the calculation of the above variables, the cuts in Table 4.1 are applied to the data to remove events in which any of the criteria were not satisfied.

4.2.5 Stage 2: Event-by-Event Data Reduction

Events passing the cuts in Table 4.1 are passed to stage 2 analysis routines which, unlike the C-based stage 1, are executed entirely within the R environment. Stage 2 involves the calculation of the following variables, and the subsequent application of the stage 2 and 3 cuts listed in Table 4.2, which were developed by other members of the collaboration in order to set the limit on $\sigma_{WN}(M_W)$ appearing in Daw et al. [187].

Cut	Name	Pass condition
1.1	anode.zero.nip.cut	At least one anode channel crossed the analysis threshold.
1.2	anode.tmin.cut	No anode channels have hits that extend before the ROI.
1.3	anode.tmax.cut	No anode channels have hits that extend after the ROI.
1.4	anode.clipping.cut	No anode channels clip the rails of the digitiser.
1.5	grid.tmin.cut	No grid channels have hits that extend before the ROI.
1.6	grid.tmax.cut	No grid channels have hits that extend after the ROI.
1.7	grid.clipping.cut	No grid channels clip the rails of the digitiser.
1.8	veto.cut	The veto sum channel does not exceed the veto threshold.

Table 4.1: Stage 1 (channel-by-channel) cut variables.

The only difference between the stage 2 and 3 cuts in this table is that the stage 3 cuts are applied after all the data have been combined into a user-accessible data frame object inside the R environment.

Anode Hits. The *anodeHits* event parameter is the number of anode channels that exceeded the analysis threshold.

Anode Contiguous Hits. The largest number of contiguous hits in an event. Nuclear recoils are expected to leave an unbroken trail of ionisation in the gas.

Anode Sum NIPs. The *anodeSumNips* parameter is simply the pulse area, A_p, on the sum channel calculated at stage 1, multiplied by the *anodeNipsConversion*.

Grid Sum NIPs. As above, *mutatis mutandis*.

Anode Minimum t_{min}. *anodeMinTmin* is the minimum of the stage 1 anode t_{min} values for the event in question.

Anode Maximum t_{max}. As above, *mutatis mutandis*.

Anode Minimum Risetime. The minimum of the risetimes on all hit anode channels.

Anode Minimum FFWHM. The minimum of the anode FFWHM values on the hit anode channels.

Cut	Name	Pass condition
2.1	single.side.cut	The track exceeds threshold on only the left *or* right, but not both.
2.2	eight.channel.cut	The number of channels hit on each side is < 8.
2.3	adjacent.cut	The number of contiguous hits = the total number of hits.
2.4	anode.max.SD.crossings.cut	The maximum number of SD crossings on a single channel is < 5.
3.1	anode.sum.nips.grid.nips.cut	Ratio of ionisation measured on anode to that measured on grid $0.78 < R_{A/G} < 1.12$.
3.2	anode.nips.anode.sum.nips.cut	Ratio of track to anode sum channel ionisation $0.99 < R_{A/A_s} < 1.15$.
3.3	anode.track.sigma.anode.track.rmst.cut	Anode track sigma to anode track RMST ratio $R_{\sigma/RMST} > 0.9$.
3.4	grid.ph.ratio.cut	*gridPHratio* < 1.4.
3.5	anode.min.risetime.cut	*anode.min.risetime* > 7 μs
3.6	anode.min.ffwhm.cut	*anode.min.ffwhm* > 26 μs

Table 4.2: Stage 2 and 3 (event-by-event) cut variables.

Anode Maximum SD Crossings. The maximum of the anode SD crossings on the hit anode channels.

Grid PH Ratio. The ratio of the largest to second-largest V_{max} on all grid channels.

Anode Track NIPs. The *anodeTrackNips* parameter is A_p for the anode track waveform, multiplied by the *anodeNipsConversion* for the MWPC in question.

Anode Track RMST. The stage 1 RMST variable, calculated for the anode track waveform.

Anode Track Sigma. The stage 1 FFWHM variable, calculated for the anode track waveform and divided by 2.35.

4.2.6   Neutron Calibration and Monte-Carlo Simulation

Approximately once per fortnight, a plastic tube on top, 50 cm from the front, and in the centre of the vacuum vessel is cleared of shielding pellets, and a ~ 1.5 kBq ^{252}Cf neutron source is lowered down to sit on top of the vacuum vessel above the central cathode. The energy spectrum of the recoils caused by these neutrons is very similar to that which is expected from WIMPs (see Figure 4.13). Therefore, these neutron calibration runs can be used to give a rough measure of the sensitivity of the detector to WIMP-nucleus interactions. Neutron data was used by other members of the collaboration to design the stage 2 and 3 cuts in order to maximise the rate of accepted events from neutron calibration runs whilst minimising background contamination [178]. Neutron data will be used in Chapter 8 to estimate the limit-setting capability of the detector in a new mode of operation.
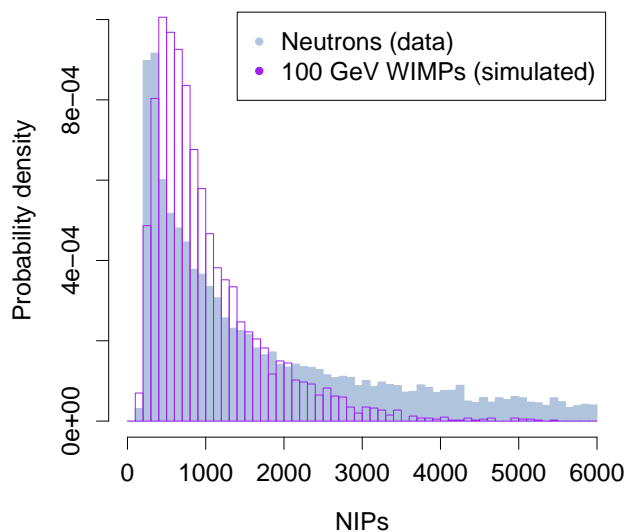
Figure 4.13: Energy spectrum of neutron (blue) and simulated (purple) recoil events in the DRIFT-IId detector.

Whilst neutron events are very useful for providing a 'quick and dirty' verification of the detector's sensitivity to WIMPs, to do this properly and calculate the true WIMP

efficiency of the detector, a bespoke Monte Carlo simulation written by the collaboration is used [188]. Briefly, the standard halo parameters of Chapter 2 are assumed and used to generate a population of WIMPs with a chosen mass originating from the direction of Cygnus. An arbitrary SD WIMP-nucleus interaction cross-section of 10^{-34} cm^2 (100 pb) is then assumed, in order to convert the simulated WIMPs into a population of simulated nuclear recoils in the DRIFT detector. Using quenching factor data from Hitachi [180], the number of ion pairs created in the interaction is computed, and SRIM used to calculate the range of the recoil [185]. The liberated electrons are uniformly distributed along this track, and captured on CS_2 molecules to form a track of negative ions.

The track is diffused both laterally and longitudinally based upon its z-position from the MWPC according to Equation 4.9, to simulate the negative ion transport process. The symbols in this equation have their usual meanings.

$$\sigma_{[lat,long]} = \sqrt{\frac{2kTz}{eE}}.$$ (4.9)

Upon reaching the MWPC, the number of electrons is multiplied by a random number drawn from a Polya distribution [189] to simulate the electromagnetic avalanche. For each avalanche, the resulting current signal is generated on the closest anode wire, which has been pre-prepared with simulated noise determined experimentally prior to the simulation, and this current is converted to a voltage using the specifications of the CR-110 preamplifier. The δ-function voltage pulses are then converted into Gaussian pulses with FWHM= 2.35×4 µs shaping time, and height determined by the avalanche multiplicity, to simulate the effect of the CR-200 shaper. Induced pulses are generated on neighbouring and other anode wires, and grid signals are simulated following the method of Blum, Riegler, and Rolandi [190].

The DAQ parameter *Bits/Volt* is chosen to match the real WIMP search data for which the detector efficiency is being calculated, and the waveforms are written out in *.ndd* format. Finally, the simulated data is processed by the stage 1 and 2 analysis code in exactly the same way as real data. The simulation has been validated by comparing simulated with real neutron data [178, 188].

4.2.7   Background-Free Signal Region

Following the stage 2 and 3 cuts, a population of background events remains that is almost indistinguishable from a population of true recoils. At this stage the data is plotted in RMST-NIPs parameter space as in Figure 4.14, and over-plot with neutron calibration data to provide a model population of 'signal' events. It can be seen from this figure that an area of parameter space at low RMST and moderate-to-high energy is populated by neutron signal events, but devoid of all background, and it is therefore within this region that the WIMP search takes place.

The discriminating power of the RMST variable comes from the fact that all known classes of background originate on the central cathode, and therefore suffer maximal diffusion when drifting to the MWPC. Longitudinal diffusion has the effect of broadening signal pulses in time, and RMST, being a measure of the width of a pulse, is therefore sensitive to diffusion, and hence to the z distance from the MWPC at which an event occurred. Defining a signal region below a certain RMST allows events coming from the central cathode to be effectively rejected, which includes all known backgrounds. The nature of the cathode backgrounds that limit the size of the signal region is described in Chapter 5, along with methods to reduce and monitor the levels of contaminants that cause them.

4.2.8   WIMP Efficiency

The fraction of simulated events that survive all cuts and appear in the signal region gives the WIMP efficiency of the detector, and this is plotted for a sample of simulated 100 GeV WIMPs in Figure 4.15. Here, for example, from a total of 9000 simulated 100 GeV WIMP-induced nuclear recoil events, 1960 passed all stage 2 and 3 cuts, whilst 463 also survived the RMST-NIPs signal region cut shown in black, giving an efficiency for detecting 100 GeV WIMP-induced nuclear recoils of $\epsilon = 0.65 \times (463/9000) = 3.33\%$. The factor of 0.65 is introduced to correct for the effect of omitting several stage 2 cuts when analysing simulated data, which is necessary due to discrepancies between real and simulated data caused by problems with the simulation described in Section 4.2.6. These are described in detail in Pipe [178].
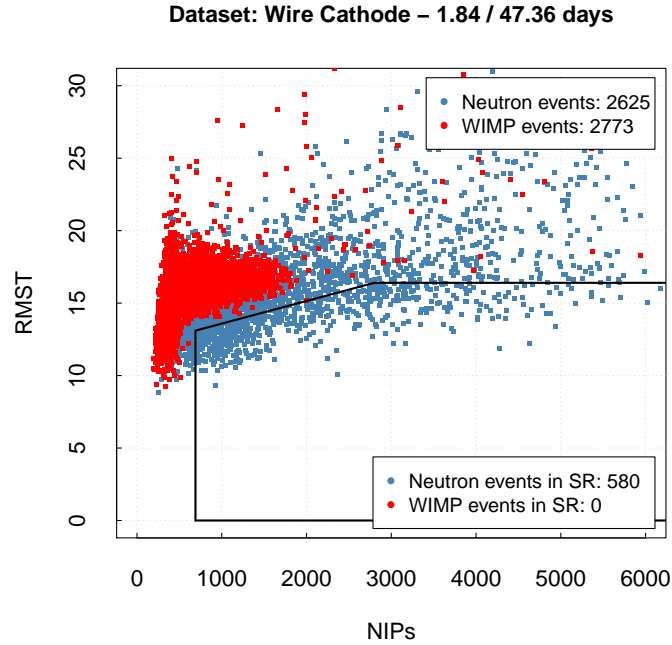
Figure 4.14: RMST-NIPs plot for neutron (blue) and WIMP search (red) data, showing the background-free signal region at low RMST.

4.2.9 Limits on the Spin-Dependent WIMP-Proton Cross Section

If no events appear in the signal region after running the detector for some time t_{live}, then the efficiency from simulation can be combined with the theoretical rate calculated in Chapter 2 to yield limits on $\sigma_{Wp}^{SD}(M_W)$. The following method uses 100 GeV WIMPs for illustrative purposes, but is repeated 31 times for the simulated WIMP masses in the range $11 < M_W < 100,000$ GeV / c ^{2}.

The work of Feldman and Cousins [191] reveals that the observation of zero events in a signal region expected to contain zero events from known background populations implies 90% confidence that, were the experiment to be repeated several times, the average number of events falling in the signal region would be < 2.44. Given the arbitrary WIMP-nucleon cross section of 1×10^{-34} cm^2 assumed in Section 4.2.6 (4.84×10^{-37} cm^2 WIMP-proton for a 100 GeV WIMP), the total rate of WIMP interactions expected in the DRIFT detector is 361 yr^{-1}. Multiplying by the efficiency of 3.33%
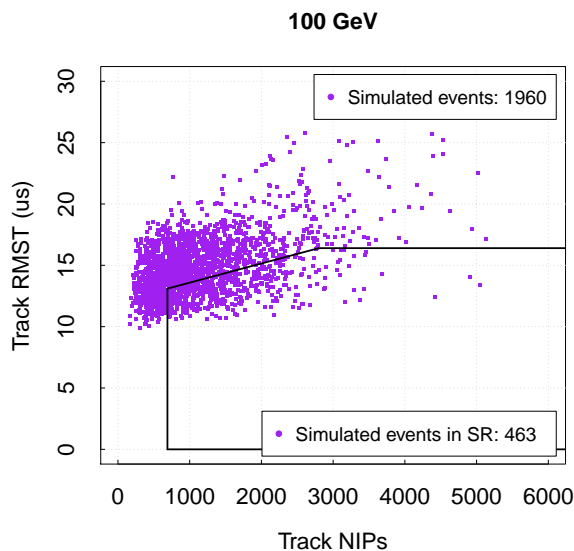
100 GeV

Figure 4.15: Signal region in NIPs-RMST space from the analysis of Daw et al. [187], showing the acceptance of simulated events from 100 GeV / c ^{2} WIMPs. A set of 32 of such plots spanning WIMP masses from $11 < M_W < 100{,}000$ GeV / c ^{2} were generated in order to calculate the efficiency as a function of WIMP mass.

calculated from simulations in Section 4.2.8 yields an expected event rate into the signal region for this arbitrarily-assumed cross section of 12.02 yr^{-1}, or 1.56 events during the full t_{live} = 47.4 day livetime of the run.

It would therefore be possible to increase the assumed cross section by a factor of 2.44/1.56 = 1.56, and still (just) remain 90% confident that no WIMP recoil events would appear in the signal region in subsequent repeat experiments. Doing this yields a WIMP-nucleon cross section limit of 1.56×10^{-34} cm^2 (7.55×10^{-37} cm^2 WIMP-proton) for a 100 GeV WIMP. Repeating the procedure for the remaining 31 WIMP masses yields the WIMP-proton cross section limit curve shown in black in Figure 4.16. For a given mass, all cross sections above the line are excluded by the data. Also shown are limits c. 2012 from several other experiments probing the spin-dependent WIMP-proton cross section. Chapter 8 is concerned with improving upon this limit using a new mode of operation and data analysis.
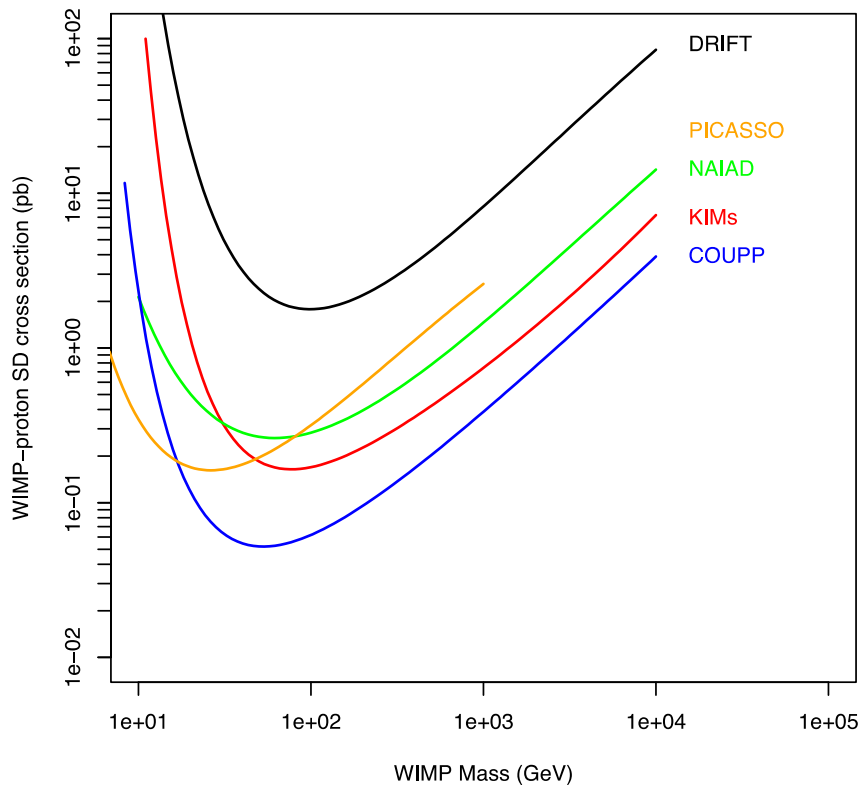
Figure 4.16: Latest published $\sigma_{Wp}^{SD}(M_W)$ limit curve from DRIFT [187], alongside several other experiments introduced in Section 3.1.

Chapter 5

Radon Background Reduction

Radon is a problem in the DRIFT-IId detector, because its presence produces background events that may mimic the signal from WIMP-nucleon interactions. The DRIFT experiment suffers from several classes of such background events that can be attributed to radon, and this chapter is concerned with ways to monitor and reduce these confounding events. In Section 5.2, a method for calculating the rate of radon emanation from detector materials into the target gas is presented, which is based upon a golden class of events that give a very clean signature of radon. Section 5.3 presents a complimentary measurement of the radon emanation rate, using an off-the-shelf solid-state alpha spectrometer. Section 5.4 describes a radon emanation apparatus based around the same detector, which was used to identify the most 'radon hot' detector materials in DRIFT and mark them for replacement. Finally, the same tests were carried out on proposed replacement materials for DRIFT-IId and also new materials for the next-generation DRIFT-IIe detector, to ensure that no significant sources of radon were considered for inclusion in the experiments.

5.1 Radon Backgrounds

Although the DRIFT-IId detector has been designed to be as leak tight as possible, a small pressure increase on the order of 0.1% of 40 torr per day is typically observed when the vacuum vessel is pumped out and sealed immediately following a run. There are two possible contributions to this pressure increase, namely: leaking in of lab air

through seals (particularly the o-ring forming the door seal), and outgassing from detector materials. Either one of these mechanisms can potentially lead to increased levels of radon in the detector, although the Boulby underground lab is an extremely low-radon environment, with a measured air radon activity of 3.73 ± 0.79 Bq m^{-3} that has not changed since 2006 when it was measured to be 2.5 ± 1.6 Bq m^{-3} [192]. Figure 5.1 shows the section of the ^{238}U decay chain that gives rise to radon gas.
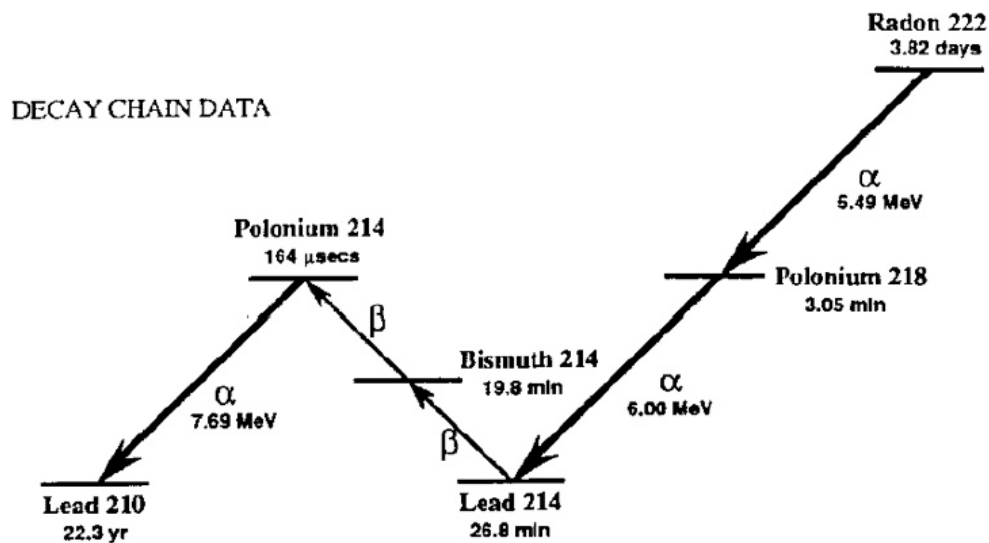
Figure 5.1: Part of the ^{238}U decay chain.

5.1.1 Radon Progeny Recoils

Radon gas inside the fiducial volume decays with a half-life of 3.82 days [193] into ^{218}Po, which has a $\approx 88\%$ chance of being positively charged [194]. If this is the case, the ^{218}Po ion, with a half-life of 3.05 minutes, has ample time to be swept to the cathode under the influence of the drift field, where it may 'plate out' on the aluminium surface. The subsequent decay produces a 6.0 MeV α particle and a slowly recoiling ^{214}Pb nucleus, which produces ionisation in the target gas in exactly the same way as a hypothetical dark matter particle. Figure 4.5 in the previous chapter shows a typical event of this type in the DRIFT detector. These tracks are easily identified, both by the large amount of energy deposited by the α particle, and also the characteristic repeated pattern of hits caused by the particle traversing a distance greater than the 16 mm

periodicity of the readout grouping scheme. Identification of the α particle therefore provides a means of 'tagging' these events and rejecting them, in which case the event is dubbed a 'tagged radon progeny recoil', or tagged RPR. However, if the α particle loses most of its energy in the Mylar cathode material instead of in the gas, then what is seen by the detector is a small amount of energy deposited by the recoiling ^{214}Pb nucleus, which is difficult to distinguish from the signature expected from dark matter particles. Figure 5.2 shows several examples of both classes of events, generated using Stopping Range of Ions in Matter (SRIM) 2011 [185], which is a sophisticated Monte Carlo simulation of charged particle propagation. Tracks that end between the layers labelled 'Aluminium' are caused by α particles 'ranging out' inside the cathode, giving rise to RPR background events. α particles that make it out of the cathode are tagged, allowing the event to be rejected.

5.1.2 Low Energy Alphas

A second, similar class of radon-produced background events appeared after the installation of the thin film cathode in March 2010. These events appear with large RMST, and extend to higher energies than the tagged RPR events. Dubbed Low Energy Alphas (LEAs), they are hypothesised to arise when an α particle is emitted in the decay of a radon progeny on the central cathode at a very acute angle to the cathode plane. In this case, the α particle may deposit most of its energy in the cathode material, but re-emerge on the same side as the recoiling radon progeny nucleus, depositing energy comparable to that expected from a dark matter event in the gas. This explanation is consistent with the appearance of another class of event dubbed 'double recoils', where a small amount of energy is observed to be deposited on both sides of the detector simultaneously, which could occur if small wrinkles were present on the cathode surface. Visual inspection of the cathode confirms the presence of such wrinkles, but these events do not contribute a background to the dark matter search since WIMP-induced nuclear recoil events are not expected to deposit energy on both sides of the detector.
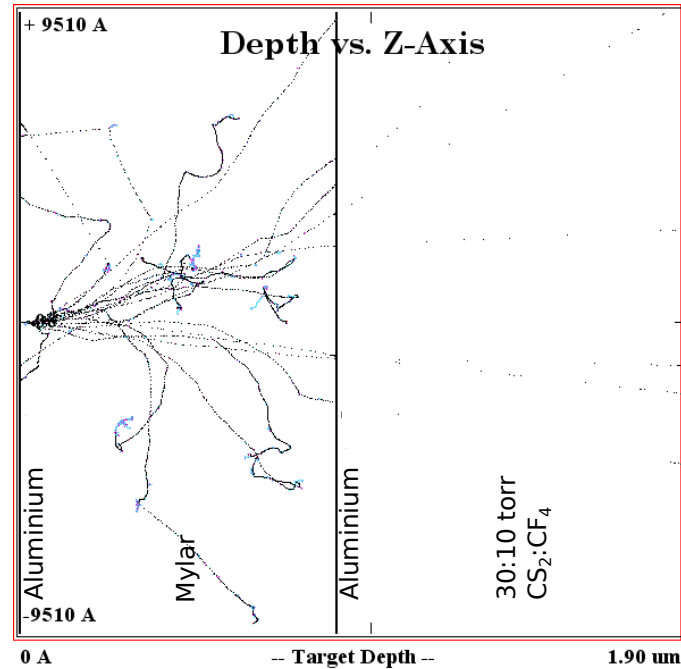
Figure 5.2: Plot from SRIM showing the simulated path of several α particles originating on the surface of the cathode (left-hand aluminium surface) and being emitted into the Mylar at an angle of 89°. Events such as these may give rise to the RPR and LEA populations described in the text.

5.2 Radon Monitoring in DRIFT

There exists a class of events in DRIFT called 'gold-plated cathode crossers' (GPCCs), which are an unambiguous tracer of the Rn level in the detector. The name derives from the fact that charge is detected in time coincidence on both sides of the detector, and therefore must have been deposited by a particle crossing the cathode plane (time-coincident events from separate sources are extremely unlikely). In order to qualify as a GPCC, the particle must also be fully contained, and hence not cross the veto threshold. The only particles capable of depositing a detectable amount of charge in a track crossing both sides of the detector are α particles. The absence of a signal on the veto channel means that the particle must have originated in the bulk of the gas, and not from the decay of a 'plated-out' daughter on the central cathode (see Sections 5.1.1 and 5.1.2), therefore the only remaining possibility is that the α particle

was produced in the decay of an unstable, neutral atom in the gas, within the fiducial volume. Figure 5.3 shows an example of such an event. The repeated pattern of hits is the signature of an alpha particle, and the late-time coincidence at ~ 2500 μs shows that the two sides are part of the same alpha track, joined at the point where they cross the central cathode.
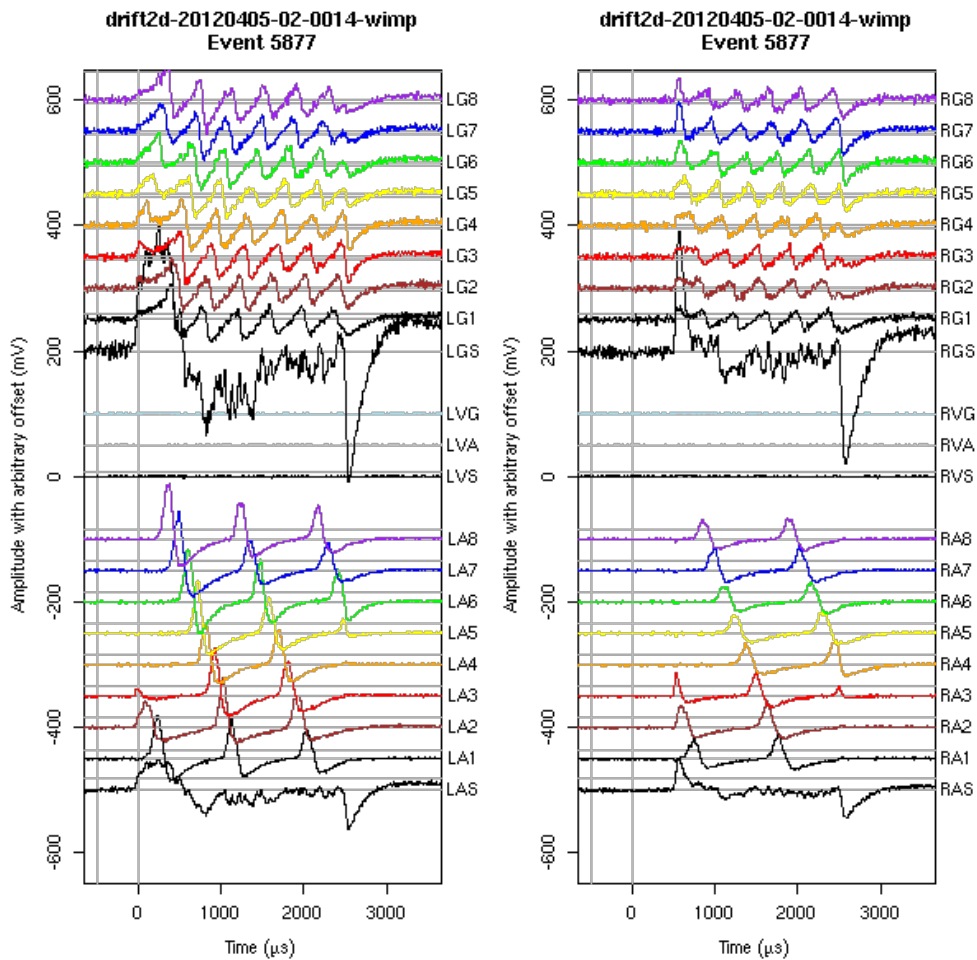
Figure 5.3: A candidate Gold Plated Cathode Crossing (GPCC) event in the DRIFT-IId detector. The characteristic repeated pattern of hits on all lines can be clearly seen, along with the time-coincidence of the ends of the tracks on either side.

It is therefore possible, knowing the detector's efficiency for detecting GPCCs from a given radioactive species, to infer the rate of decays of that species inside the vacuum

Name	Definition	Description	Acceptance
Charge on both sides	anode.Nips.left $\times$ anode.Nips.right $!= 0$	Charge above threshold on both sides	5%
Eight wires hit	anode.hits.left $== 8$ & anode.hits.right $== 8$	Part of the α particle PID. Ensures $\Delta x > 16$ mm	24%
Delta z cut	$\Delta z > 50$ mm	Track is long enough in time to be well-measured	98%

Table 5.1: Cuts used to select GPCC events. Acceptances are calculated based only on the events that make it through the preceding cuts, and are therefore dependent upon the order in which they are applied.

vessel. Then, with knowledge of the flow rate of gas through the vessel and the species' half-life, it is possible to calculate the rate of appearance of that species inside the vessel under equilibrium conditions. The following sections describe this procedure in detail, culminating in a calculation of the rate of ^{222}Rn emanation into the DRIFT target gas.

5.2.1 GPCC Event Selection

A dataset of 6.6 days' live time from April 2012 (drift2d-20120405-02) was used to investigate the rate of GPCC events in DRIFT. This dataset was chosen as it is the closest in time to the full detector radon emanation measurement using an α spectrometer described in Section 5.3, and immediately follows a full evacuation of the vacuum vessel. From a total trigger rate of 1.22 Hz, 689 GPCC candidate events were selected using the cuts listed in Tables 4.1 and 5.1, with an average rate of 104 ± 4 events per day. These events may originate from any uncharged radioactive species in the fiducial volume. However, in order to unambiguously identify a given GPCC event with a radon decay, the three dimensional range of the GPCC alpha particles was calculated with an R code (*alpha.range.functions.v2.r*), details of which are given in Section 5.2.2. Different radioactive species emit α particles of characteristic energies when they decay, and higher-energy particles are able to travel further in the detector before 'ranging out'. Using SRIM 2011 [185] along with the density and composition of the DRIFT gas, a table of alpha particle energy vs range was computed, and linear interpolation used to extract the range and straggling of α particles of energies between 0.1 and 10 MeV (Figure 5.4). The α particle from radon decay carries 5.49 MeV of energy

which, according to Figure 5.4, gives it a range of 354 ± 14 mm in the DRIFT target gas. Other ranges of interest are αs from ^{218}Po decay at 6.00 MeV (404 ± 16 mm), ^{216}Po with 6.78 MeV (489 mm), and ^{220}Rn at 5.29 MeV (335 mm).
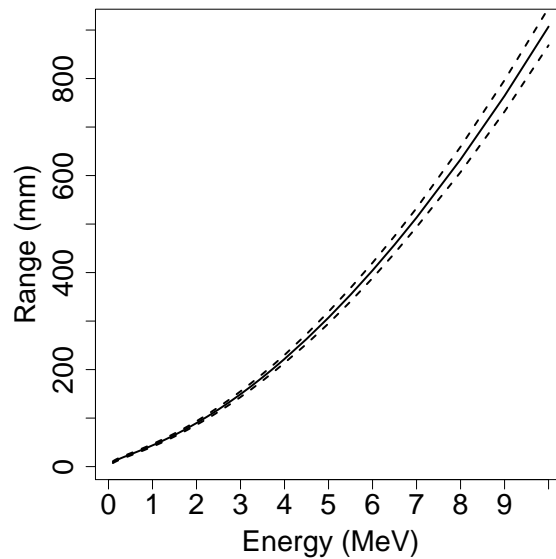
Figure 5.4: Alpha particle range in a 30:10 torr mixture of CS_2:CF_4 as a function of initial energy, calculated using SRIM 2011 [185]. Dashed lines represent upper and lower limits from the SRIM estimate of longitudinal straggling.

5.2.2 Calculating α Particle Ranges

x Range

The *x* extent of α particle tracks was reconstructed by counting hits on the anode wires, which are oriented in the y-direction. As discussed in Chapter 4, the DRIFT-IId detector is read out in a grouped configuration, whereby every 8th wire is connected together to form a periodic set of 8 channels, with periodicity 16 mm. Since α particles typically have ranges considerably longer than the extent of one 'period' of the readout, their signals wrap around to form the very characteristic pattern seen in Figure 5.3, and

each individual detection signifies that the particle has travelled a distance equal to the wire spacing, or two mm in this case.

The most robust method for counting the number of hits was achieved by counting crossings of a fixed threshold by the time derivative of the waveforms, rather than the raw traces, after smoothing with a Savitsky-Golay smoothing filter. The line was smoothed with a smoothing window half-width of (*anode.duration* / 32 μs), differentiated numerically with a step of 5 μs, then smoothed again with a half-width of *anode.duration*/21, where *anode.duration* represents the sum of time extent of the event on the two sides of the detector. This waveform will be referred to as the 'SDS waveform' from now on. The effect of this procedure was to smooth out noise peaks which may otherwise have been counted as true charge depositions, and scaling the smoothing width in proportion to the time-extent of the event ensured that the α particle peaks of fast events were not erroneously 'smoothed out'. Counting the number of times the SDS waveform crossed, and then re-crossed the -1.0 mV threshold in the opposite direction on each of the 16 anode lines, then summing and multiplying by the wire pitch (2 mm), gave a measurement of the projected x range of the α particle track.

y Range

The projected *y* range of GPCC events was calculated in a similar way to the *x* range, this time using the SDS waveforms on the orthogonal grid channels. The S/N ratio of the grid channels is $\approx 3.5\times$ lower than that of the anode channels, which meant that some adjustment of the peak counting algorithm was necessary in order to apply it to the grid. Due to the increased noise, extra care had to be taken when setting the width of the smoothing window and the threshold for SDS crossings, and it was found that a window width of (*anode.duration*/37.7) and a variable threshold at $1/(anode.duration \times v.drift \times 1 \times 10^{-6} - 0.0542)$ kept down both missed peaks and spurious noise triggers.

z Range

The *z* range of GPCC α particles was calculated based on the time duration of the charge deposition. For each channel on each side, the quantities Δt_{left} and Δt_{right} were calculated as (*anodeMaxTmax* $-$ *anodeMinTmin*) for the respective sides of the de-

tector. Equation 5.1 was then used to calculate the z-extent of the track.

$$\Delta z = \frac{(\Delta t_{left} + \Delta t_{right})v_{drift}}{R_{sample}}, \tag{5.1}$$

where v_{drift} is the drift velocity (59.4 m s^{-1} for this run), and R_{sample} is the anode sampling rate. v_{drift} is calculated for each run as

$$v_{drift} = \frac{\mu E}{P}, \tag{5.2}$$

where μ is the reduced mobility [149], E is the electric field, and P is pressure.

A quality diagnostic, defined in Equation 5.3, was developed to ensure that the range measurement algorithms were doing a good job of calculating α particle ranges in the x-y plane. Any event caused by an α particle should have adjacent channels on a given side that differ in count by no more than 1. Missed peaks, or over-counting due to noise peaks, should show up as large q-values.

$$q = \sum_{i=1}^{n-1} |c_{i+1} - c_i| + |c_1 - c_n| \tag{5.3}$$

The maximum 'true' q value expected for any event is 8, therefore $q > 8$ implies that mistakes have been made during the peak-counting process. Figure 5.5 shows the histograms of anode and grid quality factors. Integrating these histograms up to $q = 8$ shows that 90% of events have a well-measured x-range, whilst the equivalent for the grid (the y dimension) is 62%. This difference is a direct consequence of the reduced S/N ratio of the grid relative to the anode. However, it is worth noting that even a quality factor as high as 18 implies at most an error of 10% of the mean length of an α particle track from ^{222}Rn decay, since alpha particles from ^{222}Rn decay are expected to have range ~ 350 mm, and an event with $q = 18$ has, at most, an error of 36 mm. 99 (91) % of anode (grid) events satisfy $q < 18$.

Figure 5.6 shows a histogram of the three-dimensional range of GPCC events in the 20120405-02 dataset, fit with a double Gaussian profile. The peaks at 347 and 393 mm are ~ 3% lower than the α particle ranges for ^{222}Rn and ^{218}Po decay calculated by the SRIM program. This discrepancy may be due to energy loss in the thin-film, which was not modelled. There is no evidence for any of the ^{220}Rn (thoron) peaks in the
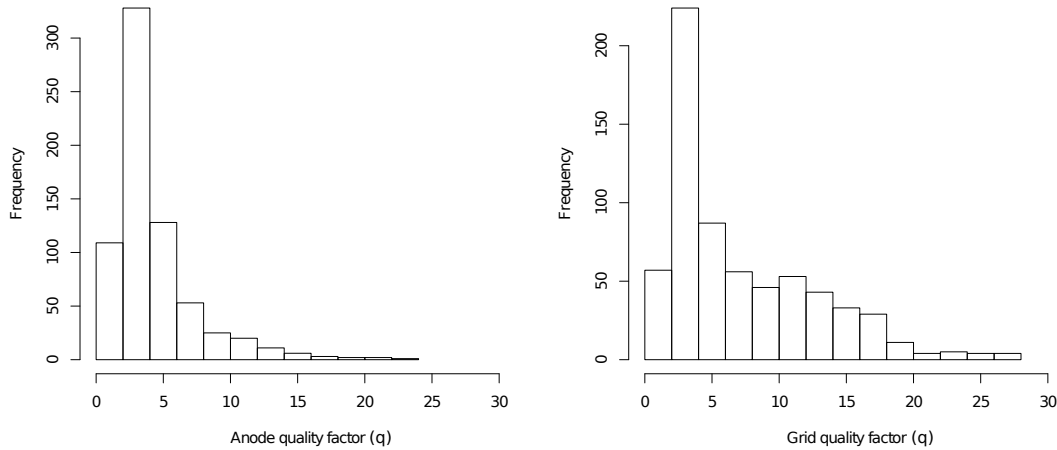
Figure 5.5: (left) Histogram of the anode quality factor. (right) The equivalent histogram for the grid.

distribution, but possibly a hint of the peak at 489 mm from ^{216}Po decay. The area under the Gaussian peak divided by the detector livetime gives the average event rate for the whole run for the respective species. However, as will be shown in Section 5.2.5, the fact that the vacuum vessel was evacuated shortly before the 20120405-02 run means that this total integrated rate gives an underestimate of the true equiibrium rate. It will be shown that a better estimate of the rate can be made by discarding the first 25% of the data.

5.2.3 Efficiency Corrections

A Monte Carlo code was written in R (*GpccMonteCarlo.r*) to allow the conversion of a given species' measured GPCC rate into the true rate of decays in the vacuum vessel. This code generates a population of α particles randomly distributed throughout a 1.5×1.5×1.5 m volume representing the DRIFT vacuum vessel. The particles are then transported in a straight line with uniform random orientation, and range as calculated by SRIM 2011. Finally, checks are made that:
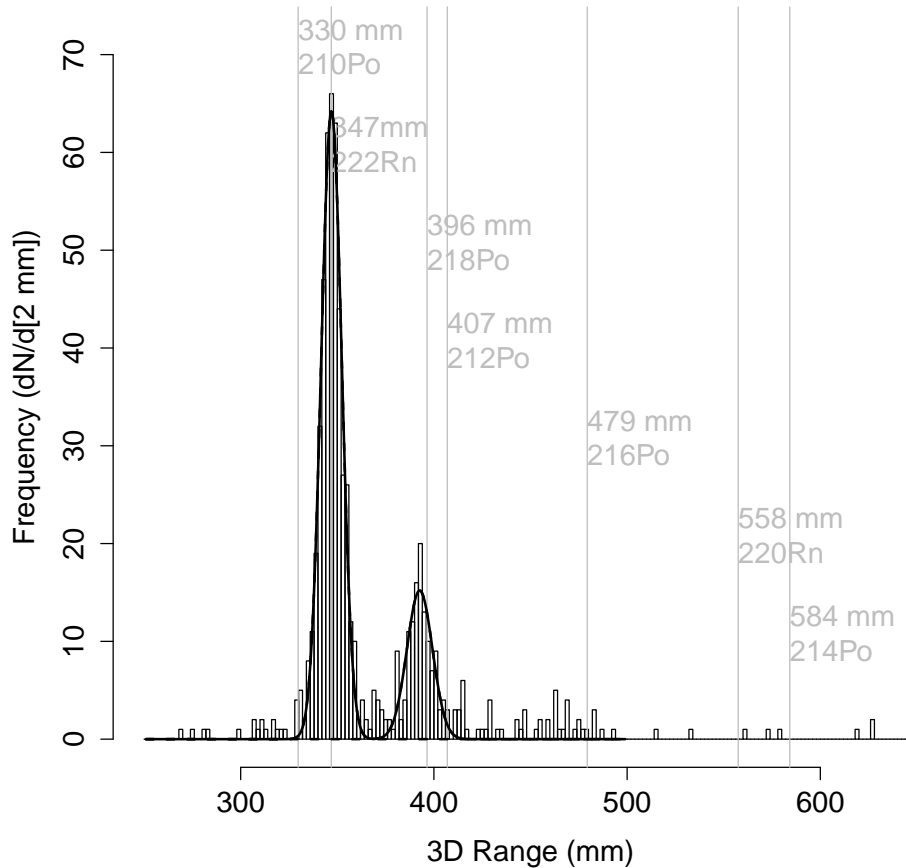
Figure 5.6: Reconstructed 3D ranges for GPCC events in the 20120405-02 dataset. α particles from ^{222}Rn decay populate the peak at 347 mm, whilst those from ^{218}Po decay give rise to the peak at 393 mm.

- The particle track was fully contained within the limits of an 896×896×1000 mm cuboid at the centre of the vessel representing the fiducial volume.

- The track crossed the plane bisecting the fiducial volume, representing the central cathode.

The output of the code is therefore the estimated fraction of decays from a given neutral, radioactive species in the vacuum vessel that go on to produce a fully-contained GPCC in the fiducial volume, called the 'geometric efficiency factor' from now on.

Inserting the SRIM ranges for ^{222}Rn and ^{218}Po yields geometric efficiency factors of 0.0286 ± 0.0016 for ^{222}Rn and 0.0309 ± 0.0017 for ^{218}Po, where the numbers are the mean and standard deviation of the efficiency factors calculated by 100 identical Monte Carlo experiments. The small difference is a consequence of the different ranges of the α particles emitted in the decay of the two species.

The simulation was then used to plot the expected angular distributions of the simulated GPCC population in $\cos\theta$ and ϕ, where θ is the polar angle measured from the z (drift) axis, and ϕ is the azimuthal angle. These distributions were compared with the distributions from data to determine the detector's efficiency for detecting GPCCs as a function of these two angles. Figure 5.7 shows the results of this comparison, where the simulated distributions (blue) have been normalised to the data between the limits indicated by the vertical lines. These lines define regions at moderate angles within which the shape of the distribution from data matches closely the prediction from simulation, and where the efficiency was assumed to be 100%.
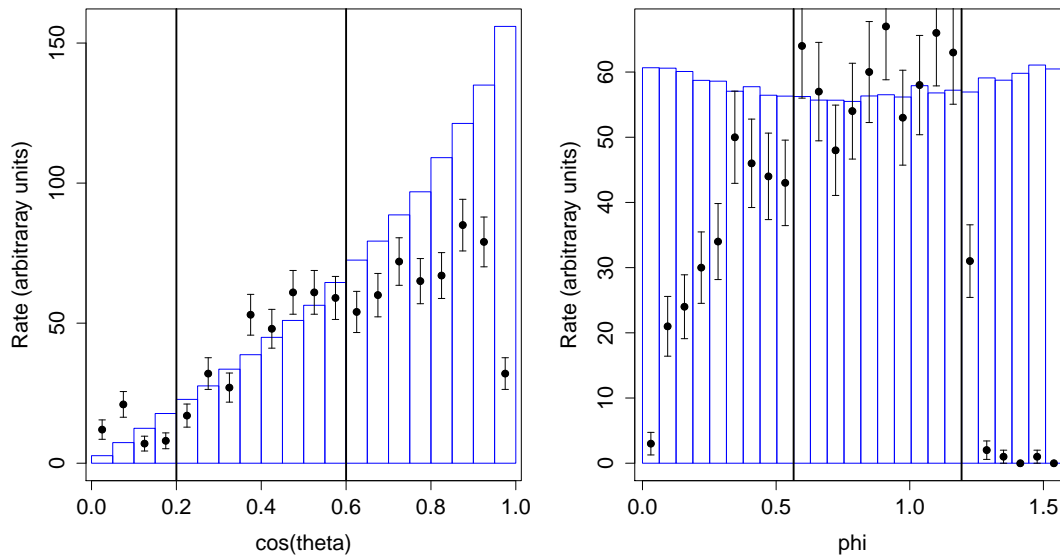
Figure 5.7: GPCC rate as a function of $\cos\theta$ and ϕ for data (black points) and MC (blue histogram). The blue histogram has been normalised to the data between the black lines, where the efficiency is assumed to be 100%. Error bars on data points are statistical uncertainties on the counts in each bin.

The efficiency was calculated as the area of the data distribution divided by the area of the simulated distribution, which was found to be $(49 \pm 8)\%$ for θ and $(60 \pm 6)\%$ for ϕ, giving a total 'angular efficiency' of $47.4 \pm 8.0\%$. Here, the uncertainty is the sum, in quadrature, of statistical and systematic uncertainties for the angle in question, which were calculated as follows. The statistical uncertainty was calculated by adding, in quadrature, the Poisson noise on the counts in each of the data bins (shown as black bars in Figure 5.7) to a second contribution equal to the standard deviation of the difference in the efficiency when each of the individual bins in the '100% efficiency' region (between the vertical black lines in Figure 5.7) was used alone to do the normalisation. The systematic uncertainty was calculated by shifting this region one bin to the left and right, re-calculating the efficiency, taking the difference from the efficiency as calculated using the whole region to do the normalisation, and picking the larger of the two resultant values.

The geometric efficiency from Monte Carlo simulation was multiplied by this angular efficiency to give a total efficiency, including the angular response function of the detector, of $(1.36 \pm 0.24)\%$ for radon, and $(1.46 \pm 0.26)\%$ for polonium. The drop in efficiency at high $\cos\theta$ is caused by the detector's difficulty in reconstructing events that are close to parallel to the MWPC detector planes. An excess can be seen in the ϕ data at $\phi \sim 1.2$, which can be interpreted as misreconstructed low-ϕ events that are close to parallel to the grid wires, or high-ϕ events that are close to perpendicular to the anode wires. The deficit is greater than the excess, which leads to efficiency factors < 1, as expected.

5.2.4 The Effect of Gas Flow

Under isolated, equilibrium conditions where there is no flow of gas through the vessel and the system has been isolated for a time $t \gg t_{\frac{1}{2}}$, the calculated event rates are equal to the emanation rates of respective species into the vessel. However, there was a constant flow rate of 2.07 mbarl/s through the vessel before and during these tests, and $t \sim t_{1/2}$, at least for ^{222}Rn near the beginning of the run. These effects must be accounted for, and this is done using Equation 5.4, which describes how the rate of radon decays in the vessel changes as a function of time immediately following the pumping out of the vacuum vessel, as the radon decay rate grows logarithmically to

114

bring the emanation rate and the radon removal rate into balance [165]:

$$D_x = A_x \frac{1}{1 + \frac{\tau_e}{\rho}} \left(1 - \exp\left(\frac{-(t - t_0)}{\tau}\right) \exp\left(\frac{-(t - t_0)}{\rho}\right) \right). \qquad (5.4)$$

Here, for a given species, D_x is the measured rate of decay in the vessel and A_x is the appearance rate, which represents the sum of processes that are adding the species in question to the vessel volume. In the case of ^{222}Rn, this is emanation from radium-containing detector materials, whereas the ^{218}Po is produced directly in the volume from the decay of ^{222}Rn itself. τ_e is the decay time $\left(\frac{t_{1/2}}{\ln(2)}\right)$, t is the time since t_0, the time at which the vessel was sealed (-0.21 days relative to the start of the 20120405-02 run), and ρ is the characteristic 'flush time' of the vessel, which is given by Equation 5.5 [165]:

$$\rho = \frac{m_0}{F} \left(1 - 1/e\right). \qquad (5.5)$$

Here, F is the mass flow rate and m_0 is the mass of gas in the vessel, which gives a flush time of $\rho = 0.63$ days when flowing at the nominal rate of one complete change of gas per day (2.07 mbar l s^{-1}). Under equilibrium conditions, the final term in Equation 5.4 becomes unity, which results in the following relationship between decay rate and appearance rate for a given species, as a function of the decay time and flush time:

$$D_x = A_x \frac{1}{1 + \frac{\tau_e}{\rho}}. \qquad (5.6)$$

5.2.5 Results and Discussion

The ^{222}Rn decay rate in the vessel rose logarithmically during the first few days, reaching 97% of its equilibrium value 2.1 days after the vessel evacuation ($\frac{1}{4}$ of the way through the run, 1.69 days after the start). The first $\frac{1}{4}$ of the data, which is 'out of equilibrium', was therefore discarded, and a histogram of the range of α particles in the remaining $\frac{3}{4}$ plotted. Following the procedure of Section 5.2.2, the ^{218}Po and ^{222}Rn α particle range peaks were fit with Gaussian functions, which were integrated and divided by the total detector live time to yield event rates for ^{222}Rn and ^{218}Po of 64.2 ± 2.8 and 19.1 ± 3.1 events per day, respectively. Dividing by the relevant species' efficiency factor yields the total rate of decay of that species in the entire vessel: $D_{Rn} = 4721 \pm 859$ decays/d and $D_{Po} = 1301 \pm 310$ decays/d. Finally, equation 5.6

allows the equilibrium appearance rates of ^{222}Rn and ^{218}Po to be calculated, yielding in this case:

$$A_{Rn} = 0.533 \pm 0.097 \text{ atoms/s.} \tag{5.7}$$

$$A_{Po} = 0.015 \pm 0.004 \text{ atoms/s.} \tag{5.8}$$

It might be expected that under conditions of secular equilibrium, these two numbers should be equal. The difference comes from the fact that whereas the parent population of ^{222}Rn is 100% uncharged, the daughter ^{218}Po has a charged fraction that is a strong function of several difficult-to-control variables such as relative humidity and trace aerosol concentration, as well as pressure. The neutral fraction implied by the DRIFT data is lower than most other measurements, at 2.8%, which is probably explained by the low operating pressure of DRIFT compared with atmospheric pressure at which other measurements, for example those of Hopke [194], have been made.

5.3 Measuring the Radon Emanation Rate Using an α Spectrometer

An experiment was designed, tested and deployed underground to make the first independent measurement of the total radon emanation rate inside the DRIFT vacuum vessel, using the commercially-available Durridge RAD7 radon detector [195]. The aim of this work is to build up a coherent picture of radon emanation in DRIFT by comparing results collected here with the GPCC results of the previous section.

5.3.1 Experimental Method

Following a run of data acquisition with DRIFT, the vacuum vessel was left pumping down for one week using an Edwards XDS10 scroll pump. This removed any old radon from the vessel, and also evacuated CS_2 and CF_4 that had outgassed from the detector materials. The vessel was then sealed and left for a further week to allow the detector to emanate radon into the vessel, exactly as it would during normal running conditions

At the end of the week of emanation the vessel was backfilled with 8 torr of dry nitrogen, which was pumped, along with the emanated radon and any residual gasses, into the smaller Rn vessel 1. The backfill pressure was chosen such that after transferring, the pressure in the smaller vessel was 1 bar, which is the nominal operating pressure of the RAD7. Concentrating the gas in this way improves the sensitivity of the measurement by a factor equal to the ratio of the two volumes, or $\approx 100\times$ compared with sampling directly from the vacuum vessel. The experiment was repeated omitting the emanation stage, to obtain a background measurement. Each test lasted four hours, and each run consisted of 12 tests spanning a period of 48 hours. During this time, the RAD7's internal pump circulated the gas through its 1.3 l alpha spectrometer detector at a measured rate of $1.075 \pm 0.012 \text{ m}^3 \text{ s}^{-1}$.

A µm mesh filter at the input to the detector ensures that no charged particles or reactive species are admitted to the sensitive volume, which guarantees that the dominant alpha-producing species in the detector is radon. Charged daughter particles produced in radon decays in the sensitive volume are swept to the silicon diode radiation detector at the centre of the dome under the influence of the electric field between the 0 V silicon detector and the 2000 V dome. Due to the geometry of the detector, there is then a 50% chance that the radon daughter's subsequent α decay will deposit the α particle's energy in the detector, which is large enough to fully contain these particles and therefore guaranteed that their full energy is measured.

Each time an α particle is detected, the count in one of the 200 50 kV bins is incremented by one, which results in a spectrum of α particle energies at the end of the experiment. Since decays of different radon daughters produce α particles of different, characteristic energies, by summing the counts in carefully-chosen energy windows, the RAD7 is able to calculate the concentration of radon in the sensitive volume. Counts from two energy windows are summed: $5.40 \rightarrow 6.40$ MeV to catch the 6.0 MeV α particles from ^{218}Po , and $7.2 \rightarrow 8.2$ MeV, which includes the 7.69 MeV α decay of ^{214}Po. Dividing by the detector live time, the activity of ^{222}Rn in the sensitive volume can be calculated. Counts in a third window: $8.2 \rightarrow 9.5$ MeV are summed, which includes the α decay from ^{212}Po, part of the Thoron decay chain. The counts in this window are used to correct the counts in the $5.40 \rightarrow 6.40$ MeV window, which gets contaminated with these thoron-genic α counts. The count in the $8.2 \rightarrow 9.5$ MeV window is multiplied by the ratio of the branching fractions of the two ^{212}Bi decays

(33/64), and this is subtracted from the count in the 5.40 $\rightarrow$ 6.40 MeV window. The complete set of relevant α decays in the uranium-238 and thorium-232 decay chains are shown in Figures 5.1 and 5.8, respectively.
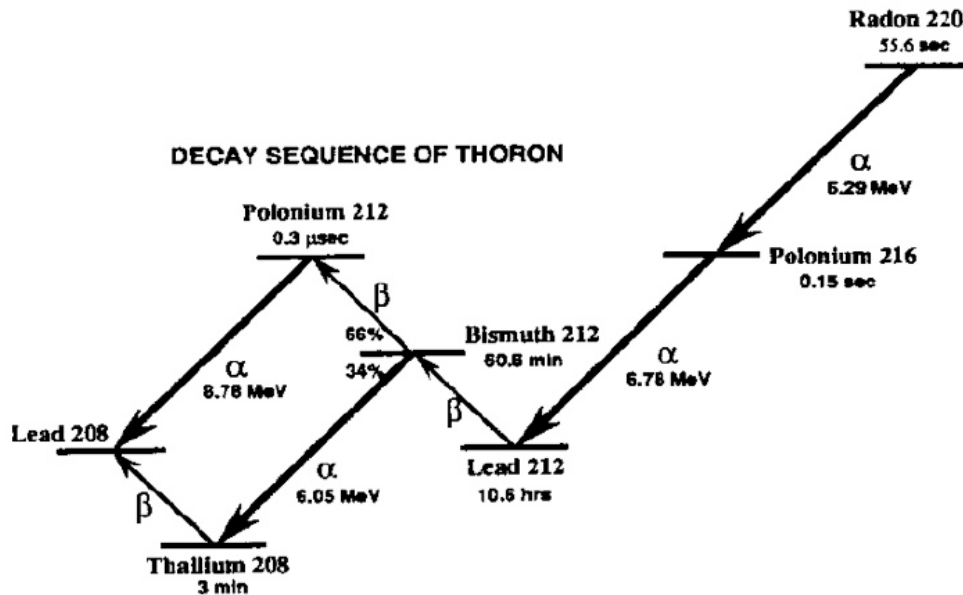
Figure 5.8: Part of the ^{235}U decay chain. The α decay of ^{212}Bi contaminates the window sensitive to ^{218}Po decay α particles, but these extra counts can be removed by detecting the α decay of ^{212}Po.

5.3.2 RAD7 Data Analysis

On completion of a run, the RAD7 detector outputs a text file of data with one line per cycle. The first two tests of any run were discarded, to allow time for the RAD7's internal pump to fully mix the gas throughout the system. The remaining 10 data points were then subject to the five corrections described below. Figure 5.9 shows an example of the resulting corrected data.
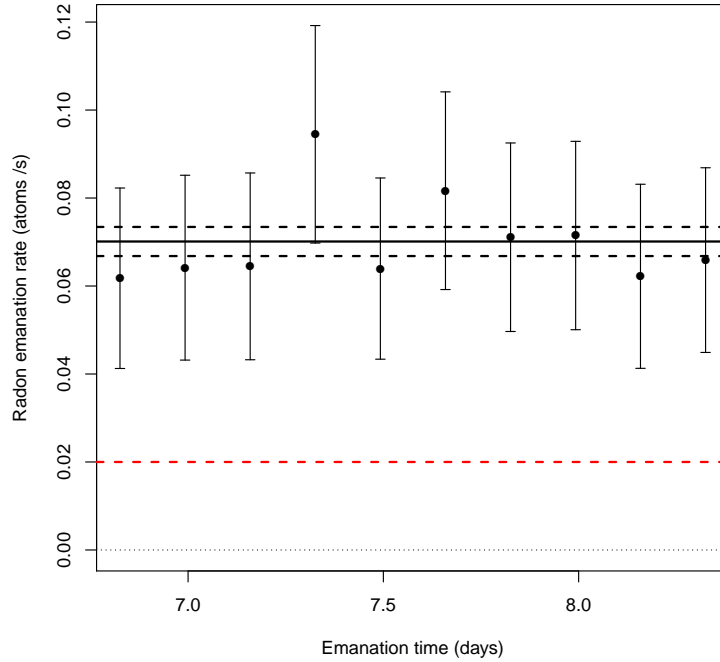
Figure 5.9: Example RAD7 output graph for a 40-hour run detecting the radon emanated from 10 fluoroelastomer rubber bungs. Each data point represents a single 4-hour cycle, with error bars showing the 95% confidence interval from Poisson statistics. The solid and dashed black lines represent the mean and error on the mean of all 10 measurements. The red dashed line shows the limit of sensitivity of the RAD7 assuming 3 counts are needed in a single 4-hour cycle to claim detection.

Volume Correction The RAD7 outputs the radon concentration inside its sensitive volume in $\mathrm{Bq\,m^{-3}}$ by converting the count rate using a factory-measured calibration constant. This was converted into the total activity by multiplying by the volume of gas being sampled:

$$\mathrm{Bq} = \mathrm{Bq\,m^{-3}} \times (V_{chamber} + V_{RAD}), \tag{5.9}$$

where $V_{chamber} = 35.5$ l, and the RAD7 internal volume $V_{RAD} = 1.3$ l.

Emanation Time Independent Background Subtraction The 'emanation time independent' background comes mainly from inherent electronic noise in the cir-

cuitry of the detector. This was measured to be 0.0012 ± 0.0003 Bq during a run with the pump turned off and the input and output blocked.

Humidity Correction Being a polar molecule, water vapour attracts ions and causes them to 'plate out' on its surface. Therefore, any water vapour in the sensitive volume acts to reduce the sensitivity of the instrument by preventing radon daughters from reaching the detector. The RAD7 monitors the relative humidity (RH) of the sample gas, allowing its effects to be accounted for using the empirical formula in Equation 5.10:

$$A_{\text{after}} = A_{\text{before}} \times \frac{100}{116.67 - 1.1 \times RH} , \qquad (5.10)$$

where A represents Rn activity, and RH stands for relative humidity. RH values were found to be extremely variable, ranging from $10 < RH < 70\%$.

Emanation Time Adjustment During the emanation period the rate of radon emanation into the volume remains constant, whilst the rate of radon decays increases in proportion to the number of radon atoms in the volume, approaching equilibrium where $R_{\text{decay}} = R_{\text{emanation}}$. Since it is not possible to wait until t= ∞, Equation 5.11 was used to correct the measured activity to that which would have been measured under equilibrium conditions, which is equal to the equilibrium emanation rate.

$$R_{\text{em}} = A_{\text{meas}} \times \frac{1}{1 - \exp\left(\frac{t}{t_e}\right)} , \qquad (5.11)$$

where t is the emanation time and t_e is the time taken for a sample of radon to decay by at factor of 1/e (5.52 days) [193].

Emanation-Time-Dependent Background Subtraction This background comes from Rn emanating materials in the apparatus such as fluoroelastomer o-ring seals. Flushing with dry N_2 immediately before each test ensures that no old radon contributes to the background, but new radon will emanate from these components to mix with the 'signal' radon in the gas being tested. Therefore, a background measurement from emanation vessel 1 was made, following exactly the

same procedure as a normal run, and the result subtracted from the emanation rate. Typical backgrounds were ~ 0.02 atoms/s.

5.3.3 Results and Discussion

Subtracting the zero-emanation control yields a radon emanation rate of

$$0.257 \pm 0.022 \text{ atoms/s}. \tag{5.12}$$

This is lower than the value of 0.533 ± 0.097 atoms/s implied by the GPCC rate measured in Section 5.2. A possible source of the discrepancy is the effect of residual electronegative CS_2 gas interfering with the efficiency of the RAD7, by causing ^{214}Po and ^{218}Po to stick to CS_2 molecules instead of the detector. Notwithstanding, the fact that two completely different measurement techniques were used to obtain these similar results lends weight to both measurements, and goes some way towards validating the new technique of in-situ radon emanation measurement with the RAD7.

5.4 Radon Reduction

Knowing the total rate of radon emanation into the DRIFT vacuum vessel, two questions arise: which detector components contribute significantly to this rate, and are there radon-cold alternatives? This section addresses these questions, with the help of another radon emanation apparatus similar to that described in Section 5.3.

5.4.1 A High-Sensitivity Emanation Apparatus

An apparatus consisting of the RAD7 radon detector connected in a closed loop to a radon emanation chamber was constructed in order to measure the total rate of radon emanation from samples of material placed in the chamber (Figure 5.10).

A sample of material to be tested was placed into one of three emanation chambers (one small – S – 3.5 l, and two large – 1, 2 – 35.5 l), which was then pumped down to a pressure below 0.1 torr. This removed ambient radon and neutral daughter particles from the chamber, as well as any other gases such as water vapour, which might reduce
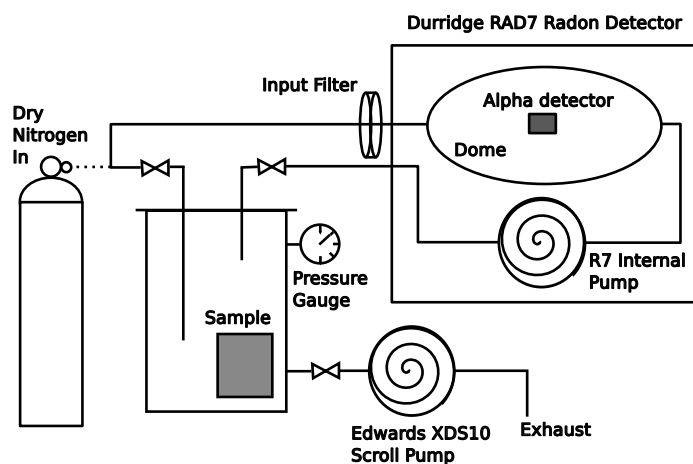
Figure 5.10: Sketch of the radon emanation apparatus.

the detection efficiency of the radon detector. This vacuum was taken to be a good approximation of the normal operating conditions in the DRIFT vacuum vessel (40 torr), and the size of the emanation vessel was chosen to minimise the emanation volume, and thus maximise the radon concentration. The sample was left in the chamber for 48 hours to allow outgassing to occur. The chamber was then evacuated and sealed once more, and the start time of the radon emanation process was taken to be the time at which the valve was sealed. After 7 days, the chamber was backfilled to 756 torr (1 bar) with dry nitrogen from a compressed nitrogen cylinder, and the RAD7 radon detector was connected to the chamber via $\frac{1}{4}$" Swagelok inlet and outlet pipes. The inlet and outlet valves were opened, exposing the RAD7 to the emanation vessel, and data acquisition commenced.

Data analysis proceeded exactly as described in Section 5.3.2, with one exception. Because the emanation vessel now contained a sample as well as the gas to be analysed, an additional term was added to Equation 5.9 to take account of the consequent volume reduction:

$$\mathrm{Bq} = \mathrm{Bq/m}^3 \times \left(V_{chamber} + V_{RAD} - V_{sample} \right). \tag{5.13}$$

Sample volumes were calculated based on measurements with a ruler/callipers if their shape was regular enough to allow this, otherwise water displacement was used to estimate the volume.

Sample	Vessel	E. time (days)	RH (%)	Rn emanation (atoms/s)
Example background	S	8.24	28.4	0.0206 ± 0.0023
Example background	2	8.30	11.6	0.0201 ± 0.0053
Ribbon cables	2	9.1	18.2	0.4036 ± 0.0293
Ribbon cables	1	6.94	21.3	0.3737 ± 0.0120
Ribbon cables [1]	-	6.5	23	0.50 ± 0.03
Nitrile O-ring	2	8.7	26.2	0.1204 ± 0.0136
10 rubber bungs	S	7.6	38.5	0.0464 ± 0.0033
Aluminized Mylar	S	19.1	44.8	0.0012 ± 0.0022
Aluminized Mylar	S	8.14	19.9	0.0056 ± 0.0020
Aluminized Mylar	S	10.36	21.9	0.0045 ± 0.0018
Electronics Boxes [1]	-	12	37	0.05 ± 0.01
Black HV cables	2	9.3	14.6	0.1069 ± 0.0134
DRIFT-IId	1	8.41	68.8	0.2694 ± 0.019
DRIFT-IId (background)	1	0.00	76	0.0126 ± 0.0114

Table 5.2: Results of Rn emanation tests on DRIFT-IId detector material samples.

5.4.2 Suspected Radon Emanators

Table 5.2 contains the complete set of results from suspected radon hot detector components, acquired in Sheffield and underground at Boulby mine between February 2011 and August 2012. Example background measurements are also presented, followed by measurements of a set of ribbon cables – a known radon-emitting component from a previous detector (DRIFT-IIb) – which were measured by the collaboration in 2006, and measured again here as a consistency check. The ribbon cables were tested for radon emanation in two different vessels (1 & 2) with separately-measured backgrounds, and the results were found to be in agreement. Repeatability was verified by measuring the aluminised Mylar cathode material three times with exactly the same setup, and the fact that these results are close to the lower limit of the apparatus' sensitivity validates the measurement technique down to these levels. Suspected radon emanators appear in bold font in Table 5.2, and the full-detector radon emanation rate measured in Section 5.3 is included at the bottom of the table for scale. The nitrile o-ring that forms the door seal of the DRIFT-IId detector had long been suspected of being a significant source of radon, and this was confirmed by these measurements. Similarly, a set of 10 bungs of an unknown fluoroelastomer composition were tested

---

[1]Measurements made in 2006 by another member of the DRIFT collaboration [196].

Sample	Vessel	E. time (days)	RH (%)	Rn emanation (atoms/s)
Teflon O-ring	2	7.9	14.2	-0.0006 ± 0.0073
Teflon O-ring	S	8.0	25.5	0.0052 ± 0.0025
20 Silicone bungs	S	9.3	26	0.0192 ± 0.0023
20 Silicone bungs	S	17.4	27.0	0.0166 ± 0.0017
White cable	2	21.4	14.4	-0.0191 ± 0.0052
White HV cables (complete)	S	9.2	45.5	0.0053 ± 0.0019
White HHV cable	S	14.3	22.9	-0.0168 ± 0.0024
HV putty disc	S	12.1	20.1	-0.0073 ± 0.0015
HV putty disc	S	14.4	23.3	-0.0043 ± 0.0015
Lexan	1	7.86	19.7	-0.0098 ± 0.0067
Epoxy-laminated Kevlar	2	8.1	22.1	-0.0166 ± 0.0058
DRIFT-IIe vessel (air)	1	19.3	69.3	0.3882 ± 0.0266
DRIFT-IIe vessel (N_2)	1	19.2	37	0.0645 ± 0.0087
DRIFT-IIe vessel + ribbon cables	1	8.5	43.0	0.3469 ± 0.0262

Table 5.3: Results of Rn emanation tests of replacement DRIFT-IId and proposed DRIFT-IIe materials.

and found to be emitting a significant amount of radon. Twenty of these bungs were used to seal unused holes in the two signal feedthrough flanges on top of the DRIFT-IId vessel. The HV distribution cables were also found to be a significant source of Rn in the vacuum vessel, with an emanation rate similar to that of the fluoroelastomer rubber bungs. The aluminised Mylar sample was from the same batch as that which made up the cathode operating on the DRIFT -IId detector from March 2010 to April 2012. This was found to be a low, but non-zero radon emitter.

5.4.3   Replacement of Rn-Emanating Materials

Following the identification of the major radon-emanating components in the detector, a set of low-radon replacement components were selected. Table 5.3 contains the results of emanation tests of each of these components.

A polytetrafluoroethylene (PTFE) encapsulated o-ring was ordered to replace the nitrile one that was found to be radon hot. PTFE has a very low gas permeability [197], and it was hoped that combining this with the elasticity of the elastomer core

would produce an o-ring that could provide both a low radon emanation rate and an effective vacuum seal. A similar o-ring was installed on the DRIFT-IIc detector at Occidental College, and has shown to be capable of maintaining a vacuum seal over a period of more than one year. The first two lines in Table 5.3 give two separate measurements of the radon emanation rate of this o-ring, and show that it has at least a 20× lower radon emanation rate than its nitrile predecessor. Silicone was chosen as the material to replace the radon for rubber bungs, due to its elasticity and low radon permeability [198]. A full set of 20 replacement bungs were tested, and found to have a radon emanation rate five times lower than the old bungs (0.018 ± 0.002 compared with 0.092 ± 0.007 for an equivalent number of fluoroelastomer bungs).

A new set of HV distribution cables was manufactured, using a radio-pure material for the cables' insulating sheath. An unwound reel of this cable was tested initially ('White cable' in Table 5.3), and found to be radon cold, before the cables were made by soldering on mini banana plug connectors and finishing with clear heat shrink. The completed cables were then tested for radon emanation, and found to be a low, but non-zero, radon emanator. It can be inferred from these two measurements that this minor source of radon is in either the solder, the connectors, the heat shrink, or a combination of the three. Notwithstanding, the replacement cables represent a 20-fold improvement over the old ones.

Finally, the HV putty, Lexan and Epoxy-laminated Kevlar are all proposed new materials for the DRIFT-IIe detector. Samples of these were tested, and were all found to have radon emanation rates below the sensitivity of the apparatus. These materials were therefore deemed suitable for inclusion in the new detector.

5.4.4   Have All Radon Sources Been Identified?

It is interesting to ask how much of the total emanation rate calculated in Sections 5.2.5 and 5.3.3 can be accounted for by identified sources of radon. If the sum of individual contributions falls short of the total as measured in the previous sections, this would imply that there are still more emanating materials in the detector to be discovered. To answer this question, Table 5.4 was created, which collects all the radon emanation measurements of detector components that were present when the 20120405-02 dataset was recorded. The emanation rates have been scaled, where appropriate, based upon

Sample	Rn emanation (atoms/s)	Scaling & notes
Nitrile O-ring	0.0602 ± 0.0068	×0.5.
Black HV cables	0.1069 ± 0.0134	None, full set tested.
DRIFT-IIe vessel	0.0645 ± 0.0087	None, whole vessel tested.
Electronics boxes [1]	0.05 ± 0.01	None
Rubber bungs (old)	0.0333 ± 0.0027	×2 and ×0.718. $\frac{1}{2}$ number of bungs.
Aluminized Mylar	0.0076 ± 0.0046	×2. Sample was $\frac{1}{2}$ cathode area.
FEP ribbon cables [1]	0.00 ± 0.02	None
PTFE signal cables [1]	0.00 ± 0.02	None
Total	0.323 ± 0.035	GPCC implied rate: 0.533 ± 0.097

Table 5.4: Radon emanation from detector materials present during the 20120405 run.

the surface area of the sample in contact with the vacuum.

The total radon emanation rate obtained by summing the scaled rates in Table 5.4 is

$$0.323 \pm 0.035 \text{ atoms/s.} \tag{5.14}$$

Here, the measured emanation rate for the o-ring has been scaled by a factor of $\frac{1}{2}$, the fractional surface area that is in contact with the inside of the DRIFT vacuum vessel. Similarly, the rubber bung measurement has been scaled by a factor of 0.718 ± 0.028, the uncertainty coming from calliper measurements of a single rubber bung. It is assumed that the remaining fraction of the emanated radon escapes harmlessly into the lab, and therefore does not contribute to the total rate measured in Sections 5.2 and 5.3. The sum of individual emanation rates (0.323 ± 0.035 atoms/s) is in reasonable agreement with the measured total (0.257 ± 0.022 atoms/s), but lower than the rate implied by GPCCs (0.533 ± 0.097 atoms/s), which may suggest that there is an unaccounted-for source of radon inside the vacuum vessel.

The same calculation was made for dataset 201212, where all but one of the known radon emanating components have been replaced. Table 5.5 shows the emanation rates for the individual components. Finally, the GPCC rate analysis of Section 5.2 was applied to the 201212 dataset (13.9 days' live time), resulting in a measured GPCC event rate in the fiducial volume of 35.7 ± 1.6 per day, implying a radon emanation rate of

$$0.297 \pm 0.054 \text{ atoms/s.} \tag{5.15}$$

---

[1]Measurements made by another member of the DRIFT collaboration in 2006 [196].

Sample	Rn emanation (atoms/s)	Scaling & notes
DRIFT-IIe vessel	0.0645 ± 0.0087	None, whole vessel tested.
Nitrile O-ring	0.0602 ± 0.0068	$\times 0.5$.
White HV cables	0.0053 ± 0.0019	None, full set tested.
20 silicone bungs	0.0129 ± 0.0015	$\times 0.718 \pm 0.028$.
Aluminized Mylar	0.0076 ± 0.0046	$\times 2$. Sample was $\frac{1}{2}$ cathode area.
Electronics boxes [1]	0.05 ± 0.01	None
FEP ribbon cables [1]	0.00 ± 0.02	None
PTFE signal cables [1]	0.00 ± 0.02	None
Total	0.201 ± 0.032	GPCC implied rate: 0.297 ± 0.054

Table 5.5: Radon emanation from detector materials present during the 201212 run.

This is again slightly higher than the sum of individual components (0.201 ± 0.032 atoms/s), which hints at the presence of an unaccounted-for source of radon in the detector.

5.5   Radon Emanation Rate as a Function of Time

Armed with a method for determining the radon emanation rate from the rate of GPCC events in DRIFT, it becomes possible to examine the effect of changes to the detector over a long time period. The analysis of Section 5.2 was applied to carefully-selected datasets that had a constant flow rate and were recorded a long time (> 2 days) after the last pump out, to allow the assumption of equilibrium conditions to be made. Figure 5.11 shows the results of this analysis. Vertical dashed lines represent changes to the detector configuration that may have affected the total radon emanation rate:

1. Radon refit (cables stripped and inner detector sealed).

2. Signal cables replaced with Teflon-insulated equivalents.

3. Central cathode etched in nitric acid to remove long-lived parent isotopes (see Pipe [178]).

4. MWPCs similarly etched.

5. Gas target changed from 40 torr CS_2 to 30:10 torr CS_2:CF_4.

6. Right MWPC swapped for one that had not been etched.

---

[1]Measurements made by another member of the DRIFT collaboration in 2006 [196].

7. Right MWPC swapped back and thin-film cathode installed.

8. Radio-pure thin-film cathode installed.

9. Silicone bungs and Teflon-insulated HV cables installed.
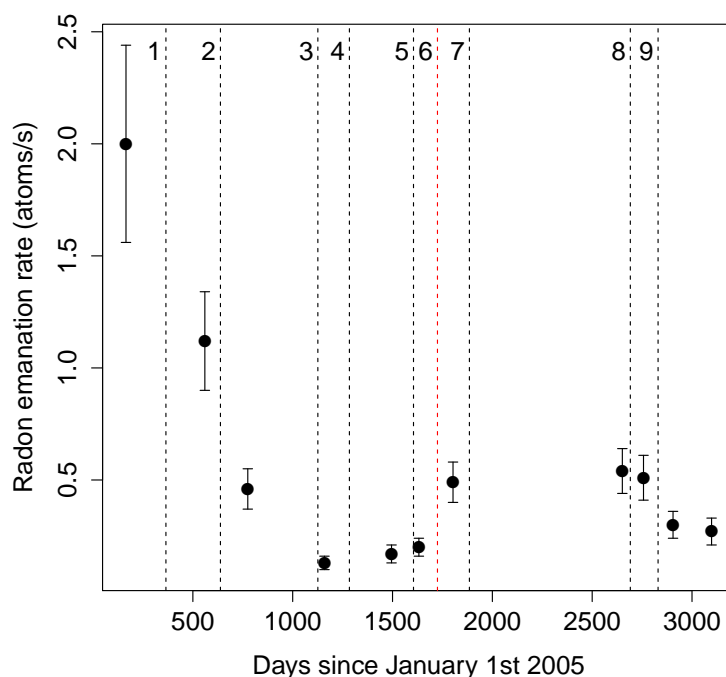
Figure 5.11: Radon emanation rate vs. time. Dashed vertical lines represent changes to the detector configuration (see text for details).

Overall, an improvement by a factor of $\sim$ 10 has been achieved. The radon re-fit, replacement of signal cables, nitric acid etching of the wire central cathode, and the replacement of the bungs and HV cables all produced significant reductions in the radon emanation rate. The only targeted radon reduction activity that did not produce a reduction was the etching of the MWPCs. Taking this together with the fact that the cathode etch *did* have an effect suggests that, as expected, radon daughters are produced predominantly positively charged, and are therefore swept toward the cathode rather than the detector plane. However, the increase in radon with the swapping in of a dirty MWPC (red line) suggests it is possible for contamination to be introduced

by the MWPCs. The fact that the radon emanation rate then remained approximately constant with the swapping back of the MWPC and the installation of the thin-film cathode implies that the original thin-film cathode was a radon contributor. Since then, a source of radiological contamination on rollers that form part of the manufacturing process has been identified, and a new, 'clean' cathode installed.

5.6   DRIFT as a Radon Assay Instrument

Having confirmed that DRIFT data can be used to reliably measure radon levels in the detector, the possibility of using DRIFT itself as a radon assay instrument presents itself. The radon sensitivity (that is, the smallest concentration of added radon detectable by the experiment above background) of the new low-radon DRIFT detector was determined according to the following procedure. An available livetime of 7 days was assumed.

The raw rate of GPCC events detected in the fiducial volume was multiplied by the assumed livetime to give the expected number of background GPCC events during a week-long assay run, and the square root taken to give the Poisson noise on this count (N_p):

$$N_p = \sqrt{35.7 \text{ events/day} \times 7} = 15.8 \tag{5.16}$$

This is the minimum number of counts that must be produced by a sample in order for its radon emanation rate to be detectable above background. Using the previously-determined efficiency factor, this count was converted into the total number of produced radon atoms that decayed in the fiducial volume during the week-long run, and divided by the livetime in seconds and total detector volume in litres to yield DRIFT's radon sensitivity (S_D):

$$S_D = 2.4 \, \mu\text{Bq}\,\text{l}^{-1}. \tag{5.17}$$

Comparing this with the RAD7's sensitivity of 100 μBq l^{-1} [195], it can be seen that DRIFT has $\sim$ 40$\times$ superior sensitivity. For a sense of scale, radon activity of the air in the Boulby Underground Laboratory (radon-cold compared with typical surface locations) was recently measured to be 3,730±790 μBq l^{-1}, whilst that at Gran Sasso is found to be $\sim$ 20,000 μBq l^{-1} [199]. DRIFT's radon sensitivity is limited by background from the identified sources of radon appearing in Table 5.5, plus a likely

unattributed contribution. With further materials substitution it should be possible to reach sub-μBq sensitivities.

5.7 Conclusions

The first direct measurement of the radon emanation rate from detector materials into the DRIFT vacuum vessel has been made, using an α spectrometer radon detector, and the results of this test are in reasonable agreement with the results of an analysis of α data recorded with DRIFT. Together, these two independent techniques provided a powerful 'snapshot' measurement of the radon background level in the DRIFT detector. Individual detector components, both existing and proposed, were tested separately for radon emanation. Comparing the sum of individual contributions with the measured overall rate suggests that the collaboration is close to identifying every significant contributor of radon in DRIFT-IId, and can successfully screen materials to ensure that the radon emanation rate in DRIFT-IIe is minimised. The fact that these three measurements: the detector total rate, the rate inferred from DRIFT data, and the sum of individual detector components all form a reasonably consistent picture provides a cross-validation of the techniques. Possible explanations of the remaining discrepancies have been given. After substituting several detector components with radon-cold alternatives, the emanation rate was found to reduce, although based on an audit of the known radon emanators, the presence of a further, unidentified source of radon cannot yet be ruled out. Work is underway to redesign the signal feedthrough flange, which will eliminate the need for the Silicone bungs, and the Teflon-encapsulated o-ring will be fitted in the immediate future. Together, these changes are expected to reduce the radon emanation rate by a further factor of 2. Finally, DRIFT was shown to be a sensitive radon detector at the $\approx$ μBq level, opening up the possibility of using a NITPC detector as a radon assay instrument to support other rare event search experiments in the future.

Chapter 6

Characterisation of a Simplified Electronics Scheme for Scale-Up

Scaling up to the 24 m^3 DRIFT-III detector will necessitate a corresponding scale-up of the readout electronics. It is therefore critical to make the electronics chain as simple as possible, to reduce cost, reduce the amount of necessary maintenance, and reduce the chance of malfunction. Any changes to the current system must maintain DRIFT-IId's current levels of background discrimination and directional sensitivity, and in fact there are good reasons to believe that information is being lost from the waveforms with the current scheme, which suggests that improvements may be expected when moving to a simplified scheme. This chapter presents a characterisation study of a simplified electronics chain omitting the shaping amplifier and high-pass filter described in Chapter 4.

6.1   Simplified Electronics

As described in Chapter 4, the DRIFT-IId electronics scheme can be broken down into three stages: charge-to-voltage conversion by charge preamplifiers, Gaussian shaping by shaping amplifiers, and removal of low-frequencies by high-pass filtering at the input to the DAQ. The combined effect of the first and last stage on a simulated waveform is shown in Figure 6.1a. Here, the grey lines represent 20 'toy' impulse charge depositions separated in time by 10 μs that have been converted into a voltage by the pream-

131

plifier, and then summed to give the waveform shown in dashed blue. The Orange line shows the effect of adding the high-pass filter, which acts to make the waveform bipolar, reducing the peak height and the duration for which the waveform is above the baseline. This distorts several of the stage 1 waveform parameters introduced in Chapter 4, such as t_{max}, A_p, V_{min} and V_{max}, and may result in loss of information from the original charge deposition. Adding the shaping amplifier has the effect of forcing each impulse charge deposition to acquire a Gaussian shape with width 4 µs, which gives rise to the signal shape of the form shown in Figure 6.1b. Here the grey preamplifier output shape has been replaced by the Gaussian shaping amplifier output shape (shown in red), which further distorts the waveforms.

(a) Input: preamp output.

(b) Input: shaper output.
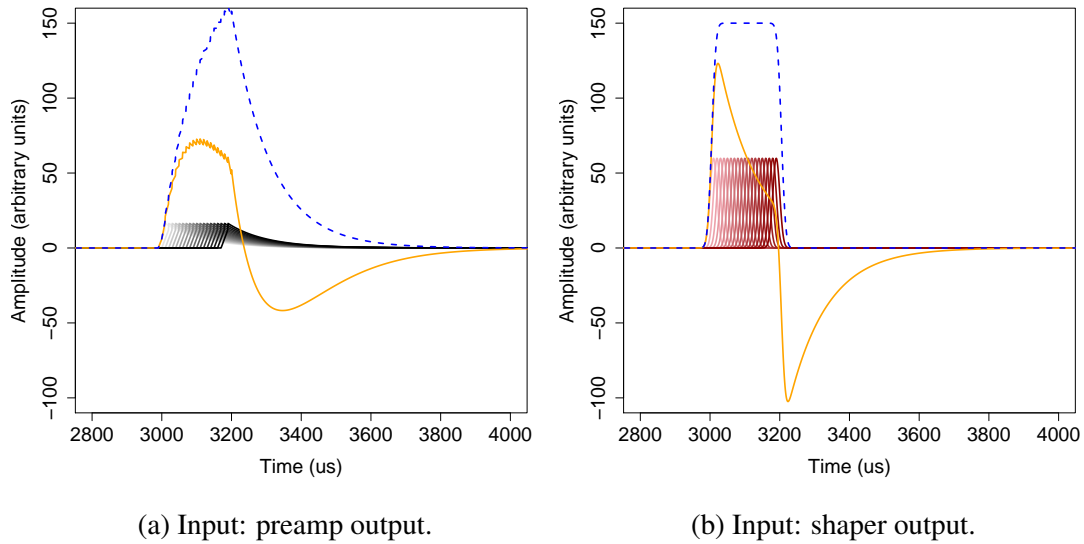
Figure 6.1: Simulated signal from 20 charge depositions, separated in time by 10 µs (blue dashed line), then subjected to the high-pass filter (orange line).

6.1.1 Experimental Method

A series of neutron calibration and background datasets (Table 6.1) were collected with the DRIFT-IId detector operating in a one-sided configuration, as shown in Figure 6.2. In this mode only one MWPC was read out. However, the signal was split and processed simultaneously by parallel 'normal' and 'simplified' electronics schemes,

132

Run number	Description	Livetime (hours)
drift2d-20130122-04	*x*-directed neutron run	15.2
drift2d-20130123-01	*z*-directed neutron run	23.0
drift2d-20130124-01	*y*-directed neutron run	19.5
drift2d-20130125-03	background run	88.8

Table 6.1: Datasets with electronics in the 'tee' configuration.

enabling an event-by-event comparison of the signals to be made. The differences between the two schemes were as follows:

- The final high-pass filter formed by the 50 Ω input impedance of the digitiser channel and the 2.2 μF capacitor was removed in the simplified electronics.

- The CR-200 Gaussian shaping amplifiers were bypassed.
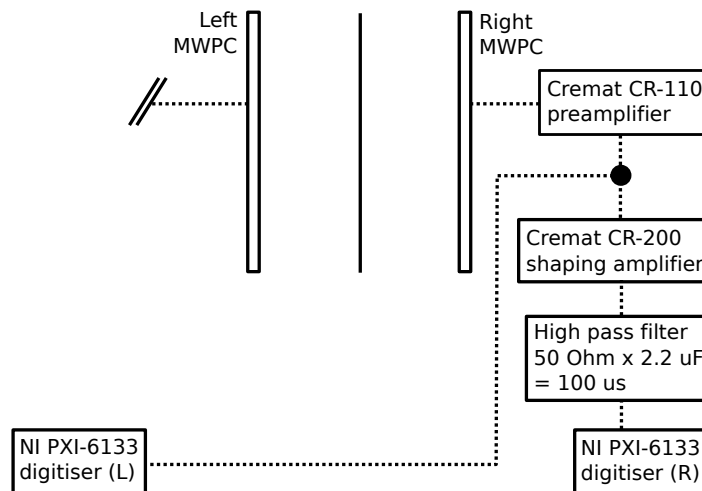
Figure 6.2: Sketch of the 'tee' readout scheme, bypassing the shaping amplifiers and the high-pass filter before the digitisers.

The tee was placed after the Cremat preamplifier, which is inside the vacuum vessel. Therefore, the input to both sets of electronics was the output of the CR-110 preamplifier, the impulse response function of which is shown in Figure 6.3. This

input signal is made up of the sum of many such impulses, and the output of the electronics chain as seen by the digitiser is the convolution of this sum with the transfer function of the electronics. Triggering occurred on the normal channels only, but data
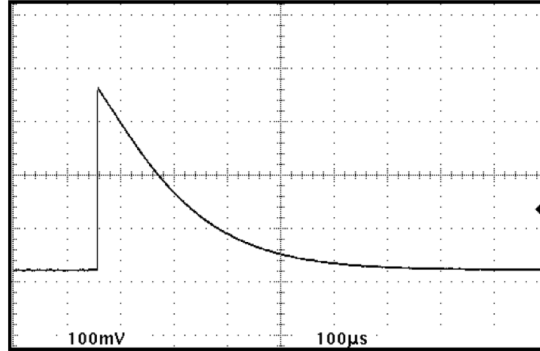
Figure 6.3: Impulse response of the CR-110 preamplifier.

was recorded for both sets of electronics. Figure 6.4 shows an example event display from this run, where the right-hand MWPC was read out. Waveforms processed in the normal way appear on the right, whilst the same channels read out through the simplified electronics appear in the left panel.

Three 'overnight' neutron calibration datasets were recorded, with the ^{252}Cf source oriented along the x, y and z directions, and set back 50 cm from the outside of the vacuum vessel wall to provide some degree of distance collimation. A final background dataset was collected with no source present to investigate the difference in background/signal separation between the normal and simplified electronics configurations.

The baseline wander increased dramatically with the removal of the shaping amplifiers, to the point where it was no longer possible to extract basic event parameters such as charge and Δz from the waveforms. Therefore, a digital high-pass filter with the same time constant as the removed hardware high-pass filter (110μs) was developed and implemented in software, to remove low-frequency oscillations and allow further analysis to proceed. The expression for the filter is given in Equation 6.1, where τ_f is the filter time constant (100 μs), τ_s is the sampling rate (1 MS/s), n is the sample index, and x and y are the waveform amplitudes before and after filtering, respectively.

$$y_n = \frac{2\tau_f - \tau_s}{2\tau_f + \tau_s}y_{n-1} + \frac{2\tau_f}{2\tau_f + \tau_s}(x_n - x_{n-1}) \tag{6.1}$$
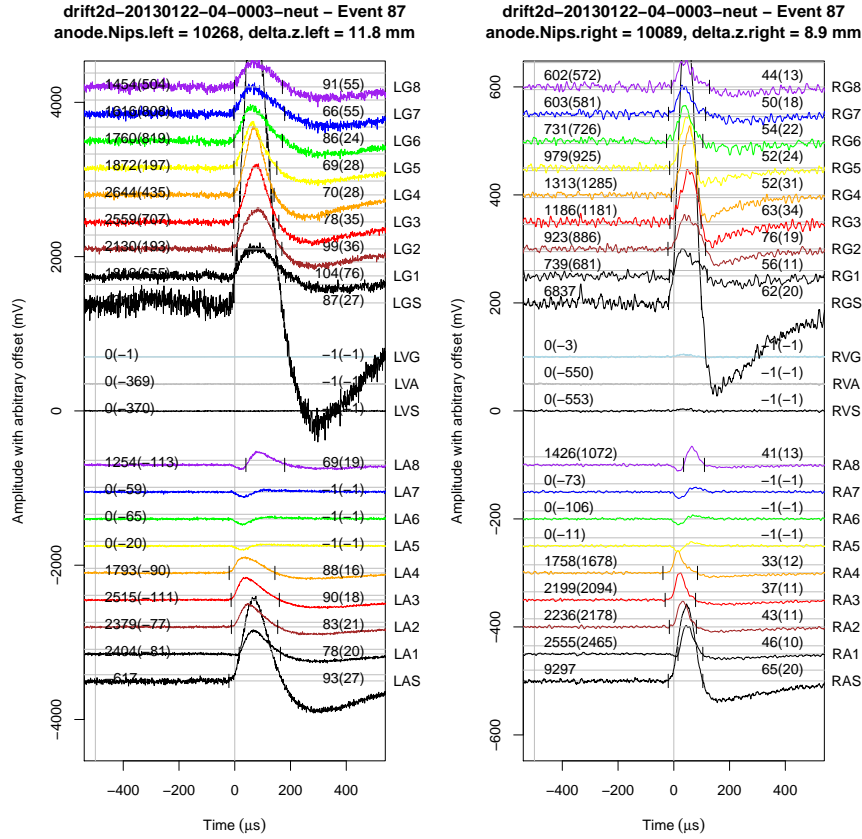
Figure 6.4: Example event display from a one-sided run (left = simplified electronics, right = normal electronics). Due to the increased size of the signals from the simplified electronics, the ordinate of the left hand panel has been rescaled.

The effect of the filter can be seen in Figure 6.1. The replacement of the filter was necessary in order to extract meaningful event parameters from the waveforms.

6.1.2   Signal-to-Noise Ratio and ^{55}Fe Calibration

The signal-to-noise ratio (S/N) was measured separately for the normal and simplified electronics, in order to determine appropriate analysis thresholds for the two different configurations. The noise was determined by fitting a Gaussian curve to the distribution of waveform sample amplitudes outside the region of interest. Figure 6.5 shows Gaussian fits to the noise on the anode and grid. The 1σ noise value increased from

135

1.08 to 6.96 ADC counts (×6.4), when moving from the normal to simplified electronics scheme. A similar noise enhancement factor of 7.2 was observed on the grid.

The change in signal size was measured using the integrated charge of events from ^{55}Fe calibrations. Figures 6.6a and 6.6b show the anode and grid ^{55}Fe peaks for the normal and simplified electronics schemes. The factor of 12.5 increase in mean signal amplitude implied by the ratio of the central values of the two Gaussian fits on the anode gives an estimate of the increase in signal strength with the simplified electronics. It is assumed that the ratio measured at the low energy of the ^{55}Fe calibration point (5.9 keV - see Section 4.2) remains constant up to the recoil energies of interest ($\sim 50 - 350$ keV).
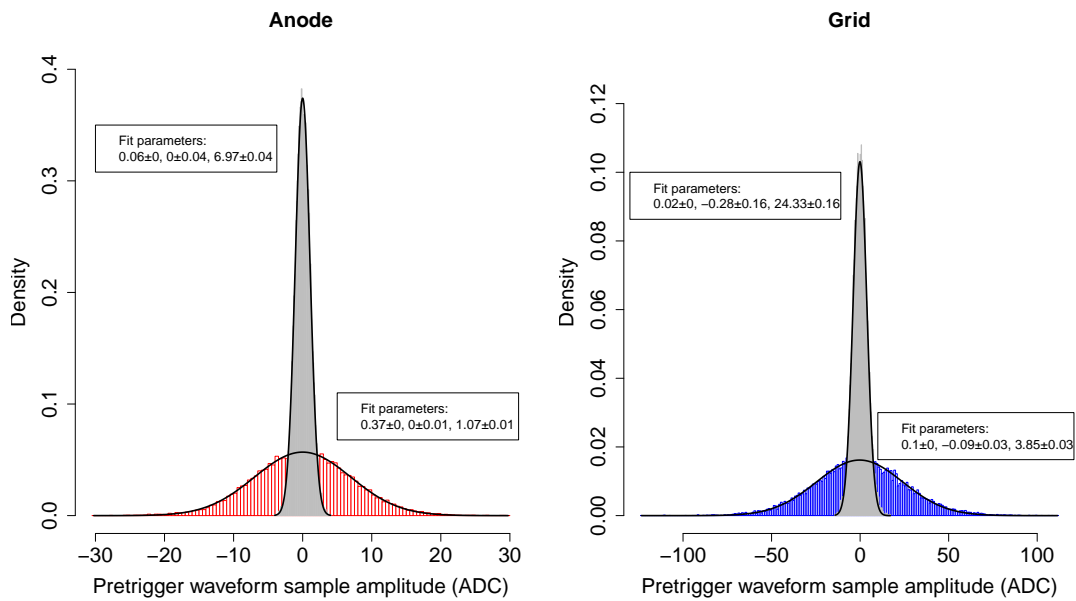
Figure 6.5: Gaussian fit to the anode and grid pre-trigger noise for the normal (grey) and simplified (red/blue) electronics schemes.

Combining the noise and signal measurements for the normal and simplified electronics yields an anode signal-to-noise improvement factor of $\frac{12.5}{6.4} = 1.9$. This is a direct consequence of the fact that the pulse shape from the simplified scheme is more unipolar, which results in a much smaller fraction of the pulse area being negative in the region of interest (see Figure 6.1).

(a) Anode   (b) Grid
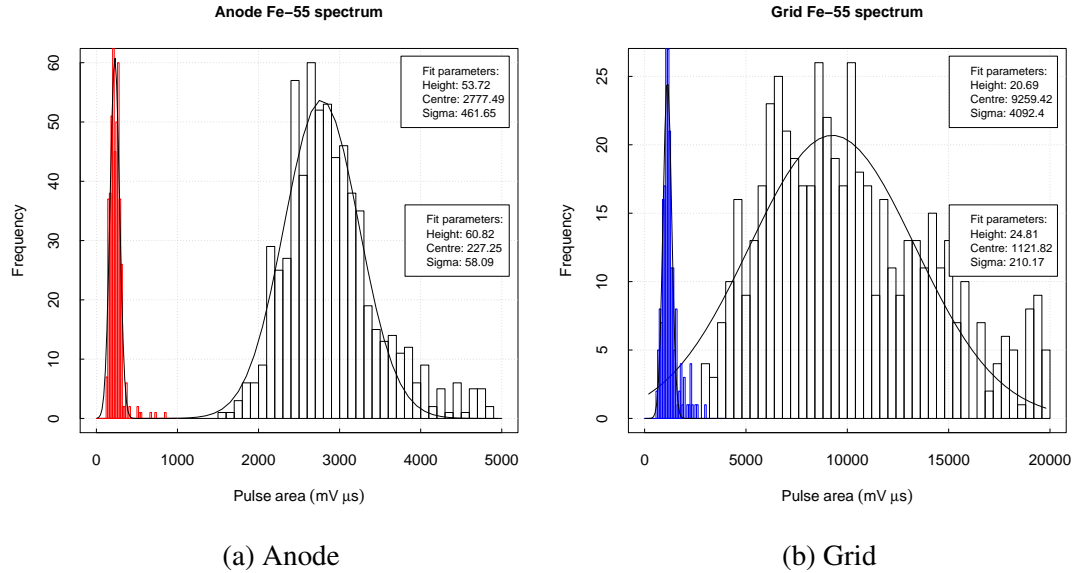
Figure 6.6: ^{55}Fe amplitude distributions from a single file, read out through the normal (coloured) and simplified (black) electronics.

Naively, the grid and anode thresholds would be increased by the same factor (×6.4) for the simplified electronics to maintain a similar effective analysis threshold. However, implicit in this is the assumption that the pulse area is proportional to its height. The shaper ensures that this assumption is valid for the normal electronics, however due to broadening of the pulses in the absence of the shaper, the same cannot be said for the simplified electronics. A pulse with a fixed area has a higher peak amplitude when read out through the normal electronics, and consequently it was necessary to limit the threshold increase to a factor of four, to ensure that low-energy events were not lost. Later analysis stages removed spurious low-energy background events that exceeded this threshold; the only downside was a slight increase in data processing time.

The MWPC was calibrated as described in Section 4.2, but the channels read out through the simplified electronics had their calibration threshold raised by a factor of 4 to account for the increase in noise.

137

Run	Livetime (days)	Number of events	Rate (events/day)
x neutrons	0.633	742	1172
z neutrons	0.958	709	740
y neutrons	0.813	920	1132
background	3.7	254	69

Table 6.2: Event rates after all cuts.

6.2 Event selection

The stage 1 and 2 cuts described in Chapter 4 were used to select nuclear recoil candidate events, with the exception of the 'single side' cut (2.1), which could not be applied since only one side of the detector was read out, making it impossible to tag and reject events with ionisation appearing on the opposite side of the detector. Under normal running conditions, this procedure removes $8 \pm 1\%$ of background events. Multiplying this number by the total number of events passing the 'tee' cuts, it was estimated that 214 ± 24 'opposite side' events contaminated the dataset. The percentage of missed tags was calculated by applying the 'tee' cuts to normal data, and counting events that would have been removed had the opposite side been available for tagging the associated α particle.

The plots in Figure 6.7 show histograms of background and neutron data for each of the stage 3 cut variables, Gaussian fits to the neutron signal, and the resulting three, two or 1.5 sigma cut levels that were chosen to maximise signal and minimise background. The histogram variables are all calculated from the waveforms read out through the normal electronics.

After applying the stage 1, 2 and 3 cuts to the total dataset comprising three neutron runs and one background run, a population of 2625 candidate recoil events remained. The event rates after cuts for each of the runs is shown in Table 6.2. As expected, the rate during the background run is considerably lower, which confirms that DRIFT is sensitive to the injected neutrons. The event rates for the x- and y-directed runs are very similar, however the rate during the z-directed run appears to be suppressed. A likely cause of this discrepancy is the additional layer of plastic absorber present between the z-directed neutron source and the fiducial volume, in the form of the plastic MWPC strongback.
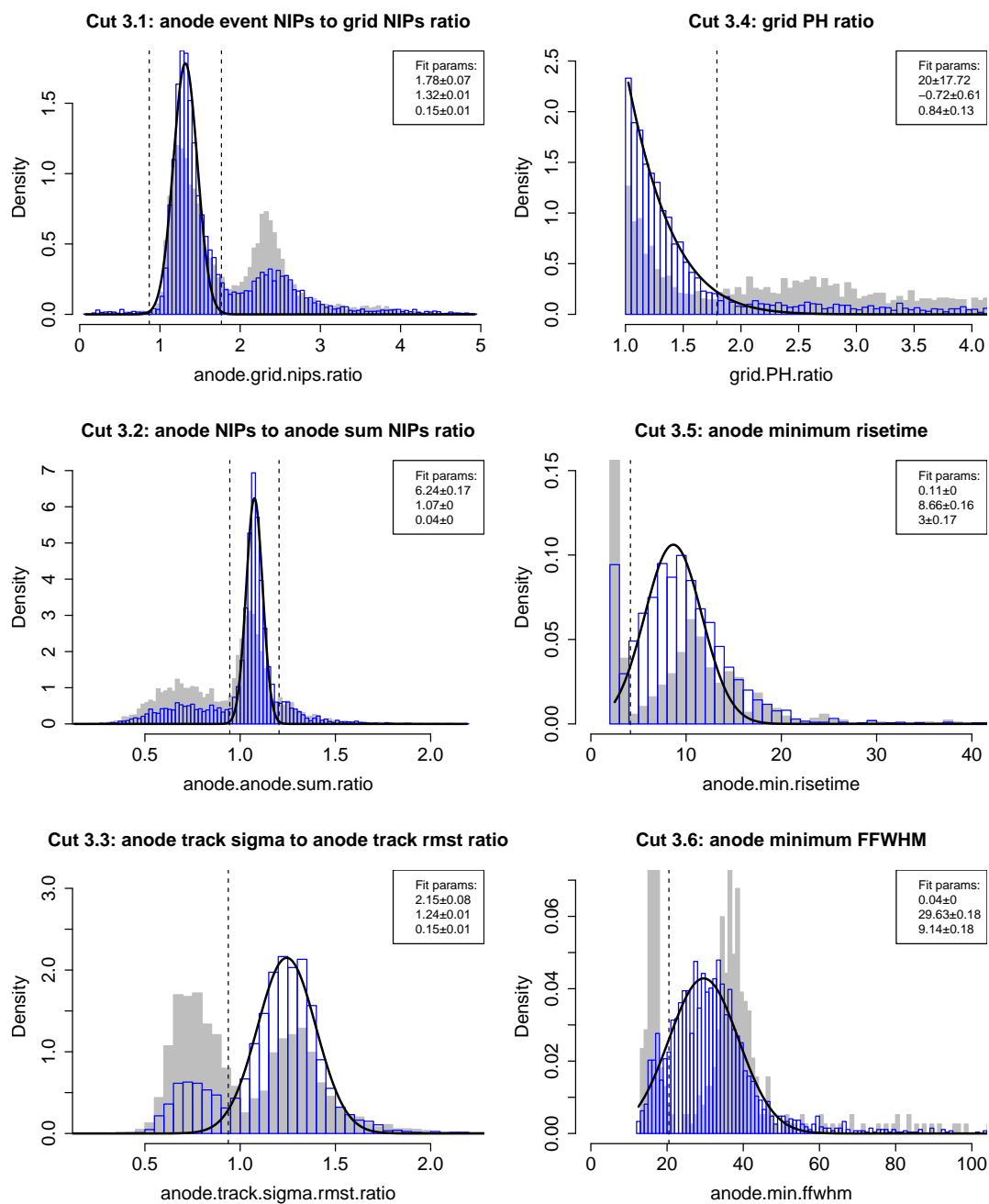
Figure 6.7: Background and neutron calibration distributions for stage 3 cut variables calculated for events recorded with the normal electronics.

6.3 Range Components

The x, y and z range components of selected events were calculated for both the normal and simplified data. Due to the nature of the readout hardware, the method for calculating the range was necessarily very different in each of the three directions. These methods are described in the following subsections.

6.3.1 *x* Range

Since electron avalanches happen in close proximity to the y-oriented anode wires, it was possible to measure the x range of an event by counting hits above a threshold on these wires. The threshold was set to 60 mV, and the x range of an event was calculated according to Equation 6.2:

$$\Delta x = 2p - 1 \pm p/2, \tag{6.2}$$

where p is the pitch of the anode wires, 2 mm. In this way, single-wire hits are assigned a range of 1 mm. The wire-counting technique for calculating Δx works equally well for both normal and simplified electronics configurations because it depends on the integrated voltage rather than the detailed pulse shape. This is not the case for Δy and Δz.

6.3.2 *z* Range

According to TPC convention, the z dimension is defined parallel with the drift direction. An event's Δz is calculated according to Equation 6.3:

$$\Delta z = (t_{max} - t_{min}) \times v_{drift}, \tag{6.3}$$

where v_{drift} is defined in Equation 5.2. The key to a good measurement of an event's Δz therefore lies in the determination of t_{min} and t_{max}.

In the normal electronics scheme, with the shaping amplifiers in place, all signals acquire a Gaussian shape with a width approximately proportional to the time extent

of the charge deposition. t_{min} and t_{max} are therefore calculated as the FWHM of the 'track' waveform, which is the sum of all lines that crossed the analysis threshold. The FWHM has been found to be less susceptible to noise than the alternative of using the baseline crossings of the track waveform to determine t_{min} and t_{max} [145]. The shaping process is designed to preserve the time extent of the input pulse. However, it has been shown that a correlation exists between the total integrated charge of a pulse and the measured Δz [172], which suggests that the shaping amplifiers are destroying some information about the time extent of events.

In the case of the simplified electronics, the shaping amplifier is not present to force all waveforms to acquire a Gaussian shape, and therefore the signal shape shown in blue in Figure 6.1a is preserved. Here, the grey waveforms represent the CR-110 preamplifier output from individual impulse charge depositions, which sum to give the pulse shape shown in dashed blue. The pulse is then filtered in software to restore the baseline, producing the shape seen in the solid orange curve. t_{min} was taken as the time of the first baseline crossing. However, doing the equivalent for the last baseline crossing for t_{max} does not make sense due to the long exponential decay of the pulse. t_{max} was instead taken to be the time of the latest anode peak.

Contributions to the measured Δz come from the following sources:

1. **True z range of the event, Δz**

2. Thermal diffusion (z-dependent)

3. Shaping time (9.4 μs)

4. Path delay (3.3 μs)

It would be useful to subtract the effect of items 2, 3 and 4 to recover the target parameter, Δz. In practise this is only possible for items 3 and 4, since the diffusion is a strong function of the unknown z position according to Equation 4.9 [149].

It has recently been shown that the addition of a small admixture of O_2 into the gas mixture can provide a means of measuring the absolute z position of events [200], and this will be discussed further in Chapter 8. In this case, subtraction of the z-dependent diffusion component of the Δz becomes possible. The 9.4 μs contribution from the shaping amplifier is the σ corresponding to its FWHM of 4 μs: with the

shaper in the electronics chain, a point-like event gains a Δz corresponding to 9.4 μs. This subtraction was not necessary for the simplified electronics data since the shaping amplifier was not present. Finally, a small time delay arises from the geometry of the MWPC field lines, which can be seen in the difference in the lengths of red ion drift lines in Figure 4.2. Ions that arrive at the grid plane (top) directly above an anode wire (bottom) take, on average, 3.3 μs less to traverse the MWPC than those that arrive directly in between two anode wires, thanks to the shorter path [149]. This effect is independent of the readout electronics, and therefore the subtraction was applied to both the normal and simplified electronics data.

6.3.3   *y* Range

The y range (Δy) of events cannot be computed by counting grid wires in analogy with Δx, because the separation of the anode and grid planes is large compared with the pitch of the wires, and therefore the signals induced on the grid wires are, at least initially, all of similar magnitude. This is in contrast with the anode, where the charge induced on wires around which an avalanche has taken place is considerably larger than that induced on more distant anode wires. Instead, the Δy of events was calculated based on the movement of the charge barycentre between t_{min} and t_{max}^y, which was calculated using circular statistics in a similar manner to Muna [172]. The time difference between t_{min} and t_{max}^y was typically shorter for data recorded with the normal electronics due to the presence of the shaper. Notwithstanding, the following method was applies to either electronics scheme.

Circular statistics can be used to characterise data which is cyclical in nature, such as a compass bearing, or a periodic detector readout. In the case of DRIFT, the data is comprised of a set of charge measurements, 1 μs apart, on a set of 8 readout channels which are themselves comprised of wires 2 mm apart, grouped with a periodicity of 16 mm. The data at a given microsecond can be displayed as in Figure 6.8, where the positions of the bars represents the channel positions in one detector period, relative to some arbitrary zero, and the heights represent the charge on the channels at a given μs, normalised by the total charge at the μs in question such that the heights of the bars always sum to unity ($\sum_{j=1}^{8} w_j = 1$). The red line denotes the mean circular position,

which is taken as the position of the charge barycentre. The movement of the mean position between t_{min} and t_{max}^y gives a measurement of the y range of the track, Δy.

(a) Approximately isotropic.

(b) Peaked.
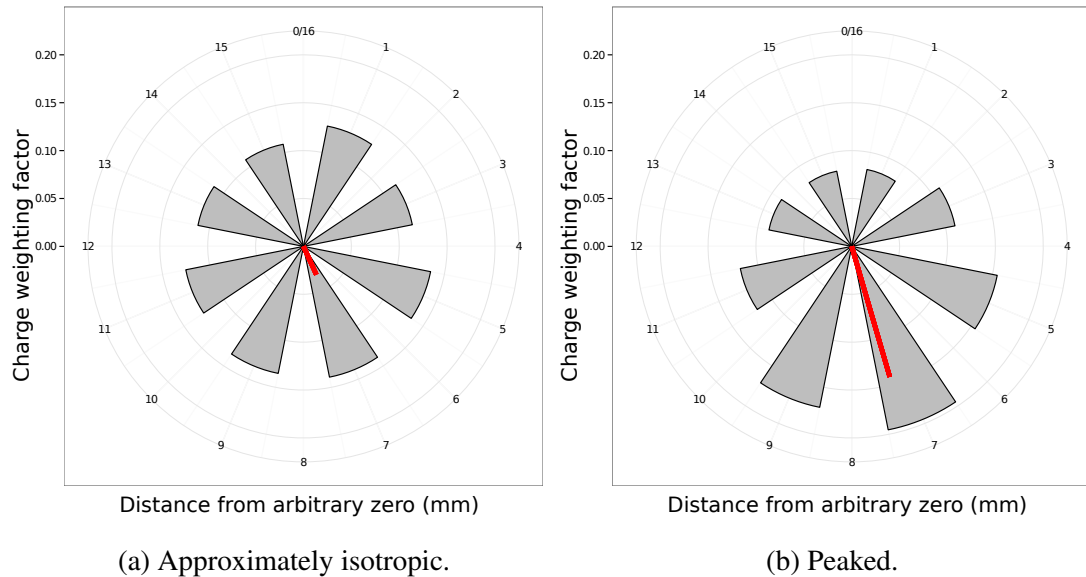
Figure 6.8: Circular bar charts showing charge barycentre at two different μs samples. Bar positions represent the channel position in one detector period, and heights represent the normalised charge weighting factor w_i at the μs in question (see text). The red line shows the position of the charge barycentre, and its length is proportional to the magnitude of the mean vector, which is a measure of the data's 'peakedness'.

In fact, the process is complicated slightly by the fact that recoil tracks may cross from channel 8 to channel 1, or vice versa. Therefore, before the circular mean calculations are applied, the track is 'centred' such that the position at the voltage-weighted mean time is at 8 mm, halfway though one period of the readout. This is permissible because the parameter of interest is Δy rather than absolute y position (which is not recorded by the detector anyway), and ensures that the track is contained within one 16 mm period without 'wrapping around'. Wrapping may still occur for long tracks, however SRIM simulations show that at the recoil energies of interest, tracks will be fully contained in one period (Figure 6.9).
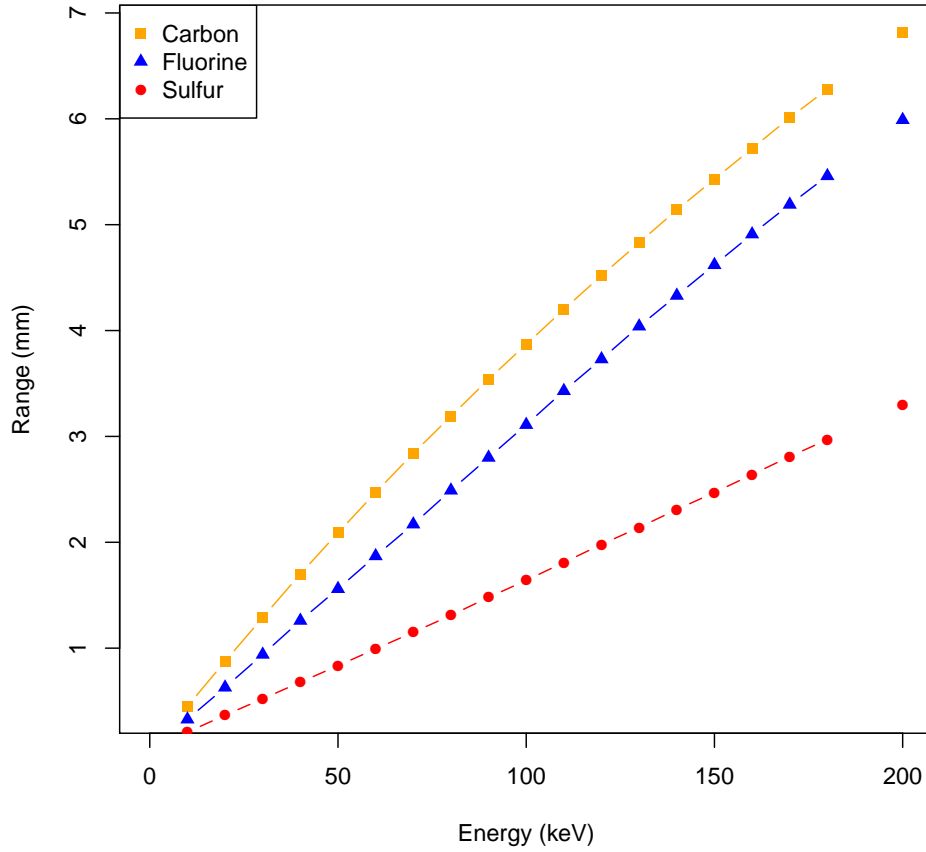
Figure 6.9: Range as a function of energy for C, F and S recoils in a 30:10 torr mixture of CS_2:CF_4. Calculated using SRIM [185].

In order to calculate the position of the charge barycentre at a given μs, the charge-weighted average sin and cos positions were first calculated according to Equations 6.4 and 6.5.

$$\overline{X} = \frac{\sum\limits_{j=1}^{n} w_j \cos x_j}{n},$$ (6.4)

$$\overline{Y} = \frac{\sum\limits_{j=1}^{n} w_j \sin x_j}{n},$$ (6.5)

where w_j and x_j are the charge weighting factor and the fraction through one period of the jth channel, respectively, and n is the number of channels (eight). The magnitude of the mean vector (red line in Figure 6.8) can then be calculated as follows:

$$r = \sqrt{\left(\overline{X}^2 + \overline{Y}^2\right)}. \tag{6.6}$$

The target is the mean angle $\overline{\theta}$, which satisfies

$$\cos\overline{\theta} = \frac{\overline{X}}{r}, \tag{6.7}$$

$$\sin\overline{\theta} = \frac{\overline{Y}}{r}, \tag{6.8}$$

the solutions of which depend on the quadrant of the circle, and are as follows:

$$\overline{\theta} = \begin{cases} \arctan\left(\frac{\overline{Y}}{\overline{X}}\right) & \overline{X} > 0 \text{ and } \overline{Y} > 0 \\ \arctan\left(\frac{\overline{Y}}{\overline{X}}\right) + \pi & \overline{X} < 0 \\ \arctan\left(\frac{\overline{Y}}{\overline{X}}\right) + 2\pi & \overline{X} > 0 \text{ and } \overline{Y} < 0. \end{cases} \tag{6.9}$$

The uncertainty on this measured angle, ϵ_θ, is given by:

$$\epsilon_\theta = \frac{\sqrt{-2\log r}}{n}. \tag{6.10}$$

Armed with $\overline{\theta}$, the y position can be calculated according to Equation 6.11:

$$y = \frac{\overline{\theta} n p_g}{2\pi}, \tag{6.11}$$

where p_g is the pitch of the grid wires (2 mm). This y position is calculated for each µs, but any µs in which one or more of the signals fell below zero was not assigned a charge barycentre position, which removed many of the points outside the ROI. Finally, Δy was calculated as the range of y between t_{min} and t_{max}^y. An example for an event of moderate energy, read out through the simplified electronics, is shown in Figure 6.10a alongside a plot of the mean vector magnitude as a function of time in the region of the event (Figure 6.10b), which was used to define t_{max}^y.

t_{min} was defined in the 'z range' section above, however it was found that using the t_{max} defined there caused the late-time portion of the track to be cut off, leading to an underestimate of Δy. An alternative approach was developed based upon the change in the mean vector magnitude as a function of time, which for all selected events was found to exhibit a shape similar to that in Figure 6.10b. By setting t_{max}^y as the time at which r reaches its minimum following its maximum in the region of the charge induction (less 5 μs), it was possible to include all y points right up to the messy late-time event tail that can be seen in Figure 6.10a. This tail is caused by grid lines undershooting and dropping below zero, making the charge barycentre movement at these times unphysical.

(a) y position.

(b) Mean vector magnitude.
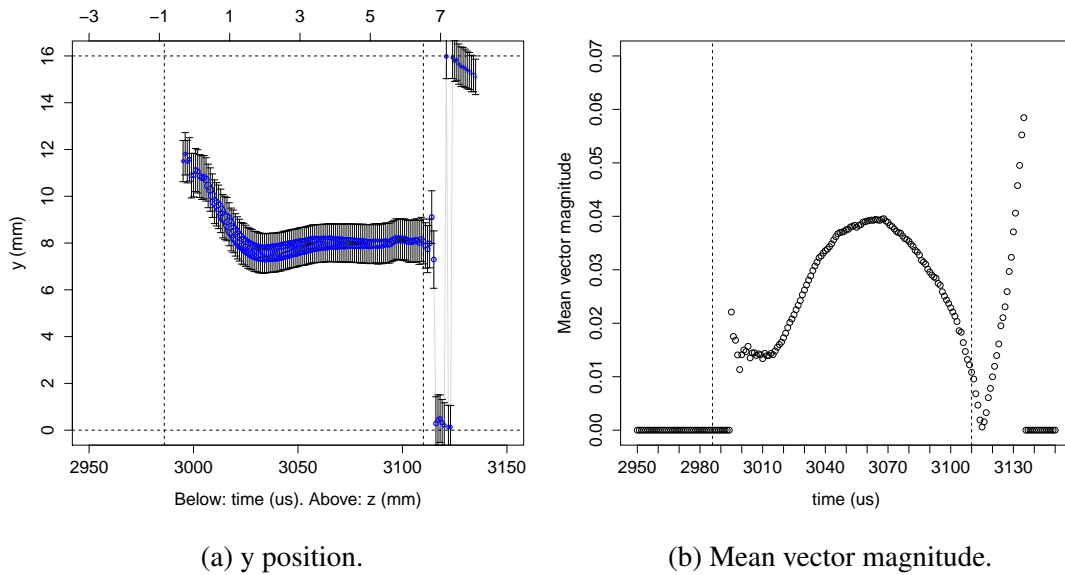
Figure 6.10: Left: y position as a function of time for a 3400 NIP candidate neutron recoil event, measured on the grid. Dashed vertical lines represent t_{min} and t_{max}^y, whilst the blue circles are proportional in radius to the induced charge on the anode 38 μs earlier. This time offset is a consequence of the finite drift time of positive ions within the MWPC. Statistical error bars were calculated using Equation 6.10. Right: Change in mean vector magnitude with time. Again, t_{min} and t_{max}^y appear as dashed vertical lines. Points at zero near the start and end of the plot region had at least one grid channel with negative charge (see text).

6.4 Quantifying the Directional Signature

6.4.1 Range Component Distributions

Having applied the methods of Section 6.3 to the events in Table 6.2, the sensitivity of DRIFT to the position of a ^{252}Cf neutron source was investigated. Events with relatively high energy ($5000 - 10000$ NIPs, or $234 - 437$ keV) were selected, to maximise the contribution of the true range, minimising the effects of diffusion. The range component distributions of selected events were plotted, split by neutron source orientation, giving three panels for the three different range components (x, y, z), each with three overlaid histograms representing the x, y and z neutron source orientations. The varying position of the source simulates the diurnally varying position of the WIMP wind vector, and it was expected that runs in which the neutron source was aligned parallel to a given dimension would yield a larger measurement of the range component than the other two dimensions. The range component distributions are shown in Figure 6.11. Data from runs where the source was parallel to the range component in question appear as block colours, whereas the other two dimensions are shown in outline only.

The directional signature appears strongest in the Δx histograms (top row), where it is clear that the distribution is shifted to higher Δx for the x-directed neutron run, for both electronics schemes. The shift is also visible in the Δz distributions, showing that DRIFT has directional sensitivity in this dimension also. The Δy histograms show an unexpected second peak at high Δy. Scanning a sample of these events reveals that this was caused by a problem with the track reconstruction algorithm described in Section 6.3. Many iterations of the algorithm were tested and, although the one presented here struggles with long events, it is on the whole robust. Therefore, rather than modify the Δy calculation further, a cut of $\Delta y < 12$ mm was placed on the data. Very few true WIMP recoil events are expected with a range greater than 12 mm. There is little evidence of a shifted peak for the y-directed neutron data in the Δy data below 12 mm, suggesting a lack of Δy sensitivity. In order to quantify the directional sensitivity, a summary statistic for each of the histograms was calculated according to the procedure described in the following subsection.
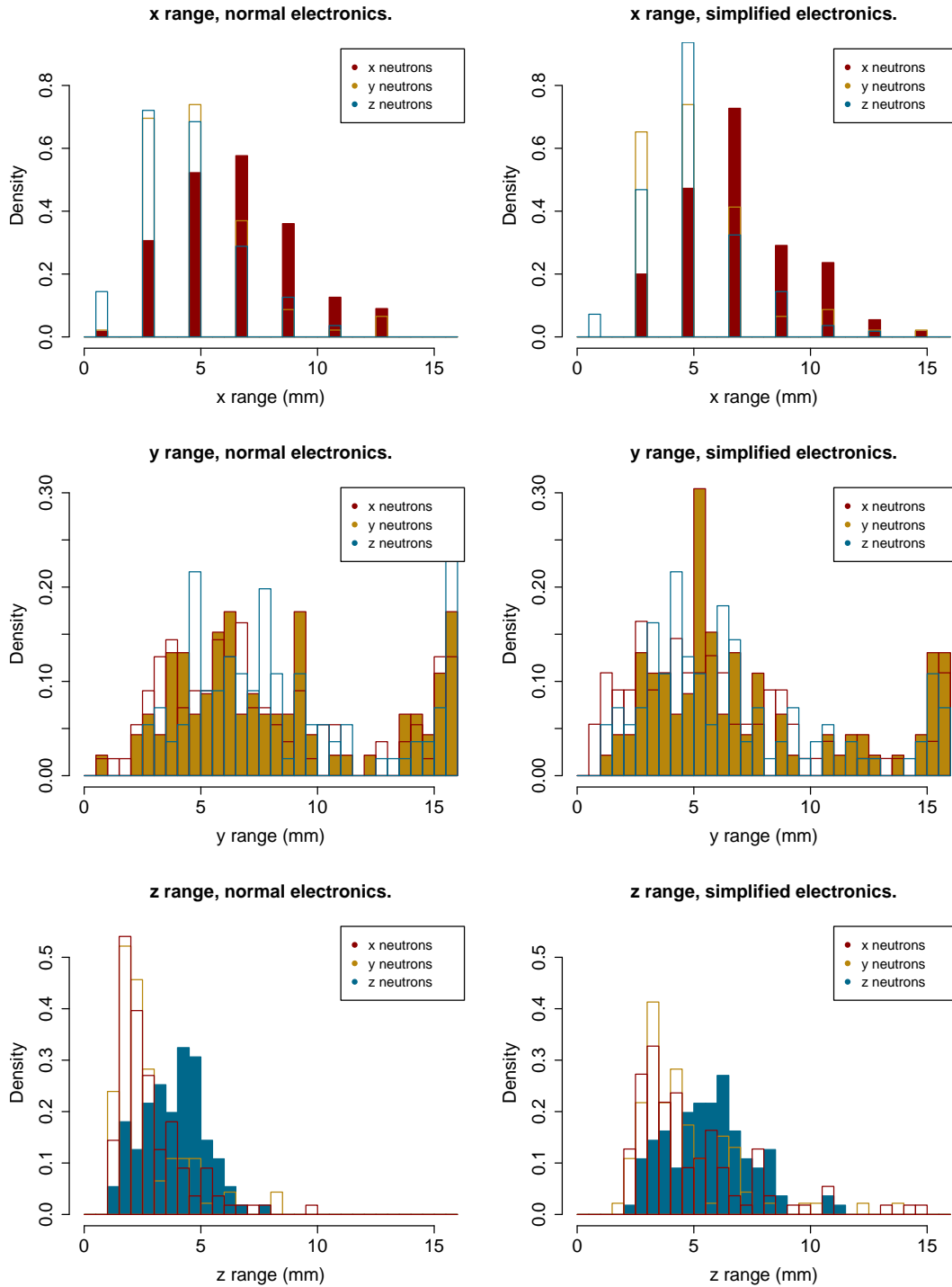
Figure 6.11: Range component distributions for the x, y and z-directed neutron runs. Left column: normal electronics. Right column: simplified electronics.

6.4.2 Summary Statistics

The increase in the mean of a given range component when the neutron source is moved from perpendicular to parallel to it gives a measurement of DRIFT's directional sensitivity in that dimension. In order to quantify this directional sensitivity for a given range component, the means of data with the neutron source is each of the orientations was calculated. A constant equal to the mean of the data taken with the neutron source perpendicular to the range component in question was then subtracted. These differences in means are plotted in Figure 6.12, grouped by range component. The points for which the range component and the neutron source orientation were aligned were expected to appear above zero, showing an enhancement due to the source's orientation, whilst the points for which the source orientation was perpendicular to the measured range component should lie on the zero line, showing no enhancement. A larger separation between matched and unmatched points indicates better directional sensitivity.

The apparent superiority of the Δx directional signature is borne out by Figure 6.12. The separation between the mean Δx in the x-directed neutron run, and the two orthogonal directions was larger than the other two range components, at 2.2 ± 0.3 mm (1.9±0.3 mm) for the normal (simplified) electronics. The fact that there was very little change in the directional signature when moving to the simplified electronics scheme suggests that the Δx measurement is limited by the 2 mm wire spacing, and not by the electronics. The mean Δx in the y- and z-directed neutron runs appear around zero, by construction.

The z directionality, as defined here, is again similar for the normal and reduced electronics, albeit with a slightly weaker signature than for the x dimension. A closer look at the Δz histograms on the bottom row of Figure 6.11 reveals that, although the difference in the mean of the parallel (z) and perpendicular (x,y) neutron runs was similar in both cases, the simplified electronics appears to systematically measure a slightly higher range, producing distributions that are more in keeping with those of the other two range components. Removal of systematics like this is crucial for a future fully-directional analysis.
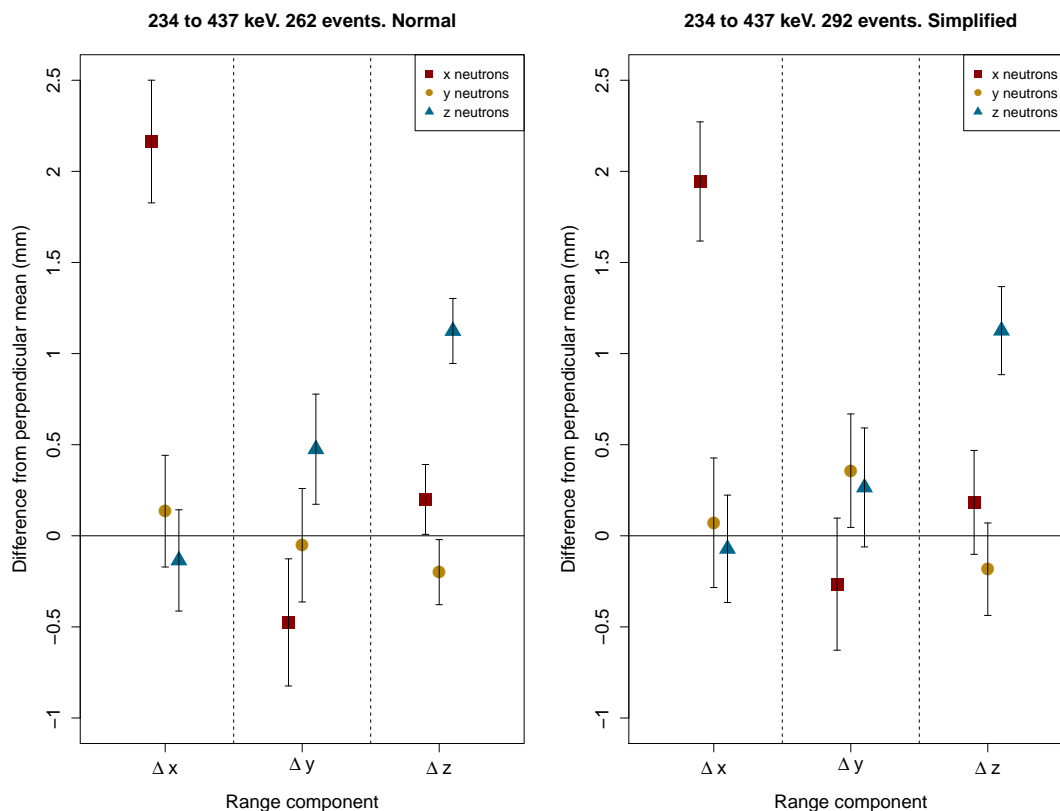
Figure 6.12: Difference between the mean of a given range component with the neutron source oriented in a given direction, and the mean of the same range component with the neutron source oriented in either of the perpendicular directions. All 9 permutations of directions are shown for both the normal (left) and reduced (right) electronics schemes.

The Δy distributions show no sign of *y* directional sensitivity with the normal electronics, which is somewhat at odds with the conclusion of Burgos et al. [145], where marginal *y*-sensitivity was observed. However, the neutron source used here had a significantly lower activity, which motivated the choice of relatively short source-vessel separation (50 cm compared with 250 cm in the previous work). Moving the source much further away would have necessitated unreasonably long run times to build the equivalent statistics, therefore the degree of collimation was instead reduced, giving a mean angular spread of $\sim 40°$ instead of the $10°$ achieved by Burgos et al. [145]. The situation is marginally improved with the simplified electronics, where the *y*-directed

150

neutron run produced the highest mean range, however the mean y ranges in each of the x-, y- and z-directed neutron runs agree within uncertainties.

6.4.3 Energy Dependence

It was hypothesised that a difference between the two electronics configurations may appear at lower energies closer to those of interest for a dark matter search, due to improved S/N of the simplified electronics scheme. Therefore, the dependence of the directional signature on energy was investigated. The direction sensitivity was redefined as:

$$d_{zx} = \frac{\left(\frac{\Delta z}{\Delta x}\right)_z - \left(\frac{\Delta z}{\Delta x}\right)_x}{\overline{\left(\frac{\Delta z}{\Delta x}\right)}} \times 100, \tag{6.12}$$

and equivalent for permutations of Δx, Δy and Δz, to give a measure of directionality in three orthogonal planes (z-x, x-y and y-z) and allow a comparison with previous work. Based on Figures 6.11 and 6.12, as well as previous measurements [145], the z-x plane was expected to yield the strongest signature of directionality. The subscripts in the numerator refer to the orientation of the neutron source, and the mean in the denominator is calculated for all events in the relevant source orientation runs (x and z runs in Equation 6.12). Therefore, d is a difference between two range component ratios as measured with the neutron source in the corresponding orientations, expressed as a percentage of the mean of this ratio for all events in the two neutron source orientation runs. A higher percentage difference corresponds to a stronger directional signature. The d parameter was calculated for equivalent sulphur recoil energies between 10 and 350 keV, for all three permutations of the range component parameters, and the results appear in Figures 6.13, 6.14 and 6.15.

Figure 6.13 shows that the directional signature in the z-x plane falls as the sulphur recoil equivalent energy decreases, reaching zero (no directional sensitivity) at around 50 keV for both datasets. The simplified electronics preserve the signature marginally better in the low-energy bins, but the normal electronics perform better at energies above ~ 130 keV. The data are in agreement with previous measurements for the low-energy bins, but both sets of electronics appear to perform better than the 2009 apparatus used by Burgos et al. [145] at energies above 130 keV.

The same reduction in sensitivity with decreasing energy is seen in the x-y d param-
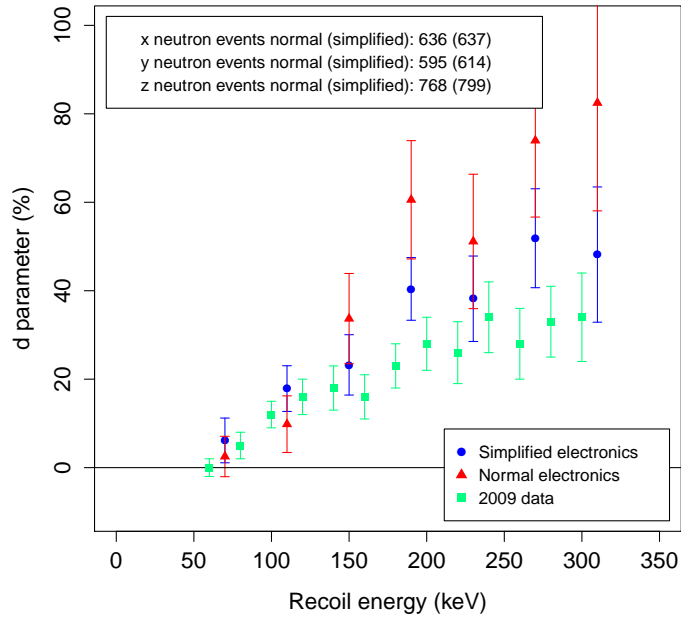
Figure 6.13: Directionality parameter d_{zx} as a function of energy.
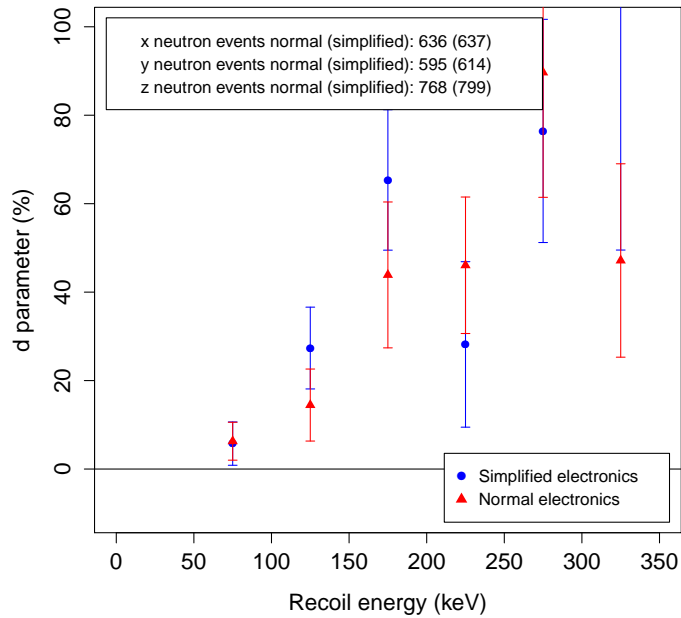
Figure 6.14: Directional parameter d_{xy} as a function of energy.

eter, which also falls to zero at around 50 keV. There is not much to choose between the normal and simplified electronics for the x-y directional sensitivity, however the large uncertainties make the data difficult to interpret.
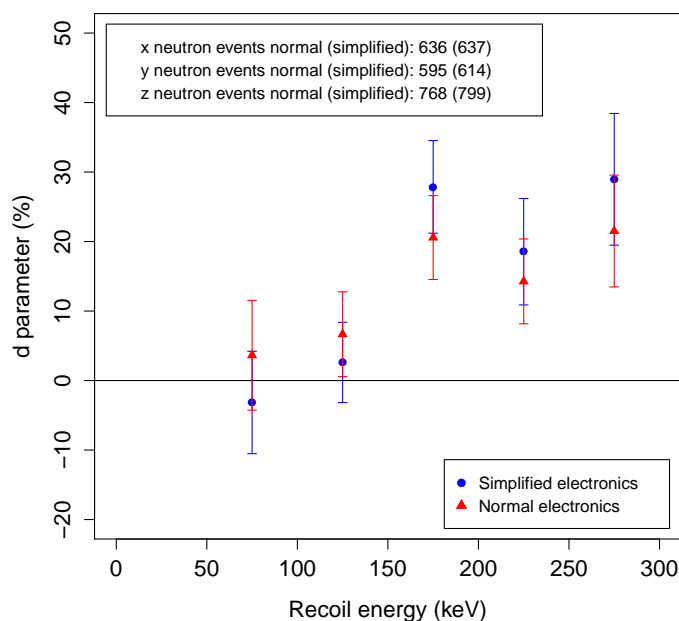
Figure 6.15: Directional parameter d_{yz} as a function of energy.

The *y-z d* parameter exhibits the weakest overall sensitivity, again with little difference between the two electronics schemes. There is a hint that the simplified scheme outperforms the normal at the lowest energies which, if true, would support the hypothesis that directional information is being destroyed by the shaping electronics in the normal configuration.

Care must be taken when comparing the absolute percentage differences between plots, since a systematic offset or multiplicative factor in the calculation of one of the range components can cause the percentage difference to be over/underestimated.

6.5   Separating Signal from Background

The DRIFT collaboration has previously demonstrated that the parameter 'R2' (the *x-z* projected track range - Equation 6.13) exhibits some ability to discriminate between background and neutron calibration data [201].

$$R2 = \sqrt{\Delta x^2 + \Delta z^2} \tag{6.13}$$

Background events from the cathode tend to exhibit a higher R2 than signal events distributed more evenly throughout the fiducial volume due to the larger amount of diffusion they suffer as they drift the full 50 cm from the cathode to the anode. This is confirmed for this data by Figure 6.16, which shows the NIPs vs R2 distributions for the two electronics schemes, as well as 6.17 and 6.18, which are y-axis projections of these plots divided into three large energy bins as follows:
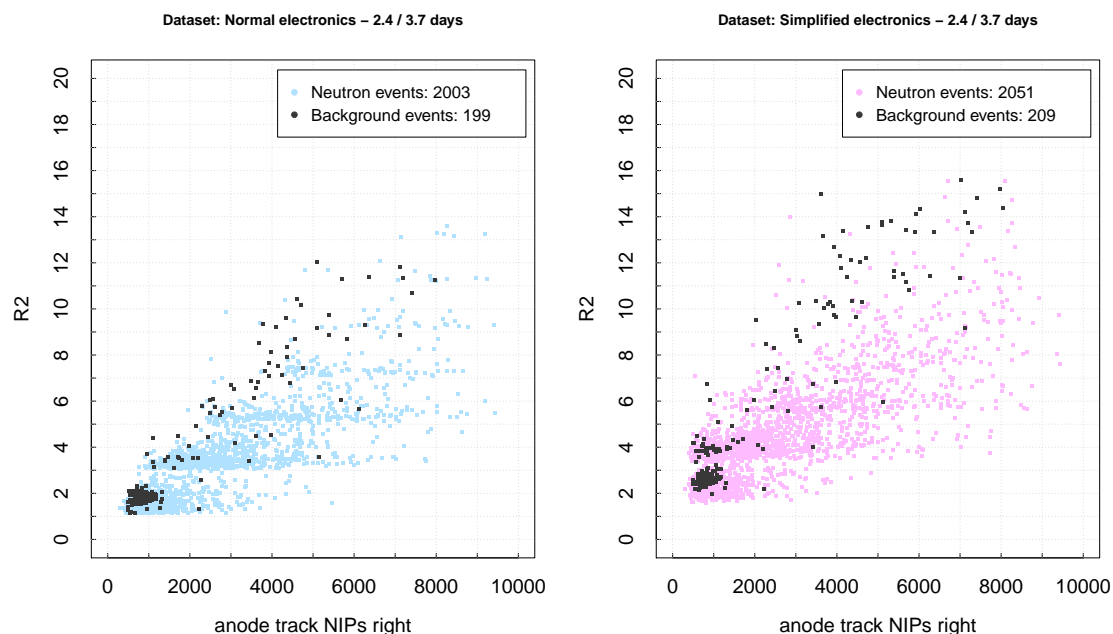
Figure 6.16: R2 vs NIPs for the normal (left) and simplified (right) electronics schemes to compare background / signal discrimination.

Figure 6.17: R2 distributions, separated into three NIPs regions. Normal electronics.

0 – 1500 NIPs (0 – 66 keV). This low-energy bin contains a large number of recoils events from neutron interactions, as well as background contamination from radioisotopes on/in the thin-film cathode or MWPC wires.

1500 – 3000 NIPs (66 – 115 keV). This moderate energy bin contains a smaller fraction of contamination events, and mostly neutron recoils.

>3000 NIPs (>115 keV). This high energy bin contains mostly neutron recoils and a few background events.

The banded structure of Figures 6.16, 6.17 and 6.18 is a consequence of the fact that Δx can only take discrete values equal to the anode wire separation. The background population is made up of the following classes of events:

Figure 6.18: R2 distributions, separated into three NIPs regions. Simplified electronics.

- 'True' RPRs from the central cathode.

- 'Untagged' RPRs from the central cathode that would have been removed had the detector been operating in its usual, two-sided configuration.

- Recoils associated with radioactive species in the cathode material itself.

- RPRs from negatively charged radon progeny plated out on the MWPC wires.

The high energy, low range background events that overlap the neutron recoil distributions in the $3000 - 10000$ NIPs bins likely originate on the MWPC, since an ionisation track drifting from the cathode would be expected to exhibit a larger range due to diffusion.

156

It was expected that the full 3D track range, R3, should provide an improved level of background/signal discrimination. Figure 6.19 shows the R3–NIPs distributions for the normal and simplified electronics schemes, whilst Figures 6.20 and 6.21 show R3 distributions, which are the *y*-projections of Figure 6.19 in the three energy bins, plus the total. A quantitative measurement of the discrimination is developed in Section 6.5.1.
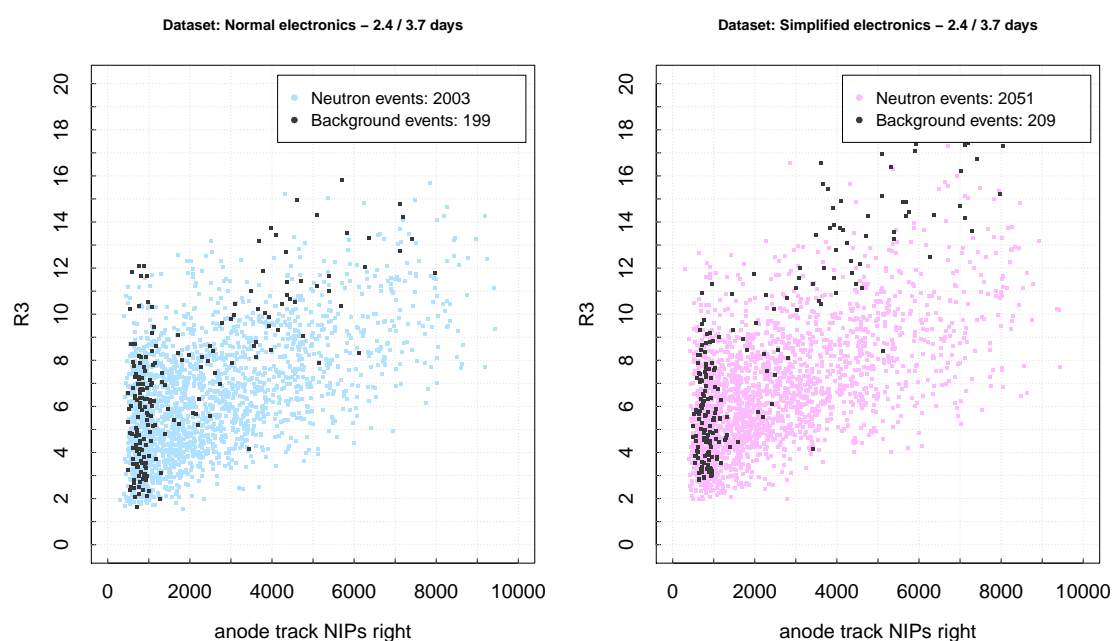
Figure 6.19: R3 vs NIPs for the normal (left) and simplified (right) data to compare background / signal discrimination.

6.5.1 Receiver Operating Characteristic Analysis

Receiver Operating Characteristic (ROC) analysis was used to quantify the degree to which signal and background events were separated in R2 and R3. The technique is designed to evaluate the quality of a binary classifier by varying the threshold at which the classifier switches from 'true' to 'false'. In this case, the data are two random distributions in R3 or R2: neutron calibration and background data, and the threshold is a cut value, above which events are assumed to come from the background population,
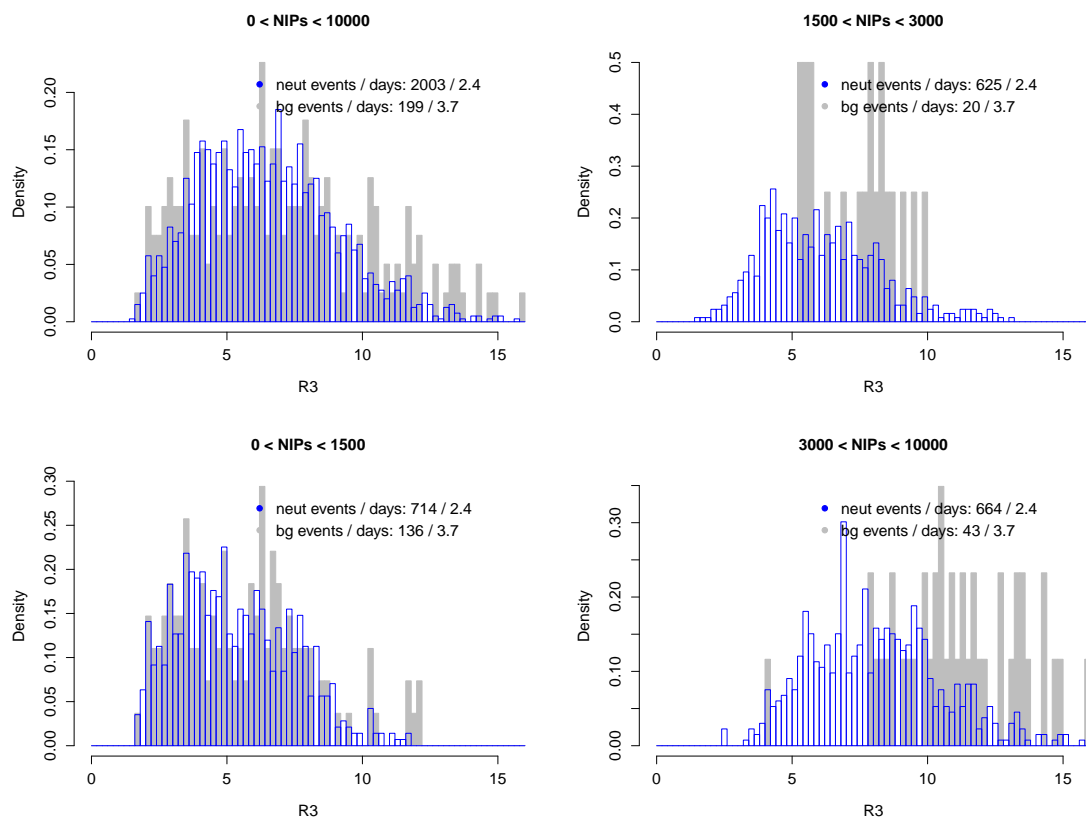
Figure 6.20: R3 background and signal distributions for the normal electronics, binned in energy.

and below which signal is assumed. The classifier is then 'true' or 'false' for a given event, depending on whether or not it passed the R3 (or R2) cut. The probability P(TP) of obtaining a 'true positive', that is, a randomly chosen event from the signal dataset passing the cut with value c_j, is given by

$$P(TP) = \frac{\sum_{i=1}^{n^{sig}} R3_i^{sig} > c_j}{n^{sig}}, \tag{6.14}$$

where n^{sig} is the total number of events in the signal dataset, and c_j is one of a discrete set of cut values spanning the entire range of R3 (or R2), for which this calculation will be repeated. The equivalent probability P(FP) of obtaining a 'false positive' can
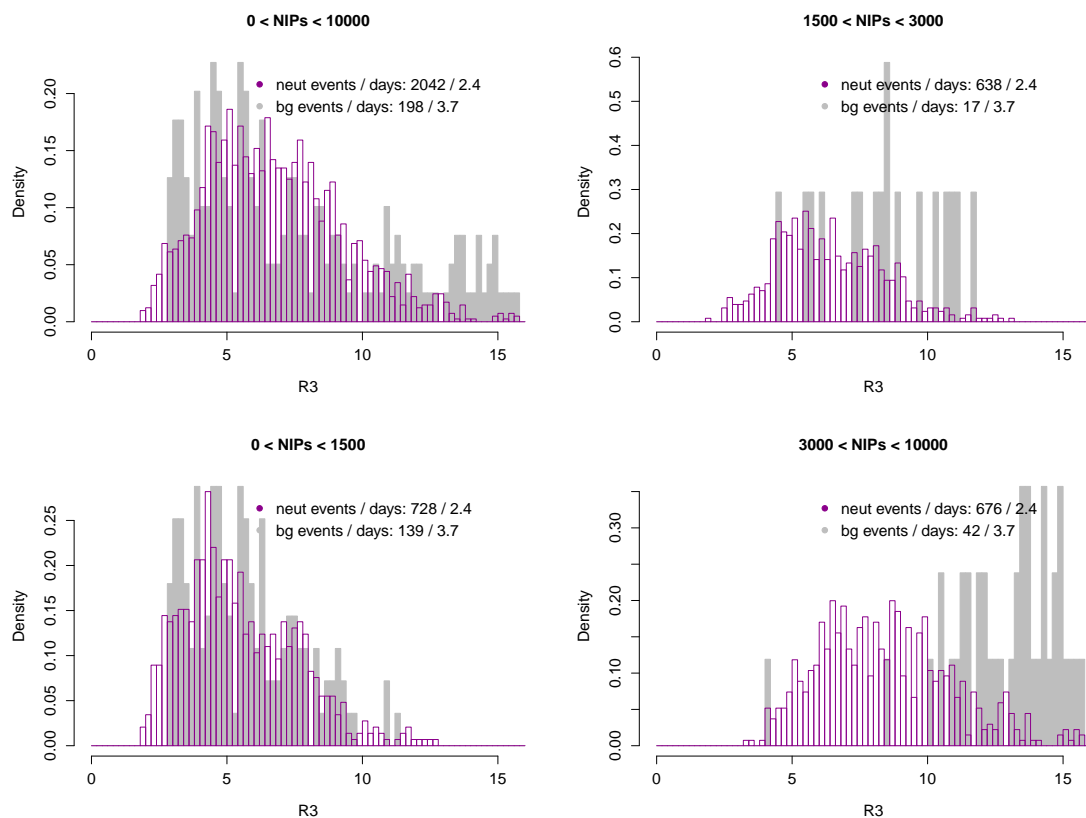
Figure 6.21: R3 background and signal distributions for the simplified electronics, binned in energy.

be calculated by applying the same formula to the background dataset:

$$P(FP) = \frac{\sum\limits_{i=1}^{n^{bg}} R3_i^{bg} > c_j}{n^{bg}}. \tag{6.15}$$

The above quantities were calculated for each of the c_j cut values, and plotted against each other to yield the ROC curves for R2 and R3 shown in Figures 6.22 and 6.23. The curves depict the tradeoff between P(TP) and P(FP), with points above the diagonal showing a degree of discrimination between signal and background, and points on the diagonal showing no discrimination. Points below the diagonal indicate that for that particular value of c_j, the probability of obtaining a false positive (passing a random

159

event from the background dataset) is actually higher than that of obtaining a true positive (passing a random event from the signal dataset), otherwise known as 'negative discrimination'. Constructing a cut which aims to select signal events *below* a certain value has specified the direction of the discrimination, and therefore points below the diagonal 'no discrimination' line were not expected. Finally, the area under the curve yields the 'integrated discrimination', which ranges from 1 (perfect discrimination) to 0.5 (no discrimination). This 'A' statistic was used to compare the different energy bins for a given set of electronics, and also to compare the normal and simplified electronics schemes.

(a) Normal electronics   (b) Simplified electronics
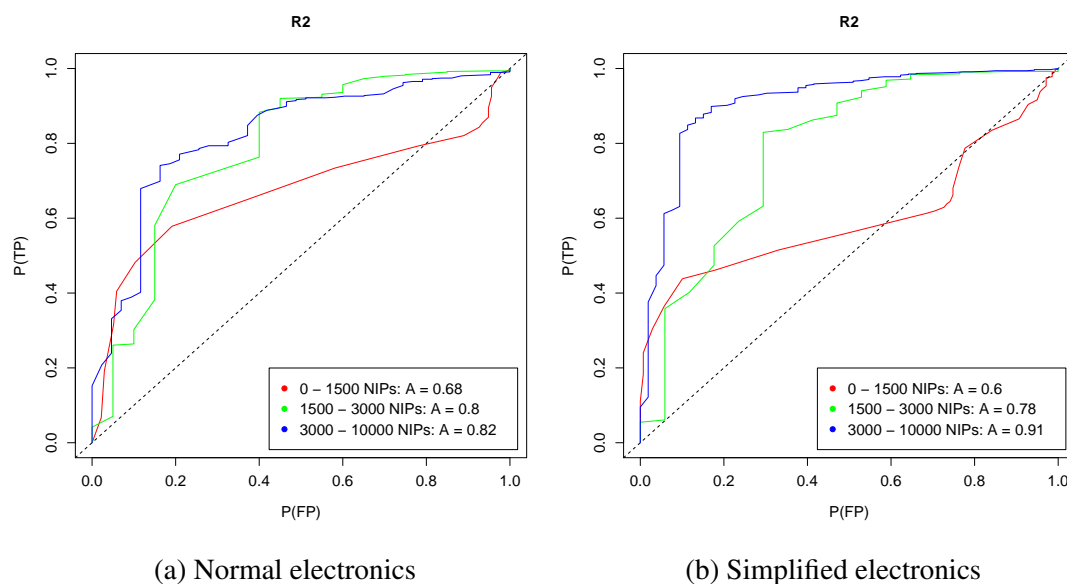
Figure 6.22: Receiver Operating Characteristic curves for background and signal discrimination in the R2 distributions of Figures 6.17 and 6.18. The top-left corner of the plot represents perfect discrimination (100% true positive detection and 0% false positive detection), whilst the diagonal line represents no discrimination.

The background/signal separation in R2 improves as energy increases, moving from the bottom left, to top right, to bottom right panels in Figures 6.17 and 6.18. The separation is similar regardless of electronics in the two lower energy bins, however the final high energy bin shows a significant improvement with the simplified electronics, which can be seen by comparing the areas under the blue curves (A) in Figures 6.22a and 6.22b.

160

(a) Normal electronics (b) Simplified electronics
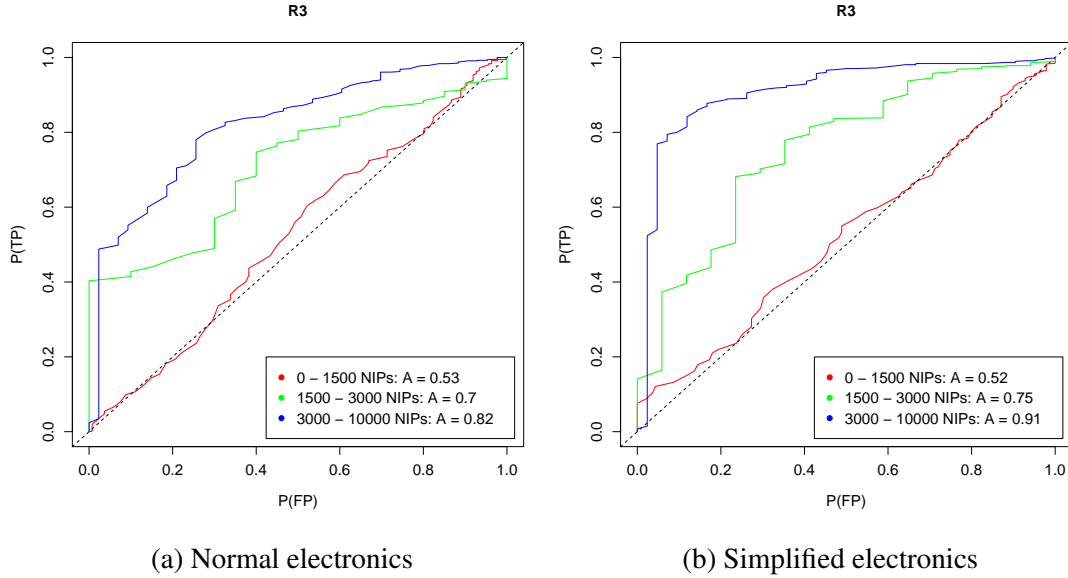
Figure 6.23: Receiver Operating Characteristic curves for background and signal discrimination in the R3 distributions of Figures 6.20 and 6.21.

In R3 (Figure 6.23), again there is not much to distinguish the normal and simplified electronics in the two lower energy bins, and again the simplified electronics appear to provide improved discrimination for events above 3000 NIPs, as evidenced by the larger 'A' parameter. In fact, the 'A' parameter for this bin is identical to the equivalent bin for R2, which shows that no improvement was made by moving from R2 to R3. Since the only difference between R2 and R3 is the addition, in quadrature, of the third range component, Δy, this implies that Δy encodes very little, and possibly no information that can distinguish signal from background in this data. This is not unexpected in light of the results of Section 6.4.2.

6.6 Conclusions

It has been shown that the simplified electronics scheme exhibits similar directional sensitivity to the normal scheme, and possibly slightly better signal/background discrimination, which is encouraging for scale-up to a future 24 m^3 detector.

Considering the range components in turn, Δx was found to be limited not by the electronics but by the geometry of the detector itself. The next generation detector,

DRIFT-IIe, may be able to improve upon its predecessor by using induced charge on neighbouring *collinear* grid wires to interpolate between the 2 mm pitch anode wires, but no improvements are likely to be gained by further modifications to DRIFT-IId (electronics or data analysis). Δz was found to exhibit a surprisingly similar directional signature between the two sets of electronics, and was confirmed as possessing a strong directional signature, though less strong than Δx. Building upon work by a previous member of the collaboration, methods for the calculation of Δy with both electronics schemes were developed. It was hoped that the simplified scheme would perform better than the normal setup, because the Δy calculation relies on the relative amplitudes of every channel, at every microsecond, making it the most sensitive to changes in the pulse shape of events, however the two electronics schemes were found to exhibit similar, low y sensitivity. Repeating the experiment with a more intense and better-collimated neutron source may highlight hitherto unobserved differences.

Improvements were found in background/signal discrimination power when moving to the simplified electronics scheme, however this was only the case for fairly high-energy events above around 3000 NIPs. A longer background run in the 'tee' configuration would be necessary to pin down at exactly what energy the discrimination turns on. The discriminating variables investigated were the *x-z* projected range (R2), and the full three-dimensional range (R3), with discrimination expected thanks to the contribution of diffusion to the track length, and correspondence between diffusion and the positional origin of the dominant background processes (the central cathode). Charge barycentre movement was measured on the grid channels for 2050 of the 2625 events passing recoil cuts, however adding the component that this measures (Δy) to go from R2 to R3, did not appear to improve DRIFT's background discrimination power.

Anne Green and Ben Morgan have shown that with a two-dimensional readout and a background-free detector, only $\mathcal{O}(10)$ events are needed to reject the null hypothesis of an isotropic distribution of recoil directions, which is the smoking gun directional dark matter signature [143]. The same order (only slightly fewer) events are needed for a three-dimensional readout, so further effort on Δy reconstruction in DRIFT-IId is not recommended in the context of a future directional search. The next iteration of the detector, DRIFT-IIe, will dispense with this dimension entirely, in favour of lower backgrounds and larger readout volume.

Chapter 7

Development of a Gas System for DRIFT-IIe

The gas system has been identified as an area in which substantial improvements and cost savings can be achieved when scaling up to a 24 m^3 detector. A gas mixing system for the prototype DRIFT-IIe detector was therefore designed, built and tested at the University of Sheffield, and installed and commissioned underground at Boulby in September 2013. This system incorporates several improvements over the one described in Chapter 4, motivated by the DRIFT collaboration's experience operating the DRIFT-IId gas mixing system underground at Boulby. These improvements were achieved using specific components that were significantly less expensive than those used on the DRIFT-IId system. The design of the new system, and results of successful commissioning tests underground at Boulby are detailed in Section 7.1.

The volume of waste CS_2 produced makes scale-up of the open-loop gas flow scheme detailed in Chapter 4 for a 24 m^3 detector difficult. This will be a problem in terms of cost, which for the 3.4 m^3 DRIFT-IId vacuum vessel is estimated at $\approx$ £3000 yr^{-1} for CS_2. Manpower is also a concern, which is currently required to fill input cylinders with 'fresh' CS_2, empty the 'used' distilled gas from the output water trap, and transport CS_2 to and from the mine shaft. A better solution would be a closed- or partially-closed-loop system, where a significant amount of used gas is collected at the output and recirculated back into the vacuum vessel. Such a system is only possible if the used gas can be shown to be sufficiently free from contaminants created in chemical reactions inside the vacuum vessel. Section 7.2 details preliminary

work to identify contaminants in the gas using a residual gas analyser (RGA).

7.1 Gas Mixing System

The DRIFT-IIe gas system is based upon the DRIFT-IId system described in Section 4.1.7, and its overall operational requirements are similar to those described therein. The design specifications for the system are listed in Section 7.1.1, whilst the improvements over the DRIFT-IId system are detailed in Section 7.1.2.

7.1.1 Design Specifications

The DRIFT-IIe gas system was required to meet the following specifications:

1. To mix two user-specifiable gases with a precision of $< 1\%$ and supply a 3.375 m^3 vacuum vessel with the mixture at a constant rate of up to 0.79 torr l/s, or one complete change of the vacuum vessel's gas at 40 torr total pressure per day.

2. To safely introduce and maintain a small ($\sim 1\%$) oxygen admixture to the gas via a pre-mixed CF_4/O_2 supply cylinder (see Chapter 8).

3. To maintain the pressure of 40 torr in the vacuum vessel to within $\pm 1\%$.

4. To introduce no more than 1% air contamination into the gas mixture.

5. To fail safe and halt all gas flow in the event of a power outage.

6. To be as remotely-controllable as possible, within budget constraints.

7. To interface with the NI PCI-6254 slow control DAQ, accepting digital and analogue inputs and supplying analogue outputs for remote monitoring.

8. To display information about the state of the various components (mass flow controllers, pressure gauges and valves), for the benefit of a local user in the underground lab.

9. To run fully autonomously for periods of up to one month, and for several months with only routine maintenance.

The main differences between this set of requirements and those for the DRIFT-IId gas system are Items 2 and 6. Item 2 is a consequence of the discovery of a new *z*-fiducialisation strategy based upon adding a small admixture of oxygen to the vacuum vessel. Research by the collaboration has shown that 1% is optimal [202]; this will

be covered in more detail in Chapter 8. Item 6 is an attempt to reduce the number of man-hours spent on routine detector maintenance tasks, by making as much of the system as possible controllable by a remote operator.

7.1.2 Components and Improvements

Figure 7.1 shows the layout of the panel onto which the main gas system components are mounted. This, combined with Section 3 of Figure 4.7, makes up the new DRIFT-IIe gas system. This section details the components of the gas system, and the improvements made over the old system.

Electropneumatic Valves

Electropneumatically-actuated stainless steel Swagelok ball valves (EPVs) were chosen to replace Mass-Flo Controllers (MFCs) 1, 2 and 3 of the DRIFT-IId gas system. This not only simplifies the system, but also reduces the valve cost by approximately a factor of 3. In addition, EPVs 4 and 5 were added to provide a means to remotely seal the gas system input and output from the vacuum vessel. This important piece of functionality is an improvement over the DRIFT-IId system, because it allows a remote user to seal off the scroll pump on the output, thereby halting the flow of gas. In the past it was only possible to seal off the input gas system, which evacuated the vessel over the course of several days, and required the gas fill process to be started again from scratch the next time the detector was switched on.

The EPVs have an actuation time of < 1 s, which is fast compared with the timescale for gas filling, and therefore allows the target pressure in the mixing cylinder to be reached with a precision of better than 1%. They also seal fully closed, and will close in the event of a loss of power. A 'normally closed' solenoid valve opens under an applied voltage of 24 V, which allows pressurised air at 4 bar to flow into a pneumatic actuator, which in turn rotates the ball valve through 90° into the 'open' position. When the solenoid is switched off, the pressurised gas in the actuator volume is automatically vented to atmosphere, and the actuator returns rapidly to the closed position under the action of a spring.
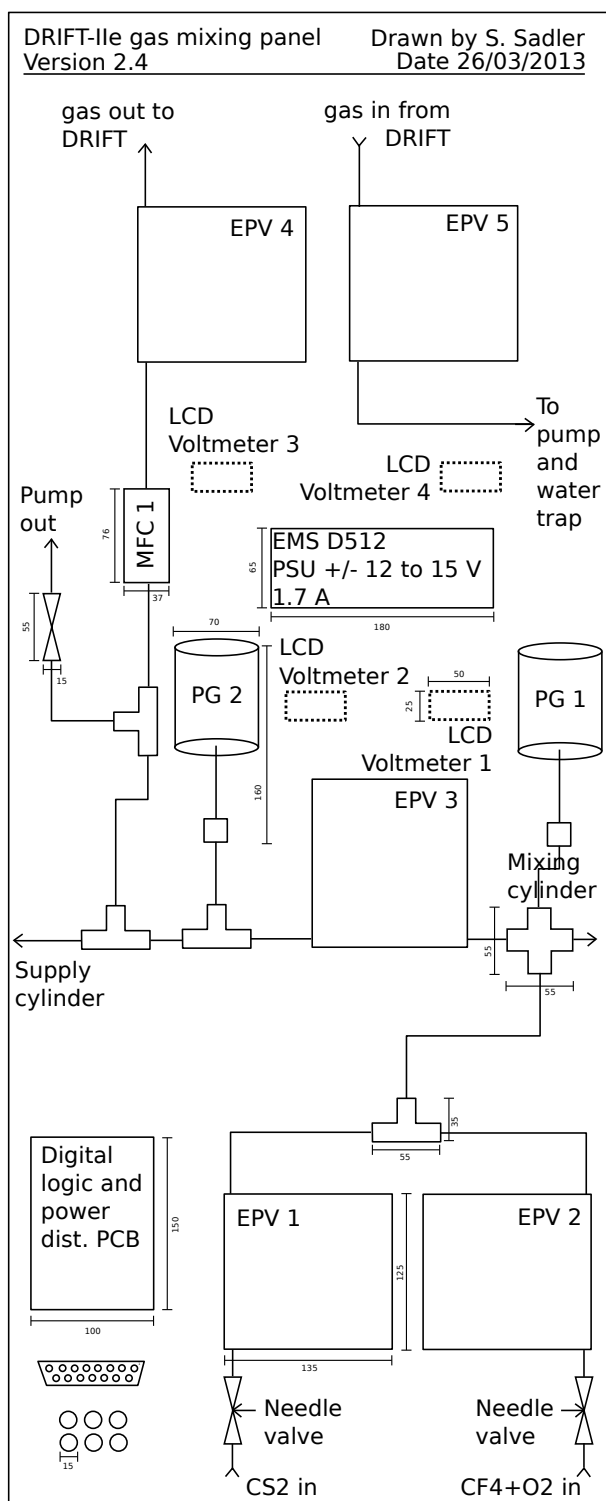
Figure 7.1: Scale drawing of the DRIFT-IIe gas mixing system panel layout.

O/C	Flow	Master o'ride	Output to MFC	MFC state
X	X	1	0	Closed
0	0	0	0	Closed
1	X	0	1	Open
0	1	0	High-Z	Flow

Table 7.1: Truth table for the MKS 1479A Mass-Flo Controller. 'X' represents any input, whilst a 'High-Z' input tells the MFC to flow according to a $0 - 5$ V analogue input signal, also supplied by the slow control DAq.

Mass Flow Controller

An MKS 1479A MFC was chosen to supply the vacuum vessel with the gas mixture. This model of mass flow controller has been tried and tested by the DRIFT collaboration, and has been operating well on DRIFT-IId for a number of years. The device has three modes: open, closed, and flow. These modes are controlled by three 5 V TTL signals from the slow control DAQ: master override, O/C, and Flow, and the output to the MFC is calculated by a set of 74LS-series logic chips on the PCB. The truth table for the MFC digital logic is given in Table 7.1.

The MFC was modified due to safety concerns over the hot element used in the flow measurement. Under the fail condition where an excess concentration of oxygen relative to CS_2 is added, a flammable mixture may be created, which could then be ignited by the element. This element was therefore disconnected, which removed the ability to read out the flow rate from this instrument. This loss of functionality is not a problem, since flow rate feedback from this device, though interesting, is not required. Instead, a feedback loop in the GasMix software compares the vessel pressure with the target pressure, and automatically adjusts the MFC's target flow rate to provide more or less gas as required.

Pressure Sensors (PGs)

Three MKS Baratron capacitance manometers were chosen for the pressure-sensing portion of the system. PGs 1, 2 and 3 monitor the pressures in the mixing cylinder, supply cylinder and vacuum vessel, respectively, with a precision of 0.25% of the reading [203]. The gas mixing software interfaces with PG1 and PG3.

167

Local Instrumentation

The front of the gas panel is instrumented with LCD voltmeters and LEDs to indicate the state and outputs of the components. Each EPV has a green indicator LED, powered by the 24 V solenoid power supply, which is switched on when the solenoid is powered and the valve is open. The MFC has a bi-colour LED which displays green when the device is in 'open' mode, yellow when the device is set to 'flow', and off when the device is set to 'close'. A set of three LCD voltmeters display the PG1 and PG2 pressures, as well as the set point signal to MFC1 . Figure 7.2 shows a photograph of the front of the gas panel.

Figure 7.2: Photograph of the DRIFT-IIe gas mixing system front panel.

Printed Circuit Board

A custom PCB was designed to process TTL digital inputs from the slow control DAQ, to control the power supply to the EPV solenoid valves, to set the MFCs to flow, open, or closed mode, and finally to distribute a master override TTL signal to the MFC and EPVs, allowing the user to close every valve in the system remotely with a single click in case of an emergency. The layout of the PCB is shown in Figure 7.3.
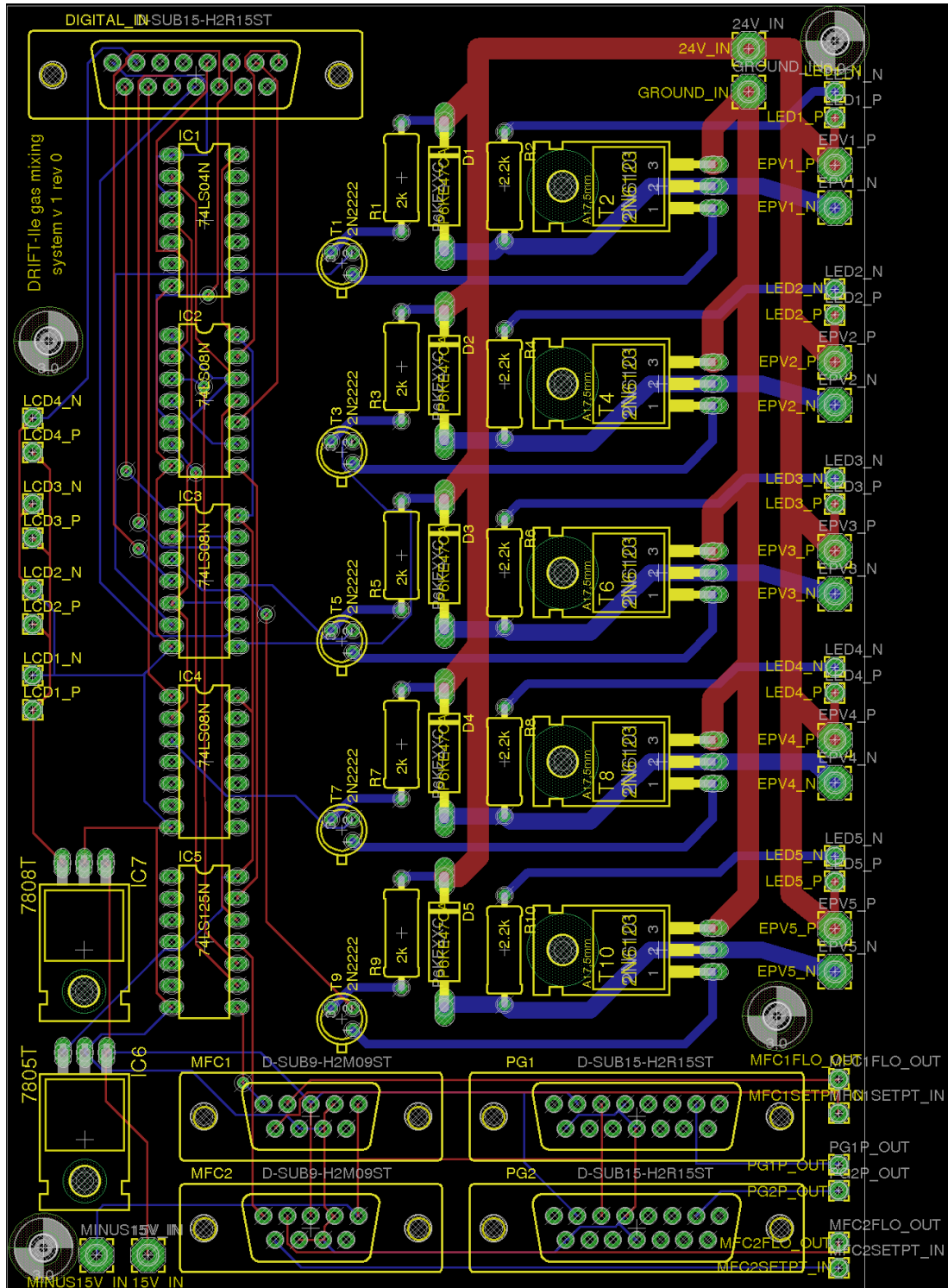
Figure 7.3: DRIFT-IIe gas system PCB layout. Red represents the top (component) side, blue represents the bottom (solder) side of the two-sided PCB. The silkscreen is shown in yellow, and solder pads are green.

The five 74-series logic chips can be seen running vertically on the left, which are powered by the 7805T voltage regulator in the bottom-left corner of the board, and control the operation of the MFC and EPVs. Digital inputs from the DAQ arrive at the board in the top-left corner, and the pressure gauges and MFC connect to the D-sub plugs in the bottom-right corner. The remaining circuitry in the top-right of the board consists of five copies of the power-switching circuit shown in Figure 7.4, which uses two transistors to control the flow of ~ Amp-scale currents to the EPV solenoids. Wide traces were chosen for this part of the circuit to prevent damage to the board from such high currents, which are most severe in the case where the master override is removed and all EPVs switch on simultaneously.
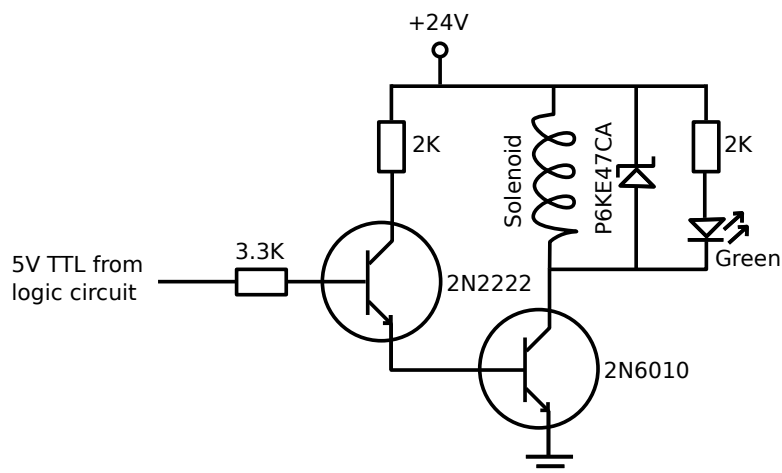
Figure 7.4: Schematic drawing of the 24 V power switching circuit. Five of these circuits control the power to the five EPV solenoids.

7.1.3 Performance Tests

Initial tests were carried out in Sheffield, where the system was connected up to the vacuum vessel and used to supply a 'mixture' of atmospheric air + air at a constant rate to the vessel. These tests confirmed that the electronics were operating as expected, that the EPVs were actuating correctly, and that the Swagelok fittings had been assembled in a leak-tight manner. Initially, no needle valves were used on the gas 1 and gas 2 inputs, however it was quickly discovered that these were necessary in order to prevent the gas from filling too quickly and overshooting the PG1 target pressure. This had not

been a problem for the DRIFT-IId system, since the MFCs on the inputs restricted the gas flow, and thus played the part of a needle valve. For the DRIFT-IIe system, it was found that a tradeoff existed between the speed of the fill, which must be fast enough to maintain the pressure in the vacuum vessel, and the precision to which the target fill pressure could be reached, which decreases with increasing fill speed. In the end it was found that only a moderate amount of fine-tuning of the needle valves was necessary in order to simultaneously fulfil items 1 and 3 of the design specifications.

Following the success of the initial tests, the vacuum vessel and gas system were transported to Boulby and installed in the underground laboratory. An Edwards XDS10 scroll pump, as well as water and charcoal traps identical to those described for the DRIFT-IId system in Chapter 4 were installed at the output, and CS_2 and CF_4 were similarly supplied. Compressed air for the EPVs was supplied from a compressed air cylinder and regulated down to 4 bar. A slight loosening of the CS_2 input needle valve was necessary to account for the difference between the atmospheric pressure used in the Sheffield tests, and the ~ 350 torr vapour pressure of CS_2. No adjustment was required for the CF_4, since this is supplied from a compressed gas cylinder regulated down to 1 bar. Figures 7.5, 7.6 and 7.7 illustrate the performance of the gas system during testing at Boulby.
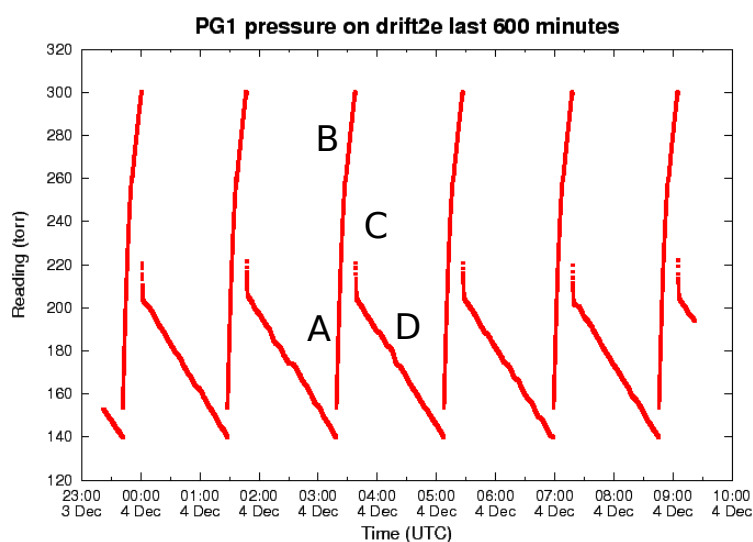
Figure 7.5: Mixing cylinder pressure (PG1) as a function of time during six fill cycles under constant flow conditions.

Regions A and B correspond to the CS_2 and CF_4 fills, respectively. During the fill, the vessel is being supplied from the supply cylinder only, which gives rise to the steeper drop in PG2 pressure compared with region D in which the gas is being supplied to the vessel from the combined 100 l volume of the mixing + supply cylinders. Region C represents the short time following the fill when EPV3 opens and the fresh gas in the mixing cylinder equilibrates with the lower-pressure residual gas in the supply cylinder. Figure 7.7 shows that the vessel pressure remained constant to within ~ 0.025% of the target 40 torr for the duration of the six cycles shown, which is comfortably inside the 1% requirement of item 3 of the design specifications.

At the time of writing, the DRIFT-IIe vacuum vessel and gas system await the arrival of the DRIFT-IIe detector at the Boulby Underground Science Facility. If the new design based around EPVs instead of MFCs proves successful, then an up-scaled version capable of supplying gas at a rate ~ 7× faster will be designed for DRIFT-III. However, at this scale, the open-loop scheme becomes extremely cost- and manpower-intensive, and a partially-closed-loop system of recirculation is favoured. Such a scheme is only possible if the used gas can be shown to be uncontaminated during its ~ 1 day exposure to the experiment, and preliminary work toward this is the subject of Section 7.2.
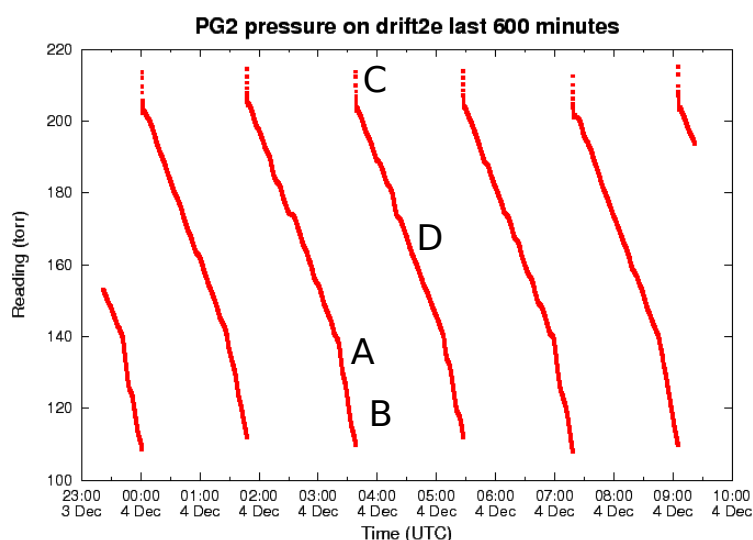
Figure 7.6: Supply cylinder pressure as a function of time during six fill cycles under constant flow conditions.
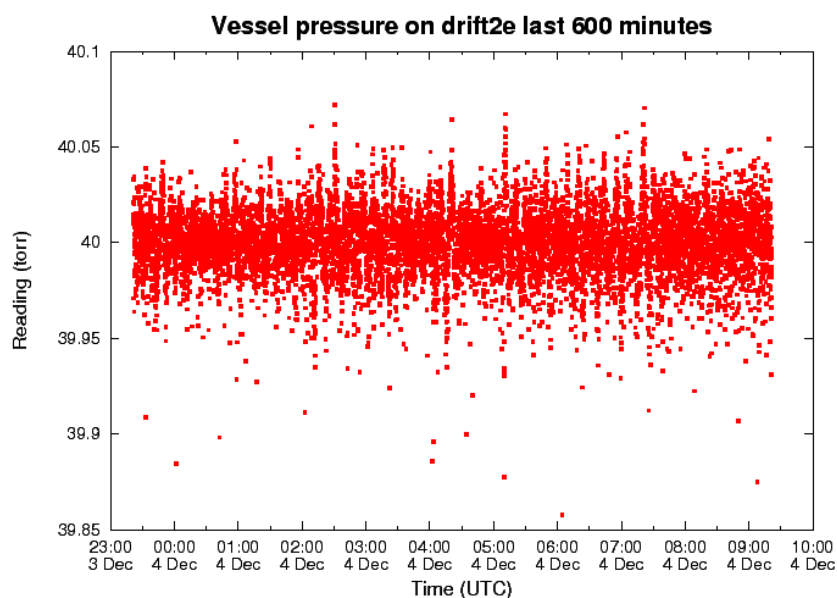
Figure 7.7: Vessel pressure as a function of time during six fill cycles under constant flow conditions.

7.2 Gas Analysis System

7.2.1 Motivation

The 30 : 10 mixture of CS_2:CF_4 has been shown to be quite 'forgiving', exhibiting only small changes in gas gain for relatively large contamination fractions. Notwithstanding, the MWPC gain is a strong function of the exact gas composition. Thus far the collaboration has had no way to directly monitor the gas composition, instead relying on gas system partial pressures to monitor the mixture and ^{55}Fe calibration constants as a proxy for the stability of the gas gain over time. It would be useful to be able to monitor the exact composition of the gas as a function of time to look for evidence of contamination from air leaks or from chemical reactions occurring inside the vacuum vessel, and also to make a direct measurement of the gas mixture to ensure that the gas system is creating the expected mixture. To this end, a residual gas analyser (RGA) system was assembled and tested in Sheffield before being deployed underground on DRIFT-IId for the first time.

7.2.2 Theory of RGA Operation

The DRIFT RGA is an MKS MicroVision Plus open-source quadrupole mass spectrometer (Figure 7.8), which samples gas at a pressure $< 1 \times 10^{-4}$ torr and produces a spectrum of the partial pressures of the mass species present. Its operation can be broken down into three stages as follows:
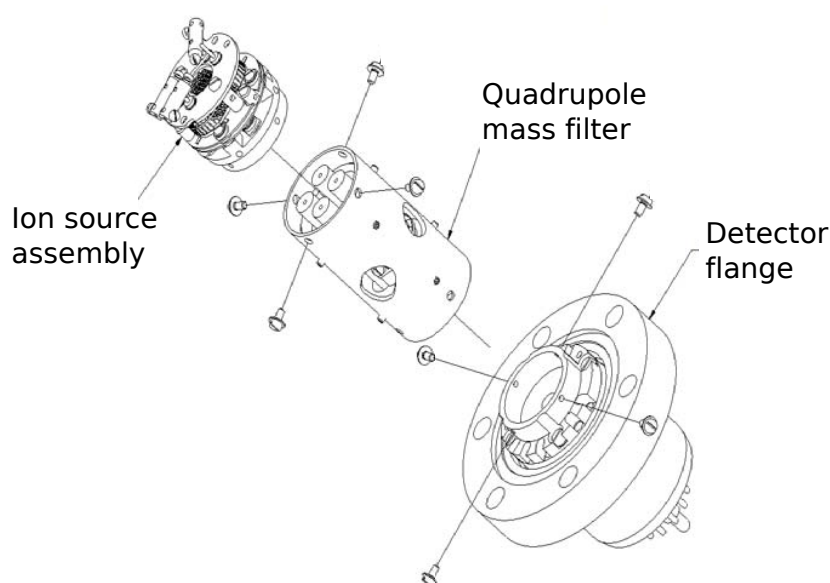
Figure 7.8: Exploded view of the residual gas analyser.

Ionisation Inside the ion source assembly at the far end of the analyser a hot emission filament supplies electrons, which are accelerated in a beam towards an anode, impacting gas atoms and ionising them as they do so.

Mass filtering The gas ions are fed into a quadrupole mass filter consisting of four parallel conducting rods. Here, the ions are subjected to oscillating electric fields set up by radio frequency (RF) AC voltages on the parallel rods. For a given frequency, only ions within a narrow range of allowed mass-to-charge ratios are able to pass down the rods along trajectories that terminate on the detector at the far end; all ions with mass-to-charge ratio outside this range travel on trajectories that terminate on the rods themselves, and are therefore filtered out. The RGA

scans the selected mass-to-charge range (0-200 amu) once every few seconds by varying the frequency of the RF electric field.

Detector At the far end of the quadrupole filter, a Faraday cup detector converts the surviving ion beam into an electric current, which is amplified by electronics inside a head unit and output via a serial connection to a Windows computer running MKS ProcessEye software. This head unit also acts as a power supply for the emission filament. The software assumes that the species are singly ionised (charge +1), and outputs a mass spectrum in real time under this assumption.

7.2.3 Experimental Method

Figure 7.9 shows a sketch of the apparatus, including the points of attachment onto the DRIFT-IId gas system. The RGA rig was connected as shown, and the system pumped down to a pressure of 1.26×10^{-5} mbar: the ultimate pressure of the whole system up to V2 and V3, with V1 fully open. The leak valve V1 was then closed to a position that is closed enough to ensure that the pressure remains below the upper working limit of the RGA when the gas mixture is introduced, but open enough to ensure that all the peaks of the spectrum are visible above the intrinsic noise of the RGA. This position is different for the used and fresh gas measurements due to the differing input gas pressures (see Figure 7.9). A set of nine background spectra were recorded immediately before any gas was allowed to enter the system, and these were later subtracted from the signal spectra to yield the spectrum of the gas mixture alone.

After recording the background, either the fresh (V2) or used (V3) input valve was opened, and the system left for around 15 minutes to equilibrate before a further nine signal spectra were recorded. Afterwards, V1 was opened, V2 and V3 closed, and the system pumped out for around 1 hour to remove the gas mixture ready for another run. The fresh gas was sampled immediately after the gas system's supply cylinder. During these runs, the DRIFT-IId detector was operating under the nominal conditions described in Chapter 4, including a gas flow rate of $2\,\mathrm{mbar\,l\,s^{-1}}$. Used gas sampled by the RGA had therefore been exposed to the experiment for, on average, 24 hours.
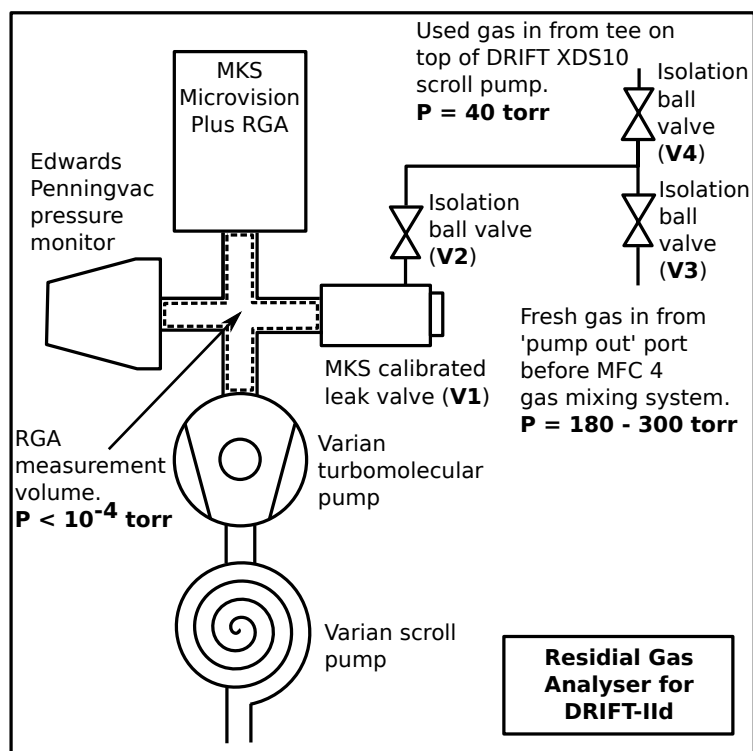
Figure 7.9: Sketch of the RGA rig connected to DRIFT-IId.

7.2.4 Results

Figure 7.10 shows a comparison of selected mass spectrometer peaks for the fresh and used gas mixture. Since the input pressures for the used and fresh gas were different (see Figure 7.9), a direct comparison of a given peak's partial pressure between the fresh and used gas was not possible. Instead, the full fresh gas mass spectrum was normalised by the ratio of the total pressures in the fresh and used gas samples, allowing a comparison to be made. Both the background and signal spectra were generated by averaging 9 scans. Table 7.2 shows the 'cracking pattern' for a selection of molecules incorporating carbon, sulphur, fluorine, oxygen and nitrogen, which may be present in the spectra. The cracking pattern comes from a combination of three effects: electron-induced molecule dissociation in the RGA, isotopes of different masses, and multiple ionisation.
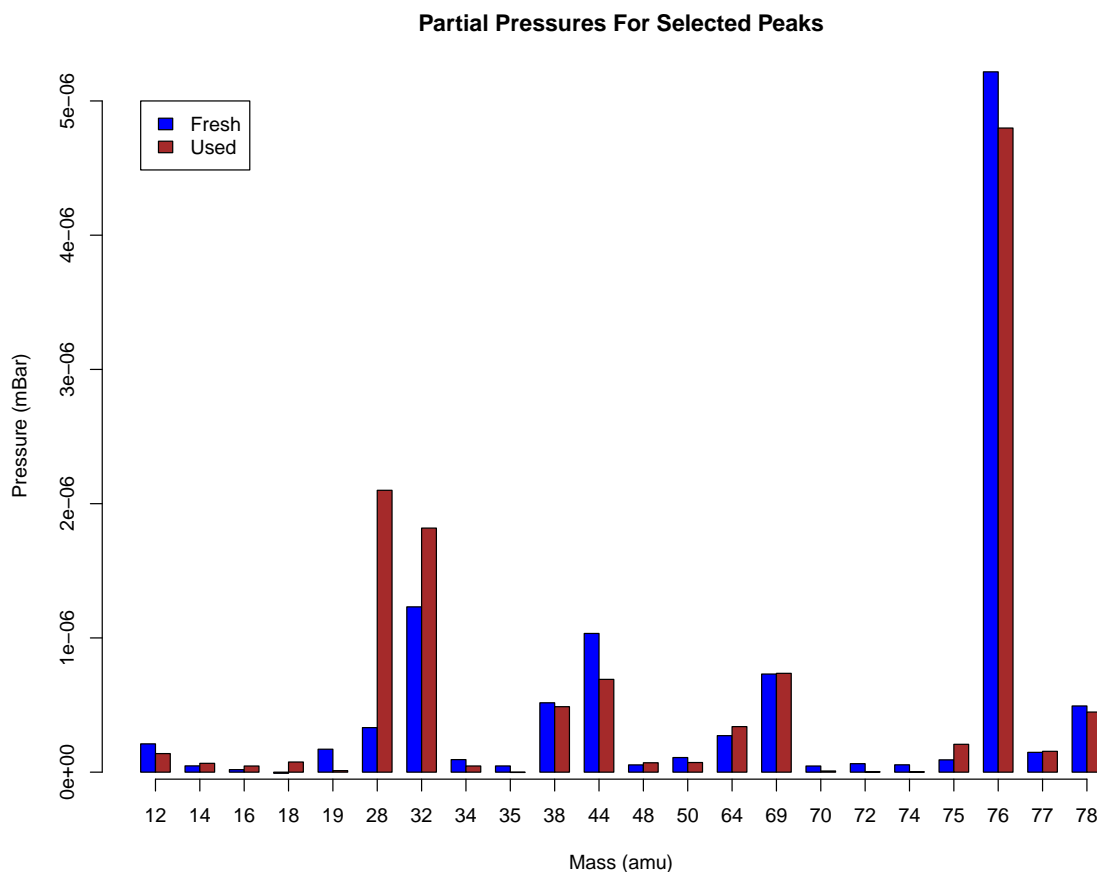
Figure 7.10: RGA spectra of new and used gas side-by-side for comparison. All peaks above the noise are shown. The fresh spectrum has been normalised by the ratio of total pressures in the fresh and used spectra, to allow direct comparison.

7.2.5 Discussion

The peak at 28 amu is 6× larger in the used spectrum. Taken together with the ∼ 50% increase in the peak at 14 amu, this suggests that nitrogen has entered the system, probably through an air leak. Another possible source for the increase in this peak is an increase in carbon monoxide in the gas mixture, and indeed there is evidence of a small increase in the 16 amu minor peak of CO to back this up. Extra CO in the detector might be explained by cracking of CS_2, and subsequent reaction of the carbon atom with oxygen from an air leak. The signatures of the two gases are very similar,

177

Species	Peak 1/%	Peak 2/%	Peak 3/%	Peak 4/%	Peak 5/%	Rel. sens.
CS_2	76 / 100	32 / 21	44 / 17	78 / 9	38 / 6	?
CF_4	69 / 100	50 / 12	19 / 7	31 / 5	-	1
CO_2	44/ 100	28 /11	16 / 9	12 / 6	45 / 1	1.4
CO	28 / 100	16 / 10	12 / 5	29 / 1	-	1.05
SO_2	64 / 100	48 / 49	32 / 10	66 / 5	16 / 5	2.1
O_2	32 / 100	16 / 11	-	-	-	0.86
N_2	28 /100	14 / 7	29 / 1	-	-	1 (def.)
NF_3	52 /100	33 / 40	71 / 31	14 / 9	19 / 8	?
H_2S	34 / 100	32 / 44	33 / 42	36 / 34	35 / 2	2.2
H_2O	18 / 100	17 / 23	16 / 1	-	-	0.9

Table 7.2: Cracking pattern data for selected interesting gases. Percentages are in relation to the height of the primary peak. From Hiden [204].

making it difficult to determine how much of the 28 amu peak is generated by either N_2 or CO by considering this peak alone.

There is also a 50% increase in the peak at 32 amu, which is suggestive of oxygen contamination. Taken together with the 28 peak, which increased by 6×, this is good evidence for air contamination. Another interesting possible contributor to the enhancement of the 32 amu peak comes from sulfur ions from 'cracked' CS_2. If CS_2 were being broken apart in the detector, we might expect to observe a reduction in the height of the primary CS_2 peak at 76 amu in the used gas spectrum, which does indeed seem to be in evidence. However, no corresponding increase in the carbon peak at 12 amu is observed. Perhaps this carbon is reacting with oxygen to form carbon monoxide, enhancing the 28 amu peak instead.

An enhancement of the 64 amu primary peak of SO_2 is observed, along with a corresponding enhancement of the minor peak at 48 amu by the same factor (≈ 1.25). There is another minor peak of SO_2 at 32, so this species may have a small contribution to the enhancement of that peak. The decrease in the CS_2 primary (76 amu: 92%), doubly-ionised (38 amu: 94%) and heavy isotope (78 amu: 91%) peaks agrees to within 3% of the initial values, which is good evidence that some process or combination of processes is decreasing the CS_2 concentration inside the vacuum vessel.

The primary CF_4 Peak at 69 amu remains unchanged after the gas has flowed through the detector, however the minor peaks at 50 and, in particular, 19 amu show significant decreases, and are in better agreement with the cracking pattern of CF_4 in

the used spectrum. It is possible that the excess seen in the 19 amu peak of the fresh gas spectrum was due to monatomic fluorine. Fluorine tends to form diatomic molecules, and diatomic fluorine has a mass of 38 amu. Similarly, the 44 amu minor peak of CS_2 (also the major peak of CO_2), which was unexpectedly enhanced in the fresh spectrum, is much closer to its expected fraction of the 69 amu major CS_2 peak in the used spectrum. One possible explanation is that the fresh CS_2 is contaminated with dissolved CO_2. Finally, the primary peak of water at 18 amu is small compared with the signal peaks for both the fresh and used gas, which vindicates the omission of a 'bake out' phase of the sampling procedure.

7.2.6 Future Work

There are several improvements planned for the RGA apparatus. The first involves the sampling point of the fresh gas mixture, which is currently inside MFC4 of the DRIFT-IId gas mixing system (see Figure 4.7). This means that the RGA samples the fresh gas mixture at a much higher pressure (180 - 300 torr) than the used gas ($\sim$ 40 torr), and therefore requires a large normalisation by the total pressure to be applied to the spectra. Moving the sampling point of the fresh gas to the downstream side of MFC4 would enable both fresh and used gas to be sampled at a pressure of $\sim$ 40 torr, reducing the normalisation factor and hence the effect of any associated systematic error.

It would be advantageous to integrate the RGA with the existing DRIFT-IId slow control, to enable correlations between anomalies in the physics data and changes in the gas composition to be searched for. In order to realise this, the hand-operated isolation ball valves (V3 and V4) would need to be replaced by electropneumatically-operated ones to enable the system to switch from sampling fresh to used gas, in order to make a comparison akin to that in Figure 7.10. The RGA would sample the used gas for the majority of the detector livetime, with the fresh gas being sampled occasionally to verify that the initial gas composition remained the same. The ProcessEye software contains functionality to allow the user to monitor the amplitudes of up to twelve mass peaks as a function of time.

The RGA head unit can accept at 'external trip' signal via a 3.5 mm plug, which could be set up in order to disable the RGA in the event that the pressure in the sampling volume exceeded the RGA's maximum operating pressure. This is a necessary

precaution to take if the device is to be operated underground unattended. An investigation into the RGA's sensitivity to the relative concentrations of the two fill gases is possible with the current setup, and will be undertaken in the near future to find out whether the RGA can provide a cross-check on the gas mixture.

The next step toward recirculation is to syphon a sample of condensed CS_2 from the water trap, and measure the mass spectrum of the evaporating liquid to determine whether the contaminants are still present in significant quantities. Comparison of this spectrum with the 'used' spectra measured here will reveal the effect of the water trap distillation process. In the event that contaminants are still present, the alternative method of condensing CS_2 in a cold trap could be investigated.

7.3 Conclusions

A gas mixing system for the DRIFT-IIe detector has been designed, built and tested in Sheffield, and installed and commissioned at the Boulby Underground Science Facility where, at the time of writing, it awaits the arrival of the new detector. Simplified components were used, which allows remote control with only minor maintenance, and also makes the new system cheaper than the equivalent system for DRIFT-IId upon which it is based. Modifications were made to the system to enable it to operate with mixtures containing oxygen, which have recently been shown to achieve the 'holy grail' of DRIFT: z-fiducialisation, and this will be the subject of the final chapter.

An RGA has been assembled and operated on DRIFT-IId, and preliminary results demonstrate that real-time monitoring of gas contamination is achievable. There is some evidence for chemical reactions occurring inside the vacuum vessel, probably driven by the high electric fields in the vicinity of the MWPC wires, however further experiments with the RGA are necessary to determine whether or not the resulting contaminants can be distilled out of the CS_2 to allow gas recirculation, which will be important in a future 24 m^3 detector.

Chapter 8

New Spin-Dependent Dark Matter Limit

In 2013, experiments at Occidental College in the USA revealed that introducing a small admixture of oxygen to the gas mixture provides a means to measure the absolute z position of events [205]. This revolutionary technique has the potential to make DRIFT a truly background-free experiment, by virtue of the fact that all known sources of background originate on either the MWPC wires (minimal z) or the central cathode (maximal z). It was expected to provide an improvement in efficiency for detecting WIMP-induced nuclear recoils, with a corresponding improvement in limit setting power (or discovery potential) of the DRIFT-IId detector. This chapter describes this 'minority carrier' technique of z-fiducialisation, and presents a new, and vastly simplified analysis of DRIFT-IId data taken in this mode of operation.

8.1   Minority Carrier z Fiducialisation

Nicknamed the 'holy grail' of DRIFT, fiducialisation of events in the z (drift) direction has long been understood to be a vital step toward producing a background-free dark matter search experiment with a gas TPC. This is because the known background populations discussed in Chapter 5 originate either on the central cathode or in the vicinity of the MWPC detectors. In contrast, the target WIMP-nucleon elastic scatter events have equal probability to occur anywhere in the fiducial volume. Therefore, an

accurate measurement of the z position of events should provide a powerful method of differentiating signal from background.

The breakthrough at Occidental College was the discovery of a method for measuring the z-position of events by adding a small admixture of oxygen (at the 1% level) to the DRIFT fill gas [205]. It was found that this small addition changes dramatically the shape of signal pulses on individual readout channels for events produced at distances $\gtrsim 5$ cm from the MWPC, by reducing the height of the 'main' peak, and giving rise to one, two and occasionally three 'minority' peaks *before* the main peak, which are referred to hereafter as the 'S', 'P' and 'D' peaks in order of increasing drift speed. The existence of these minority peaks implies that, in the presence of oxygen, there are now several charge carriers all drifting with different velocities in the detector, with the majority carrier being the slowest species. Figure 8.1 shows an example event display from such an event. The nature of these minority carriers remains under investigation at the time of writing. Isotope effects appear to be ruled out, because a heavier molecule would be expected to drift more slowly, and therefore arrive at the MWPC *after* the main ionisation, not before. An alternative possibility is that the minority carriers are 'normal' 76 amu CS_2 that has a slightly different bond angle, and therefore a slightly different collisional cross section [205].

The z position of an event relative to the MWPC can be calculated using Equation 8.1:

$$z = (t_m - t_p)\frac{v^m_{drift}v^p_{drift}}{v^m_{drift} - v^p_{drift}},\tag{8.1}$$

where $v^{[m,p]}_{drift}$ represent the drift velocity of the majority and secondary minority carriers in the 660 V cm^{-1} drift field (typically 60.17 and 63.66 m s^{-1}, respectively), and $t_{[m,p]}$ are the arrival times of the majority and secondary minority peaks. In principle, any of the minority peaks can be used in this way to calculate an event's z position. However, in practise it was found that the P minority peak was the most consistent, giving the lowest fraction of unmeasurable z positions.
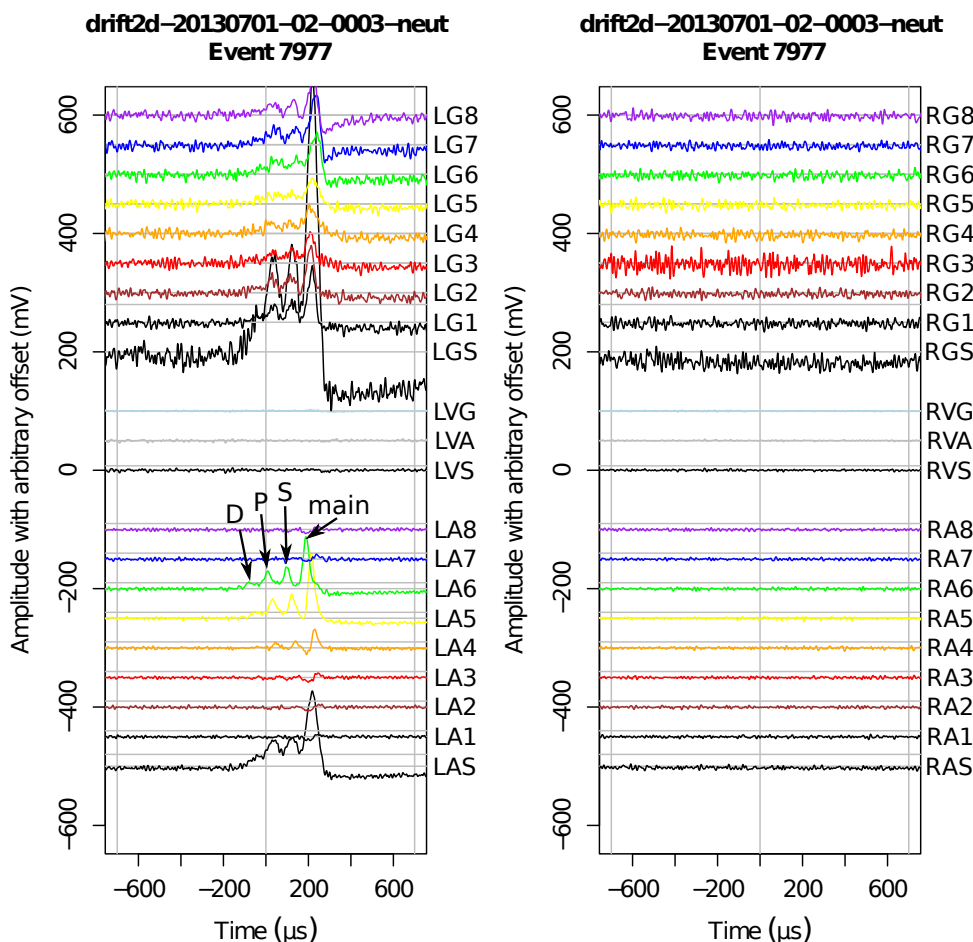
Figure 8.1: Example event display from minority carrier data. The main peak and the earlier 'S', 'P' and 'D' minority peaks can be seen on LA 3, 4, 5 and 6.

8.2 Analysis of Minority Carrier Data

A dataset of 53.7 days of shielded running was chosen to search for WIMP-induced nuclear recoils in the fiducial volume. A gas mixture of 30:10:1 torr CS_2:CF_4:O_2 was used, giving a total spin-dependent target mass of 33 g. Due to safety concerns over a possible ignition source inside the MKS 1497A mass flow controllers of the DRIFT-IId gas system (see Chapter 4, Figure 4.7), it was not possible to run in continuous flow mode with an admixture of oxygen gas. Instead, the DRIFT-IId vacuum vessel

was filled with the gas mixture, sealed, and run for several days. This process was repeated several times during the 53.7 day data-taking period to mitigate the effects of gas ageing.

8.2.1 Calibration

The ^{55}Fe calibration procedure described in Chapter 4 was used to set the energy scale of the detector, with energy calibrations interleaved with dark matter search running every six hours. No modifications to the calculation of the calibration constants were necessary, as the events were found to be almost identical to those under oxygen-free running. The reason for this is that the ^{55}Fe calibration sources are mounted directly behind the MWPC planes, so that electrons from the interactions of their emitted X-rays occur in close proximity to the detectors, and hence with minimal z. The resulting time difference between the main and minority peaks is short enough that they all overlap, giving the events a structure that is almost indistinguishable from that observed under oxygen-free running. The distribution of measured pulse areas is shown in Figure 8.2.

Anode Fe–55 spectrum

Fit parameters:
Height: 26.79
Centre: 352.86
Sigma: 67.45

Events:
Total: 270
In plot region: 267
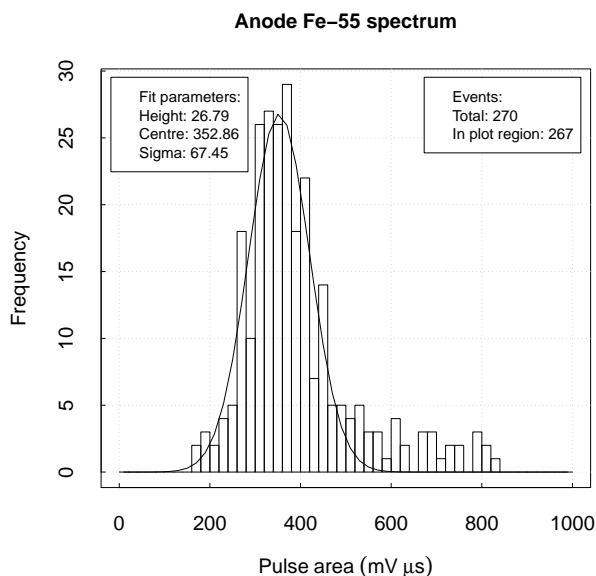
Figure 8.2: Distribution of pulse areas from a single oxygen ^{55}Fe calibration file.

The stability of the gas gain was verified by plotting the ^{55}Fe calibration constants

184

as a function of time for individual runs, an example of which is shown in Figure 8.3. The calibration constants remained constant over periods of several days, implying that the contamination of the gas due to outgassing or leakage into the vacuum vessel remained tolerably small.
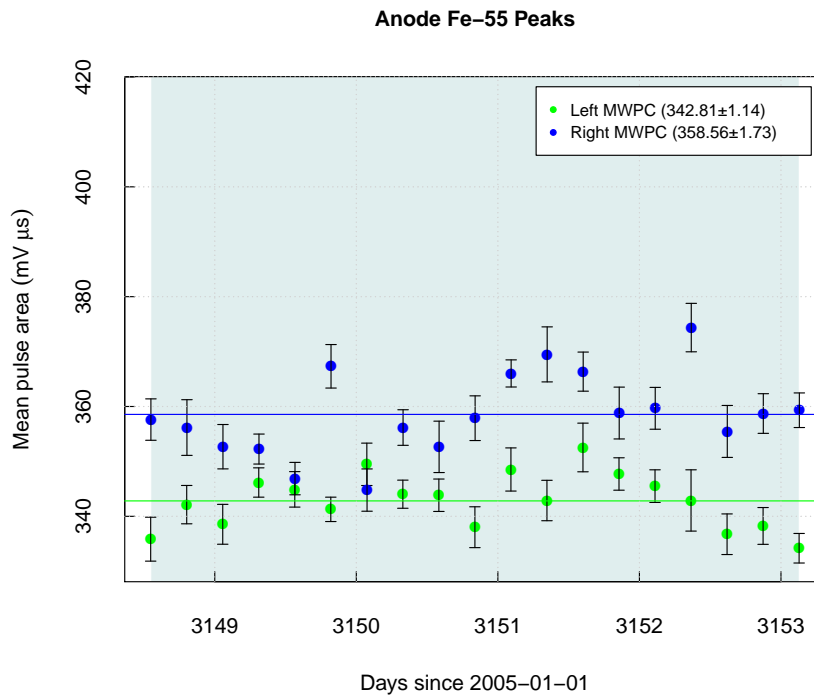
Figure 8.3: ^{55}Fe calibration constants vs time for a single run. The stability over the course of the run indicates that the gas gain is not being adversely affected by running without gas flow.

The mean ^{55}Fe pulse area during the run was measured to be 95% its value with the CS_2:CF_4 gas mixture. The W value of the gas was taken to be 25.2 ± 0.6 eV. This is the value measured for a 30:10 mixture of CS_2:CF_4 [179], and will be updated in the near future when the techniques of Pushkin and Snowden-Ifft [179] have been applied to the new 30:10:1 gas mixture. This approximation is justified to some extent by the results of that work, which show that adding 25% CF_4 to the CS_2 only produces a small change in the W value, from 24.9 ± 0.8 to 25.2 ± 0.6 eV.

8.2.2 Undershoot Removal

The undershoot issue highlighted in Chapter 6 affects minority carrier data to a greater extent than normal data, because there are now at least two, and perhaps three or four undershoots all acting to 'pull down' the waveforms and reduce the measured peak areas. To mitigate the effects of this, the time constant of the undershoot was measured for each channel in turn, on both the anode and grid, using a sample of impulse spark-like events, and the results input into the undershoot removal filter shown in Equation 8.2, which is derived from the transfer function of a simple high-pass filter [206]:

$$f(t) = I(t) + \frac{1}{\tau} \int_{-\infty}^{t} I(t')dt'. \tag{8.2}$$

Here, τ is the measured time constant for the channel in question, $I(t')$ is the measured current at time t', which spans the ROI, and $f(t)$ is the undershoot-removed current signal. The effect of the filter on a typical minority carrier waveform is shown in Figure 8.4. The software filter brings more waveform samples above the baseline,
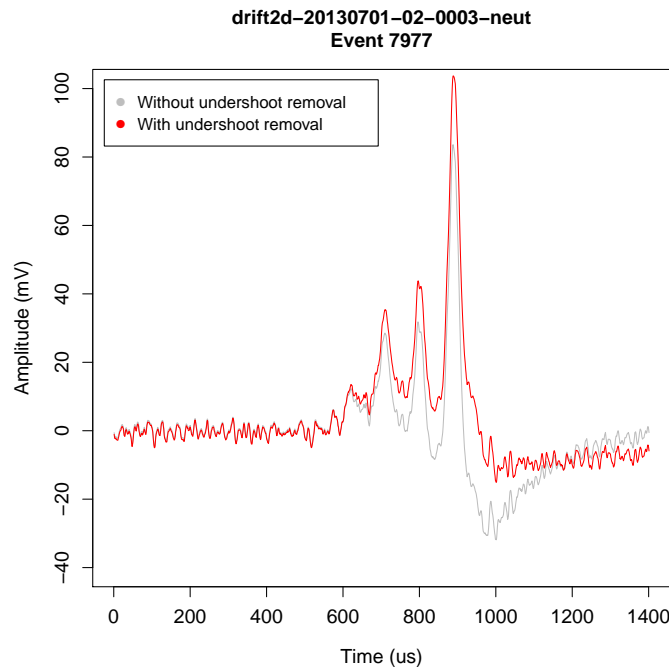
Figure 8.4: Effect of the undershoot removal filter given in Equation 8.2.

Cut	Definition	Description	Acceptance (d^{-1})
-	-	Raw trigger rate	131277
1.1	anode.zero.nip.cut	NIPs > 0 on the anode	131113
1.2	anode.tmin.cut	No anode charge before roi.start + 5us	129213
1.3	anode.tmax.cut	No anode charge after roi.stop - 5us	101440
1.4	anode.clipping.cut	No line hits digitiser rails	101440
1.5	grid.tmin.cut	No grid charge before roi.start + 5us	100742
1.6	grid.tmax.cut	No grid charge after roi.stop - 5us	99341
1.7	grid.clipping.cut	No line hits digitiser rails	99341
1.8	veto.cut	No veto activity	49597
2.1	anode.10000.nips.cut	Remove events with > 10000 NIPs	48678
2.2	anode.one.side.cut	Charge on one side only (anode and grid)	48513
2.3	anode.adjacent.cut	Anode hits are contiguous	41735
2.3.2	anode.eight.wire.cut	Neither side hits all 8 channels	41504
2.4	anode.min.risetime	Remove fast events with *anode.min.risetime* < 3 μs	9453
2.5	anode.mp.ratio.cut	Minority peak area > 0.4× majority peak area	856

Table 8.1: The full set of stage 1 and 2 cuts used to select recoil-like events in minority carrier data. Acceptance values in the fourth column were calculated using the full 4.7 d neutron dataset.

partially counteracting the effect of the hardware high-pass filter. The undershoot removal is not perfect towards the late-time portion of the waveform; however, this is unimportant since these samples are not used in the analysis that follows.

8.2.3 Event Selection

The shape of the signals in oxygen data is considerably different from those in the 'conventional' gas mixture. Therefore, the old stage 2 and 3 cuts described in Section 4.2.5 were abandoned, and a new set of cuts developed to sort signal from background events. A full list of cuts appears in Table 8.1.

As in Chapter 6, Cuts 1.1 – 1.8 are low-level cuts designed to ensure that events are analysable, the only difference being that the region of interest (ROI) was truncated to $-700 < t < 700$ μs relative to the trigger time to speed up analysis. Cut 2.1 sets an upper limit on the recoil energies under consideration, which at NIPs values of around $10,000$ makes no significant difference to the acceptance since neither WIMP nor neutron events are expected with this high energy. Cut 2.2 removes events where charge was detected on both sides of the detector simultaneously, which is useful for removing the tagged RPR and double recoil events discussed in Chapter 5. Cut 2.3

ensures that the event consists of an unbroken track of ionisation charge, which is true of nuclear recoils, but not of electron tracks [160]. The *anode.min.risetime* cut (2.4) is designed to remove fast, spark-like events such as those used to measure the decay constants of the undershoots in Section 8.2.2. The *anode.mp.ratio* cut (2.5) is powerful enough to warrant a detailed description, as follows.

8.2.4 *anode.mp.ratio* Cut

It was found that requiring events to exhibit the characteristic shape shown in Figure 8.4 was an extremely effective way to separate signal neutron calibration events from background events. To that end, the variable *anode.mp.ratio* was calculated for each event according to Equation 8.3:

$$anode.mp.ratio = \frac{A_{min}}{A_{main}}, \tag{8.3}$$

where A_{min} is the total area of the minority peaks from the start of the ROI to the first baseline crossing stepping back from the highest waveform sample (the main peak), and A_{main} is the area in the main peak, summed between the end of the minority peak region and the final baseline crossing. The *anode.mp.ratio* distributions for background and neutron calibration data appear in Figure 8.5, where it can be seen that the signal events appear at higher *anode.mp.ratio* than the large background peak, which is comprised mainly of short, spark events on the MWPC. A cut at *anode.mp.ratio* > 0.4 was chosen, below which events were removed.

The average rate of events passing all cuts up to and including Cut 2.5 in the background and neutron runs is plotted in Figure 8.6 where, as expected, the rate is significantly enhanced by the presence of the neutron source above the central cathode. Interestingly, the rate of events passing stage 1 and 2 cuts is not consistent across different neutron runs, and nor does the rate appear to be correlated with the time since the last fill, which would be indicative of gas ageing effects. Instead, a likely explanation is that small changes in the oxygen fraction between runs lead to dramatic changes in the size of the minority peaks, and hence the fraction of legitimate neutron-induced recoils surviving the *mp.ratio* cut. This is in agreement with the findings of Snowden-Ifft and Gauvreau [149], and suggests that the efficiency for detecting WIMPs was not constant during the 53.7 day DM search run. This issue will be overcome in upcoming
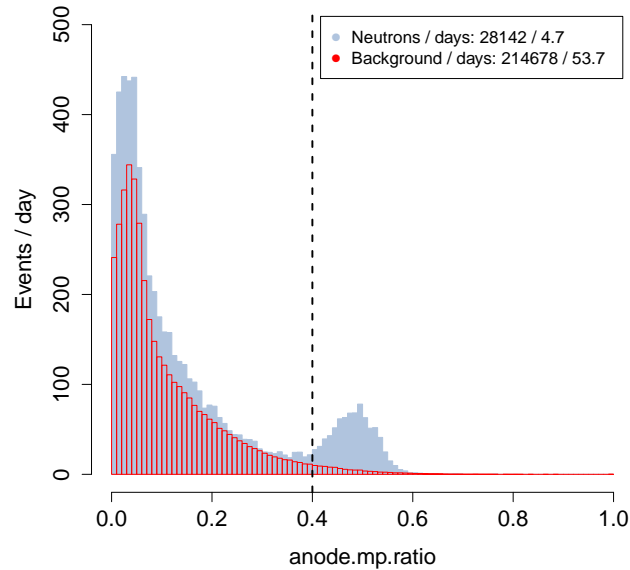
Figure 8.5: Histogram of *anode.mp.ratio*. All events with *anode.mp.ratio* < 0.4, shown by the dashed black line, are rejected according to cut 2.5.

runs by switching to continuous flow mode, for which oxygen safety modifications to the gas system MFCs are being made.

8.3 Measuring *z*

8.3.1 Peak-Finding Algorithm

An algorithm was written to identify the minority peaks in an event, and calculate its z-position using Equation 8.1. The algorithm is shown as a flow chart in Figure 8.7.

The channel with the largest maximum amplitude was identified, to give the algorithm the best possible chance of identifying the minority peaks. For long tracks, this introduces an uncertainty in the z position of several mm, but this is negligible in comparison with the uncertainty introduced by the drift velocities appearing in Equation 8.1, and was therefore neglected.

The time of the maximum waveform amplitude within the ROI was identified, and

189
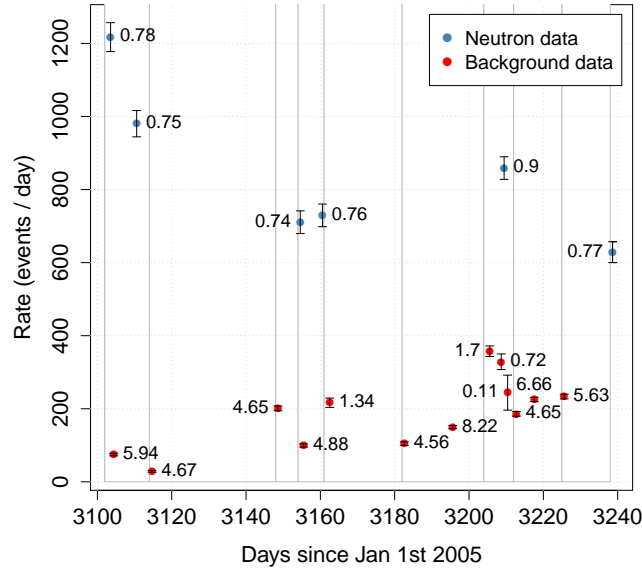
Figure 8.6: Mean rate of events passing all stage 1 and 2 cuts for each of the WIMP search and neutron runs as a function of time. Vertical grey lines mark re-filling of the vacuum vessel with fresh gas, and text labels show the run livetime in days.

passed as the initial guess to a non-linear least-squares fitting routine, which fit a Gaussian to the peak. This was assumed to be the main peak, and its central value was taken to be the time of the charge deposition from the majority carriers. A new waveform was then created with three σ_{main} either side of the central value notched out. The maximum amplitude sample in the resulting waveform was then found, and the second peak removed from the waveform by notching out samples within three σ_{main} either side of the second peak. This process was repeated once more to find a point close to the third-highest peak, and the notched-out waveform discarded.

The three points were passed to a three-Gaussian least-squares fitting routine as initial guesses for the peak positions, and the details of the resultant fits were saved. The two time differences between the three consecutive peaks were calculated (Δt_1, Δt_2), and their ratio taken. This was checked against the following condition:

$$0.7 < \frac{\Delta t_1}{\Delta t_2} < 1.3. \tag{8.4}$$
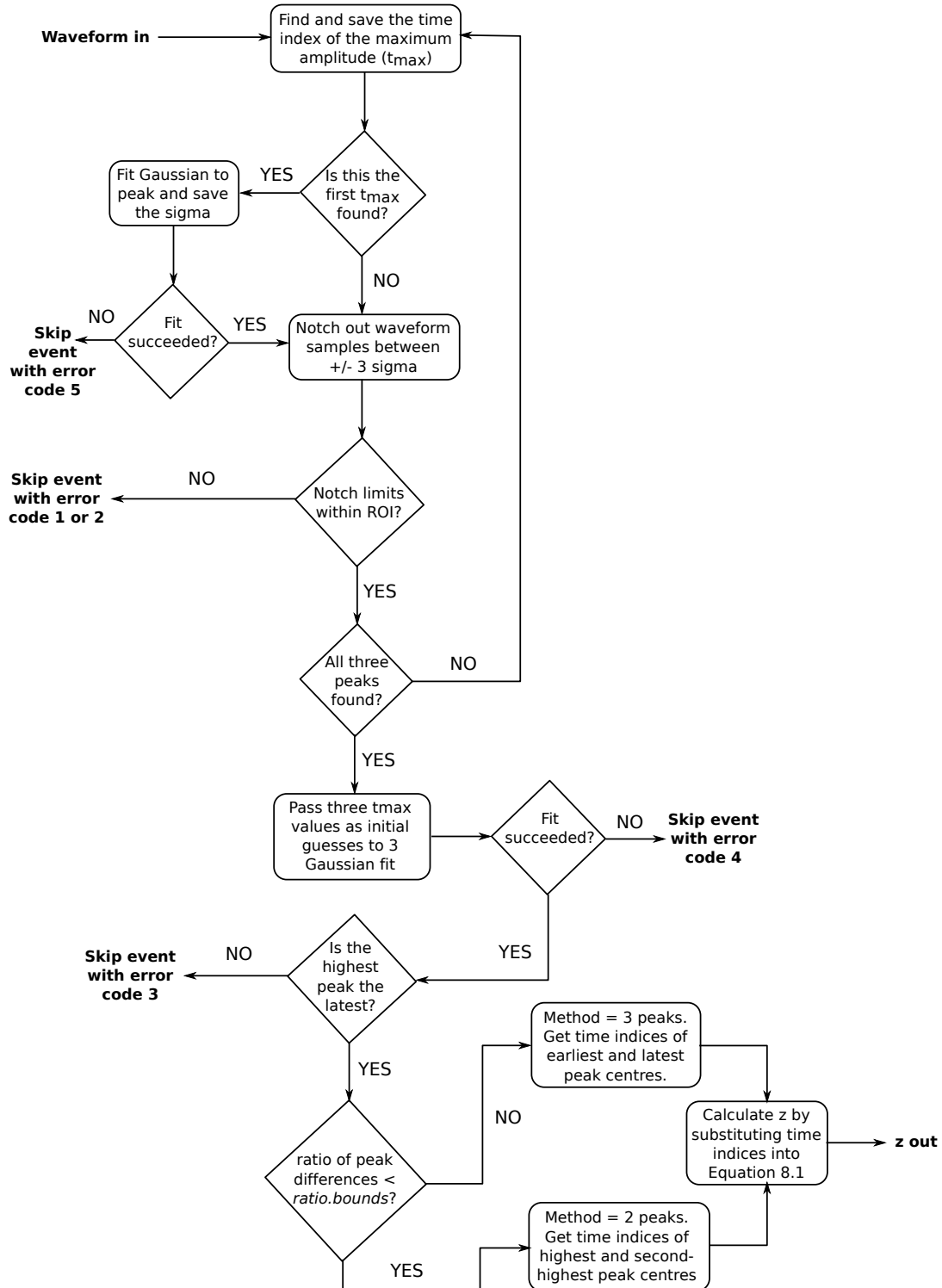
Figure 8.7: Flow chart describing the peak-finding algorithm used to calculate absolute *z* position for minority carrier events.

Cut	Definition	Description	Neut acceptance (d^{-1})
-	-	Rate passing stage 1 and 2 cuts.	855.8
3.1	$ok == TRUE$	Peak finding algorithm finished without errors.	751.3
3.2	$0.25 < \frac{A_p}{A_m} < 2.20$	Ratio of P to main peak.	702.9
3.3	$0.5 < \frac{AnodeNips}{GridNips}$	Ratio of NIPs measured on the anode / grid.	650.3

Table 8.2: Stage 3 cuts used to remove residual background events.

If the condition was satisfied, signifying that three equidistant peaks were found as expected from a minority carrier event, the *method* parameter was set to 3, and the time difference $(t_m - t_p)$ appearing in Equation 8.1 was set to the difference between the earliest and latest peak.

If instead the condition was not met, signifying that one of the peaks in the three-Gaussian fit was erroneous, then *method* was set to 2, and $(t_m - t_p)$ was taken as the time difference between the largest and second-largest area peak. Implicit in this is the assumption that the second-largest peak is the P, rather than the S minority peak. From visual inspection of 'method 2' minority carrier neutron events, this appears to always be the case. Finally, Equation 8.1 was used to calculate the absolute *z* position of the event. In this way, events for which only a single minority peak was found were retained.

8.3.2 Zero-Background Cuts

After running the *z* algorithm, the cuts listed in Table 8.2 were developed and applied to the data with the aim of opening up an area of NIPs-*z* parameter space containing signal events, but no background events. Histograms of the cut variables for background and neutron calibration runs are shown in Figure 8.8.

Cut 3.1 simply checks that the event was processed by the *z*-finding algorithm, exiting normally instead of with any of the error codes shown in Figure 8.7. The well-separated background peak on the left of Figure 8.8a was fit with a Gaussian profile, and the lower limit of the cut (black line) set at a value of 0.21, which is 3σ above the mean of this population. The upper limit of this cut was set to retain all neutron events, but remove some spurious background events with high A_p/A_m. The variable used in Cut 3.3 (*anode.grid.Nips.ratio*) did not exhibit any obvious separation between signal

(a) Cut 3.2   (b) Cut 3.3
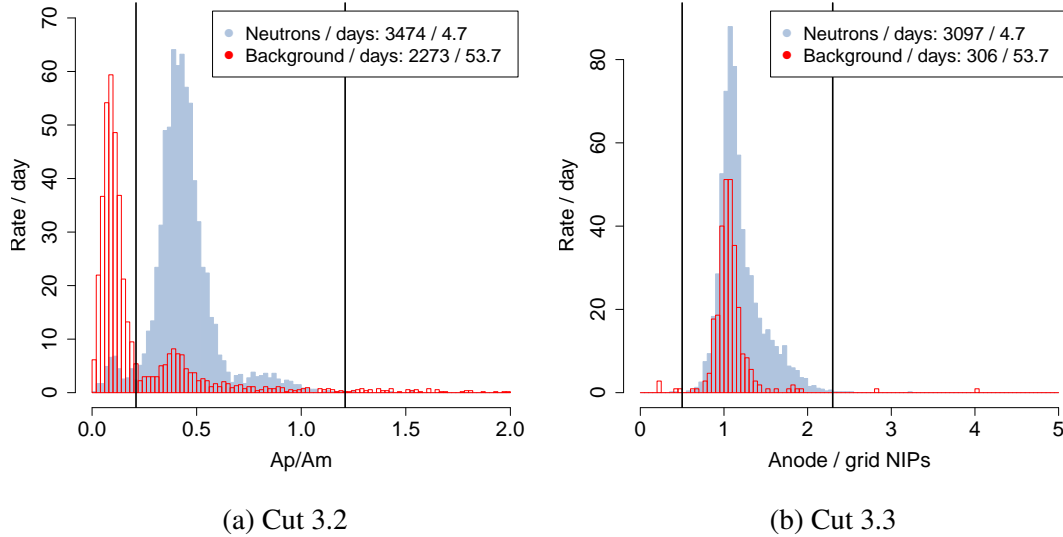
Figure 8.8: Histograms of the variables used in stage 3 cuts. Events outside the limits shown by the vertical black lines were cut.

and background, but was extremely useful for removing the last few spurious events in the $12 \lesssim z \lesssim 46$ cm region. These are made up predominantly of a type of event called 'ringers', which, as their name suggests, have an oscillatory form that can mimic the multiple peaks of minority carrier events and evade other cuts [201]. However, ringers also exhibit a deficit of charge on the grid channels, which makes Cut 3.3 very effective at removing them. Overall, the set of stage 2 and 3 cuts is considerably simpler than those used in the 'traditional' analysis presented in Chapter 4, despite the shape of the signal waveforms being more complicated.

The resulting rate of events passing cuts in each of the neutron and background runs is shown as a function of time in Figure 8.9, in analogy with Figure 8.6. The total event rate in the neutron runs was reduced to 76% of its pre-stage 3 value by the stage 3 cuts, giving an average event rate of 650.3 ± 5.4 d^{-1} after stage 3 cuts. The efficiency loss was split approximately equally between the algorithm Cut 3.1 (104.3 ± 4.7 d^{-1}), and Cuts 3.2 and 3.3 (101 d^{-1}). The events that were not reconstructed, and therefore failed Cut 3.1 (490 in total) were examined to determine whether or not they exhibited the characteristic minority carrier event profile of Figure 8.4. Only 31 events (6.6 ± 1.2 events /d) were identifiable as missed minority carrier events, showing that the

algorithm was > 99% efficient at producing a z value for true minority carrier events making it as far as stage 3 analysis.
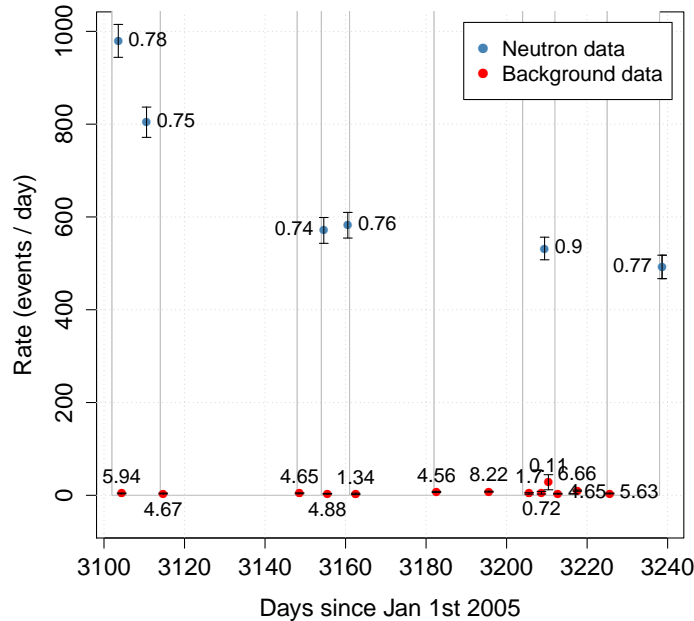
Figure 8.9: Mean rate of events passing all stage 1, 2 and 3 cuts for each of the WIMP search and neutron runs as a function of time. Vertical grey lines mark re-filling of the vacuum vessel with fresh gas, and text labels show the run livetime in days.

8.3.3 Calibrating the z Measurement

The parameter v_{drift} appearing in the z calculation of Equation 8.1 is dependent upon the strength of the drift field E, the vessel pressure p, and the reduced mobility μ according to Equation 5.2. The first two have nominal set values, but small departures from these values are possible. As mentioned previously, the measured reduced mobility for a similar gas mixture has been assumed here, pending up-to-date measurements of the 30:10:1 torr mixture. Each of these effects has the potential to introduce a small systematic error into the z calculation. Therefore, a population of RPR events known to originate from the central cathode at $z = 50$ cm was used to calibrate the z measure-

194

ment. The distribution was fit with a Gaussian profile as shown in Figure 8.10, and the mean was found to be 46.9 ± 1.3 cm. A multiplicative factor equal to the ratio of the expected to the measured z position (50/46.9) was then used to correct all measured z values. The underestimate of the z position is likely caused by an incorrect assumed mobility, which will be updated shortly when new measurements become available.
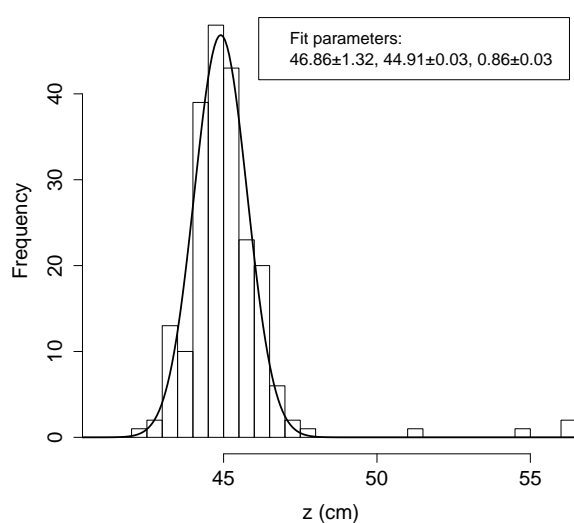
Figure 8.10: Histogram of z position for a sample of RPR events. The mean was found to be slightly lower than the expected 50 cm, suggesting a small systematic offset in the z calculation, which was corrected for.

8.4 Quantifying the Efficiency Improvement

One of the key inputs into the limit calculation presented in Chapter 4 is the efficiency of the detector for detecting WIMP-induced nuclear recoils. The analysis described there used an efficiency calculated using simulated nuclear recoil events, however no such simulation exists for minority carrier data at the time of writing. This is an active area of research for the DRIFT collaboration. For the work presented in this chapter, instead of directly calculating the WIMP efficiency for minority carrier data, an efficiency improvement factor was estimated by taking the ratio of acceptance rates into

background-free signal regions in neutron runs with and without an admixture of oxygen. This is a valid approach as long as the raw neutron rate in the two runs is the same, which is the case since the runs were taken with the neutron source in exactly the same position. This method allowed a limit on the SD WIMP-proton cross section to be estimated following the method described in Chapter 4, which is presented in Section 8.5.

8.4.1 Neutron Acceptance

Traditional Analysis

The traditional DRIFT analysis presented in Pipe [178] and Daw et al. [187] was used to calculate the acceptance rate in a recently-acquired neutron run without oxygen, and with the neutron source in exactly the same position as in the oxygen runs. The analysis detailed in Chapter 4 was applied, including the background-free RMST-NIPs signal region shown in Figure 4.14, and the results are shown in Figure 8.11. This analysis gives a rate of accepted neutrons of 226 ± 16 events /d.
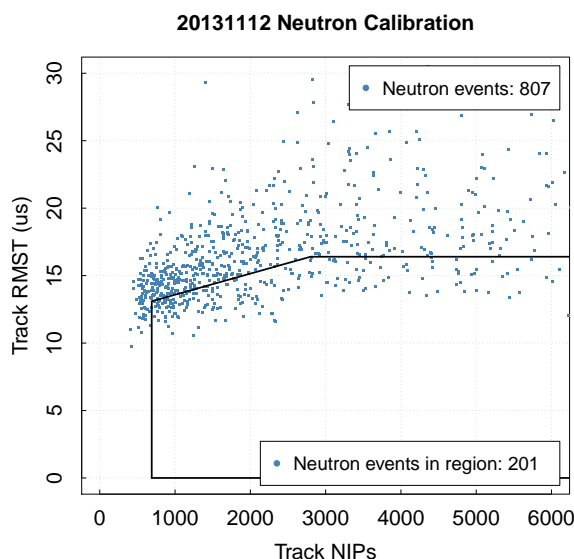
Figure 8.11: NIPs vs RMST distribution for the 0.89-day 20131112 neutron calibration run with a 30:10 torr mixture of CS_2:CF_4. The signal region determined in Pipe [178] (Figure 4.14) is shown.

Minority Carrier Analysis

Figure 8.12 shows the NIPs-z distribution of all events passing the cuts listed in Table 8.2. The population of events from WIMP search runs (red) centred on the cathode at 50 cm are the RPRs and LEAs discussed in Chapter 5. Those at low z and low NIPs are spurious events that do not exhibit minority peaks, but have a wandering baseline that is positive in the region before the charge deposition and is misinterpreted as minority carrier charge by the algorithm.
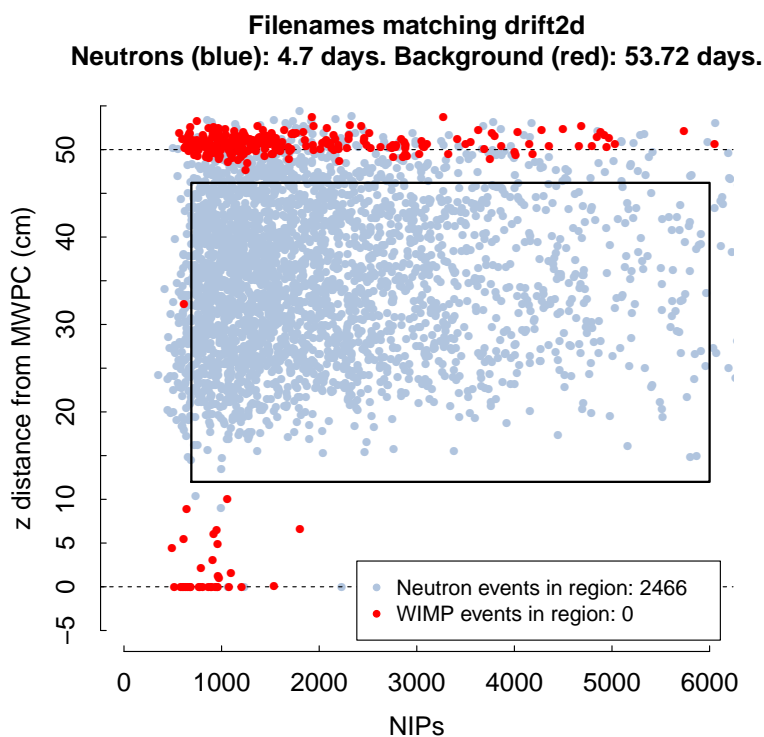
Figure 8.12: NIPs vs z distribution for 53.4 days of dark matter search running (red), and 4.7 days of neutron calibration running (blue) with a 30:10:1 torr mixture of CS_2:CF_4:O_2 and minority carrier analysis.

An unblind signal region has been drawn, which is bounded in NIPs from below at 690 (50 keV$_r^F$) to match the signal region of the analysis described in Chapter 4, and from above at 6000 NIPs to avoid several misidentified α fragments at $\sim$ 8000 NIPs. The region is bounded in z from below at 12 cm from the MWPC plane, which is the

point at which the main and P peaks become so close that they are indistinguishable by the algorithm. Low-z events are therefore cut by either the *mp.ratio* cut or subsequent stage 3 cuts, and do not appear on this plot. The high-z boundary of the signal region was determined from a sample of 50 of the tagged RPR events described in Chapter 5. A Gaussian was fit to the distribution of their corrected z positions in exactly the same way as Section 8.3.3, and the upper boundary of the signal region was set 3σ below the mean of this distribution at 46.2 cm.

A total of 2466 events were accepted by this signal region during the 4.7 days of neutron calibration data, which gives an average neutron acceptance rate of 525 ± 11 d^{-1}. However, the blue points in Figures 8.6 and 8.9 show that the neutron efficiency was not constant over the 53.7 days of WIMP search running. This is likely due to small changes in the oxygen fraction of the mixture driving large changes in the fraction of charge that is transported by minority carriers. Therefore, the first and last neutron runs were used to derive upper and lower limits on the acceptance rate of 809 ± 32 d^{-1} and 303 ± 22 d^{-1}, respectively. The signal regions for the two runs are shown in Figure 8.13.

8.4.2 Efficiency Improvement Factor

The ratio of the neutron acceptance rates for the traditional and minority carrier analyses calculated in Section 8.4.1 gives an estimate of the factor by which the efficiency for detecting WIMPs improved when moving from the former to the latter. The improvement factor was found to be

$$F = \frac{R_{trad.}}{R_{min.\ car.}} = \begin{cases} \text{highest acceptance,} & 3.58 \pm 0.29 \\ \text{mean acceptance,} & 2.32 \pm 0.17 \\ \text{lowest acceptance,} & 1.34 \pm 0.14, \end{cases} \tag{8.5}$$

depending on the assumed neutron acceptance rate. The neutron rate under continuous flow conditions will be investigated once the aforementioned MFC safety modifications have been made to allow running in this mode.

(a) 20131113 Neutron data. (b) 20130701 Neutron data.
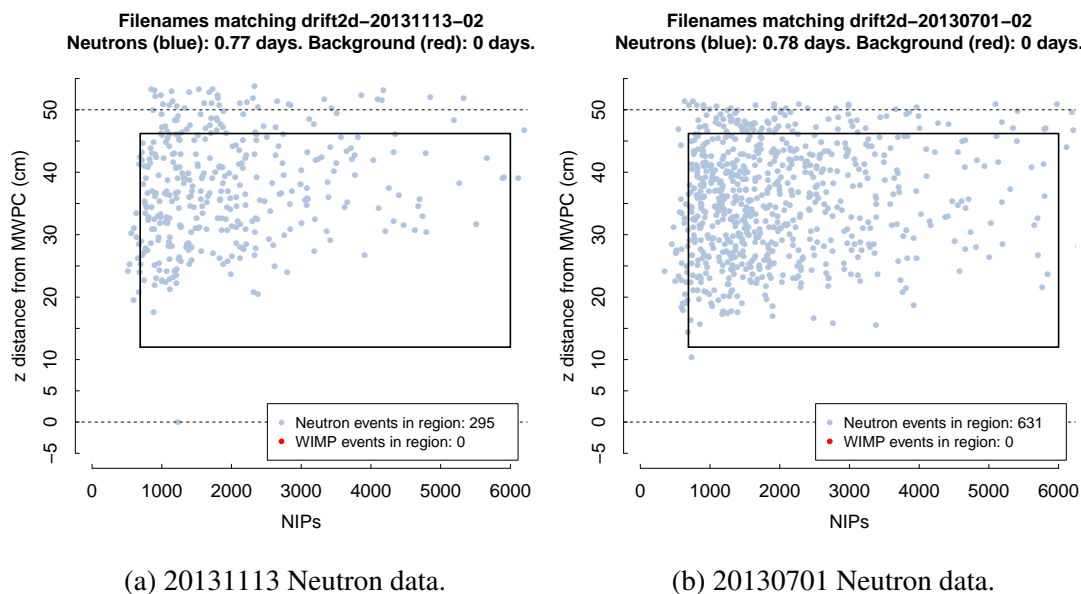
Figure 8.13: RMST-NIPs for the highest- and lowest-efficiency neutron runs.

8.5 Limit on $\sigma_{WN}^{SD}(M_W)$ from Minority Carrier Data

A set of 32 plots of RMST vs NIPs such as the example in Figure 4.15 spanning WIMP masses from $11 < M_W < 100000 \, \text{GeV} / \text{c}^2$ were generated in order to calculate the blue traditional analysis efficiency curve presented in Figure 8.14, following the method detailed in Chapter 4. Multiplying this curve by the mean-acceptance F factor calculated in the previous section yielded the curve shown in red, whilst the maximum- and minimum-acceptance F factors define the upper- and lower- bounds of the range of measured neutron efficiencies shown in orange.

The efficiency improvement shown in Figure 8.14 translates directly into a strengthening of the $\sigma_{WN}^{SD}(M_W)$ limit curve relative to the analysis of Pipe [178]. This improvement is shown in Figure 8.15, along with limits from the two leading spin-dependent direct detection experiments, COUPP and SIMPLE, which are described in Chapter 3.
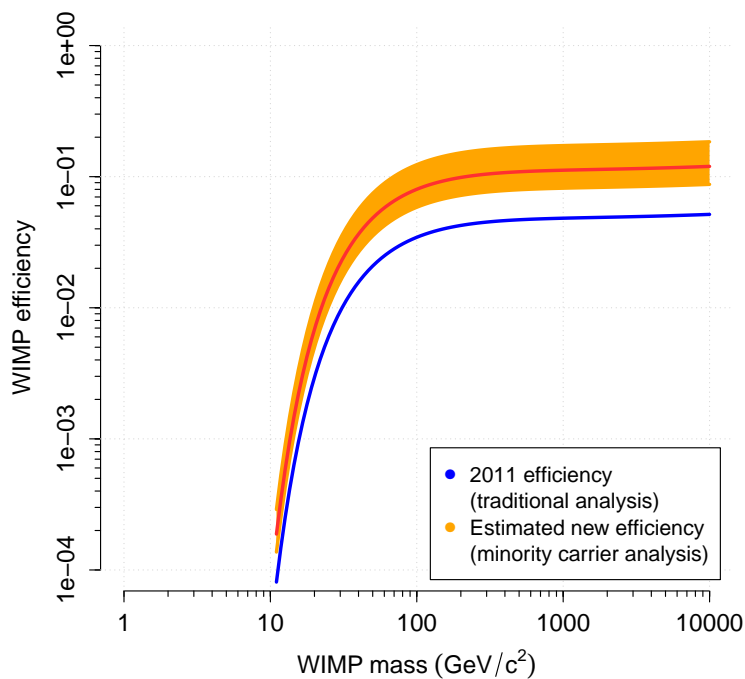
Figure 8.14: WIMP efficiency as a function of M_W after stage 3 cuts.

Figure 8.15 clearly demonstrates that moving to minority carrier operation and analysis improves the limit-setting power of the experiment. The exact factor improvement is somewhat uncertain due to uncertainty in the minority carrier neutron efficiency caused by differences in the oxygen partial pressure between runs. This is shown by the wide orange bands representing the best- and worst- case neutron efficiency scenarios. However, in the immediate future the detector will begin taking data in constant flow mode instead of the sealed mode that was employed here, which is expected to stabilise the efficiency. It is expected that with careful control of the oxygen partial pressure, a stable efficiency close to the best-case scenario can be achieved. But most importantly, this will be further improved upon by optimising the analysis chain, reducing the energy threshold and improving the peak-finding algorithm to successfully measure the z position of a higher proportion of neutron calibration events.

Looking forward to the 24 m^3 DRIFT-III detector, it will be important to ensure that as much of the fiducial volume as possible is sensitive to WIMP-nucleus interac-
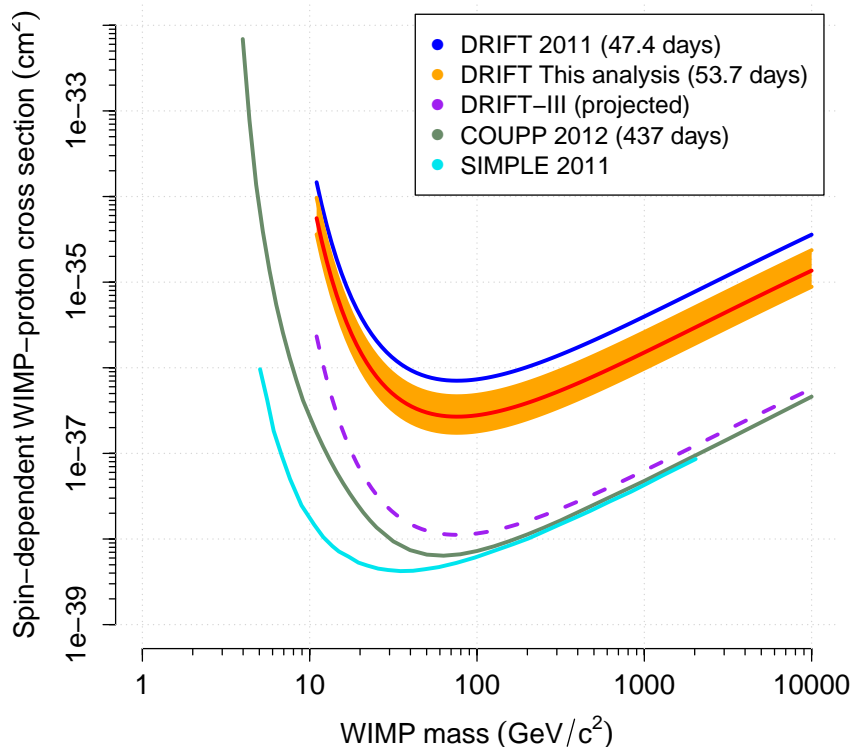
Figure 8.15: Limits on $\sigma_{Wp}^{SD}(M_W)$ from minority carrier data, compared with a previous DRIFT analysis [178] and other leading experiments. A projected limit is also shown for a 24 m^3 DRIFT-III detector (see text for details).

tions. Lacking a z measurement, in the past it has not been possible to quantify this, however the low-z cutoff of neutron events in Figure 8.12 suggests that DRIFT-IId is sensitive between $\sim 15 < z < 50$ cm, or 70% of the fiducial volume. This number can be increased by improving the algorithm to distinguish more closely-spaced peaks, allowing lower-z events to be retained, and producing a corresponding increase in efficiency. A projected limit for a 24 m^3 DRIFT-III detector is shown in dashed purple on Figure 8.15. This was calculated assuming zero events in a signal region with efficiency equal to the mean efficiency from this analysis (red line on this Figure) multiplied by the detector volume increase (a factor of 24), and 53.7 days' livetime.. Finally, an important area of work moving forward is the development and validation

of a minority carrier event simulation, which will facilitate direct limit setting with minority carrier data.

8.6   Conclusions

The minority carrier technique has been introduced for the first time, and demonstrated to provide a measurement of the absolute z position of events in the detector. Since all known background populations originate from either the MWPCs (minimal z) or central cathode (maximal z), this provides an extremely powerful method for discriminating signal from background. The cuts developed for the minority carrier analysis are also considerably simpler than those necessary to give zero background in the traditional analysis, thanks to the very distinctive shape of minority carrier charge depositions. A peak-finding algorithm was developed and employed to provide a fully-automated measurement of the z position of events. A large background-free signal region was defined in NIPS-z space, and applied to neutron data to calculate the neutron acceptance rate, which was then compared with the equivalent rate from the traditional analysis to provide an improvement in limit-setting power over the traditional analysis of a factor $F \sim 3$. This factor is expected to improve considerably as the collaboration learns how to better exploit this exciting new technique.

Chapter 9

Conclusions

There is a compelling body of evidence to suggest that the matter content of the Universe is dominated by a dark component comprised of some exotic new particle or group of particles that interacts extremely weakly with baryonic matter. A particularly well-motivated class of candidates for this dark matter (DM) are the WIMPs. The hunt for WIMPs has been underway for several decades, using many different techniques ranging from direct searches in deep underground sites to missing energy searches at colliders, to space-based searches for the tell-tale gamma line emission from annihilating dark matter.

The past three years have been an exciting time for direct searches, with hints of a signal appearing in several solid-state detectors that seem to be in broad agreement with the long-standing but contentious claim of discovery from the DAMA collaboration. Taken together, these experiments appear to favour a WIMP with mass ≈ 12 GeV $/c^2$ and spin-independent cross section $\approx 10^{-41}$ cm^2. However, such a particle is strongly disfavoured by the lack of a confirmatory signal in any of the liquid noble gas detectors, which now exclude WIMPs with a cross-section $\gtrsim 10^{-45}$ GeV $/c^2$ in this mass region, even when the properties of the DM halo are allowed to vary within reasonable limits. It is therefore not clear how one should interpret the results of direct detection experiments at the time of writing.

Meanwhile, interest has grown in the directional signature that is produced as the Earth moves through the DM halo, which can be searched for using a gas time projection chamber. There are now four groups operating such directional detectors underground in the UK, USA, France and Japan. Of these, the pioneer of the technique,

DRIFT, stands alone as the only directional detector approaching the sensitivity required to detect a WIMP with a spin-dependent cross section that has not yet been ruled out by Superheated liquid detectors such as SIMPLE and COUPP. It may be that a spin-dependent signal of DM lies just out of reach of these experiments.

This thesis has investigated possible improvements to DRIFT in preparation for scale-up to the 24 m^3 DRIFT-III detector, which will have the best chance yet to measure the directional signature of DM particles possessing a spin-dependent interaction. Chapter 5 was concerned with ways to measure, monitor and reduce radon gas, which is a problem not only for DRIFT, but also for many other rare event searches: double beta decay experiments such as SuperNEMO, solar neutrino searches such as Borexino, and other DM searches such as DEAP-3600. By using two separate techniques to measure the radon emanation rate into the DRIFT vacuum vessel, and comparing this to the sum of emanation rates from known radon-hot detector components, a coherent picture of radon in DRIFT was presented. Through materials substitution the radon emanation rate was reduced by a factor of two. The current detector was shown to be sensitive to radon at the ~ μBq level, which opens up the possibility of using DRIFT as an assay instrument to support other rare event searchess such as those listed above.

Chapter 6 investigated the effect of simplifying the DRIFT electronics chain, which will be necessary when scaling up to a larger detector that will require thousands of readout channels. The directional capability and background discrimination power of such a simplified electronics scheme were investigated and found to be similar to the present scheme, which is encouraging from the point of view of scale-up. Other members of the collaboration are investigating further improvements to the electronics chain to be trialled on DRIFT-IIe, including multiplexing the signals using high-frequency analogue electronics, which should help to keep costs down for DRIFT-III.

Another area identified for simplification and improvement was the gas mixing system, as detailed in Chapter 7. A new system was designed and built at the University of Sheffield, and installed underground on the prototype detector DRIFT-IIe. This system incorporates simpler, cheaper components than the current system, and is also more remotely-controllable, which should help to save on manpower when moving to a 24 m^3 detector. However, at this scale, operating the gas system in the current open-loop configuration is disfavoured due to the large amount of CS_2 required, which is an issue of both cost and manpower in transporting it to and from the underground lab. To

this end, preliminary work on an RGA rig was undertaken, which showed that the gas composition does change when it is exposed to the operational detector. Further tests will show whether or not recirculation of used, condensed CS_2 gas is possible. Other R&D is in progress at Sheffield into alternatives such as active scrubbing of radon from the gas using activated carbon filters.

Finally, in 2013 the collaboration made a breakthrough with the discovery that adding a small admixture of oxygen to the gas mixture produces minority charge carriers that can be used to fiducialise events in the z-dimension by virtue of their differing drift velocities. An automated analysis of minority carrier data was developed in Chapter 8, the first of its kind, and applied to 53.7 days of WIMP search data. As expected, the main background population comes from the decay of radon daughter particles plated out on the central cathode at $z = 50$ cm. A cut of $z < 46.2$ cm was therefore used to define a signal region in z-NIPs space that was shown, using neutron calibration data, to be considerably more efficient than the RMST-NIPs signal region of previous analyses. Uncertainty remains over the precise efficiency during the WIMP search run, because of the sensitivity of the minority carrier mechanism to changes in the oxygen partial pressure of the gas mixture, but this will be rectified in the near future when continuous flow minority carrier operation is realised. In this work, an estimated limit is presented, where even the most conservative low estimate of the efficiency brings a significant improvement to the limit-setting power of the experiment.

Appendix

The induction of a current in a conductor by a charge moving in its vicinity can be understood by application of the 'weighting field' concept [170].

The reciprocity theorem of electrostatics [207] relates an electrostatic potential V_1 on an electrode (either real, or an infinitesimal 'test' electrode) inducing a charge Q_2 on a nearby electrode, to a different potential V_2' inducing a charge Q_1' on the original electrode:

$$Q_1' V_1 = Q_2 V_2' \tag{1}$$

Now, consider an infinitesimal test electrode with potential V_m, which has a charge q_m induced on it by a nearby real Electrode 1 at potential V_1, itself having a charge of Q_1 induced on it by the test electrode. All other conductors are assumed to be grounded. According to Equation 1, then:

$$q_m V_m = Q_1 V_1 \tag{2}$$

The current induced on Electrode 1 by a movement of the test electrode along the vector $d\mathbf{l}$, at velocity $\mathbf{v} = \frac{d\mathbf{l}}{dt}$ can be calculated as follows:

$$I_1 = \frac{dQ_1}{dt} = q_m \cdot \frac{d\left(\frac{V_m}{V_1}\right)}{dt} = q_m \cdot \frac{d\left(\frac{V_m}{V_1}\right)}{d\mathbf{l}} \cdot \mathbf{v}. \tag{3}$$

V_m/V_1 is simply a normalised electrical potential, therefore its differential with respect to $\mathbf{l}$ can be written as:

$$\frac{d\left(\frac{V_m}{V_1}\right)}{d\mathbf{l}} = \boldsymbol{\nabla}\left(\frac{V_m}{V_1}\right) = -E_w, \tag{4}$$

where we E_w, the weighting field, has been introduced. Requiring that q_m remains constant (to mimic a real carrier of fixed electric charge) and substituting Equation 4 into Equation 3 gives an expression for the current induced on Electrode 1 by the test charge 'm', as a function of m's velocity ($\mathbf{v}$), and the weighting field E_w, which itself depends only upon the gradient of the scalar potential field V_m/V_1:

$$I_1 = -q_m \mathbf{E_w} \mathbf{v}. \tag{5}$$

To obtain the weighting field $\mathbf{E_w}$, we set $V_1 = 1$ and the potential of all other conductors to zero. $\mathbf{v(l)}$ can be calculated from the true applied electric field E, and converted into $\mathbf{v}(t)$ by solving the equations of motion for the test particle. Finally, substituting into Equation 5, an expression for the current as a function of time is obtained, which is the signal to be read out by the TPC electronics.

References

[1] A. Liddle. *An introduction to modern cosmology*. 2nd ed. Wiley, 2007. (Cit. on pp. 1, 2).

[2] E. Hubble. A relation between distance and radial velocity among extra-galactic nebulae. *Proc. Natl. Acad. Sci.* 15 (1929), pp. 168–173. (Cit. on p. 2).

[3] P. A. R. Ade et al. Planck 2013 results. XVI. Cosmological parameters. *arXiv Prepr. arXiv1303.5076v1* (2013). (Cit. on pp. 2–4, 7).

[4] C. L. Bennett et al. Nine-year Wilkinson Microwave Anisotropy Probe (WMAP) observations: final maps and results. *Astrophys. J. Suppl. Ser.* 208.2 (Oct. 2013), p. 20. (Cit. on p. 2).

[5] G. F. Smoot and C. L. Bennett. Structure in the COBE differential microwave radiometer first-year maps. *Astrophys. J.* 396 (1992), pp. L1–L5. (Cit. on p. 2).

[6] N. Jarosik et al. Seven-year Wilkinson Microwave Anisotropy Probe (WMAP) observations: sky maps, systematic errors, and basic results. *Astrophys. J. Suppl. Ser.* 192.2 (2011), p. 14. (Cit. on p. 2).

[7] A. G. Riess et al. Obervational evidence from supernovae for an expanding universe and a cosmological constant. *Astron. J.* 116 (1998), pp. 1009–1038. (Cit. on p. 3).

[8]   J. Martin. Everything you always wanted to know about the cosmological constant problem (but were afraid to ask). *Comptes Rendus Phys.* 13.6–7 (2012), pp. 566–665. (Cit. on p. 3).

[9]   F. Zwicky. Die Rotverschiebung von extragalaktischen Nebeln. *Helv. Phys. Acta* 6 (1933), pp. 110–127. (Cit. on p. 4).

[10]   S. Smith. The mass of the Virgo Cluster. *Astrophys. J.* 83 (1936), p. 23. (Cit. on p. 4).

[11]   V. C. Rubin and W. K. Ford Jr. Rotation of the Andromeda nebula from a spectroscopic survey of emission regions. *Astrophys. J.* 159 (1970), pp. 379–403. (Cit. on p. 5).

[12]   M. S. Roberts and R. N. Whitehurst. The rotation curve and geometry of M31 at large galactocentric distances. *Astrophys. J.* 201 (1975), pp. 327–346. (Cit. on p. 6).

[13]   A. Bosma. The distribution and kinematics of neutral hydrogen in spiral galaxies of various morphological types. PhD thesis. Groningen University, 1978. (Cit. on p. 6).

[14]   A. A. Penzias and R. W. Wilson. A measurement of excess antenna temperatue at 4080 Mc/s. *Astrophys. J.* 142.1 (1965), pp. 419–421. (Cit. on p. 6).

[15]   J. Beringer et al. Review of particle physics. *Phys. Rev. D* 86.1 (July 2012), p. 010001. (Cit. on pp. 6, 8, 9, 59, 60).

[16]   R. V. Wagoner. Big-bang nucleosynthesis revisited. *Astrophys. J.* 179 (1973), pp. 343–360. (Cit. on p. 9).

[17]   M. Pettini et al. Deuterium abundance in the most metal-poor damped Lyman alpha system: converging on $\Omega_{b,0} h2$. *Mon. Not. R. Astron. Soc.* 391.4 (Dec. 2008), pp. 1499–1510. (Cit. on p. 10).

[18]   R. H. Cyburt, B. D. Fields, and K. a. Olive. An update on the big bang nucleosynthesis prediction for 7 Li: the problem worsens. *J. Cosmol. Astropart. Phys.* 2008.11 (Nov. 2008), p. 012. (Cit. on p. 10).

[19] B. D. Fields. The primordial lithium problem. *Annu. Rev. Nucl. Part. Sci.* 61.1 (Nov. 2011), pp. 47–68. (Cit. on p. 10).

[20] P. Tisserand et al. Limits on the MACHO content of the Galactic Halo from the EROS-2 survey of the Magellanic Clouds. *Astron. Astrophys.* 469.2 (2008), pp. 387–404. (Cit. on p. 11).

[21] A. C. Becker et al. The SuperMACHO microlensing survey. *Proc. IAU Symp. No. 225*. Ed. by Y. Mellier and G. Meylan. Vol. 2004. IAUS225. June 2004, pp. 357–362. (Cit. on p. 11).

[22] D. Walsh, R. F. Carswell, and R. J. Weymann. 0957+561 A, B: twin quasistellar objects or gravitational lens? *Nature* 279 (1979), pp. 381–384. (Cit. on p. 11).

[23] J. M. Kubo et al. Dark matter structures in the Deep Lens Survey. *Astrophys. J.* 702.2 (Sept. 2009), pp. 980–988. (Cit. on pp. 11–13).

[24] B. Paczynski. Gravitational microlensing by the Galactic halo. *Astrophys. J.* 304 (1986), pp. 1–5. (Cit. on p. 11).

[25] C. Alcock et al. The MACHO project: microlensing results from 5.7 years of Large Magellanic Cloud observations. *Astrophys. J.* 542 (2000), pp. 281–307. (Cit. on p. 11).

[26] M. I. Wilkinson and N. W. Evans. The present and future mass of the Milky Way halo. *Mon. Not. R. Astron. Soc.* 310.3 (Dec. 1999), pp. 645–662. (Cit. on p. 11).

[27] D. Wittman et al. Detection of weak gravitational lensing distortions of distant galaxies by cosmic dark matter at large scales. *Nature* 405 (May 2000), pp. 143–148. (Cit. on pp. 11, 14).

[28] D. Wittman et al. First results on shear-selected clusters from the deep lens survey: Optical imaging, spectroscopy, and X-ray follow-up. *Astrophys. J.* 643 (2006), pp. 128–143. (Cit. on p. 12).

[29] H. Shan et al. Weak lensing measurement of galaxy clusters in the CFHTLS-wide survey. *Astrophys. J.* 748.1 (Mar. 2012), p. 56. (Cit. on p. 12).

[30] D. Clowe, A. Gonzalez, and M. Markevitch. Weak-lensing mass reconstruction of the interacting cluster 1E0657-558: direct evidence for the existence of dark matter. *Astrophys. J.* 604 (2004), pp. 596–603. (Cit. on p. 12).

[31] M. Milgrom. A modification of the Newtonian dynamics as a possible alternative to the hidden mass hypothesis. *Astrophys. J.* 270 (1983), pp. 365–370. (Cit. on p. 12).

[32] G. Bertone. *Particle Dark matter: Observations, Models and Searches*. Cambridge University Press, 2010. (Cit. on pp. 13, 22, 57, 60, 61).

[33] L. Fu et al. Very weak lensing in the CFHTLS wide: cosmology from cosmic shear in the linear regime. *Astron. Astrophys.* 479.1 (2008), pp. 9–25. (Cit. on p. 13).

[34] V. Springel et al. Simulations of the formation, evolution and clustering of galaxies and quasars. *Nature* 435 (June 2005), pp. 629–636. (Cit. on pp. 13, 14).

[35] M. Boylan-Kolchin et al. Resolving cosmic structure formation with the Millennium-II Simulation. *Mon. Not. R. Astron. Soc.* 398 (Sept. 2009), pp. 1150–1164. (Cit. on p. 14).

[36] V. Springel, C. S. Frenk, and S. D. M. White. The large-scale structure of the Universe. *Nature* 440.7088 (Apr. 2006), pp. 1137–1144. (Cit. on pp. 14, 15).

[37] S. Dodelson, E. I. Gates, and M. S. Turner. Cold dark matter. *Science (80-.).* 274.5284 (Oct. 1996), pp. 69–75. (Cit. on p. 15).

[38] A. Knebe and B. Gibson. Galactic haloes in MONDian cosmological simulations. *Mon. Not. R. Astron. Soc.* 347.4 (2004), pp. 1055–1064. (Cit. on p. 15).

[39] M. Taoso, G. Bertone, and A. Masiero. Dark matter candidates: a ten-point test. *J. Cosmol. Astropart. Phys.* 2008 (2008), p. 022. (Cit. on p. 16).

[40] A. De Rujula, S. L. Glashow, and U. Sarid. Charged dark matter. *Nucl. Phys. B* 333 (1990), pp. 173–194. (Cit. on p. 16).

[41] F. Iocco. Dark matter capture and annihilation on the first stars: preliminary estimates. *Astrophys. J.* 677.1 (Apr. 2008), pp. L1–L4. (Cit. on p. 16).

[42] S. W. Randall and M. Markevitch. Constraints on the self-interaction cross section of dark matter from numerical simulations of the merging galaxy cluster 1E 065756. *Astrophys. J.* 679 (2008), p. 1173. (Cit. on p. 17).

[43] G. Jungman, M. Kamionkowski, and K. Griest. Supersymmetric dark matter. *Phys. Rep.* 267 (1996), pp. 195–373. (Cit. on pp. 17, 19).

[44] M. Cirelli, N. Fornengo, and A. Strumia. Minimal dark matter. *Nucl. Phys. B* 753 (2006), pp. 178–194. (Cit. on pp. 17, 20).

[45] T. Schwetz-Mangold. Dark matter phenomenology. *ISAPP 2011 , MPIK Heidelb. Dark Side Universe*. July. Heidelberg, 2011. (Cit. on p. 17).

[46] R. J. Scherrer and M. S. Turner. On the relic, cosmic abundance of stable, weakly interacting massive particles. *Phys. Rev. D* 33.6 (1986), pp. 1585–1589. (Cit. on p. 17).

[47] D. Bauer et al. *Dark Matter in the Coming Decade: Complementary Paths to Discovery and Beyond*. Tech. rep. Fermilab, 2013. (Cit. on p. 18).

[48] J. L. Feng. Dark matter candidates from particle physics and methods of detection. *Annu. Rev. Astron. Astrophys.* 48 (2010), pp. 495–545. (Cit. on pp. 18, 19, 21, 60).

[49] G. Aad et al. Observation of a new particle in the search for the Standard Model Higgs boson with the ATLAS detector at the LHC. *Phys. Lett. B* 716.1 (Sept. 2012), pp. 1–29. (Cit. on p. 18).

[50] A. Barr et al. *Searches for Supersymmetry at the high luminosity LHC with the ATLAS detector*. Tech. rep. Geneva: CERN, 2013, pp. 0–17. (Cit. on p. 20).

[51] S. Chatrchyan et al. Interpretation of searches for supersymmetry with simplified models. *Phys. Rev. D* 88.5 (2013), p. 052017. (Cit. on pp. 20, 61).

[52] M. Cirelli and A. Strumia. Minimal dark matter: model and results. *New J. Phys.* 11 (2009), p. 105005. (Cit. on pp. 20, 21).

[53] J. Hisano et al. Non-perturbative effect on thermal relic abundance of dark matter. *Phys. Lett. B* 646.1 (Mar. 2007), pp. 34–38. (Cit. on p. 20).

[54] H.-C. Cheng, J. Feng, and K. Matchev. Kaluza-Klein dark matter. *Phys. Rev. Lett.* 89.21 (Oct. 2002), p. 211301. (Cit. on p. 20).

[55] T. Kakuda et al. Universal extra dimensions after Higgs discovery. *Phys. Rev. D* 88 (2013), p. 035007. (Cit. on p. 21).

[56] M. Schmaltz and D Tucker-Smith. Little Higgs review. *Annu. Rev. Nucl. Part. Sci.* 55.3 (2005), pp. 229–270. (Cit. on p. 22).

[57] A. Birkedal et al. Little Higgs dark matter. *Phys. Rev. D* 74.3 (Aug. 2006), p. 035002. (Cit. on p. 22).

[58] I. Chakraborty and A. Kundu. Controlling the fine-tuning problem with singlet scalar dark matter. *Phys. Rev. D* 87.5 (Mar. 2013), p. 055015. (Cit. on p. 22).

[59] S. Dodelson and L. Widrow. Sterile neutrinos as dark matter. *Phys. Rev. Lett.* 72.1 (1994), pp. 17–20. (Cit. on p. 22).

[60] M. Gell-Mann, P. Ramond, and R. Slansky. *Complex Spinors and Unified Theories*. 1979. (Cit. on p. 22).

[61] A. Boyarsky, D. Iakubovskyi, and O. Ruchayskiy. Next decade of sterile neutrino studies. *Phys. Dark Universe* 1.1–2 (2012), pp. 136–154. (Cit. on p. 22).

[62] L. Canetti et al. Dark matter, baryogenesis and neutrino oscillations from right-handed neutrinos. *Phys. Rev. D* 87.9 (May 2013), p. 093006. (Cit. on p. 22).

[63] L. Canetti, M. Drewes, and M. Shaposhnikov. Sterile neutrinos as the origin of dark and baryonic matter. *Phys. Rev. Lett.* 110.6 (Feb. 2013), p. 061801. (Cit. on p. 22).

[64] C. R. Watson, Z. Li, and N. K. Polley. Constraining sterile neutrino warm dark matter with Chandra observations of the Andromeda galaxy. *J. Cosmol. Astropart. Phys.* 2012.03 (Mar. 2012), p. 018. (Cit. on p. 23).

[65] M. Loewenstein and A. Kusenko. Dark Matter Search Using Xmm-Newton Observations of Willman 1. *Astrophys. J.* 751.2 (June 2012), p. 82. (Cit. on p. 23).

[66] R. Peccei and H. Quinn. Constraints imposed by CP conservation in the presence of pseudoparticles. *Phys. Rev. D* 16.6 (1977), pp. 1791–1797. (Cit. on p. 23).

[67] C. A. Baker et al. Improved experimental limit on the electric dipole moment of the neutron. *Phys. Rev. Lett.* 97.13 (Sept. 2006), p. 131801. (Cit. on p. 23).

[68] J. E. Kim and G. Carosi. Axions and the strong CP problem. *Rev. Mod. Phys.* 82.1 (Mar. 2010), pp. 557–601. (Cit. on p. 23).

[69] N. Viaux et al. Neutrino and axion bounds from the globular cluster M5 (NGC 5904). *Phys. Rev. Lett.* 111.23 (Dec. 2013), p. 231301. (Cit. on p. 23).

[70] P Sikivie. Experimental tests of the "invisible" axion. *Phys. Rev. Lett.* 51.16 (1983), pp. 1415–1417. (Cit. on p. 23).

[71] S. J. Asztalos et al. SQUID-based microwave cavity search for dark-matter axions. *Phys. Rev. Lett.* 104.4 (Jan. 2010), p. 041301. (Cit. on p. 23).

[72] D. E. Kaplan, M. Luty, and K. M. Zurek. Asymmetric dark matter. *Phys. Rev. D* 79.11 (June 2009), p. 115016. (Cit. on p. 23).

[73] J Kumar. Asymmetric dark matter. *arXiv Prepr. arXiv1308.4513v2* (2013). (Cit. on p. 23).

[74] E. Daw. A review of the theory of WIMP scattering off target nuclei. *Priv. Commun.* (2011). (Cit. on pp. 26, 31, 33, 34).

[75] J. D. Lewin and P. Smith. Review of mathematics, numerical factors, and corrections for dark matter experiments based on elastic nuclear recoil. *Astropart. Phys.* 6.96 (1996), pp. 87–112. (Cit. on pp. 27, 31, 32, 36, 38).

[76] M. C. Smith et al. The RAVE Survey: constraining the local Galactic escape speed. *Proc. Int. Astron. Union* 235 (Apr. 2007), p. 137. (Cit. on pp. 28, 32, 41).

[77] E. Fermi. *Notes On Quantum Mechanics*. 2nd ed. University of Chicago Press, 1995. (Cit. on p. 33).

[78] J. Engel. Nuclear form factors for the scattering of neutralinos. *Nucl. Phys. B-Proceedings Suppl.* 28A (1992), pp. 310–313. (Cit. on p. 36).

[79] D. R. Tovey et al. A new model-independent method for extracting spin-dependent cross section limits from dark matter searches. *Phys. Lett. B* 488 (2000), pp. 17–26. (Cit. on pp. 38, 39).

[80] D. Chitwood et al. Improved measurement of the positive-muon lifetime and determination of the Fermi constant. *Phys. Rev. Lett.* 99.3 (July 2007), p. 032001. (Cit. on p. 38).

[81] M. Newby. *MilkyWay@Home*. http://milkyway.cs.rpi.edu/milkyway/science.php. 2014. (Cit. on p. 41).

[82] B. Morgan, A. Green, and N. Spooner. Directional statistics for realistic weakly interacting massive particle direct detection experiments. *Phys. Rev. D* 71.10 (May 2005), p. 103507. (Cit. on p. 41).

[83] J. Bovy and S. Tremaine. On the local dark matter density. *Astrophys. J.* 756 (2012), p. 89. (Cit. on pp. 41, 44).

[84] A. Sanna et al. Trigonometric parallaxes to star-forming regions within 4 kpc of the galactic center. *arXiv Prepr. arXiv1312.3181* (2013), pp. 1–31. (Cit. on pp. 41, 44).

[85] J. Diemand et al. Clumps and streams in the local dark matter distribution. *Nature* 454 (Aug. 2008), pp. 735–738. (Cit. on p. 42).

[86] J. Stadel et al. Quantifying the heart of darkness with GHALO - a multibillion particle simulation of a galactic halo. *Mon. Not. R. Astron. Soc.* 398 (Sept. 2009), pp. L21–L25. (Cit. on p. 42).

[87] J. Einasto. Kinematics and dynamics of stellar systems. *Astrofiz. Alma-Ata* 51 (1965), p. 87. (Cit. on p. 42).

[88] J. Navarro, C. Frenk, and S. D. M. White. The structure of cold dark matter halos. *Astrophys. J.* 462 (1996), pp. 563–575. (Cit. on p. 42).

[89] B. Moore et al. Dark matter substructure within galactic halos. *Astrophys. J.* 524 (1999), pp. L19–L22. (Cit. on p. 43).

[90] G. Gentile et al. The cored distribution of dark matter in spiral galaxies. *Mon. Not. R. Astron. Soc.* 351.3 (July 2004), pp. 903–922. (Cit. on p. 43).

[91] E. Hayashi, J. F. Navarro, and V. Springel. The shape of the gravitational potential in cold dark matter halos. *Mon. Not. R. Astron. Soc.* 377.1 (2007), pp. 50–62. (Cit. on p. 43).

[92] P. Bode, J. P. Ostriker, and N. Turok. Halo formation in warm dark matter models. *Astrophys. J.* 556 (2001), pp. 93–107. (Cit. on p. 43).

[93] D. N. Spergel and P. J. Steinhardt. Observational evidence for self-interacting cold dark matter. *Phys. Rev. Lett.* 84.17 (Apr. 2000), pp. 3760–3763. (Cit. on p. 43).

[94] R. Wojtak et al. Radial velocity moments of dark matter haloes. *Mon. Not. R. Astron. Soc.* 361 (July 2005), pp. L1–L5. (Cit. on p. 43).

[95]   P. Bhattacharjee et al. Deriving the velocity distribution of Galactic dark matter particles from the rotation curve data. *Phys. Rev. D* 87.8 (2013), p. 083525. (Cit. on p. 43).

[96]   F. Mandl. *Statistical Physics*. 2nd ed. The Manchester Physics Series. Wiley, 2008. (Cit. on p. 43).

[97]   M. Fairbairn, T. Douce, and J. Swift. Quantifying astrophysical uncertainties on dark matter direct detection results. *Astropart. Phys.* 47 (2013), pp. 45–53. (Cit. on pp. 44–46).

[98]   J. Diemand, B. Moore, and J. Stadel. Earth-mass dark-matter haloes as the first structures in the early Universe. *Nature* 433 (2005), pp. 389–391. (Cit. on p. 44).

[99]   A. Schneider, L. Krauss, and B. Moore. Impact of dark matter microhalos on signatures for direct and indirect detection. *Phys. Rev. D* 82.6 (2010), p. 063525. (Cit. on p. 44).

[100] M. Vogelsberger and S. D. M. White. Streams and caustics: the finegrained structure of cold dark matter haloes. *Mon. Not. R. Astron. Soc.* 413.2 (2011), pp. 1419–1438. (Cit. on p. 44).

[101] F. Governato and A. Zolotov. Cuspy no more: how outflows affect the central dark matter and baryon distribution in Λ cold dark matter galaxies. *Mon. Not. R. Astron. Soc.* 422.2 (2012), pp. 1231–1240. (Cit. on p. 45).

[102] E. Aprile et al. Dark matter results from 225 live days of XENON100 data. *Phys. Rev. Lett.* 109.18 (Nov. 2012), p. 181301. (Cit. on pp. 45, 52, 54).

[103] M. Robinson et al. Measurements of muon flux at 1070 m vertical depth in the Boulby underground laboratory. *Nucl. Instruments Methods Phys. Res. Sect. A Accel. Spectrometers, Detect. Assoc. Equip.* 511.3 (Oct. 2003), pp. 347–353. (Cit. on pp. 49, 71, 72).

[104] P. Cushman et al. Snowmass CF1 Summary: WIMP dark matter direct detection. *arXiv Prepr. arXiv1310.8327* (2013). (Cit. on pp. 49–51, 56).

[105] C. E. Aalseth et al. Results from a search for light-mass dark matter with a p-type point contact germanium detector. *Phys. Rev. Lett.* 106.13 (Mar. 2011), p. 131301. (Cit. on p. 49).

[106] R. Agnese et al. Silicon detector dark matter results from the final exposure of CDMS II. *Phys. Rev. Lett.* 111.25 (Dec. 2013), p. 251301. (Cit. on p. 50).

[107] Z. Ahmed et al. Results from the final exposure of the CDMS II experiment. *arXiv Prepr. arXiv0912.3592* (2009), pp. 1–6. (Cit. on p. 50).

[108] B. Censier. Final results of the EDELWEISS-I dark matter search with cryogenic heat-and-ionization Ge detectors. *Nucl. Instruments Methods Phys. Res. Sect. A Accel. Spectrometers, Detect. Assoc. Equip.* 559.2 (Apr. 2006), pp. 381–383. (Cit. on p. 50).

[109] G. Angloher et al. Results from 730 kg days of the CRESST-II dark matter search. *Eur. Phys. J. C* 72.4 (Apr. 2012), p. 1971. (Cit. on p. 50).

[110] D. S. Akerib et al. First results from the LUX dark matter experiment at the Sanford Underground Research Facility. *arXiv Prepr. arXiv1310.8214* (2013), pp. 1–11. (Cit. on pp. 51, 54).

[111] T. J. Sumner. The ZEPLIN III dark matter project. *New Astron. Rev.* 49.2-6 (May 2005), pp. 277–281. (Cit. on p. 52).

[112] M. Boulay. DEAP-3600 dark matter search at SNOLab. *J. Phys. Conf. Ser.* 375 (2012), p. 012027. (Cit. on p. 52).

[113] D. McKinsey. The Mini-CLEAN experiment. *Nucl. Phys. B-Proceedings Suppl.* 173 (2007), pp. 152–155. (Cit. on p. 52).

[114] A. Wright. The DarkSide program at LNGS. *Proc. DPF-2011 Conf.* Providence, 2011, pp. 1–7. (Cit. on p. 52).

[115] S. Archambault et al. Constraints on low-mass WIMP interactions on 19F from PI-CASSO. *Phys. Lett. B* 711.2 (May 2012), pp. 153–161. (Cit. on p. 52).

[116] M. Felizardo et al. Final analysis and results of the phase II SIMPLE dark matter search. *Phys. Rev. Lett.* 108 (2012), pp. 4–7. (Cit. on p. 52).

[117] E. Behnke et al. First dark matter search results from a 4-kg CF3I bubble chamber operated in a deep underground site. *Phys. Rev. D* 86.5 (2012), p. 052001. (Cit. on p. 53).

[118] R. Bernabei et al. Searching for WIMPs by the annual modulation signature. *Phys. Lett. B* 424 (1998), pp. 195–201. (Cit. on p. 53).

[119] R. Bernabei et al. New results from DAMA/LIBRA. *Eur. Phys. J. C* 67 (Mar. 2010), pp. 39–49. (Cit. on pp. 53, 54).

[120] J. Cherwinka et al. A search for the dark matter annual modulation in South Pole ice. *Astropart. Phys.* 35.11 (2011), pp. 749–754. (Cit. on p. 53).

[121] J. Amaré et al. Dark matter searches with NaI scintillators in the Canfranc underground laboratory: ANAIS experiment. *J. Phys. Conf. Ser.* 39 (May 2006), pp. 123–125. (Cit. on p. 53).

[122] S. C. Kim et al. New limits on interactions between weakly interacting massive particles and nucleons obtained with CsI(Tl) crystal detectors. *Phys. Rev. Lett.* 108.18 (2012), p. 181301. (Cit. on p. 53).

[123] K. Fushimi et al. Dark matter search by means of segmented scintillator (PICO-LON). *J. Phys. Conf. Ser.* 203 (Jan. 2010), p. 012046. (Cit. on p. 53).

[124] M. T. Frandsen et al. Resolving astrophysical uncertainties in dark matter direct detection. *J. Cosmol. Astropart. Phys.* 2012 (Jan. 2012), p. 024. (Cit. on p. 54).

[125] A. Desai and A. Moskowitz. *Dark Matter Tools*. http://dmtools.brown.edu/. 2013. (Cit. on p. 55).

[126] E. A. Baltz et al. Pre-launch estimates for GLAST sensitivity to dark matter annihilation signals. *J. Cosmol. Astropart. Phys.* 07 (2008), p. 013. (Cit. on p. 57).

[127] M. Ackermann et al. Fermi LAT search for dark matter in gamma-ray lines and the inclusive photon spectrum. *Phys. Rev. D* 86.2 (2012), p. 022002. (Cit. on p. 56).

[128] G. Zaharijas et al. Constraints on the galactic halo dark matter from Fermi-LAT diffuse measurements. *Proc. 8th Int. Work. Identif. dark matter (IDM 2010)*. 2010, p. 113. (Cit. on p. 56).

[129] D. Hooper, C. Kelso, and F. Queiroz. Stringent constraints on the dark matter annihilation cross section from the region of the Galactic Center. *Astropart. Phys.* 46 (2013), pp. 55–70. (Cit. on p. 57).

[130] A. Geringer-Sameth and S. M. Koushiappas. Exclusion of canonical weakly interacting massive particles by joint analysis of Milky Way dwarf galaxies with data from the Fermi gamma-ray space telescope. *Phys. Rev. Lett.* 107.24 (Dec. 2011), p. 241303. (Cit. on p. 57).

[131] C. Weniger. A tentative gamma-ray line from dark matter annihilation at the Fermi Large Area Telescope. *J. Cosmol. Astropart. Phys.* 2012 (Aug. 2012), p. 007. (Cit. on p. 57).

[132] W. C. Huang, A. Urbano, and W. Xue. Fermi Bubbles under dark matter scrutiny. Part I: astrophysical analysis. *arXiv Prepr. arXiv1307.6862* (2013). (Cit. on pp. 57, 58).

[133] A. Ibarra, D. Tran, and C. Weniger. Indirect searches for decaying dark matter. *Int. J. Mod. Phys. A* 28.27 (2013). (Cit. on p. 59).

[134] R. Abbasi et al. Multiyear search for dark matter annihilations in the Sun with the AMANDAII and IceCube detectors. *arXiv Prepr. arXiv1112.1840v2* (2012), pp. 1–14. (Cit. on p. 59).

[135] R. Abbasi et al. Search for neutrinos from annihilating dark matter in the direction of the galactic center with the 40-string IceCube neutrino observatory. *arXiv Prepr. arXiv1210.3557v3* (2013), pp. 1–11. (Cit. on p. 59).

[136] S. Orsi. PAMELA: A payload for antimatter matter exploration and light nuclei astrophysics. *Nucl. Instruments Methods Phys. Res. Sect. A Accel. Spectrometers, Detect. Assoc. Equip.* 580.2 (Oct. 2007), pp. 880–883. (Cit. on p. 59).

[137] O. Adriani et al. An anomalous positron abundance in cosmic rays with energies 1.5-100 GeV. *Nature* 458.7238 (Apr. 2009), pp. 607–9. (Cit. on p. 59).

[138] M Aguilar et al. First result from the alpha magnetic spectrometer on the International Space Station: precision measurement of the positron fraction in primary cosmic rays of 0.5350 GeV. *Phys. Rev. Lett.* 141102.April (2013), pp. 1–10. (Cit. on pp. 59, 60).

[139] A. Abdo et al. Measurement of the cosmic ray e++e- spectrum from 20 GeV to 1 TeV with the Fermi Large Area Telescope. *Phys. Rev. Lett.* 102.18 (May 2009), p. 181101. (Cit. on p. 59).

[140] G. Aad et al. Search for dark matter candidates and large extra dimensions in events with a jet and missing transverse momentum with the ATLAS detector. *J. High Energy Phys.* 2013.4 (Apr. 2013), p. 75. (Cit. on p. 61).

[141] L. Covi. Large Hadron Collider and Dark Matter. *Astron. Nachrichten* 334.6 (2013), pp. 605–610. (Cit. on pp. 61, 62).

[142] O. Buchmueller, M. J. Dolan, and C. McCabe. Beyond effective field theory for dark matter searches at the LHC. *J. High Energy Phys.* 2014.1 (2014). (Cit. on pp. 61, 62).

[143] A. Green and B. Morgan. Optimizing WIMP directional detectors. *Astropart. Phys.* 27.2-3 (Mar. 2007), pp. 142–149. (Cit. on pp. 62, 63, 70, 162).

[144] D. N. Spergel. Motion of the earth and the detection of weakly interacting massive particles. *Phys. Rev. D* 37.6 (1988), pp. 1353–1355. (Cit. on p. 63).

[145] S. Burgos et al. Measurement of the range component directional signature in a DRIFT-II detector using 252Cf neutrons. *Nucl. Instruments Methods Phys. Res. Sect. A Accel. Spectrometers, Detect. Assoc. Equip.* 600.2 (Mar. 2009), pp. 417–423. (Cit. on pp. 63, 141, 150, 151).

[146] S. M. Paling and A. S. J. Murphy. The Boulby Mine Underground Science Facility: the search for dark matter, and beyond. *Nucl. Phys. News* 22.1 (2012). (Cit. on p. 63).

[147] J. Billard et al. Directional detection as a strategy to discover Galactic dark matter. *Phys. Lett. B* 691.3 (July 2010), pp. 156–162. (Cit. on p. 64).

[148] E. Daw et al. Radon backgrounds in the DRIFT-II directional dark matter experiments. *arXiv Prepr. arXiv1307.5525* (2013). (Cit. on p. 63).

[149] D. P. Snowden-Ifft and J. L. Gauvreau. High precision measurements of carbon disulfide negative ion mobility and diffusion. *Rev. Sci. Instrum.* 84.5 (2013), p. 053304. (Cit. on pp. 63, 65, 110, 141, 142, 188).

[150] G. Alner et al. The DRIFT-II dark matter detector: design and commissioning. *Nucl. Instruments Methods Phys. Res. Sect. A Accel. Spectrometers, Detect. Assoc. Equip.* 555.1-2 (Dec. 2005), pp. 173–183. (Cit. on pp. 65, 80).

[151] D. Santos et al. MIMAC: A micro-TPC matrix for directional detection of dark matter. *J. Phys. Conf. Ser.* 309 (Aug. 2011), p. 012014. (Cit. on p. 65).

[152] J. Billard, F. Mayet, and D. Santos. Three-dimensional track reconstruction for directional dark matter detection. *J. Cosmol. Astropart. Phys.* 2012 (Apr. 2012), p. 006. (Cit. on pp. 65, 66).

[153] D. Dujmic et al. Results from DMTPC 10-liter detector. *J. Phys. Conf. Ser.* 203 (Jan. 2010), p. 012029. (Cit. on p. 66).

[154] S. Ahlen et al. First dark matter search results from a surface run of the 10-L DMTPC directional dark matter detector. *Phys. Lett. B* 695 (2011), pp. 124–129. (Cit. on p. 66).

[155] J. B. R. Battat et al. DMTPC: dark matter detection with directional sensitivity. *arXiv Prepr. arXiv1012.3912* (2010). (Cit. on pp. 66, 67).

[156] K. Nakamura et al. Low pressure gas study for a direction-sensitive dark matter search experiment with MPGD. *J. Instrum.* 7 (Feb. 2012), p. C02023. (Cit. on p. 66).

[157] A. Ochi et al. A new design of the gaseous imaging detector: Micro Pixel Chamber. *Nucl. Instruments Methods Phys. Res. Sect. A Accel. Spectrometers, Detect. Assoc. Equip.* 471.1–2 (Sept. 2001), pp. 264–267. (Cit. on p. 66).

[158] K. Nakamura et al. Newage. *J. Phys. Conf. Ser.* 375.1 (July 2012), p. 012013. (Cit. on p. 67).

[159] A. Ochi et al. Micro Pixel Chamber with resistive electrodes for spark reduction. *J. Instrum.* 9 (2014), p. C01039. (Cit. on pp. 67, 68).

[160] D. Loomba. R&D with implications for a directional low mass dark matter search. *Proc. 4th Work. Dir. Detect. Dark Matter (CYGNUS 2013)*. Ed. by T. Naka and K. Miuchi. DRIFT Collaboration. Toyama, 2013. (Cit. on pp. 68, 69, 80, 188).

[161] T. Naka et al. R&D status of nuclear emulsion for directional dark matter search. *Cygnus 2011 Third Int. Conf. Dir. Detect. Dark Matter*. EAS, 2011, pp. 51–58. (Cit. on p. 68).

[162] T. Katsuragawa et al. Status and analysis system of directional dark matter search with nuclear emulsion. *J. Phys. Conf. Ser.* 469 (2013), p. 012004. (Cit. on p. 68).

[163] D. Nygren. Columnar recombination: a tool for nuclear recoil directional sensitivity in a xenon-based direct detection WIMP search. *J. Phys. Conf. Ser.* 460 (2013), p. 012006. (Cit. on p. 69).

[164] M. Carson et al. Simulations of neutron background in a time projection chamber relevant to dark matter searches. *Nucl. Instruments Methods Phys. Res. Sect. A Accel. Spectrometers, Detect. Assoc. Equip.* 546.3 (July 2005), pp. 509–522. (Cit. on p. 72).

[165] S. Burgos et al. Track reconstruction and performance of DRIFT directional dark matter detectors using alpha particles. *Nucl. Instruments Methods Phys. Res. Sect. A Accel. Spectrometers, Detect. Assoc. Equip.* 584.1 (Jan. 2008), pp. 114–128. (Cit. on pp. 72, 115).

[166] H. Bethe and J Ashkin. Passage of Radiation Through Matter. *Exp. Nucl. Phys.* Ed. by E. Segré. New York: Wiley, 1953. (Cit. on p. 74).

[167] D. Snowden-Ifft, C. Martoff, and J. Burwell. Low pressure negative ion time projection chamber for dark matter search. *Phys. Rev. D* 61.10 (Apr. 2000), p. 101301. (Cit. on p. 74).

[168] R. Veenhof. *GARFIELD Software*. http://garfield.web.cern.ch/garfield/. 1984. (Cit. on p. 74).

[169] F. Sauli. *Principles of operation of multiwire proportional and drift chambers*. Tech. rep. 09. Geneva: CERN, 1977. (Cit. on pp. 74, 76).

[170] V. Radeka. Low-noise techniques in detectors. *Annu. Rev. Nucl. Part. Sci.* 38 (1988), pp. 217–277. (Cit. on pp. 75, 206).

[171] E. Daw and M. Pipe. Physics of charge readout in DRIFT. *Priv. Commun.* (2010). (Cit. on p. 75).

[172] D. N. Muna. Three Dimensional Analysis and Track Reconstruction in the DRIFT-II Dark Matter Detector. PhD thesis. University of Sheffield, 2008. (Cit. on pp. 76, 141, 142).

[173] J. Gauvreau. DRIFT private communication. *Priv. Commun.* (2012). (Cit. on p. 76).

[174] Cremat. *Cremat Charge Sensitive Preamplifiers*. `http://www.cremat.com/CSP_intro.htm`. 2013. (Cit. on p. 76).

[175] Cremat. *Cremat CR-200 Gaussian Shaping Amplifiers*. 2013. (Cit. on p. 77).

[176] E. R. Lee. Field cage simulations. *Priv. Commun.* (2011). (Cit. on p. 81).

[177] J. C. Davies. Neutron Backgrounds in the DRIFT Dark Matter Detector. PhD thesis. University of Sheffield, 2005. (Cit. on p. 80).

[178] M. Pipe. Limits on Spin-Dependent WIMP-Proton Cross-Sections using the DRIFT-IId Directional Dark Matter Detector. PhD thesis. University of Sheffield, 2011. (Cit. on pp. 81–83, 96–98, 127, 196, 199, 201).

[179] K. Pushkin and D. Snowden-Ifft. Measurements of W-value, mobility and gas gain in electronegative gaseous CS2 and CS2 gas mixtures. *Nucl. Instruments Methods Phys. Res. Sect. A Accel. Spectrometers, Detect. Assoc. Equip.* 606.3 (July 2009), pp. 569–577. (Cit. on pp. 83, 84, 185).

[180] A. Hitachi. Bragg-like curve for dark matter searches: binary gases. *Radiat. Phys. Chem.* 77.10–12 (Oct. 2008), pp. 1311–1317. (Cit. on pp. 84, 97).

[181] M. Robinson. *DRIFT Watch*. `https://www.hep.shef.ac.uk/research/dm/driftwatch/`. 2013. (Cit. on p. 85).

[182] R. C. Team. *R: A Language and Environment for Statistical Computing*. `http://www.r-project.org`. Vienna, 2013. (Cit. on p. 86).

[183] M. Robinson. *University of Sheffield PPPA Computing Cluster*. https://www.hep.shef.ac.uk/ganglia/. 2013. (Cit. on p. 87).

[184] W. H. Press et al. *Numerical Recipes*. 3rd ed. Cambridge University Press, 2007, pp. 650–655. (Cit. on p. 88).

[185] J. F. Ziegler. *Stopping Range of Ions in Matter (SRIM) Software*. http://www.srim.org/. 1985. (Cit. on pp. 92, 97, 104, 107, 108, 144).

[186] A. Savitzky and M. J. E. Golay. Smoothing and differentiation of data by simplified least squares procedures. *Anal. Chem.* 36.8 (1964), pp. 1627–1639. (Cit. on p. 92).

[187] E. Daw et al. Spin-dependent limits from the DRIFT-IId directional dark matter detector. *Astropart. Phys.* 35.7 (2012), pp. 397–401. (Cit. on pp. 93, 100, 101, 196).

[188] D. Snowden-Ifft. DRIFT-II simulations and limits. *Priv. Commun.* (2009). (Cit. on p. 97).

[189] W Feller. *An introduction to probability theory and its applications. Vol. I.* 3rd ed. Wiley, 1968. (Cit. on p. 97).

[190] W. Blum, W. Riegler, and L. Rolandi. *Particle detection with drift chambers*. Springer Verlag, 2008. (Cit. on p. 97).

[191] G. Feldman and R. Cousins. Unified approach to the classical statistical analysis of small signals. *Phys. Rev. D* 57.7 (1998), p. 3873. (Cit. on p. 99).

[192] T. Lawson. *Background measurements and activities at Boulby for JRA1*. Tech. rep. Paris: University of Sheffield, 2006. (Cit. on p. 103).

[193] R. Colle. A precise determination of the 222Rn half-life by 4pi-alpha-beta liquid scintillation measurements. *Radioact. Radiochem.* 6.1 (1995), pp. 16–29. (Cit. on pp. 103, 120).

[194] P. K. Hopke. The initial atmospheric behavior of radon decay products. *J. Radioanal. Nucl. Chem. Artic.* 203.2 (Mar. 1996), pp. 353–375. (Cit. on pp. 103, 116).

[195] L. Grodzins. *RAD7 Radon Detector.* `http://www.durridge.com/products_rad7.shtml`. 2009. (Cit. on pp. 116, 129).

[196] S. Paling. DRIFT radon emanation tests. *Priv. Commun.* (2006). (Cit. on pp. 123, 126, 127).

[197] G.-G. Park et al. Effect of PTFE contents in the gas diffusion media on the performance of PEMFC. *J. Power Sources* 131.1–2 (May 2004), pp. 182–187. (Cit. on p. 124).

[198] G. Keller, B. Hoffmann, and T. Feigenspan. Radon permeability and radon exhalation of building materials. *Sci. Total Environ.* 272.1–3 (May 2001), pp. 85–89. (Cit. on p. 125).

[199] A. Bassignani et al. Measurements of radon concentration and gamma ray activity in hall B of the Gran Sasso Laboratory. *Radiat. Meas.* 28 (1997), pp. 609–612. (Cit. on p. 129).

[200] D. Snowden-Ifft. Improved accuracy and precision in DRIFT-IIds Δz measurement. *Priv. Commun.* (2013). (Cit. on p. 141).

[201] D. Snowden-Ifft et al. Neutron recoils in the DRIFT detector. *Nucl. Instruments Methods Phys. Res. Sect. A Accel. Spectrometers, Detect. Assoc. Equip.* 498.1–3 (Feb. 2003), pp. 155–164. (Cit. on pp. 154, 193).

[202] D. Snowden-Ifft. Discovery of multiple, ionization-created anions in gas mixtures containing CS2 and O2. *Rev. Sci. Instrum.* 85.1 (2014), p. 013303. (Cit. on p. 164).

[203] MKS. *Baratron Capacitance Manometer.* `http://www.mksinst.com/product/category.aspx?CategoryID=72`. 2013. (Cit. on p. 167).

[204] Hiden. *Cracking Pattern Table*. www.hidenanalytical.com/index.php/en/cracking-patterns. 2013. (Cit. on p. 178).

[205] D. Snowden-Ifft. Minority carriers in DRIFT. *Priv. Commun.* (2013). (Cit. on pp. 181, 182).

[206] E. Miller. Removing high-pass filter overshoot. *Priv. Commun.* (2013). (Cit. on p. 186).

[207] W Shockley. Currents to conductors induced by a moving point charge. *J. Appl. Phys.* 9.1 (1938), pp. 635–636. (Cit. on p. 206).